

THE DISTRIBUTION OF ULTRASONIC HEATING
IN LOSSY CYLINDERS AND SPHERES

BY

LESTER ANDERSON LONGLEY

S.B., Massachusetts Institute of Technology, 1978

THESIS

Submitted in partial fulfillment of the requirements
for the degree of Master of Science in Electrical Engineering
in the Graduate College of the
University of Illinois at Urbana-Champaign, 1980

Urbana, Illinois

UNIVERSITY OF ILLINOIS AT URBANA-CHAMPAIGN

THE GRADUATE COLLEGE

January, 1980

WE HEREBY RECOMMEND THAT THE THESIS BY

LESTER ANDERSON LONGLEY

ENTITLED THE DISTRIBUTION OF ULTRASONIC HEATING IN LOSSY CYLINDERS

AND SPHERES

BE ACCEPTED IN PARTIAL FULFILLMENT OF THE REQUIREMENTS FOR

THE DEGREE OF MASTER OF SCIENCE

William D. Brown, Jr.

Director of Thesis Research

G. W. Swenson, Jr.

Head of Department

Committee on Final Examination†

Chairman

† Required for doctor's degree but not for master's.

ACKNOWLEDGEMENTS

I sincerely thank Professor Bill O'Brien for providing me with a very interesting and educational project, and for being flexible and understanding throughout the work. He has encouraged me and has frequently guided me toward reasonable approaches to difficult problems.

Many others have contributed in various ways. I am grateful to Professor Leon Frizzell for several helpful discussions, and to Professor Don Sechrest for supplying me with the spherical Bessel routines. I appreciate Professor O. L. Gaddy's generous yet practical attitude toward funding. Thanks go to Stan Kerr for solutions to numerous computer puzzlements and for his advice in general. I also wish to express my gratitude to Steve Holland for an excellent job of figure drawing, and to Jerry Bauck for assisting me in checking my computer programs. Finally, I thank Brenda Masters for a careful job of typing this thesis and for much help in satisfying format rules.

TABLE OF CONTENTS

CHAPTER	Page
1. INTRODUCTION.....	1
1.1 Perspective and Motivation.....	1
1.2 Problem to Be Solved.....	3
1.3 Approach for Solving Problem.....	4
2. THEORETICAL ANALYSIS AND COMPUTATIONAL METHODS.....	6
2.1 General.....	6
2.2 Calculation of Wave Distributions--Analytical Approach...	8
2.2.1 Soft cylinder.....	8
2.2.2 Rigid cylinder.....	17
2.2.3 Soft sphere.....	21
2.2.4 Rigid sphere.....	29
2.2.5 Computational issues.....	31
2.3 Calculation of Wave Distributions--Numerical Approach....	43
2.4 Estimation of Loss.....	60
3. COMPUTATIONAL DATA AND RESULTS.....	68
3.1 Data.....	68
3.2 Analytical Results.....	74
3.2.1 Checkout of programs.....	74
3.2.2 Spatial distributions.....	83
4. DISCUSSION AND CONCLUSIONS.....	117
REFERENCES.....	121
APPENDIX.....	123

LIST OF TABLES

	Page
1. Computer Programs.....	32
2. Mathematical Function Subroutines.....	34
3. "Standard" Values for Computational Parameters.....	69
4. Additional Quantities Calculated from Computational Parameters.....	70

1. INTRODUCTION

1.1 Perspective and Motivation

Ultrasound is widely used in medical diagnostics. Applications include fetal examination, diagnosis of cardiac problems, and blood-flow measurements. Although acoustic imaging is useful in its own right as a complement to x-ray examination, it is also desirable because low-level acoustic irradiation appears to be safer than that using x ray. Yet, it is known that sufficiently high acoustic intensity levels can destroy tissue, so that care must be exercised in ultrasonic irradiation of tissue. Topics currently under investigation include the mechanisms of acoustic effects on tissues and the levels at which these effects are manifested.

It is well known that warm-blooded creatures depend on a carefully regulated internal temperature for proper system functioning. It is possible for acoustic irradiation to interfere with this temperature balance, because the tissues are, in general, "lossy," meaning that some fraction of the acoustic wave energy is absorbed by the tissue and converted into heat. It is thought that this energy loss occurs as friction, by means of a bulk-viscosity mechanism.

This thesis is concerned with the possibility that unexpectedly high levels of heat generation might result from the nonuniform wave distributions which develop within irradiated tissues. The wave

distributions are nonuniform because each tissue component possesses distinct acoustic characteristics. Refraction and reflection at component interfaces can result in positive reinforcement of the wave, or a resonance. The degree of nonuniformity depends on the mismatch between the material properties and on the shapes of the distinct components.

This issue has been addressed by A. K. Chan and co-workers (1974), who determined the amount and distribution of heat generation in lossy tissue, for the specific case of longitudinal and shear wave propagation through multiple plane layers. For that problem, they verified that maximum heating always occurs at the layer boundaries; the amount of heating is dependent on the layer thicknesses and acoustic property mismatches.

H. N. Kritikos and H. P. Schwan (1972; 1975) analyzed the similar problem of heat generation by electromagnetic waves (termed "heating potential") in conducting spheres, of radii 5 and 10 cm. The latter sphere notably resembles a baby's head in both size and shape. For intermediate frequency ranges, maximum heating occurs near the center of the sphere, and otherwise is found at the front boundary. A later paper (Kritikos and Schwan, 1976) extended this work to include multi-layered spheres, which can be configured to correspond even more closely to a baby's head. Their most recent work (Kritikos and Schwan, 1979) analyzes the effects of heat conduction, and heat convection by means of blood flow.

1.2 Problem to Be Solved

The ultimate knowledge desired in the search for hot spots in tissue components is the temperature distributions within the objects. However, the determination of temperature distributions requires consideration of heat generation both by absorption in tissue of energy in the ultrasonic wave and by metabolic processes, and also heat removal by blood flow through the tissue. In addition, the effects of heat flow within the tissue and across its boundaries must be included. Of all these factors, only the first, that of absorptive energy loss (by the wave), is considered in this thesis. Certainly, sites of maximum heat generation by this mechanism are likely to exhibit higher temperatures than the surrounding tissue.

The wave energy loss is analyzed for two cases, an infinitely long cylinder and a sphere. It is assumed that each object has a uniform, lossy interior, similar to tissue, and that it is surrounded by a lossless material (assumed solely for simplicity) with different acoustical properties, similar to water. The loss occurring in the interior of each object has been calculated for the situation of a plane wave, originating an infinite distance away, being incident on the object. These calculations were made for various object sizes and acoustical properties, in order to elicit general trends in the locations and relative magnitudes of "hot spots."

The cylinder and sphere were chosen for examination partly for geometrical simplicity, and also because of biological relevance. Many vessels, tubes, axons, fibers, and small bones can be grossly

modelled as cylinders. Also, certain cell masses, such as glands, small tumors, and young fetuses are approximately spherical.

1.3 Approach for Solving Problem

The first step in determining loss is the calculation of steady-state pressure (p) and velocity (\bar{u}) distributions inside (and outside, for flexibility) a lossless cylinder or sphere, in the presence of the source wave. From these calculations, estimates for absorptive heat generation in lossy--but otherwise identical to the lossless--objects are obtained using two methods: the first based on a bulk-viscosity mechanism, and the other derived by extrapolating the use of the absorption coefficient (α). No perturbation of the lossless distributions was attempted to refine these estimates.

It was desired to calculate the p and \bar{u} distributions using a more flexible "numerical" approach, which would permit later modification of the incident wave, currently a plane wave, to represent arbitrary sources and also to allow expansion to more complicated geometrics. These solutions were to have been checked using a more restrictive--but simpler--"analytical" approach. However, because of the computational instabilities and inefficiencies associated with the "method of lines" technique described in Section 2.3, this particular numerical approach was unsuccessful, so that distributions were only obtained using the analytical approach.

The latter approach involves seeking general series-sum solutions which satisfy the differential equations describing acoustic wave

propagation, and then applying boundary conditions to arrive at a specific solution, by determining the values of the weighting coefficients of the series expression; this scheme follows the standard pattern for solving boundary-value problems.

Both the object and its surroundings are composed of fluid-like materials, so that the analytical approach is used to calculate wave solutions ("interior" and "scattered") for "soft," i.e., nonrigid, cylinders and spheres. However, as a check of the computational method, the p and \bar{u} distributions (scattered only) are also obtained for rigid objects, for which case results are available for comparison which are known to be correct (see Section 3.2.1). However, all numerical work was done with regard to the soft cylinder only.

All calculations were performed on a Cyber 175, using programs written in FORTRAN Extended, Version 4, including the package "FORSIM," on which the numerical work is based. The pressure and velocity distributions, and both of the estimated loss distributions, have been plotted in the form of isomagnitude contours; in addition, isophase contours are available for pressure and velocity. These plots make possible visible interpretation of the computational results.

2. THEORETICAL ANALYSIS AND COMPUTATIONAL METHODS

2.1 General

The subsequent analysis of acoustic wave spatial distributions under lossless conditions is based on the following "first-order" wave equations:

$$\frac{\partial p}{\partial t} = -\rho c^2 (\bar{\nabla} \cdot \bar{u}) \quad (1a)$$

and

$$\rho \frac{\partial \bar{u}}{\partial t} = -\bar{\nabla} p \quad (1b)$$

These equations are stated in terms of two wave variables, the scalar pressure (p) and the particle velocity vector (\bar{u}), and two material parameters, the acoustic velocity (c) and the density (ρ).

The first-order equations assume that the pressure and velocity amplitudes are small enough such that the particle displacements are linearly dependent on the pressure gradient; therefore, Equations 1 are valid only for lower-intensity waves. A second assumption, that the wave propagates adiabatically, is discussed in Section 2.4; this condition means that the entropy content of the wave remains approximately constant during compression (Morse and Ingard, 1968:230). Finally, the use of the scalar-variable pressure instead of the stress tensor follows from the assumption that all particle motion is longitudinal, so that no shear wave is present. This assumption is justified as follows, as shown by L. A. Frizzell (1975): because of its relatively

high attenuation in tissue, the shear wave exists only near the boundary, where it is created by mode conversion. Although the high attenuation results in a surface region of concentrated heating, the overall effect is low, owing to the relatively low conversion in tissue of energy from an incident longitudinal wave to a reflected or transmitted shear wave.

The wave equations (1) are coupled, by means of both variables p and \bar{u} . Alternatively, these equations can be restated as a single second-order differential equation (where "order" now refers to the order of the derivative--the motion is still first order, of course) in terms of pressure, by differentiating (1a) with respect to time (2), and substituting for $\partial \bar{u} / \partial t$ from (1b):

$$\begin{aligned}
 \frac{\partial^2 p}{\partial t^2} &= \frac{\partial}{\partial t} [-\rho c^2 (\bar{\nabla} \cdot \bar{u})] \\
 &= -\rho c^2 (\bar{\nabla} \cdot \frac{\partial \bar{u}}{\partial t}) \\
 &= c^2 \bar{\nabla} \cdot (\bar{\nabla} p) \\
 &\equiv c^2 \nabla^2 p
 \end{aligned} \tag{2}$$

If needed, \bar{u} can still be obtained from (1b), using p as found from (2).

The following notational conventions, illustrated using pressure (2), are used throughout the remainder of this thesis. The variables representing physical processes are real and time-varying, and are

simply denoted as p . Since the source wave is assumed to vary sinusoidally with time, the steady-state solutions for the wave variables are conveniently represented with complex notation:

$$p(\bar{r}, t) \equiv \text{Re}[\underline{p}(\bar{r}, t)] \quad (3)$$

where

$$\underline{p}(\bar{r}, t) \equiv \underline{p}'(\bar{r})\exp(-i\omega t) \quad (4)$$

and where \bar{r} is the coordinate position vector, i represents $\sqrt{-1}$, and ω is the angular frequency of the source wave. The use of $-i$ follows Morse and Ingard (1968:12) and simplifies subsequent wave expressions. Note the use of the underscore, as in \underline{p} , to denote a complex quantity. The complex variables, such as \underline{p} , depend on time and space, just as do the real variables, such as p . Both sets of variables can be used interchangeably in linear relations, in particular in the first-order wave equations. The complex amplitudes, such as \underline{p}' , are only spatially dependent and thus provide a concise description of the steady-state solution. Finally, the magnitude and phase of a complex quantity \underline{p} are written as $|\underline{p}|$ and $\angle \underline{p}$, respectively.

2.2 Calculation of Wave Distributions--Analytical Approach

2.2.1 Soft cylinder. It is desired to find the acoustic wave distribution resulting when a source plane wave is incident on a "soft" cylinder, as shown in Figure 1.

The wave equations (1) in terms of cylindrical coordinates are

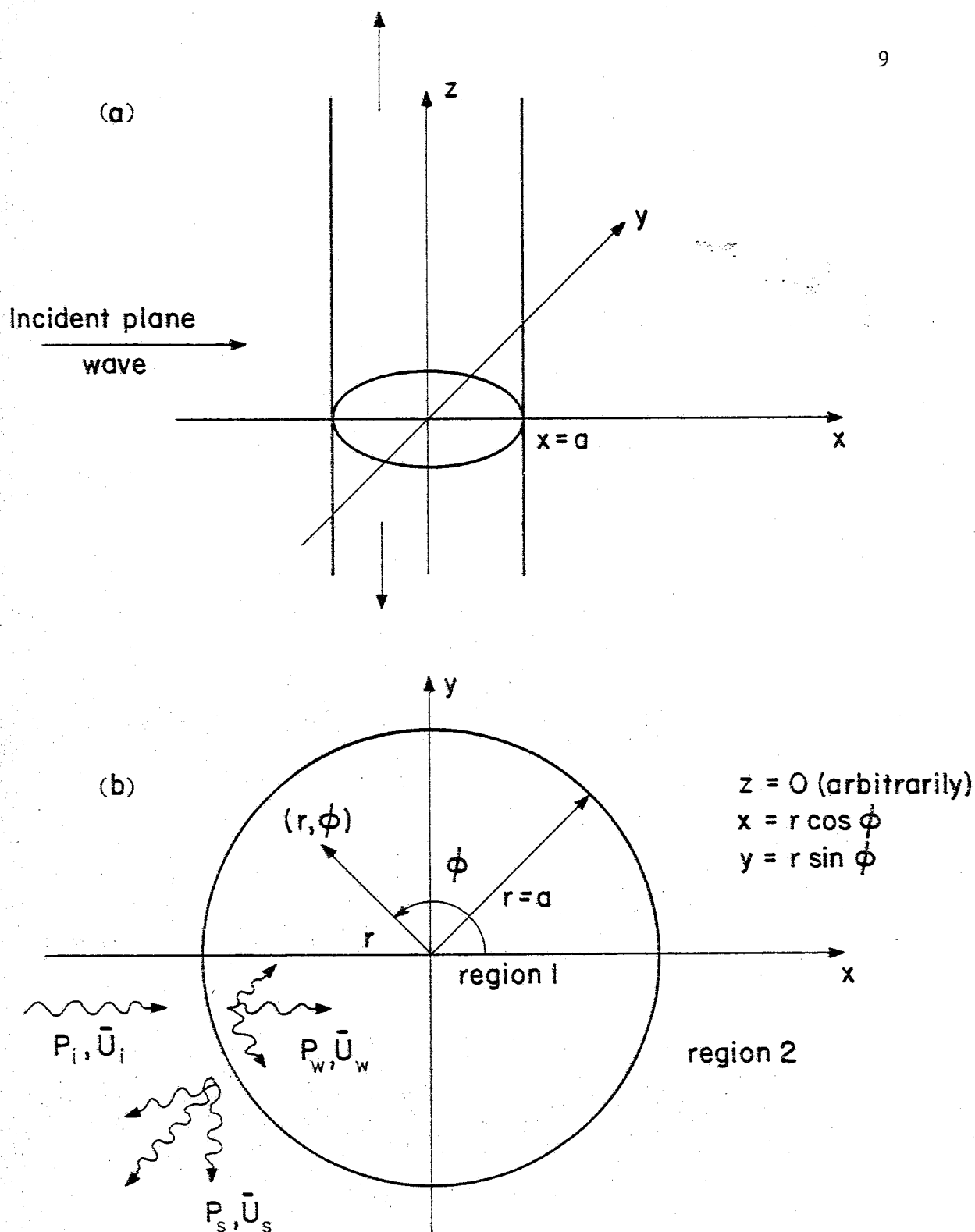


Figure 1. Illustration of soft-cylinder problem geometry. (a) Three-dimensional drawing of cylinder of radius a and of infinite extent in the \hat{z} direction, showing cylindrical coordinate system and incident plane wave (travelling in the $+\hat{x}$ direction). (b) Cross section of cylinder, showing polar coordinate subsystem, wave components, and region definitions.

$$\begin{aligned}
\frac{\partial p(r, \phi, z, t)}{\partial t} &= -\rho c^2 (\bar{\nabla} \cdot \bar{u}) \\
&= -\rho c^2 \left[\left(\frac{1}{r} \right) \frac{\partial}{\partial r} (r u_r) + \left(\frac{1}{r} \right) \frac{\partial u_\phi}{\partial \phi} + \frac{\partial u_z}{\partial z} \right]
\end{aligned} \tag{5a}$$

and

$$\begin{aligned}
\rho \frac{\partial \bar{u}(r, \phi, z, t)}{\partial t} &= -\bar{\nabla} p \\
&= - \left[\hat{r} \frac{\partial p}{\partial r} + \hat{\phi} \left(\frac{1}{r} \right) \frac{\partial p}{\partial \phi} + \hat{z} \frac{\partial p}{\partial z} \right]
\end{aligned} \tag{5b}$$

where \hat{r} , $\hat{\phi}$, and \hat{z} are unit vectors in the indicated directions.

For the specific case pictured in Figure 1, all variables are independent of the coordinate z , so that Equations 5 reduce to the form:

$$\frac{\partial p(r, \phi, t)}{\partial t} = -\rho c^2 \left[\left(\frac{1}{r} \right) \frac{\partial}{\partial r} (r u_r) + \left(\frac{1}{r} \right) \frac{\partial u_\phi}{\partial \phi} \right] \tag{6a}$$

and

$$\rho \frac{\partial \bar{u}(r, \phi, t)}{\partial t} = - \left[\hat{r} \frac{\partial p}{\partial r} + \hat{\phi} \left(\frac{1}{r} \right) \frac{\partial p}{\partial \phi} \right] \tag{6b}$$

where

$$\bar{u} \equiv \hat{r} u_r + \hat{\phi} u_\phi \tag{7}$$

However, coupled wave equations (6) are presented here mainly for later reference. The wave solution is found much more easily by combining the relations into a single second-order equation in terms of a single variable (p). After the solution for p is obtained, an expression for \bar{u} can be found from (6b).

The combined wave equation (2) (derived in Section 2.1), written using polar coordinates, is

$$\begin{aligned} \frac{\partial^2 p}{\partial t^2} &= c^2 \nabla^2 p \\ &= c^2 \left[\left(\frac{1}{r} \right) \frac{\partial}{\partial r} \left(r \frac{\partial p}{\partial r} \right) + \left(\frac{1}{r^2} \right) \frac{\partial^2 p}{\partial \phi^2} \right] \end{aligned} \quad (8)$$

This equation can be solved by the method of separation-of-variables, resulting in a general solution containing a sinusoidal time factor, a radial factor in terms of cylindrical Bessel functions, and a sinusoidal angular factor. The proposed total solution of (8) is made up of a linear combination of all possible solutions of the form just described:

$$p(r, \phi, t) = \left\{ \sum_{m=0}^{\infty} [A_m J_m(kr) + B_m Y_m(kr)] \cos(m\phi) \right\} \exp(-i\omega t) \quad (9)$$

where k is the wavenumber, A_m and B_m are complex weighting amplitudes, and J_m and Y_m are cylindrical Bessel functions of the first and second kind, respectively, and of order m . Only the cosine function is used for angular dependence, because the problem is symmetrical with respect to the x -axis, or the line $\phi = 0$.

The wave equation (8) must be solved separately in the two regions shown in Figure 1. The pressure within the interior of the cylinder (region 1) is denoted by p_w , while the pressure outside (region 2) is given by $p_s + p_i$. The symbol p_s represents the scattered component, and p_i is the known incident plane wave (Morse and Ingard, 1968:401), travelling in the $+\hat{x}$ direction:

$$\begin{aligned}
p_i(x, t) &= P \exp[i(k_2 x - \omega t)] \\
&= P \exp[i(k_2 r \cos \phi - \omega t)] \\
&= \left[P J_0(k_2 r) + \sum_{m=1}^{\infty} (2P i^m) J_m(k_2 r) \cos(m\phi) \right] \exp(-i\omega t), \\
&\qquad\qquad\qquad r \geq a \quad (10)
\end{aligned}$$

where P is the wave amplitude, and a is the cylinder radius. Note the use of the subscript "2" to signify values of constants describing the properties of the material in region 2 (and similarly for region 1).

The incident wave component can be thought of as the wave which would be present everywhere (not just in region 2, where it is used for this problem) if the cylinder were not present. The latter condition occurs if the acoustic properties of region 1 are identical to those of region 2.

Certainly, p_w and $p_s + p_i$ must satisfy the wave equation (8). Because the equation is linear, p_s and p_i (in addition to p_w) must individually be valid solutions. It can be readily verified in Equation 10 that p_i is of the required form (9). Expressions are sought for p_w and p_s which are also of this general form. In fact, the following more specific forms are proposed:

$$p_w(r, \phi, t) = \left[\sum_{m=0}^{\infty} \frac{W_m}{m} J_m(k_1 r) \cos(m\phi) \right] \exp(-i\omega t), \quad 0 \leq r \leq a \quad (11a)$$

and

$$p_s(r, \phi, t) = \left[\sum_{m=0}^{\infty} \frac{S_m}{m} H_m(k_2 r) \cos(m\phi) \right] \exp(-i\omega t), \quad r \geq a \quad (11b)$$

where

$$\underline{H}_m(k_2 r) \equiv J_m(k_2 r) + i Y_m(k_2 r) \quad (12)$$

is the Hankel function of the first kind and of order m , and \underline{W}_m and \underline{S}_m are complex weighting amplitudes (to be determined). The function $Y_m(k_1 r)$ is not included in the expression for \underline{p}_w because $Y_m(k_1 r) \rightarrow -\infty$ (for all orders $m = 0, 1, \dots$) as $r \rightarrow 0$, which would prevent \underline{p}_w from being finite everywhere in region 1, as required physically. The Hankel function is used to express \underline{p}_s because \underline{H}_m represents an outgoing wave as $r \rightarrow \infty$, as shown in Hildebrand (1962:147-154).

Before the boundary conditions can be applied (to solve for \underline{W}_m and \underline{S}_m), expressions must be obtained for \underline{u}_w , \underline{u}_s , and \underline{u}_i (the velocity vectors corresponding to \underline{p}_w , \underline{p}_s , and \underline{p}_i , respectively) in terms of \underline{W}_m and \underline{S}_m . The velocity vectors are found by substituting the expressions for pressure given in Equations 11a,b and 10 into the wave equation (6b). The velocity \underline{u} is obtained as a pair of scalars: the radial component u_r , and the tangential component u_ϕ . Accordingly, the vector wave equation for velocity is first rewritten as a pair of scalar equations:

$$\frac{\partial u_r}{\partial t} = -\left(\frac{1}{\rho}\right) \frac{\partial p}{\partial r} \quad (13a)$$

and

$$\frac{\partial u_\phi}{\partial t} = -\left(\frac{1}{\rho r}\right) \frac{\partial p}{\partial \phi} \quad (13b)$$

Expressions for the radial velocity components are thus immediately found from Equation 13a and Equations 11a,b and 10:

$$\begin{aligned} u_{rw}(r, \phi, t) = \frac{i}{Z_1} \left\{ W_0 J_1(k_1 r) + \sum_{m=1}^{\infty} \left(\frac{1}{2} W_m \right) [J_{m+1}(k_1 r) - J_{m-1}(k_1 r)] \right. \\ \left. \times \cos(m\phi) \right\} \exp(-i\omega t) \end{aligned} \quad (14a)$$

$$\begin{aligned} u_{rs}(r, \phi, t) = \frac{i}{Z_2} \left\{ S_0 H_1(k_2 r) + \sum_{m=1}^{\infty} \left(\frac{1}{2} S_m \right) [H_{m+1}(k_2 r) - H_{m-1}(k_2 r)] \right. \\ \left. \times \cos(m\phi) \right\} \exp(-i\omega t) \end{aligned} \quad (14b)$$

and

$$\begin{aligned} u_{ri}(r, \phi, t) = \frac{i}{Z_2} \left\{ P J_1(k_2 r) + \sum_{m=1}^{\infty} (P i^m) [J_{m+1}(k_2 r) - J_{m-1}(k_2 r)] \right. \\ \left. \times \cos(m\phi) \right\} \exp(-i\omega t) \end{aligned} \quad (14c)$$

where

$$Z_1 \equiv \rho_1 c_1 \quad (15a)$$

and

$$Z_2 \equiv \rho_2 c_2 \quad (15b)$$

(The quantities Z_1 and Z_2 are called characteristic acoustic impedances.)

In obtaining the above expressions, the following relation (Morse and Ingard, 1968:7-8) concerning derivatives of Bessel functions is used:

$$\frac{d}{dx} [J_m(x)] = -\frac{1}{2} [J_{m+1}(x) - J_{m-1}(x)] \quad (16)$$

where

$$J_{-m}(x) = (-1)^m J_m(x) \quad (17)$$

Equations 16 and 17 also hold true with J replaced by \underline{H} (or Y).

Although they are not needed for the application of boundary conditions, expressions for the tangential velocity component \underline{u}_ϕ are also presented now. The formulas for \underline{u}_ϕ are obtained in the same manner as those for \underline{u}_r , except that Equation 13b is used instead of (13a),

resulting in

$$\underline{u}_{\phi w}(r, \phi, t) = \frac{i}{Z_1 \cdot k_1 r} \left\{ \sum_{m=1}^{\infty} \frac{W}{m} J_m(k_1 r) [m \sin(m\phi)] \right\} \exp(-i\omega t) \quad (18a)$$

$$\underline{u}_{\phi s}(r, \phi, t) = \frac{i}{Z_2 \cdot k_2 r} \left\{ \sum_{m=1}^{\infty} \frac{S}{m} H_m(k_2 r) [m \sin(m\phi)] \right\} \exp(-i\omega t) \quad (18b)$$

and

$$\underline{u}_{\phi i}(r, \phi, t) = \frac{i}{Z_2 \cdot k_2 r} \left\{ \sum_{m=1}^{\infty} (2P i^m) J_m(k_2 r) [m \sin(m\phi)] \right\} \exp(-i\omega t) \quad (18c)$$

The following dispersion relations, implied by the wave equation (2), have been used in reaching both Equations 14 and Equations 18:

$$\frac{\omega}{k_1} = c_1 \quad (19a)$$

and

$$\frac{\omega}{k_2} = c_2 \quad (19b)$$

If c_1 and c_2 were assumed to be frequency-independent, then these relations would imply that both media would be nondispersive (i.e., the phase velocities ω/k_1 and ω/k_2 would be constant with respect to frequency). However, such an assumption does not simplify this development, because all steady-state solutions are of a single frequency, owing to the simple-harmonic source wave of Equation 10. Therefore, no assumptions are made about the frequency dependence of c_1 and c_2 , in order to maintain the generality of this analysis. Note that

frequency independence is assumed in Section 3.1 in accordance with physical properties, in spite of the theoretical generality.

It is now appropriate to apply the boundary conditions at the cylinder boundary ($r = a$). These conditions require continuity of pressure (p) and of the normal (i.e., radial) component of particle velocity (u_r):

$$p_w(r = a, \phi, t) = p_s(r = a, \phi, t) + p_i(r = a, \phi, t) \quad (20a)$$

and

$$u_{rw}(r = a, \phi, t) = u_{rs}(r = a, \phi, t) + u_{ri}(r = a, \phi, t) \quad (20b)$$

Expressions for \underline{W}_m and \underline{S}_m are obtained by substituting the infinite-series descriptions of p and u_r given in Equations 10, 11 and 14, and equating coefficients of $\cos(m\phi)$ (since (20) must hold true for all ϕ). After some algebraic manipulations, the final results for $m = 0$ are

$$\underline{W}_0 = \frac{P}{\underline{\Delta}_0} [\underline{H}_1(k_2 a) J_0(k_2 a) - \underline{H}_0(k_2 a) J_1(k_2 a)] \quad (21a)$$

and

$$\underline{S}_0 = - \frac{P}{\underline{\Delta}_0} [J_1(k_2 a) J_0(k_1 a) - J_0(k_2 a) J_1(k_1 a) \cdot Z_r] \quad (21b)$$

where

$$\underline{\Delta}_0 = \underline{H}_1(k_2 a) J_0(k_1 a) - \underline{H}_0(k_2 a) J_1(k_1 a) \cdot Z_r \quad (22)$$

and

$$Z_r \equiv \frac{Z_2}{Z_1} \quad (23)$$

The corresponding expressions for $m > 0$ are

$$\begin{aligned} \underline{W}_m = \frac{(2P_i^m)}{\underline{\Delta}_m} \left\{ [\underline{H}_{m+1}(k_2\alpha) - \underline{H}_{m-1}(k_2\alpha)] J_m(k_2\alpha) \right. \\ \left. - \underline{H}_m(k_2\alpha) [J_{m+1}(k_2\alpha) - J_{m-1}(k_2\alpha)] \right\} \end{aligned} \quad (24a)$$

and

$$\begin{aligned} \underline{S}_m = \frac{(-2P_i^m)}{\underline{\Delta}_m} \left\{ [J_{m+1}(k_2\alpha) - J_{m-1}(k_2\alpha)] J_m(k_1\alpha) \right. \\ \left. - J_m(k_2\alpha) [J_{m+1}(k_1\alpha) - J_{m-1}(k_1\alpha)] \cdot Z_r \right\} \end{aligned} \quad (24b)$$

where

$$\begin{aligned} \underline{\Delta}_m = [\underline{H}_{m+1}(k_2\alpha) - \underline{H}_{m-1}(k_2\alpha)] J_m(k_1\alpha) \\ - \underline{H}_m(k_2\alpha) [J_{m+1}(k_1\alpha) - J_{m-1}(k_1\alpha)] \cdot Z_r \end{aligned} \quad (25)$$

2.2.2 Rigid cylinder. The rigid-cylinder problem is a special case of the soft-cylinder problem (Section 2.2.1), for which the inelastic cylinder is described by its elasticity κ_1 approaching zero ($\kappa_1 \rightarrow 0$). As shown by the following equation (Morse and Ingard, 1968: 233), derived from an energy balance constraint, an object is rigid (i.e., has low κ_1) is either (or both) its density ρ_1 or its acoustic velocity c_1 is high:

$$\kappa_1 = \frac{1}{\rho_1 c_1^2} \quad (26)$$

Certainly, the latter case of high c_1 describes the typical rigid object. However, the complementary case of a very dense (high ρ_1) object is considered here, because it is mathematically more convenient. After all, the rigid-cylinder problem is analyzed only for the sake of checking the more general soft-cylinder problem, and not for learning more about realistic rigid cylinders.

Now, for a rigid cylinder with finite c_1 and infinite ρ_1 (i.e., $\rho_1 \rightarrow \infty$), it is readily seen from Equation 15a that the specific acoustic impedance Z_1 is also infinite (i.e., $Z_1 \rightarrow \infty$). Note, however, that the wavenumber k_1 is unaffected as $\rho_1 \rightarrow \infty$, as shown by (19a), so that the Bessel functions in the series solutions are well behaved. Therefore, the interior particle velocity $\bar{u}_w \rightarrow 0$, in accordance with $Z_1 \rightarrow \infty$ in (14a) and (18a); this assumes $\frac{W}{m}$ remains bounded, as can be easily shown. A nonzero pressure does, however, exist in the interior of a (very dense) rigid cylinder. (Note that for a rigid cylinder with $c_1 \rightarrow 0$, the wavenumber $k_1 \rightarrow 0$, resulting in "strange" behavior of the Bessel functions and, even more importantly, requiring special interpretation of the results.)

Using the fact that $\bar{u}_w = 0$ for the rigid-cylinder case, the variables describing the scattered wave (\bar{p}_s and \bar{u}_s) can be determined (without attention to \bar{p}_w). Note that \bar{p}_i and \bar{u}_i are still given by (10), (14c), and (18c). Region 1 needs no further consideration, because the subsequent analysis applies solely to region 2. Accordingly, the subscript "2" is dropped from the various constants and variables pertaining to that region (i.e., this becomes a single-region problem).

The wave equation (8) and thus the general expressions for p_s (11b), u_{rs} (14b), and $u_{\phi s}$ (18b) are unchanged (this is assumed earlier in showing that $u_w \rightarrow 0$). The boundary conditions (from Equations 20) are now

$$p_w(r = a, \phi, t) = p_s(r = a, \phi, t) + p_i(r = a, \phi, t) \quad (27a)$$

and

$$u_{rw}(r = a, \phi, t) = 0 = u_{rs}(r = a, \phi, t) + u_{ri}(r = a, \phi, t) \quad (27b)$$

The second relation can be rewritten as

$$u_{rs}(r = a, \phi, t) = -u_{ri}(r = a, \phi, t) \quad (28)$$

so that the scattered solution (u_{rs} , and eventually p_s and $u_{\phi s}$) is fully determined by the incident wave. The first relation (27a) is not needed for present purposes, although it can be used to obtain p_w (the condition $u_w = 0$ is already known).

The weighting coefficients S_m are obtained directly from this equation, again by matching coefficients of $\cos(m\phi)$, as done in the soft-cylinder case. The solution is easily found to be

$$S_0 = \frac{-PJ_1(ka)}{H_1(ka)} \quad (29a)$$

and

$$S_m = \frac{(-2Pi^m)[J_{m+1}(ka) - J_{m-1}(ka)]}{[H_{m+1}(ka) - H_{m-1}(ka)]}, \quad m > 0 \quad (29b)$$

After some algebraic manipulation, it can be verified that this solution matches that obtained by Morse and Ingard (1968:401). Furthermore, the solution for the soft-cylinder problem (which this author has been unable to locate in any textbook) can be checked in the limiting case of the rigid cylinder. Thus for $\rho_1 \rightarrow \infty$ and thus $Z_1 \rightarrow \infty$, then $Z_p \rightarrow 0$ according to Equation 23. Applying this condition to (21b) and (24b) and also to (22) and (25) of the soft-cylinder problem, substituting for $\underline{\Delta}_m$ in \underline{S}_m , and replacing k_2 by k , yield the above expressions for \underline{S}_m , obtained for the rigid-cylinder problem. This procedure also served as a computational check of the soft-cylinder program "SCL" (see Section 3.2.1).

The task of solving only for the scattered wave variables might seem irrelevant in the light of the primary focus of this thesis on the wave distribution within the cylinder. The motivation behind solving the rigid-cylinder problem lies in its usefulness for checking the numerical results of the more general soft-cylinder case, as just mentioned. The rigid-cylinder program "RCL" was itself checked on the basis of its far-field radial intensity distribution; these procedures are described in Section 3.2.1. For present purpose, it is sufficient to note that the time-averaged intensity vector is given by

$$\langle \bar{I} \rangle = \frac{1}{2} \text{Re}[\underline{p}'(\underline{u}')^*] \quad (30)$$

where the brackets ($\langle \rangle$) denote time-averaging and the superscript asterisk (*) signifies the complex conjugate. Thus the (time-averaged) radial component of the intensity of the scattered wave, i.e., the

variable of interest in the checkout process, is obtained as follows:

$$\langle I_{rs} \rangle = \frac{1}{2} \operatorname{Re} [p'_s(u'_{rs})^*] \quad (31)$$

2.2.3 Soft sphere. This problem (see Figure 2) bears a remarkable similarity to that of the soft cylinder, so that its treatment is somewhat abbreviated, in order to avoid repetition. Much of the notation is the same to emphasize the similarity, but it must be kept in mind that the repeated symbols do not necessarily represent exactly the same quantities.

In terms of spherical coordinates, the wave equations are

$$\begin{aligned} \frac{\partial p(r, \theta, \psi, t)}{\partial t} &= -\rho c^2 (\bar{\nabla} \cdot \bar{u}) \\ &= -\rho c^2 \left[\left(\frac{1}{r^2} \right) \frac{\partial}{\partial r} (r^2 u_r) + \left(\frac{1}{r \sin \theta} \right) \frac{\partial}{\partial \theta} (u_\theta \sin \theta) \right. \\ &\quad \left. + \left(\frac{1}{r \sin \theta} \right) \frac{\partial u_\psi}{\partial \psi} \right] \end{aligned} \quad (32a)$$

and

$$\begin{aligned} \rho \frac{\partial \bar{u}(r, \theta, \psi, t)}{\partial t} &= -\bar{\nabla} p \\ &= - \left[\hat{r} \frac{\partial p}{\partial r} + \hat{\theta} \left(\frac{1}{r} \right) \frac{\partial p}{\partial \theta} + \hat{\psi} \left(\frac{1}{r \sin \theta} \right) \frac{\partial p}{\partial \psi} \right] \end{aligned} \quad (32b)$$

where \hat{r} , $\hat{\theta}$, and $\hat{\psi}$ are unit vectors in the specified directions.

As can be seen in Figure 2, all variables are independent of the angle ψ , because of the symmetry resulting from the plane wave source. The following simplified wave equations are thus obtained:

$$\frac{\partial p(r, \theta, t)}{\partial t} = -\rho c^2 \left[\left(\frac{1}{r^2} \right) \frac{\partial}{\partial r} (r^2 u_r) + \left(\frac{1}{r \sin \theta} \right) \frac{\partial}{\partial \theta} (u_\theta \sin \theta) \right] \quad (33a)$$

and

$$\rho \frac{\partial \bar{u}}{\partial t}(r, \theta, t) = - \left[\hat{r} \frac{\partial p}{\partial r} + \hat{\theta} \left(\frac{1}{r} \right) \frac{\partial}{\partial \theta} \right] \quad (33b)$$

where

$$\bar{u} \equiv \hat{r} u_r + \hat{\theta} u_\theta \quad (34)$$

Note that the simplified spherical and cylindrical wave equations, (33) and (6), respectively, resemble each other much more than do the general forms of those equations, namely (32) and (5). In fact, equating θ and ϕ makes (33b) and (6b) identical.

Again, these first-order coupled equations are combined into a single second-order wave equation:

$$\begin{aligned} \frac{\partial^2 p}{\partial t^2} &= c^2 \nabla^2 p \\ &= c^2 \left[\left(\frac{1}{r^2} \right) \frac{\partial}{\partial r} \left(r^2 \frac{\partial p}{\partial r} \right) + \left(\frac{1}{r^2 \sin \theta} \right) \frac{\partial}{\partial \theta} \left(\sin \theta \frac{\partial p}{\partial \theta} \right) \right] \end{aligned} \quad (35)$$

The general solution obtained using the method of separation-of-variables again includes a sinusoidal time factor (as in the cylindrical case), a radial factor in terms of spherical Bessel functions, and an angular factor made up of Legendre polynomials. The corresponding total solution is a linear combination of terms of the preceding form:

$$p(r, \theta, t) = \left\{ \sum_{m=0}^{\infty} [A_m j_m(kr) + B_m y_m(kr)] P_m(\cos \theta) \right\} \exp(-i\omega t) \quad (36)$$

where j_m and y_m are spherical Bessel functions of the first and second kind, respectively, and $P_m(\cos \theta)$ is the Legendre polynomial, all of order m . The remaining quantities are defined the same as for Equation 9. Note that $P_m(\cos \theta)$ is an even function with respect to θ , as required for a problem which exhibits independence with respect to ψ .

As illustrated in Figure 2, regions 1 and 2 correspond to the interior and exterior of the sphere, respectively. The incident plane wave first given in Equations 10 is now reoriented in the $+\hat{z}$ direction and reexpressed in terms of spherical coordinates and the basis functions just described (Morse and Ingard, 1968:419):

$$\begin{aligned} p_i(r, \theta, t) &= P \exp[i(k_2 z - \omega t)] \\ &= P \exp[i(k_2 r \cos \theta - \omega t)] \\ &= \left\{ \sum_{m=0}^{\infty} [(2m+1)P_m^m] j_m(k_2 r) P_m(\cos \theta) \right\} \exp(-i\omega t), \\ &\qquad\qquad\qquad r \geq a \quad (37) \end{aligned}$$

where a is the radius of the sphere, and again, the remaining quantities assume the same definitions as in the cylindrical case.

The pressure within the sphere (p_w) and the scattered component (p_s) are sought in the following forms:

$$p_w(r, \theta, t) = \left[\sum_{m=0}^{\infty} \frac{W_m}{m} j_m(k_1 r) P_m(\cos \theta) \right] \exp(-i\omega t), \quad 0 \leq r \leq a \quad (38a)$$

and

$$p_s(r, \theta, t) = \left[\sum_{m=0}^{\infty} \frac{S_m}{m} h_m(k_2 r) P_m(\cos \theta) \right] \exp(-i\omega t), \quad r \geq a \quad (38b)$$

where

$$\underline{h}_m(k_2 r) \equiv j_m(k_2 r) + i y_m(k_2 r) \quad (39)$$

is the spherical Hankel function of the first kind and of order m , and \underline{W}_m and \underline{S}_m are the complex weighting coefficients whose values are sought. The same reasoning applies to these particular choices of spherical Bessel functions, as with the corresponding cylindrical Bessel functions, because y_m becomes infinite as $r \rightarrow 0$ (Morse and Ingard, 1968:337).

In order to obtain expressions for the velocity components (the radial component is again required for application of boundary conditions), the wave equation for the velocity vector (33b) is rewritten in scalar form:

$$\frac{\partial u_r}{\partial t}(r, \theta, t) = -\left(\frac{1}{\rho}\right) \frac{\partial p}{\partial r} \quad (40a)$$

and

$$\frac{\partial u_\theta}{\partial t}(r, \theta, t) = -\left(\frac{1}{\rho r}\right) \frac{\partial p}{\partial \theta} \quad (40b)$$

Expressions for the radial components of the velocity vectors are obtained by substituting into (40a) the pressure functions given in Equations 38a,b and 37, yielding

$$\begin{aligned} \underline{u}_r(r, \theta, t) = \frac{i}{Z_1} \left\{ \sum_{m=0}^{\infty} \left(\frac{\underline{W}_m}{2m+1} \right) [(m+1)j_{m+1}(k_1 r) - m j_{m-1}(k_1 r)] \right. \\ \left. \times P_m(\cos \theta) \right\} \exp(-i\omega t) \end{aligned} \quad (41a)$$

$$\begin{aligned} \frac{u_{rs}}{Z_2}(r, \theta, t) = \frac{i}{Z_2} \left\{ \sum_{m=0}^{\infty} \left(\frac{S_m}{2m+1} \right) [(m+1)h_{m+1}(k_2 r) - mh_{m-1}(k_2 r)] \right. \\ \left. \times P_m(\cos \theta) \right\} \exp(-i\omega t) \end{aligned} \quad (41b)$$

and

$$\begin{aligned} \frac{u_{ri}}{Z_2}(r, \theta, t) = \frac{i}{Z_2} \left\{ \sum_{m=0}^{\infty} (P_i^m) [(m+1)j_{m+1}(k_2 r) - mj_{m-1}(k_2 r)] \right. \\ \left. \times P_m(\cos \theta) \right\} \exp(-i\omega t) \end{aligned} \quad (41c)$$

where Z_1 and Z_2 are defined in Equations 15. The expressions (41) are reached through the use of the following relationship (Morse and Ingard, 1968:338) between spherical Bessel functions:

$$\frac{d}{dx}[j_m(x)] = -\left(\frac{1}{2m+1}\right) [(m+1)j_{m+1}(x) - mj_{m-1}(x)] \quad (42)$$

An expression for $j_{-m}(x)$ in terms of nonnegative orders is not required, because the coefficient of j_{-1} in the term $m=0$ is zero. Thus no spherical counterpart of the cylindrical relation (17) is required, nor is separate handling of the term $m=0$ needed. Again, the above statements regarding spherical Bessel relations hold true for j replaced by \underline{h} (or y).

The following expressions for the tangential velocity components are derived using Equation 40b:

$$\frac{u_{\theta w}}{Z_1}(r, \theta, t) = \frac{i}{Z_1 \cdot k_1 r} \left\{ \sum_{m=0}^{\infty} \frac{W}{m} j_m(k_1 r) [P'_m(\cos \theta) \sin \theta] \right\} \exp(-i\omega t) \quad (43a)$$

$$\frac{u}{\theta}_s(r, \theta, t) = \frac{i}{Z_2 \cdot k_2^r} \left\{ \sum_{m=0}^{\infty} \frac{S}{m} h(k_2^r) [P'_m(\cos \theta) \sin \theta] \right\} \exp(-i\omega t) \quad (43b)$$

and

$$\begin{aligned} \frac{u}{\theta}_z(r, \theta, t) &= \frac{i}{Z_2 \cdot k_2^r} \left\{ \sum_{m=0}^{\infty} [(2m+1)P'_m] j_m(k_2^r) [P'_m(\cos \theta) \sin \theta] \right\} \\ &\times \exp(-i\omega t) \end{aligned} \quad (43c)$$

where

$$\begin{aligned} P'_m(\cos \theta) \sin \theta &\equiv \frac{\partial [P_m(\cos \theta)]}{\partial (\cos \theta)} \cdot \sin \theta \\ &= - \frac{\partial}{\partial \theta} [P_m(\cos \theta)] \\ &= \begin{cases} \sin \theta \sum_{\substack{l=0 \\ l \text{ even}}}^{m-1} (2l+1) P_l(\cos \theta), & m \text{ odd} \\ \sin \theta \sum_{\substack{l=1 \\ l \text{ odd}}}^{m-1} (2l+1) P_l(\cos \theta), & m \text{ even} \\ 0, & m = 0 \end{cases} \end{aligned} \quad (44)$$

The above formula for the derivative of the Legendre polynomial is obtained using the recursion relation (Morse and Ingard, 1968:334)

$$\frac{d}{dx} [P_m(x)] = (2m-1)P_{m-1}(x) + \frac{d}{dx} [P_{m-2}(x)] \quad (45)$$

and the initial conditions

$$P_0(x) = 1$$

and

$$\frac{d}{dx}[P_0(x)] = 0$$

Also note that the dispersion relations (19) are used in reaching Equations 41 and Equations 43.

The boundary conditions of continuity of pressure and of the normal velocity component, applied at the sphere boundary ($r = a$), are expressed as follows:

$$p_w(r = a, \theta, t) = p_s(r = a, \theta, t) + p_i(r = a, \theta, t) \quad (46a)$$

and

$$u_{rw}(r = a, \theta, t) = u_{rs}(r = a, \theta, t) + u_{ri}(r = a, \theta, t) \quad (46b)$$

Finally, expressions for \underline{W}_m and \underline{S}_m are obtained by the same method as used in Section 2.2.1 in reaching Equations 21 and Equations 24.

The general solution for $m \geq 0$ is

$$\begin{aligned} \underline{W}_m = \frac{[(2m+1)P_i^m]}{\underline{\Delta}_m} \left\{ [(m+1)\underline{h}_{m+1}(k_2 a) - m\underline{h}_{m-1}(k_2 a)] j_m(k_2 a) \right. \\ \left. - \underline{h}_m(k_2 a) [(m+1)j_{m+1}(k_2 a) - mj_{m-1}(k_2 a)] \right\} \end{aligned} \quad (47a)$$

and

$$\begin{aligned} \underline{S}_m = - \frac{[(2m+1)P_i^m]}{\underline{\Delta}_m} \left\{ [(m+1)j_{m+1}(k_2 a) - mj_{m-1}(k_2 a)] j_m(k_1 a) \right. \\ \left. - j_m(k_2 a) [(m+1)j_{m+1}(k_1 a) - mj_{m-1}(k_1 a)] \cdot Z_r \right\} \end{aligned} \quad (47b)$$

where

$$\begin{aligned} \Delta_m = & [(m+1)h_{m+1}(k_2a) - mh_{m-1}(k_2a)j_m(k_1a) \\ & - \frac{h}{m}(k_2a)[(m+1)j_{m+1}(k_1a) - mj_{m-1}(k_1a)] \cdot Z_r \end{aligned} \quad (48)$$

and where Z_r is defined in (23). These formulas can be simplified for the term $m = 0$ to the form

$$\Delta_0 = \frac{P}{\Delta_0} [h_1(k_2a)j_0(k_2a) - h_0(k_2a)j_1(k_2a)] \quad (49a)$$

and

$$\Delta_0 = -\frac{P}{\Delta_0} [j_1(k_2a)j_0(k_1a) - j_0(k_2a)j_1(k_1a) \cdot Z_r] \quad (49b)$$

where

$$\Delta_0 = h_1(k_2a)j_0(k_1a) - h_0(k_2a)j_1(k_1a) \cdot Z_r \quad (50)$$

2.2.4 Rigid sphere. As with the soft-object problems, the rigid-sphere problem is similar to that of the rigid cylinder. The rigid sphere is a special case of the soft sphere, for which $\kappa_1 \rightarrow 0$, as before. Since the same or similar relations still apply, it follows again that for c_1 finite, $\rho_1 \rightarrow \infty$ and $Z_1 \rightarrow \infty$, and finally that $\bar{u}_w \rightarrow 0$ (this time according to Equations 41a and 43a). Also as before, the interior pressure p_w remains nonzero for infinite ρ_1 .

Again, use of the condition $\bar{u}_w = 0$ permits determination of the scattered variables p_s and \bar{u}_s from the incident variables p_i and \bar{u}_i .

where the latter are given by (37), (41c), and (43c). Note that \underline{p}_w is not used in this determination. Since no further attention is paid to region 1, the regional distinction is no longer necessary, so that the subscript "2" is again eliminated for constants of that region.

Because the wave equation (35) is still applicable, the expressions for \underline{p}_s , \underline{u}_{rs} , and $\underline{u}_{\theta s}$ in (38b), (41b), and (43b) remain correct. The general boundary conditions (46) also still hold true, but the second is augmented by the additional constraint $\overline{\underline{u}}_w = 0$, resulting in

$$\underline{p}_w(r = a, \theta, t) = \underline{p}_s(r = a, \theta, t) + \underline{p}_i(r = a, \theta, t) \quad (51a)$$

and

$$\underline{u}_{rw}(r = a, \theta, t) = 0 = \underline{u}_{rs}(r = a, \theta, t) + \underline{u}_{ri}(r = a, \theta, t) \quad (51b)$$

As in the cylindrical case, the first condition is not used for obtaining the scattered variables, although it is needed to calculate \underline{p}_w , if the latter is desired. The second is used by rewriting it as follows:

$$\underline{u}_{rs}(r = a, \theta, t) = -\underline{u}_{ri}(r = a, \theta, t) \quad (52)$$

The weighting coefficients \underline{S}_m are found by the standard method of substituting into (52) the series expressions for \underline{u}_{rs} and \underline{u}_{ri} , and then matching coefficients of the Legendre polynomials $P_m(\cos \theta)$; the solution is

$$\underline{S}_0 = - \frac{Pj_1(ka)}{\underline{h}_1(ka)} \quad (53a)$$

and

$$\underline{S}_m = - \frac{[(2m+1)P_i^m][(m+1)j_{m+1}(ka) - mj_{m-1}(ka)]}{[(m+1)h_{m+1}(ka) - (m-1)h_{m-1}(ka)]}, \quad m > 0 \quad (53b)$$

It can be shown that the above solution matches that in Morse and Ingard (1968:419). As with the cylindrical cases, the rigid-sphere problem is solved only for use in checking the limiting case of the soft-sphere problem, for which no textbook solution has been found. Proceeding as with the rigid cylinder, the above rigid-sphere solution for \underline{S}_m is obtained by applying the constraint $Z_r \rightarrow 0$ (from $\rho_1 \rightarrow \infty$ and $Z_1 \rightarrow \infty$) to (49b) and (47b) and also to (50) and (48) of the soft-sphere problem, and then substituting for \underline{A}_m in \underline{S}_m . This procedure was repeated computationally to check the soft-sphere program "SSR" (see Section 3.2.1).

Prior to its use in checking the soft-sphere program, the rigid-sphere program "RSR" had to be checked. This step was again performed by means of the far-field scattered radial intensity. The time-averaged radial component of the scattered intensity follows from Equation 30. It is identical to that in Equation 31 of the cylindrical problem, and is repeated here for completeness:

$$\langle I_{rs} \rangle = \frac{1}{2} \text{Re}[\underline{p}'_s(\underline{u}'_{rs})^*] \quad (54)$$

2.2.5 Computational issues. As outlined in Table 1, four computer programs calculate the wave solutions derived in the four preceding sections, and two additional plotting programs illustrate these solutions (for the soft-object cases only) by means of isomagnitude and isophase contours. Programs SCL and SSR compute separately the interior

Table 1

Computer Programs

Name	Function Performed
SCL	Soft-cylinder problem: program calculates pressure, particle velocity, and estimated power loss at points on a two-dimensional polar grid, and passes output to plotting programs ISO and ISOLOS.
RCL	Rigid-cylinder problem: program calculates scattered pressure, radial particle velocity, and radial intensity at a series of angular samples at a specified distance from the cylinder, and plots radial intensity.
SSR	Soft-sphere problem: program calculates pressure, particle velocity, and estimated power loss at points on a two-dimensional polar grid, and passes output to plotting programs ISO and ISOLOS.
RSR	Rigid-sphere problem: program calculates scattered pressure, radial particle velocity, and radial intensity at a series of angular samples at specified distance from the sphere, and plots radial intensity.
ISO	Soft cylinder or soft sphere: program plots isomagnitude and/or isophase contours for pressure, and radial and tangential particle velocity, using output from programs SCL or SSR.
ISOLOS	Soft cylinder or soft sphere: program plots isomagnitude curves for two estimates of heat loss, using output from programs SCL or SSR.

(i.e., within the object), scattered, and incident components of the various variables (pressure, radial velocity, tangential velocity, "viscous" heat loss and "absorptive" heat loss). These separate scattered and incident components are added to get the total solution plotted by programs ISO and ISOLOS (in conjunction with a plotting package "GCS"). For the value of a variable at the object boundary, where the solutions for regions 1 and 2 coincide, the plotting programs arbitrarily use the values corresponding to region 1, i.e., the interior of the object. The plotting programs construct contours using linear (i.e., two-point) interpolation.

The routines used to calculate the Bessel functions and Legendre polynomials are summarized in Table 2. A more detailed description of subroutines NBESJ and RBESY is available in the Control Data Corp. Math Science Library manual (1973:3-97 to 3-102, 3-121 to 3-123). The functions $\frac{H_m}{h_m}$ are obtained from J_m, Y_m and j_m, y_m , according to Equations 12 and 39, respectively. All subroutines use upward and/or downward recursion to calculate their respective functions for a single argument and a series of orders. A warning is appropriate regarding parameter selection for the spherical programs SSR and RSR: the routine SBESJ incorrectly calculates $j_m(k_1 r)$ and/or $j_m(k_2 r)$ if the argument is a multiple of π , i.e., $k_1 r = n\pi$ or $k_2 r = n\pi$. This occurrence can be prevented by avoiding the exclusive use of "nice" numbers (e.g., 1, 2.5) for both the acoustic velocities c_1 and c_2 and the frequency f (see Section 3.1). A good solution is to multiply the desired "nice" frequency by 1.000 01 to get a value which prevents the

Table 2

Mathematical Function Subroutines

Name	Function/ Polynomial Calculated	Programs Used in
RBESJ	$J_m(x)$	SCL
		RCL
NBESY	$Y_m(x)$	SCL
		RCL
SBESJ	$j_m(x)$	SSR
		RSR
SBESN	$y_m(x)$	SSR
		RSR
ALEG	$P_m(x)$	SSR
		RSR

problem without significantly altering the desired parameter value.

Source listings of the six programs, including the mathematical function subroutines but excluding the plotting package GCS, total around 5000 lines. Owing to their excessive length, the listings are not included in this thesis, but are available from Prof. O'Brien upon request.

Most of the calculations made in the course of this thesis pertain to the soft-object cases; the rigid-object problems are solved mainly to provide a check for the former ones (see Section 3.2.1). Thus the subsequent comments in this section refer primarily to the soft-object problems. In addition, the following statements are in general applicable to both the cylindrical and spherical cases, the similarity between which is pointed out in Section 2.2.3. The cylindrical notation is arbitrarily used, but the spherical notation is easily obtained by replacing ϕ with θ , and x with z .

All four calculations programs compute the steady-state complex amplitudes of the different wave variables, namely p'_w , p'_s , p'_i , u'_{rw} , u'_{rs} , u'_{ri} , $u'_{\phi w}$, $u'_{\phi s}$, and $u'_{\phi i}$. These variables vary with spatial position (r, ϕ) but are time-independent. Examination of Equations 10, 14c, 18c, 21a,b, and 24a,b in the soft-cylinder case, and of Equations 37, 41c, 43c, 49a,b, and 47a,b in the soft-sphere case, shows that all pressure and velocity variables are linearly proportional to the amplitude P of the incident pressure wave, so that the relative distributions are independent of P . Therefore, P is set to 1 in all calculations and plots, but the option to use a different value is

retained for flexibility in adapting to experimental conditions specified in the future.

In Sections 2.2.1 and 2.2.3, the expressions for all three components of pressure and velocity are stated in terms of cylindrical and spherical Bessel functions. These functions are considered to be "appropriate" for describing the solution because the series expression for a given variable can be truncated at a finite term $m = N$, instead of $m \rightarrow \infty$, with the remaining finite series-sum still a good approximation to the exact solution. This truncation approximation is essential for numerical computation using a series expression. Its validity requires that the neglected higher-order terms be of much lower magnitude than the retained low-order terms.

The truncation approach is used to calculate approximate values for the interior and scattered components of pressure and velocity. However, the incident component can be calculated "exactly" using the original "closed-form" expression in (10), which is restated now in steady-state amplitude form:

$$p_i^1(r, \phi) = P \exp(k_2 r \cos \phi) \quad (55)$$

The corresponding expressions for the radial and tangential velocity components are obtained by application of Equations 13 for the cylindrical case, or, equivalently (for θ replaced with ϕ), Equations 40 for the spherical case, yielding

$$\frac{u_r}{r}^1(r, \phi, t) = \frac{P \cos \phi}{Z_2} \exp[i(k_2 r \cos \phi - \omega t)] \quad (56a)$$

and

$$\frac{u}{\phi i}(r, \phi, t) = - \frac{P \sin \phi}{Z_2} \exp[i(k_2 r \cos \phi - \omega t)] \quad (56b)$$

or, in steady-state amplitude form:

$$\frac{u}{r i}(r, \phi) = \frac{P \cos \phi}{Z_2} \exp(ik_2 r \cos \phi) \quad (57a)$$

and

$$\frac{u}{\phi i}(r, \phi) = - \frac{P \sin \phi}{Z_2} \exp(ik_2 r \cos \phi) \quad (57b)$$

Before the topic of truncation is discussed in detail, it is useful to consider the factors which make up the terms in the series expressions to be truncated: the weighting coefficients, the Bessel functions or radial factors, and the angular factors. Owing to the close resemblance between the cylindrical and spherical problems, the corresponding factors of each case behave similarly with regard to order (m) and argument. First note that the magnitudes of angular factors are bounded: it is well known, for the cylindrical case, that

$$|\cos(m\phi)| \leq 1$$

and that

$$|m \sin(m\phi)| \leq m$$

for $0 \leq \phi \leq 2\pi$, and $m = 0, 1, 2, \dots$

Likewise, for the spherical case, it seems that the Legendre polynomial (and its derivative) is bounded in a similar manner, although this property has been verified only experimentally by numerous samples, rather than mathematically. Thus it is proposed that

$$|P_m(\cos \theta)| \leq 1$$

and that

$$\left| \frac{\partial P_m(\cos \theta)}{\partial \theta} \right| < m$$

for $0 \leq \theta \leq 2\pi$, and $m = 0, 1, 2, \dots$.

In contrast, the Bessel functions span a much larger range of values: for a given argument ($x = k_1 a, k_1 r, k_2 a, k_2 r$, etc.), all Bessel functions (namely, $J_m, j_m, Y_m, y_m, \underline{H}_m, \underline{h}_m$) take on values of which the order of magnitude is near unity, for a range $m = 0, 1, 2, \dots, N_{sig}$ (N_{sig} is not intended to represent a sharply defined transition). Then J_m and j_m (Bessel functions of the first kind) begin to decrease steadily (exponentially) for increasing orders ($m = N_{sig} + 1, N_{sig} + 2, \dots$), whereas Y_m and y_m (Bessel functions of the second kind) increase with m in a complementary fashion. The Hankel functions \underline{H}_m and \underline{h}_m follow the same pattern as Y_m and y_m , since the latter functions comprise the dominant terms of the former, for higher orders. For all these functions, the low-order "plateau" range extends further (i.e., N_{sig} is larger), and the rate of increase with order m for J_m and j_m , and of decrease for $Y_m, y_m, \underline{H}_m$ and \underline{h}_m , declines, as the argument x increases.

Based on this description of Bessel functions, the behavior of the weighting coefficients \underline{W}_m and \underline{S}_m can be inferred from Equations 24a,b and 25 (cylindrical), or from the similar equations (47a,b) and (48). With similar terms in its numerator and denominator, \underline{W}_m remains fairly constant (i.e., near unity) for a wide range of orders and arguments. In contrast, \underline{S}_m decreases doubly fast with increasing m , approximately according to J_m/Y_m . This behavior of the factors of the terms of the series solutions determines the appropriate truncation point.

That the terms in the series solutions eventually "taper off" for higher orders follows directly from the previous discussion. First, the expressions for variables within the objects are considered (see Equations 11a, 14a, and 18a for the cylindrical case, or else Equations 38a, 41a, and 43a for the spherical case): the angular factors are bounded as described, and \underline{W}_m is fairly constant for increasing m , while $J_m(k_1 r)$ decreases, so that the higher-order terms decrease according to J_m , with "modulation" by the angular factors. The other case concerns the scattered variables (see the equations listed above, except refer to parts (b) instead of (a)): again the angular factors are bounded, whereas the coefficient \underline{S}_m decreases with increasing m according to J_m/Y_m , and the radial factor $\underline{H}_m(k_2 r)$ increases according to Y_m , with an overall decrease of the higher-order terms in the general pattern of J_m with angular modulation. The breakpoint for tapering off and the rate of decline are, of course, dependent on the relative values of r and α , but the general trend with m is as just described.

The terms of the series expressions (for higher orders) can be appropriately viewed as made up of a decreasing envelope (the product of the weighting coefficient and the radial (Bessel) factor) modulated by the bounded angular factor. Truncation of the series must be based on the envelope, rather than on the entire modulated product.

Since the envelope is dependent only on r (and m), truncation occurs at the same-order term for all values of ϕ , for a specified r .

The reference point is selected to be the term $m = 1$, whose value is generally of the same order of magnitude as the series-sum itself.

The term $m = 0$ cannot be used for all variables, because it is zero for tangential velocity. The truncation criterion is the simultaneous satisfaction of

$$\frac{|\text{current term } m, \text{ except for angular factor}|}{|\text{reference term } 1, \text{ except for angular factor}|} < \delta$$

for all three variables \underline{p}' , \underline{u}'_r , and \underline{u}'_ϕ , for a single wave component (namely, interior or scattered). The quantity δ is currently set to the value 10^{-6} .

For both the cylindrical and spherical cases, the largest number of terms for the solution in either region is required at the boundary $r = a$. For $\delta = 10^{-6}$, this quantity approximately follows the rule: maximum number of terms = $11 + 1.5 \cdot k_1 a$, where $1 \leq k_1 a \leq 40$ rad, and $k_1 \sim k_2$.

All three wave components are computed at values on a polar grid. In region 1 ($0 \leq r \leq a$, $0 \leq \phi \leq 2\pi$), values are obtained for the interior variables (\underline{p}'_w , \underline{u}'_{rw} , $\underline{u}'_{\phi w}$) at the set of $N_{r1} \times N_\phi$ points (r, ϕ) , such

that

$$r = \Delta r_1, 2\Delta r_1, \dots, (N_{r1} - 1)\Delta r_1, N_{r1}\Delta r_1$$

and

$$\phi = 0, \Delta\phi, 2\Delta\phi, \dots, (N_\phi - 1)\Delta\phi$$

where

$$\Delta r_1 \equiv \frac{a}{N_{r1}} \quad (58a)$$

and

$$\Delta\phi \equiv \frac{2\pi}{N_\phi} \quad (59)$$

and a is the cylinder (sphere) radius. Similarly, in region 2 ($r \geq a$, $0 \leq \phi \leq 2\pi$), values are obtained for the scattered and incident variables ($p'_s, u'_{rs}, u'_{\phi s}, p'_i, u'_{ri}, u'_{\phi i}$) at the following set of $N_{r2} \times N_\phi$ points (r, ϕ) :

$$r = a, a + \Delta r_2, a + 2\Delta r_2, \dots, a + (N_{r2} - 1)\Delta r_2$$

and

$$\phi = 0, \Delta\phi, 2\Delta\phi, \dots, (N_\phi - 1)\Delta\phi$$

where

$$\Delta r_2 = \Delta r_1 \quad (58b)$$

and $\Delta\phi$ is defined above. The two separate but equal radial discretization steps Δr_1 and Δr_2 are employed in the computer programs for the

sake of future flexibility.

Note that no values are computed in region 1 at the center ($r = 0$). This situation results from the difficulty of using the series expressions at that point, rather than because pressure and particle velocity physically take on unusual values at the center point. However, the tangential component of particle velocity does in fact "blow up" at that point, but this result owes to the meaninglessness of the tangential direction at the center--only the radial direction is meaningful there. The computational difficulties result from the Bessel routines, which cannot accept a zero argument for $J_m(k_1 r)$ and $j_m(k_1 r)$, although these functions are finite at $x = 0$ (note that $Y_m(k_1 r)$ and $y_m(k_1 r)$, which "blow up" for $r \rightarrow 0$, are not even included in the interior series expressions.) An additional problem might be the multivalued (with respect to ϕ) nature of the solution for $\underline{p}'_w(r, \phi)$ as $r \rightarrow 0$. The plotting programs attempt to circumvent the lack of calculated values at the center, by averaging all values of the variable to be plotted along the innermost circle ($r = \Delta r_1$), to estimate the actual value.

A final point concerns the savings in computation possible by taking advantage of the symmetry of the problem about the line $\phi = 0$, or the x -axis. The following relationships hold true for all three wave components, as a result of this symmetry:

$$\underline{p}'(r, \phi) = \underline{p}'(r, 2\pi - \phi) \quad (60a)$$

$$\underline{u}'_r(r, \phi) = \underline{u}'_r(r, 2\pi - \phi) \quad (60b)$$

and

$$\underline{u}'_{\phi}(r, \phi) = -\underline{u}'_{\phi}(r, 2\pi - \phi) \quad (60c)$$

Thus it is only necessary to calculate variables values for ϕ in the range $0 \leq \phi \leq \pi$; from these calculations, the remaining values can be easily obtained using Equations 60. This scheme is implemented for the soft-object programs SCL and SSR. In order to plot in the entire plane instead of merely in the calculated half-plane, programs ISO and ISOLOS construct the solutions for $\pi \leq \phi \leq 2\pi$ from those for $0 \leq \phi \leq \pi$. However, this approach is not used in the rigid-object programs RCL and RSR, because the savings in computation time and storage space scarcely justifies the extra overhead.

2.3 Calculation of Wave Distributions--Numerical Approach

Only for the soft-cylinder problem (see Section 2.2.1) was an attempt made to find a solution numerically. The attempt was based on a FORTRAN-oriented differential-equations simulation package named "FORSIM" (Carver et al., 1978). The soft-cylinder problem here is identical with that outlined in the description of the analytical solution: the incident wave variables ($\underline{p}'_i, \underline{u}'_{ri}, \underline{u}'_{\phi i}$) represent a known source wave and the interior and scattered wave variables ($\underline{p}'_w, \underline{u}'_{rw}, \underline{u}'_{\phi w}; \underline{p}'_s, \underline{u}'_{rs}, \underline{u}'_{\phi s}$) are sought as the solutions of the wave equations (6) which satisfy the boundary conditions (20).

As mentioned in Section 1.3, one advantage of the numerical method is that arbitrary incident waves, more closely resembling experimental conditions (e.g., a focused beam), can be employed. In contrast, the analytical approach is restricted to waves which can be

described using series expressions of the form (11), for which "reasonable" expressions for the coefficients are available, as with the plane wave of Equation 10.

The three wave components are again represented by samples on a polar grid simplified to a half-plane by means of symmetry, as described in Section 2.2.5 for the analytical approach. The incident wave is calculated analytically as before, while the interior and scattered components are obtained numerically.

The general approach suggested for use in conjunction with FORSIM involves guessing arbitrary initial conditions for p_w , u_{rw} , $u_{\phi w}$ and p_s , u_{rs} , $u_{\phi s}$ and integrating these variables (starting at $t = 0$) according to the time derivatives given in Equations 6a and 13a,b (for the cylindrical case only; for the spherical case, Equations 33a and 40a,b would be used), until the steady state is (approximately) achieved. For such an outcome to result, the transients excited by the arbitrary initial conditions must decay nearly to zero, leaving only the steady state, as determined by the forcing function. Thus, in a sense, time serves as a dummy variable which oversees iteration until the steady-state complex amplitudes are finally obtained.

However, this method encounters difficulty in its application to wave equations, which are included in the larger class of "hyperbolic" differential equations. In such problems, some transients tend to be increasing exponentials, causing the solution to "blow up," instead of decaying to zero or approaching the steady state. This difficulty proved significant and apparently insurmountable, so that this particular approach is considered to be inappropriate for numerical solution

of wave problems of the sort described in Sections 2.2. This topic is discussed in detail later in this section; for the present, attention is focused on the techniques used in this (unsuccessful) attempt, some of which are useful in their own right, while others need improvement or else should be avoided altogether.

Note that the numerical variables are real, time-varying. However, complex steady-state amplitudes (say, p'_w) can be determined from the time-varying quantities (such as p_w) as follows: $|p'_w|$ is obtained as the maximum of $|p_w|$ during one period ($T \equiv 1/f$) in the steady state, and $\angle p'_w$ is then $\cos^{-1}(p_w/|p'_w|)$, where p_w is (arbitrarily) evaluated at the beginning of a cycle.

For integration in time, the fourth-order Runge-Kutta method was selected from among the offerings in FORSIM. This technique was chosen because of its low storage requirements, in spite of its relative slowness in integration. Temporal step size varies as integration proceeds and is automatically determined by the package, based on a fifth-order Runge-Kutta error estimate.

The process of temporal integration is based on the time derivatives, as calculated using the aforementioned wave equations (written in a form similar to state equations). These calculations in turn require knowledge of spatial derivatives at each instant of time. The derivatives are approximated using "Lagrange interpolation" among surrounding points, the number of which is termed the "coupling order" (NCUP). This quantity is normally odd and is variable for each spatial direction, but both quantities are set to the maximum value of

7, to reduce errors which excite unstable transients. This general technique is referred to as the "method of lines," because it separates the partial differential wave equations into a set of ordinary differential equations which are integrated in time (thus, the "lines") and coupled in space. It should be noted that Lagrange interpolation produces serious errors in approximating derivatives near discontinuities, as might result from poorly chosen initial conditions.

To compute a derivative of a function at a given sample point and with respect to a given direction, one of two different forms of Lagrange interpolation is automatically selected: "central" or "skewed" differencing. The former scheme uses function values at the given sample point and at the $(NCUP/2 - 1)$ points on each side (along the given direction) of the central sample—if those points exist within the bounded region. Otherwise, skewed differencing uses the first NCUP points, beginning at the (obstructing) boundary. Central differencing is more accurate, but obviously can only be used at points sufficiently far (i.e., internal) from boundaries.

In order for a steady-state solution to be reached after starting from arbitrary initial conditions, the transients must all decay, as already mentioned, and then the system must remain in the steady state. It is expected that the entire integration process would span at least several wave periods ($0 \leq t \leq nT$), depending on the rate of decay. However, for testing purposes, a simpler problem was attempted which requires only one period of integration: the system is initialized already in the steady state, using the known analytical solution, so

that the task is to integrate through one period ($0 \leq t \leq T$), and to try to match the final state as closely as possible to the initial (steady) state. This goal was never reached—the best that was achieved was integration through a half-period, at which point increasing errors begin to swamp the solution. Merely this simplified job requires approximately 200 CPU seconds (i.e., actual run time) on a Cyber 175,¹ so that even if it had been successful, the overall problem entailing multiple-period integration would probably require an unfeasibly large amount of computation time.

At any rate, this method-of-lines approach seems inefficient for solving the current problem. Part of this inefficiency appears to be a result of the introduction of time as a third, dummy variable, for solving for the steady-state complex amplitudes, which are only spatially dependent. Certainly, some additional dummy variable is needed to coordinate iteration toward a solution. However, time seems to be a relatively inefficient choice, as shown by the tremendous difference between the amount of computation time required for numerical solution and that for analytical solution—a factor of about 10^3 .

The sample density of the polar grid is no longer decided merely to achieve a sufficient fineness in plots of solutions, as done in the analytical case, but is now also an important factor in minimizing computational errors. Certainly, it is desirable to keep the grid density

¹This figure is slightly exaggerated, because small but increasing errors cause integration step sizes to be reduced automatically, thereby requiring extra computation time.

as small as possible, in order to minimize storage requirements and computation time: each additional point on the grid represents another equation, for which spatial derivatives must be calculated and integration performed.

On the other hand, additional factors establish minimums on the number of sample points. In the first place, a sufficient number of points is required to represent the spatial variation of the wave. Based on examples in the FORSIM manual, a good rule of thumb is to use (at least) kx (in radians) as the number of sample points in a distance x . Since

$$\frac{kx}{x} = \frac{2\pi}{\lambda}$$

this rule is seen to be equivalent to placing $2\pi \sim 6$ points per wavelength. Applying this rule to region 1, it is seen that $k_1 a$ points are suggested along the radial distance a , or $N_{r1} \cong k_1 a$. Since $\Delta r_2 = \Delta r_1$ (see Equation 58b), the latter determination of N_{r1} specifies the radial point density in region 2 also; this means of specification is valid as long as $k_1 \sim k_2$. Note that N_{r2} has no effect on the radial point density in region 2, but instead determines the radial extent of the region.

The point density along the angular direction is a somewhat more difficult issue, because the angular discretization distance $r\Delta\phi$ varies with r , for a constant $\Delta\phi$; the worst case occurs at the outer boundary of region 2. It can be easily shown from the polar grid specification in Section 2.2.5 that the radial distance to that boundary is

$$R \equiv \left[\frac{N_{r2} + N_{r1} - 1}{N_{r1}} \right] \alpha ; \quad (61)$$

the -1 is required because the point $r = \alpha$ is common to both regions. Thus, the circumference along that boundary is $2\pi \left[\frac{N_{r2} + N_{r1} - 1}{N_{r1}} \right] \alpha$, so that

$$N_{\phi} = k_2 \cdot 2\pi \left[\frac{N_{r2} + N_{r1} - 1}{N_{r1}} \right] \alpha$$

points are needed in the angular direction. For a relatively small cylinder such that $k_1 \alpha \sim 1$ (see discussion on parameter values in Section 3.1) and for $N_{r1} = N_{r2}$, the previous reasoning suggests $N_{r1} = N_{r2} = 1$ or 2, and $N_{\phi} = 12$. However, much larger values are actually used, as a result of the following additional constraints.

A second minimum on the numbers of points owes to the coupling order: for spatial interpolation using 7 points, at least that many points must be contained in each dimension of the grid, for each region. This consideration gave rise to the choice $N_{r1} = N_{r2} = 10$, where a few extra points are included to decrease the relative number of points for which skewed differencing is employed. Also, the choice of $N_{\phi} = 20$ was initially made based on this reasoning, resulting in 11 points in the half-plane actually used. However, this latter choice proved insufficient to provide a good spatial description of u_r and u_{ϕ} , which vary with angle ϕ such that u_r has maximum values near the x -axis and is near zero along the y -axis, and vice versa for u_{ϕ} . Note that this angular variation is a result of the directionality of the incident

wave, rather than its wavelength, as was the case with the initial consideration based on $k_1 a$ and $k_2 a$. The value $N_\phi = 60$ is the selection which finally solved this problem.

In contrast with the analytical approach, the wave variables can be evaluated numerically at the center ($r = 0$). The use of the center as a sample point is motivated by the resulting increased accuracy obtainable for radial derivatives. However, the wave equations must be reformulated in terms of Cartesian coordinates, because u_ϕ is singular at the center (see Section 2.2.5). Thus at $r = 0$, the wave equations are

$$\begin{aligned} \frac{\partial p_w}{\partial t}(r = 0, t) &= -\rho_1 c_1^2 (\bar{\nabla} \cdot \bar{u}_w) \\ &= -\rho_1 c_1^2 \left(\frac{\partial u_{xw}}{\partial x} + \frac{\partial u_{yw}}{\partial y} \right) \end{aligned} \quad (62a)$$

and

$$\begin{aligned} \rho_1 \frac{\partial \bar{u}_w}{\partial t}(r = 0, t) &= -\bar{\nabla} p_w \\ &= -\left(\hat{x} \frac{\partial p_w}{\partial x} + \hat{y} \frac{\partial p_w}{\partial y} \right) \end{aligned} \quad (62b)$$

where

$$\bar{u}_w \equiv \hat{x} u_{xw} + \hat{y} u_{yw} \quad (63)$$

Equation 62b can be rewritten as a pair of scalar equations, giving the desired format as expressions for the time derivatives:

$$\frac{u_{xw}}{\partial t} = -\left(\frac{1}{\rho_1}\right) \frac{\partial p_w}{\partial x} \quad (64a)$$

and

$$\frac{\partial u_{yw}}{\partial t} = -\left(\frac{1}{\rho_1}\right) \frac{\partial p_w}{\partial y} \quad (64b)$$

Now, Equations 62a and 64a,b are written in the appropriate form for obtaining p_w , u_{xw} and u_{yw} by means of the method of lines. However, by the symmetry of the problem, $u_{yw}(r = 0, t) \equiv 0$, so that (64b) need not be integrated. Note that this condition does not imply that $\partial u_{yw}/\partial y = 0$ in (62a).

The remaining question is the determination of Cartesian spatial derivatives from variables on a polar grid. Now, $\partial p/\partial x$ and $\partial u_x/\partial x$ are obtained by Lagrange differencing of p and u_r , respectively, for $\phi = 0$, which is the x -axis. Similarly, $\partial p/\partial y$ and $\partial u_y/\partial y$ are evaluated as above, except using $\phi = \pi/2$, which corresponds to the y -axis. So that the latter step can always be performed, N_ϕ is required to be a multiple of 4; therefore, samples of the needed variables are evaluated for $\phi = \pi/2$. The complementary use of the center wave variables in the evaluation of radial derivatives for points near the center remains to be considered.

Each of the two spatial regions, temporarily ignoring the center point, has four boundaries, two radial and two angular: for region 1, the "central" boundary at $r = \Delta r_1$, the "object" boundary at $r = \alpha$, and the two "side" boundaries at $\phi = 0$ and $\phi = \pi$; and for region 2, again

the object boundary and two side boundaries, and also the outer boundary $r = R$. Of all these boundaries, only the object boundary is a "true" boundary to which boundary conditions are applied, while the others are artificial--the results of the inevitable finite radial extent of sample points and of the reduction of computation to the region $0 \leq \phi \leq \pi$ through the use of symmetry about the x -axis. The appearance of artificial boundaries is undesirable, because the less accurate skewed differencing must be used instead of central differencing. Even with the introduction of artificial boundary conditions (the application of boundary conditions still remains to be explained), considerable distortion is always the outcome.

The only good solution is to "virtually" eliminate artificial boundaries wherever possible; that is, to use the symmetry conditions (and the center point) to make the artificial boundaries (which the former created) "invisible" to the differencing routines. This step is feasible at all artificial boundaries (namely, central and side boundaries) except the outer boundary. The lack of a boundary-elimination technique for the latter case results in the largest errors being created there, exciting unstable solutions which eventually swamp out the steady-state response. Discussion of this topic is temporarily postponed, with attention being turned back to the central and side boundaries. As regards the latter, both regions are extended, by as many points as necessary for the given coupling order, past $\phi = 0$ and $\phi = \pi$, so that central differencing can be performed for angular derivatives at all points in the range $0 \leq \phi \leq \pi$. Thus

for angular coupling of order 7, an extension of 3 points is needed at each boundary. The extension is made using the symmetry relations similar to those of Equations 60.

An alternative approach, as previously mentioned, is to use the following boundary conditions, which are directly the result of symmetry, at both $\phi = 0$ and $\phi = \pi$:

$$\frac{\partial p_w}{\partial \phi} = 0 \quad (65a)$$

$$\frac{\partial u_{rw}}{\partial \phi} = 0 \quad (65b)$$

and

$$u_{\phi w} = 0 \quad (65c)$$

In fact, (65b) is not required because no angular derivatives of u_{rw} appear in the wave equations (6). These conditions merit consideration because they require much less computational overhead than the boundary-extension approach; but they are not used, for the sake of computational accuracy, as already stated. The reason for their inaccuracy is probably that they are necessary but not sufficient conditions to constrain the problem to be symmetrical.

Elimination of the central boundary at $r = \Delta r_1$ involves an extension of the nominal region 1 through the center ($r = 0$) and effectively into the region $r < 0$, so that central differencing can be used for radial derivatives near and at the center. Again, an extension of 3

points (beyond the center) is required for radial coupling of order 7.

Computation of the radial derivatives (only needed for p_w and u_{rw}) along an angle ϕ includes the use of the following values at the center:

$$p_w(r = 0)$$

and

$$u_{rw}(r = 0, \phi) = u_{xw}(r = 0) \cos \phi + u_{yw}(r = 0) \sin \phi$$

where the evaluation of p_w , u_{xw} , and u_{yw} at $r = 0$ has been considered previously. The following expressions for these variables for $r < 0$ make use of the symmetry relations (60) used for the side boundaries:

$$\begin{aligned} p_w(r, \phi) &= p_w(-r, \phi + \pi) \\ &= p_w(-r, \pi - \phi) \end{aligned} \tag{66a}$$

and

$$\begin{aligned} u_{rw}(r, \phi) &= -u_{rw}(-r, \phi + \pi) \\ &= -u_{rw}(-r, \pi - \phi) \end{aligned} \tag{66b}$$

No alternative boundary conditions are known for handling the artificial central boundary, as was the case with the side boundaries. However, it should be noted that the artificial condition

$$\frac{\partial p_w}{\partial r} = 0 \tag{67}$$

is not valid at $r = 0$, as suggested in the FORSIM manual (Carver et al., 1978:124); instead, a discontinuity in $\partial p_w / \partial r$ at the center is quite plausible, because the quantity varies with the angle ϕ . As concerns the outer boundary at $r = R$, neither a boundary extension nor an artificial boundary condition is known which can eliminate the artificial boundary. The variables at the boundary are thus said to "float."

In the solution of partial differential equations, the number of boundary conditions for a given variable and coordinate direction is in general equal to the highest order of derivatives of that variable with respect to that coordinate (Carver et al., 1978:46). In particular, for this first-order wave problem, this rule implies that one radial boundary condition is required for p_w and u_{rw} in region 1, and the same for p_s and u_{rs} in region 2. Of course, the angular boundary condition suggested for p_w , $u_{\phi w}$, p_s , and $u_{\phi s}$ cannot be applied, because no physical boundary exists; this is a valid exception to the general rule just stated.

The application of boundary conditions in a numerical problem involves setting the boundary sample of the appropriate variable to a value which satisfies the given boundary condition. For instance, to impose the condition

$$\left. \frac{\partial f}{\partial x} \right|_{x=C} = K$$

$f(C)$ is set to the value which causes the Lagrange approximation of $\partial f / \partial x$ at $x = C$ to equal K .

Now, since the single sample value at a given boundary provides only one degree of freedom, only one independent boundary constraint can be satisfied at that boundary. This situation places obvious limits on the total number of boundary conditions which can be applied numerically and may conflict with the actual boundary specifications. However, no conflict exists for the current wave problem: at the (radial) object boundary ($r = a$) the four samples of p_w , u_{rw} , p_s , and u_{rs} provide four degrees of freedom, which must satisfy four conditions. The first two are the boundary conditions (20), discussed in Section 2.2.1, and the other two result from the application of the wave relationship (13a) to the interior and scattered wave components.

For numerical purposes, it is best to restate Equations 20 solely in terms of pressure, and then to solve for the boundary values of p_w and p_s . The samples of u_{rw} and u_{rs} at $r = a$ are then implicitly determined, by means of the integration process. Now, (20a) is already in terms of pressure, and (20b) can be converted to this form by use of (13a); thus the set of numerical boundary conditions at $r = a$ is

$$p_w = p_s + p_i \quad (68a)$$

and

$$\left(\frac{\rho_2}{\rho_1}\right) \frac{\partial p_w}{\partial r} = \frac{\partial p_s}{\partial r} + \frac{\partial p_i}{\partial r} \quad (68b)$$

It must be emphasized that the derivatives in (68b) are represented by Lagrange polynomials, so that the process of solving for $p_w(r = a)$ and $p_s(r = a)$ from Equations 68 is an algebraic process.

This method for applying boundary conditions encountered one significant difficulty: if the density ratio (ρ_2/ρ_1) is near unity, the scattered wave component is much smaller than the other two components, because less reflection occurs. Yet, the errors in computing the boundary values of p_s and p_w are similar in value, resulting in a much larger relative error for p_s . As before, this error can grow and eventually distort p_w also. The only known cure for this problem is to increase the mismatch of the densities ρ_1 and ρ_2 .

It is suggested in the FORSIM manual that the time derivatives of the variables being integrated should be held to zero at boundary points involved in boundary conditions, so that the integration process does not upset the imposed constraints. However, this rule should only be followed for constant boundary conditions, such as

$$f(x) \Big|_{x=C} = 0$$

For dynamic conditions, as in Equations 68, better accuracy is achieved by letting the time derivatives reflect the changing state of the boundary.

Throughout this discussion, the problem of unstable solutions is mentioned. Two attempted remedies are now discussed. The first, suggested in the FORSIM manual, is called "upwind differencing" (Carver et al., 1978:125). The idea is that an error wave propagating in the opposite direction as the primary solution can be reduced by using, in the differencing process for estimating derivatives, more samples in the upwind direction of the primary solution than in the downwind

direction of the error wave. This technique seems to have an application in reducing the (inward-moving) error component of the (outward moving) scattered wave, which arises at the outer boundary ($r = R$). However, the cause and proposed solution are one-in-the-same: the error wave arises from skewed differencing at the outer boundary, yet the proposed solution is to use skewed differencing (in the same direction as at the boundary) throughout the region. As might be expected, the upwind-differencing approach did, in fact, deteriorate the solution more rapidly.

The other possible remedy, also discussed in the manual (Carver et al., 1978:125), is "artificial dissipation." Essentially, it is proposed that the system be stabilized by adding an artificial loss factor, much like the commonly used technique of increasing the damping factor of a circuit in order to improve its stability. In effect, accuracy is traded for stability. For this wave problem, the dissipative factor is viscosity; it is implemented by altering the original lossless wave equations. This implementation is based on a development by Kinsler and Frey (1962:218-221). The wave equation for pressure (1a) is modified to the form

$$\frac{\partial p}{\partial t} = -\rho c^2 (\bar{\nabla} \cdot \bar{u}) - \eta \left[\bar{\nabla} \cdot \frac{\partial \bar{u}}{\partial t} \right] \quad (69a)$$

where η is bulk viscosity (see Section 2.4) and the second term on the right-hand side is the "viscous-loss" term. The wave equation for velocity (1b) is unaltered:

$$\rho \frac{\partial \bar{u}}{\partial t} = -\bar{\nabla} p \quad (69b)$$

Except for the viscous-loss term, all terms in the above equations are given in cylindrical coordinates in Equations 6. Substitution of (69b) into the viscous-loss term yields (in cylindrical coordinates)

$$\begin{aligned} \eta \left(\nabla \cdot \frac{\partial \bar{u}}{\partial t} \right) &= - \left(\frac{\eta}{\rho} \right) \nabla^2 p \\ &= - \left(\frac{\eta}{\rho} \right) \left[\frac{\partial^2 p}{\partial r^2} + \left(\frac{1}{r} \right) \frac{\partial p}{\partial r} + \left(\frac{1}{r^2} \right) \frac{\partial^2 p}{\partial \phi^2} \right] \end{aligned} \quad (70a)$$

A similar expression in terms of Cartesian coordinates is required for use at the center sample ($r = 0$); it is obtained by substitution of (62b) into the viscous-loss term, giving

$$\eta_1 \left(\nabla \cdot \frac{\partial \bar{u}_w}{\partial t} \right) = - \left(\frac{\eta_1}{\rho_1} \right) \left(\frac{\partial^2 p_w}{\partial x^2} + \frac{\partial^2 p_w}{\partial y^2} \right) \quad (70b)$$

In fact, artificial dissipation was only used in region 2, in an attempt to reduce the error component of the scattered wave at the outer boundary. For $\eta_1 = 0$ and $\eta_2 = 1 \text{ mg/mm} \cdot \mu\text{s}$, which is about 10^3 larger than for tissue, stability is improved but still not achieved, while the accuracy of the solution is seriously altered by the high attenuation. Thus it is concluded that artifical dissipation, too, is not an adequate remedy for the instability inherent in this wave problem.

Two additional problems encountered deserve brief mention. First, even using relatively low-storage Runge-Kutta integration, the FORSIM computer runs required large total amounts of storage, including work space for the Runge-Kutta routines, arrays for the wave variables

being integrated and their temporal and spatial derivatives, and a collection of miscellaneous arrays. Some space was conserved by sharing storage for temporary arrays not needed simultaneously, by means of the FORTRAN "EQUIVALENCE" statement. This technique could be used much more extensively if necessary.

And finally, numerous "bugs" were discovered in the recently written two-dimensional routines in FORSIM, although the older routines were relatively error-free. These difficulties were overcome by virtue of the availability of the source code for FORSIM, so that the errors could be located and the use of the erroneous features altered or avoided.

2.4 Estimation of Loss

Recall that the distribution of wave energy absorbed by the tissue is desired as an indication of possible hot spots. This information is to be estimated using the pressure and velocity distributions obtained by the methods described in Sections 2.2.

To proceed, it is helpful to make two approximations: first, that the material parameters (acoustic velocity, density, etc.) are constant over the range of temperatures experienced by the irradiated tissue, and second, that the wave distribution (pressure and particle velocity) is not altered by the conversion of wave energy to heat in the tissue. The former approximation is valid for relatively small temperature variations, and the latter requires that the wave energy absorbed by the tissue be small compared with the total energy of the wave. Use

of the lossless wave distribution as that for slightly lossy tissue is termed a zeroth-order approximation, and the estimated heat generation is therefore a first-order approximation. It should be noted that the restriction to a lossless wave distribution is required only for simplicity in analytical work: the artificial-dissipation technique is employed in numerical work (discussed in Section 2.3) in an attempt to compute an actual lossy wave distribution. However, this viscous-loss mechanism is introduced in an attempt to stabilize the solution outside the object, rather than to permit more accurate estimates of energy loss within the object.

At least two mechanisms of energy absorption are known for soft (fluid-like) tissues: viscosity and heat conduction. Viscosity effectively creates hysteresis in the pressure-particle velocity relationship, resulting in loss because these quantities are forced out of phase synchronization. Heat conduction manifests itself as a loss-producing mechanism by heat flowing from the warmer, higher-pressure half of the wave to the cooler, lower-pressure region, directly reducing the energy of the wave. The case of no heat flow, called "adiabatic," results in no energy loss by the wave, whereas infinite heat conduction produces an isothermal situation, in which the wave is highly attenuated. In tissues, viscous losses are much greater than those owing to heat conduction, so that the former mechanism is considered to be the sole source of heating, and the wave is assumed to propagate adiabatically. This approximation is best for lower (sub-GHz) frequencies (Morse and Ingard, 1968:230).

A theoretical analysis of the viscous-loss problem is presented by Morse and Ingard (1968:270-275). The following relation, taken directly from that development, expresses the instantaneous (i.e., not time-averaged) power loss per unit volume (D) in terms of instantaneous, real pressure and velocity:

$$D = \left(\eta + \frac{4}{3}\mu \right) (\bar{\nabla} \cdot \bar{u})^2 + \mu |\bar{\nabla} \times \bar{u}|^2 - 4\mu \left(\frac{\partial u_x}{\partial x} \frac{\partial u_y}{\partial y} + \frac{\partial u_x}{\partial x} \frac{\partial u_z}{\partial z} \right. \\ \left. + \frac{\partial u_y}{\partial y} \frac{\partial u_z}{\partial z} - \frac{\partial u_x}{\partial y} \frac{\partial u_y}{\partial x} - \frac{\partial u_x}{\partial z} \frac{\partial u_z}{\partial x} - \frac{\partial u_y}{\partial z} \frac{\partial u_z}{\partial y} \right) \quad (71)$$

where η is the bulk viscosity coefficient, and μ the shear viscosity coefficient. This equation is actually derived for gases, but should not be seriously inaccurate when applied to (homogeneous) liquids. However, tissues are one step further removed, because they are quite heterogeneous, although fluid-like. In spite of its shortcomings for the current application, this relatively simple equation is a good starting point for this viscous-loss problem. Although (71) is stated partially in terms of Cartesian coordinates, rather than cylindrical or spherical, this particular form of the equation need not be restated, as is shown below.

For tissues, μ is typically much smaller than η , so that Equation 71 can be simplified significantly. The constant μ is assumed to have the same value for tissues as for water, for which $\mu = 10^{-6}$ mg/mm · μs. In contrast, η for tissues is generally on the order of 10^{-3} mg/mm · μs. Therefore, for $\mu \ll \eta$, and also assuming that the magnitudes of the other factors are not markedly different, (71) becomes

$$D \cong \eta(\bar{\nabla} \cdot \bar{u})^2 \quad (72)$$

This equation can be restated in a more useful form by reexpressing the divergence term. Turning back to the original wave equation (1a), it is seen that

$$\bar{\nabla} \cdot \bar{u} = -\frac{1}{\rho c^2} \frac{\partial p}{\partial t} \quad (73a)$$

or

$$\begin{aligned} \bar{\nabla} \cdot \bar{u} &= -\frac{1}{\rho c^2} \cdot (-i\omega p) \\ &= \left(\frac{i\omega}{\rho c^2} \right) p \end{aligned} \quad (73b)$$

Use of relations similar to Equations 15 and 19 yields the following more compact form:

$$\bar{\nabla} \cdot \bar{u} = \left(\frac{ik}{Z} \right) p \quad (73c)$$

Finally, taking the real part of (73c) is required, because the complex representation is prohibited in squared terms such as $(\bar{\nabla} \cdot \bar{u})^2$; thus

$$\begin{aligned} \bar{\nabla} \cdot \bar{u} &= \text{Re}(\bar{\nabla} \cdot \bar{u}) \\ &= \text{Re} \left[\left(\frac{ik}{Z} \right) p \right] \\ &= \frac{k}{Z} |p'| \sin(\omega t - \angle p') \end{aligned} \quad (74)$$

where $|p'|$ and $\angle p'$ denote the magnitude and phase, respectively, of p' , the time-independent part of p . Substituting (74) into (72) gives the desired restatement of the latter equation:

$$D \cong \eta \left(\frac{k|p'|}{Z} \right)^2 \sin^2(\omega t - \angle p') \quad (75)$$

From this expression, the time-averaged (denoted by brackets $\langle \rangle$) power loss is at last obtained:

$$E_v(r, \phi) \equiv \frac{\eta}{2} \left(\frac{k|p'|}{Z} \right)^2 \quad (76)$$

$$\cong \langle D \rangle$$

As regards use of Equation 76, k and Z are known constants, and p' for this lossy case is approximated by the previously evaluated lossless pressure distribution, but η remains to be determined. This step is achieved by turning to the simpler case of loss in plane wave propagation. The experimentally measured total power loss per unit volume ($\langle dQ \rangle$), given in terms of the absorption coefficient α , is equated with viscous power loss ($\langle D \rangle$), in terms of η . Of course, such a relationship relies on the aforesaid assumption that a bulk-viscosity mechanism is entirely responsible for power loss in the tissue.

Proceeding as outlined, power loss in terms of α is

$$\langle dQ \rangle = 2\alpha \langle I \rangle \quad (77)$$

where

$$\langle I \rangle = \frac{|p'|^2}{2Z} \quad (78)$$

is a well known expression (Kinsler and Frey, 1962:121) for the time-averaged plane wave intensity, given in terms of the pressure amplitude $|p'|$. Combining (77) and (78) gives

$$\langle dQ \rangle = \alpha \cdot \frac{|p'|^2}{Z} \quad (79)$$

For ease of comparison, the expression for $\langle D \rangle$ from (76) is restated as follows:

$$\langle D \rangle = \frac{\eta k^2}{2Z} \cdot \frac{|p'|^2}{Z} \quad (80)$$

When $\langle dQ \rangle$ and $\langle D \rangle$ are equated, it is readily seen from (79) and (80) that the following relation must hold true:

$$\alpha = \frac{\eta k^2}{2Z} \quad (81a)$$

or, solving for η ,

$$\eta = \frac{2\alpha Z}{k^2} \quad (81b)$$

It should be noted that the frequency dependence of α and k implies that η , too, is not a constant but, instead, is also a function of f . In summary, the viscous power loss per unit volume (E_v) is given in Equation 76, where the bulk viscosity coefficient η is determined according to (81b) from a known α .

An alternative approach to estimating power loss is to sidestep the question of mechanism entirely, and merely interpret (77) more broadly, as follows:

$$\langle dQ \rangle = 2\alpha \langle |\bar{I}| \rangle \quad (82)$$

where

$$\begin{aligned} |\bar{I}| &= |p\bar{u}| \\ &= p|\bar{u}| \end{aligned} \quad (83)$$

According to this expression, the estimated power loss is computed using the magnitude of the intensity vector for a generalized wave distribution (including standing and travelling wave components), as opposed to the original interpretation using the scalar intensity of a plane (travelling only) wave. A difficulty encountered with this procedure is that the magnitude of the velocity vector does not, in general, follow a simple-harmonic pattern; i.e., $|\bar{u}|$ does not have a sinusoidal time dependence. The only exception to this general rule occurs if both components of \bar{u} , namely u_r and u_ϕ , are in phase. Therefore, in general no simple exact expression is obtainable for time-averaged $|\bar{I}|$. Nevertheless, the analysis proceeds by employing the following approximation, which is valid if u_r and u_ϕ are not significantly out of phase:

$$\langle |\bar{I}| \rangle \cong |\langle \bar{I} \rangle| \quad (84)$$

Now $|\langle \bar{I} \rangle|$ is simply evaluated as follows:

$$\begin{aligned} |\langle \bar{I} \rangle| &= |\langle p\bar{u} \rangle| \\ &= \frac{1}{2} |\text{Re}[p'(\bar{u}')^*]| \end{aligned} \quad (85)$$

Rewriting (82) using (84) and (85) yields the final expression for estimated absorptive power loss:

$$\begin{aligned} E_a(r, \phi) &\equiv \alpha |\text{Re}[p'(\bar{u}')^*]| \\ &\cong \langle dQ \rangle \end{aligned} \quad (86)$$

It is worthwhile to note that the expressions for E_v and E_a given in (76) and (86) differ primarily in that the former quantity is proportional to p^2 , as seems reasonable for a bulk-viscosity mechanism,

whereas the latter varies according to the product pu , as a result of the intensity-based approach.

Computation of E_v and E_a is performed in programs SCL and SSR, based on the lossless wave distributions calculated therein. Isomagnitude plots are then produced by ISOLOS, from which likely hot spots can be located visually, as regions of peak loss.

3. COMPUTATIONAL DATA AND RESULTS

3.1 Data

The set of parameters which describe a given soft-cylinder or -sphere problem is listed in Table 3, along with standard parameter values, and restrictions in programs SCL and SSR. These values are assumed to have been used in both analytical and numerical work, unless otherwise specified. These parameters uniquely determined a given problem, but other sets of parameters could serve just as well; this set is used merely for convenience. Additional constants calculated from these parameters are presented in Table 4, which includes the equations used to perform the calculations.

The unusual set of units, mm-mg- μ s, was selected so that most constants and variables have values near unity. This situation is desirable for numerical work, because some of the error control is based on absolute instead of relative values, and performs best for variables with values near one.

For the various computational runs, the parameters α , ρ_1 , and c_1 were varied about the standard values. Changing the radius α , with f constant, permits examination of the effects of object size versus acoustic wavelength; the quantity $k_1\alpha = 2\pi\alpha/\lambda_1$ is a good indicator of this comparison. On the other hand, ρ_1 and/or c_1 were changed with ρ_2 and c_2 constant, in order to explore the importance of the impedance mismatch.

Table 3

"Standard" Values for Computational Parameters

Symbol	Value	Units	Restrictions in Programs SCL/SSR
N_{r1}	20		$0 < N_1 \leq 20$
N_{r2}	1		$0 < N_{r2} \leq 20$
N_ϕ	100		$2 < N_\phi \leq 100$
f	1	MHz	$f > 0$
α	2.5	mm	$\alpha > 0$
P	1	$\text{mg}/\mu\text{s}^2 \cdot \text{mm} = \text{kN}/\text{mm}^2$	$P > 0$
ρ_1	1	mg/mm^3	$\rho_1 > 0$
ρ_2	1	mg/mm^3	$\rho_2 > 0$
c_1	1.5	$\text{mm}/\mu\text{s}$	$c_1 > 0$
c_2	1.5	$\text{mm}/\mu\text{s}$	$c_2 > 0$
$\tilde{\alpha}_1$	0.005	$\text{Np}/\text{mm} \cdot \text{MHz}$	$\tilde{\alpha}_1 \geq 0$
$\tilde{\alpha}_2$	0	$(\text{Np}/\text{mm} \cdot \text{MHz})$	$\tilde{\alpha}_2 \geq 0$

Table 4

Additional Quantities Calculated from Computational Parameters

Symbols	Units	Equations Used for Calculations
ω	Mrad/s	$\omega = 2\pi f$
k_1, k_2	mm^{-1}	(19)
z_1, z_2	Mrayl	(15)
Δr_1	mm	(58a)
Δr_2	mm	(58b)
$\Delta\phi$	rad	(59)
α_1, α_2	Np/mm	(87)
η_1, η_2	$\text{mg/mm} \cdot \mu\text{s} = 10^4 \text{ poise}$	(81b)

The grid parameters, N_{r1} , N_{r2} , and N_ϕ , were chosen for analytical work so that region 1 alone is examined, by means of $N_{r2} = 1$. The other two parameters reflect a tradeoff between plot resolution, and computation and plotting times. In general, it is desired to have the number of points in some way proportional to the value of $k_1 a$, but the standard grid size was not altered, in deference to computational expenses. A different set of values was used for numerical work; the choice of $N_{r1} = N_{r2} = 10$ and $N_\phi = 60$ is discussed in Section 2.3.

The remaining parameters were selected with regard to ultrasonic irradiation of tissue in general medical situations and in the particular case of a pregnant mouse. In the latter case, the developing fetuses can be grossly modelled as uniform, soft spheres.

The frequency range of interest is 1-10 MHz. However, the only frequency-dependent quantities are $k_1 a$ (and $k_2 a$) (ignoring the slight frequency dependence of c_1 and c_2) and α_1 (and α_2). As is later discussed, the latter absorption coefficient is almost linearly proportional to frequency for tissue irradiated in this frequency range. Thus little new information is obtained by monitoring the overall change in loss due to the frequency dependence of α_1 . Also, variations in $k_1 a$ can be "produced" via f or a , so that it is sufficient to keep f constant and vary a , or vice versa. The former alternative was chosen; accordingly, the "standard" value $f = 1$ MHz was used for all computations.

In analytical work, the radius a was varied over the range 0.25 to 10 mm, so that $k_1 a$ took on values from about 1 to 40 rad. The former extreme approaches the long-wavelength limit ($\lambda_1 \gg a$) with $\lambda_1 \sim 6a$,

whereas the latter extreme nears the short-wavelength limit ($\lambda_1 \ll a$) with $\lambda_1 \sim a/6$. In numerical work, only the value $a = 0.25$ mm (the minimum in analytical work), was used, in an attempt to minimize excessive computation times and storage requirements. Presumably, slight increases in the radius a could be tolerated without altering the grid size. However, the value $a = 10$ mm (the maximum in analytical work) would require so many sample points that the various numerical arrays could not be accommodated in the user memory allocation of 129K 60-bit words (on a Cyber 175). The only solution would be a memory-swapping technique, which would drastically reduce execution speed.

As discussed in Section 2.2.5, the value $P = 1 \text{ kN/mm}^2$ for the incident pressure amplitude was chosen to remove P , in effect, from the various expressions, so that the pressure and velocity variables are normalized. This is a tremendously high pressure, which would certainly violate all assumptions of linear particle displacements. Yet, the physical absurdity of the value is of no consequence, because only relative distributions are sought.

The standard values of ρ_1 , c_1 , ρ_2 , and c_2 are near those of water at 20°C ($\rho = 0.998 \text{ mg/mm}^3$ and $c = 1.483 \text{ mm/us}$). The standard values constitute an arbitrary reference, in that the relative values of ρ_1 , c_1 and ρ_2 , c_2 determine the highly important impedance mismatch. The absolute values of these variables were chosen near those of water for simplicity and relevance, because the properties of soft, fluid-like tissues are quite similar to those of water (O'Brien, 1977; Goss et al., 1978). In analytical work, the values of ρ_1 and c_1 were each varied

separately by $\pm 5\%$ and $\pm 20\%$ from the standard values, while the other three parameters remained unchanged. The smaller range represents typical tissue variations, while the larger represents the maximum observed variations, and is included mainly to permit generalization of trends regarding hot spots. On the other hand, only a single case was considered in all numerical work--that of an approximately 4% increase in c_1 over the standard value. It is thought that a larger impedance mismatch might be useful to increase the scattered wave, thereby decreasing the importance of computational errors resulting from the application of boundary conditions (see Section 2.3).

Finally, the absorption proportionality constants $\tilde{\alpha}_1$ and $\tilde{\alpha}_2$ were selected in regard to the following experimental observation (Johnston et al., 1979) concerning the frequency dependence of α_1 and α_2 :

$$\alpha_1 \cong \tilde{\alpha}_1 f \quad (87a)$$

and

$$\alpha_2 \cong \tilde{\alpha}_2 f \quad (87b)$$

The standard value of $\tilde{\alpha}_1$ (shown in Table 3) is 0.005 Np/mm·MHz, a typical value for tissues with low collagen content. Thus by Equation 87a, the absorption coefficient $\alpha_1 = 0.005$ Np/mm, at the standard frequency $f = 1$ MHz. The value $\tilde{\alpha}_2 = 0$ is used to force $\alpha_2 = 0$, in accordance with the assumption that region 2 is lossless. In fact, this assumption is arbitrary--it is made merely to be consistent with the examination of loss solely in object interiors. The particular value

of α_2 does not affect the first-order estimate of loss in region 1, because this estimate is based on the lossless distribution. Also note that this first-order estimate is reasonable: in the worst case of $\alpha = 10$ mm, the intensity of a plane wave decreasing according to $\exp(-2\alpha_1 x)$ would fall only by about 18% in a distance equal to the object diameter.

3.2 Analytical Results

3.2.1 Checkout of programs. A significant portion of the programming effort and a sizeable number of experimental runs have been devoted to testing the analytical computations. In the first place, it is important that all these calculations be correct, so that the generalizations built upon them are also accurate. Also, correctness is essential because the analytical work is the checkpoint for the current and perhaps future numerical work.

The first step was to check the accuracy of the mathematical function subroutines, listed in Table 2. Routines RBESJ and NBESY are "packaged" programs which have been checked prior to their release (Control Data Corp., 1973:3-5, 3-6: Table 3.2.1). Therefore, these programs are presumed to be correct and are given no further attention.

On the other hand, routines SBESJ and SBESN are privately supplied programs which have not been thoroughly tested. Values for both routines were checked to a few digits precision for several arguments and for orders $m = 0, 1, 2$, using a table of spherical Bessel functions (Morse and Ingard, 1968:899). This check resulted in the modification of SBESN to

correctly compute $y_m(x)$, instead of $-y_m(x)$, as originally set up. In addition, routine SBESJ was checked to much higher precision and for a wider range of arguments and orders, by comparing results with a packaged program "BSJ," also checked prior to its release (Control Data Corp., 1973:3-10: Table 3.2.1), like RBESJ and NBESY. It was found that the values differed by as much as 1% for orders $m > 20$, with arguments up to 4 (for which range downward recursion is used). However, these discrepancies are of no consequence, because the series expressions are always truncated by the programs before the possibly erroneous higher-order terms are reached. It is assumed that SBESN does not suffer from a similar problem, because upward recursion is used for all arguments. It was also found that SBESJ (and BSJ) encounters gross errors for arguments near a multiple of π ; this problem and a recommended solution are discussed in Section 2.2.5.

Finally, the routine ALEG was also checked with a table to a few decimal places for a few lower orders ($m = 0, 1, \dots, 9$) with several arguments (Morse and Ingard, 1968:898). As with SBESN, the occurrence of higher-order inaccuracies with ALEG is unlikely, because upward recursion is again employed.

The next step in the programs checkout concerns the rigid-object programs RCL and RSR. These programs bear great resemblance to each other, because the rigid-cylinder and -sphere problems have very similar solutions. In fact, program RSR was obtained as a mere adaptation of RCL, so that the correctness of one program supports the correctness of the other. This relationship applies directly to the

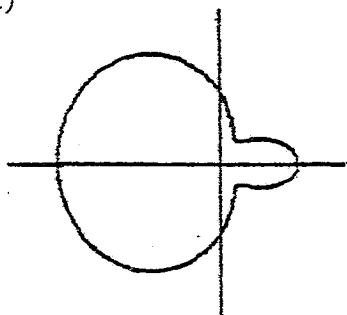
following test of program RSR. Using the regularly calculated scattered pressure p'_s and values for p'_l supplied by a temporary inclusion, the total pressure in region 2 was obtained as $p'_2 \equiv p'_s + p'_l$ (as in Equation 88a below). This pressure p'_2 was evaluated, for $k_2 a = 1$, at the sphere surface ($r = a$) and at 30° intervals in θ , and was checked with corresponding values calculated by a fellow student, using very dissimilar methods.

Of course, this procedure applies only to the pressure, and not to the velocity. As a broader check of the programs RCL and RSR, both variables p'_s and u'_{rs} were used to compute the far-field (i.e., $r \gg a$) radial intensity $\langle I_{rs} \rangle$ according to Equations 31 or 54. As shown in Figures 3 and 5, respectively, the angular distribution of $\langle I_{rs} \rangle$ was plotted using $ka = 1, 3, 5$ for both the cylindrical and the spherical cases. These plots were compared with corresponding sketches given by Morse and Ingard (1968:402: Figure 8.1; 420: Figure 8.4) and reproduced in Figures 4 and 6. In all cases, the plots and sketches match qualitatively well. The slight discrepancies are attributed to the antiquated plotting methods originally used to produce these plots, which are taken directly from a related book whose first edition was published in 1936 (Morse).

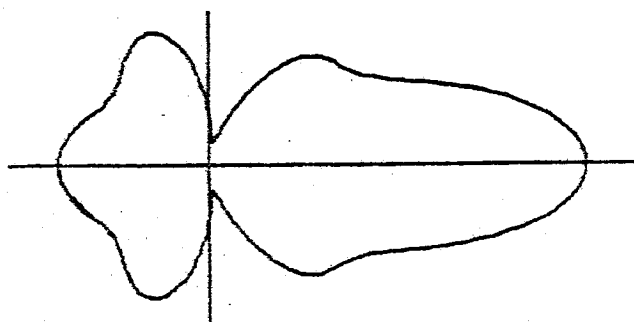
The first checkout step for the soft-object programs SCL and SSR compared solutions computed by these programs for the limiting cases of rigid objects with the respective "exact" solutions computed by the rigid-object programs. The rigid-object extremes were simulated in the soft-object programs by means of high ρ_1 and standard c_1 , in

(a)

77



(b)



(c)

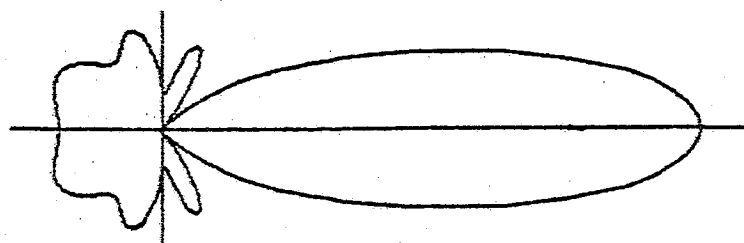
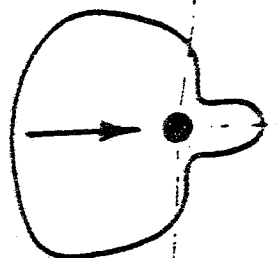
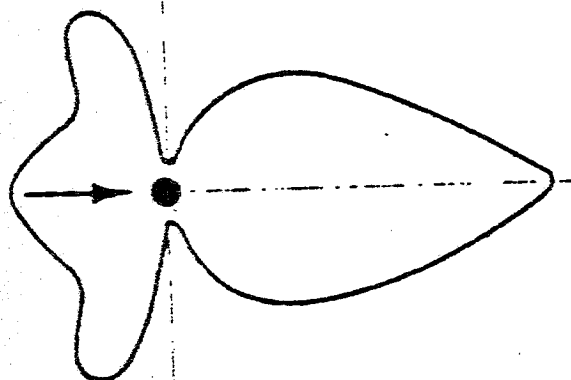


Figure 3. Angular distribution of radial intensity ($\langle I_{rs} \rangle$) of wave scattered by rigid cylinder, in the path of an incident plane wave moving to the right. Three cases are shown: (a) $ka = 1$ rad, (b) $ka = 3$, and (c) $ka = 5$. The intensity is evaluated in the "far field" ($r \gg a$), specifically at $r = 100 \cdot a$. These plots have been scaled so that the main lobes are the same length as those in the reference plots in Figure 4. The calculations and plotting were performed using program RCL.

(a)



(b)



(c)

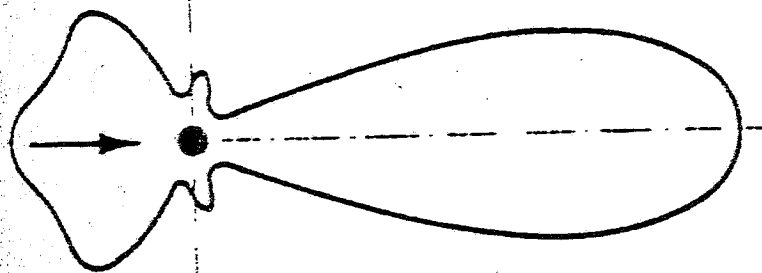


Figure 4. Scattered radial intensity for a cylinder as in Figure 3, again for the cases (a) $ka = 1$ rad, (b) $ka = 3$, and (c) $ka = 5$. A right-moving incident plane wave is indicated by the arrow on each plot. These plots are taken from Morse and Ingard (1968:402: Figure 8.1). The radius of intensity evaluation is not known.

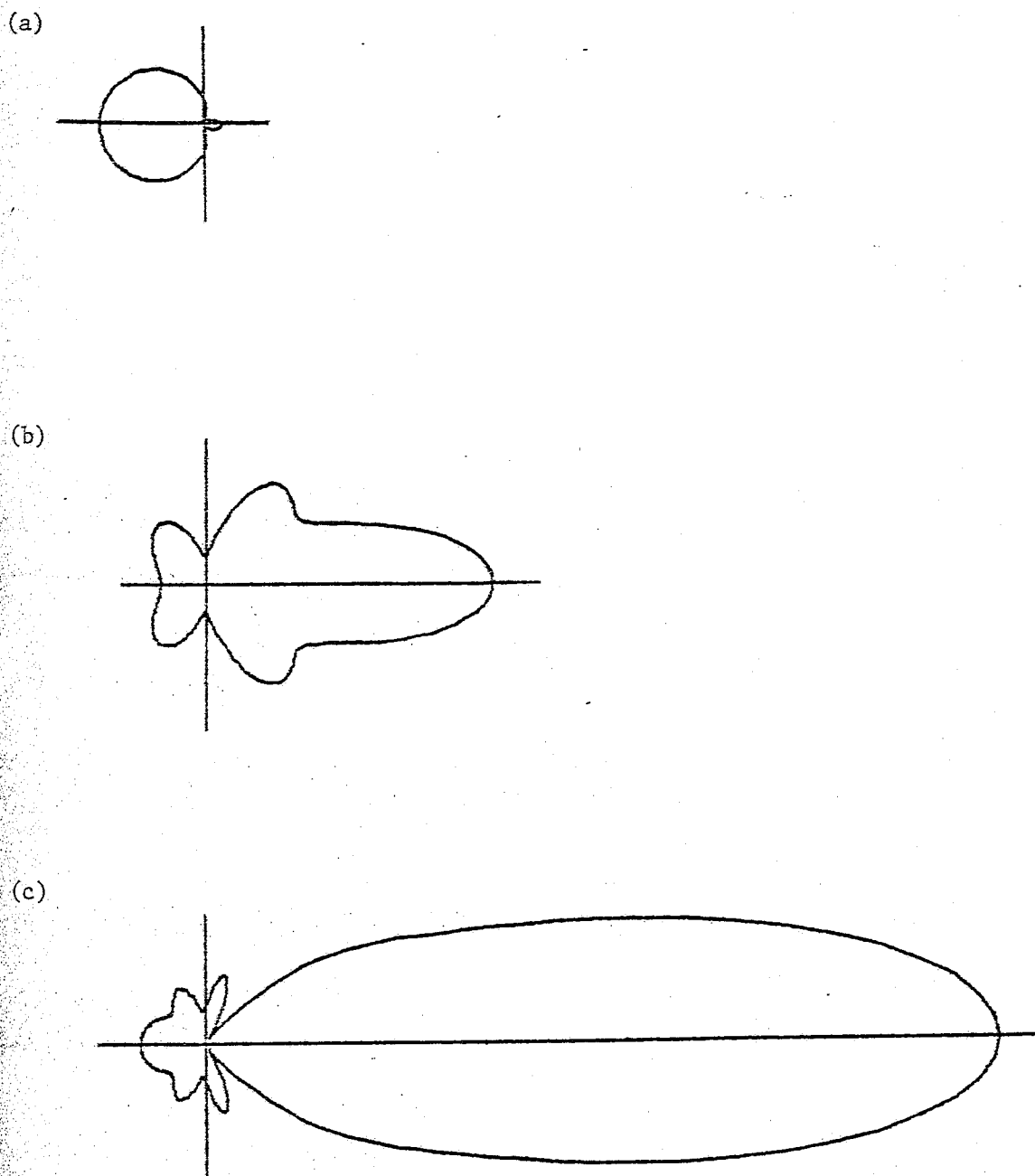


Figure 5. Angular distribution of radial intensity ($\langle I_{rs} \rangle$) of wave scattered by rigid sphere, in the path of an incident plane wave moving to the right. Three cases are shown: (a) $ka = 1$ rad, (b) $ka = 3$, and (c) $ka = 5$. The intensity is evaluated in the far field, at $r = 100 \cdot a$. These plots have been scaled so that the main lobes are the same length as those in the reference plots in Figure 6. The calculations and plotting were performed using program RSR.

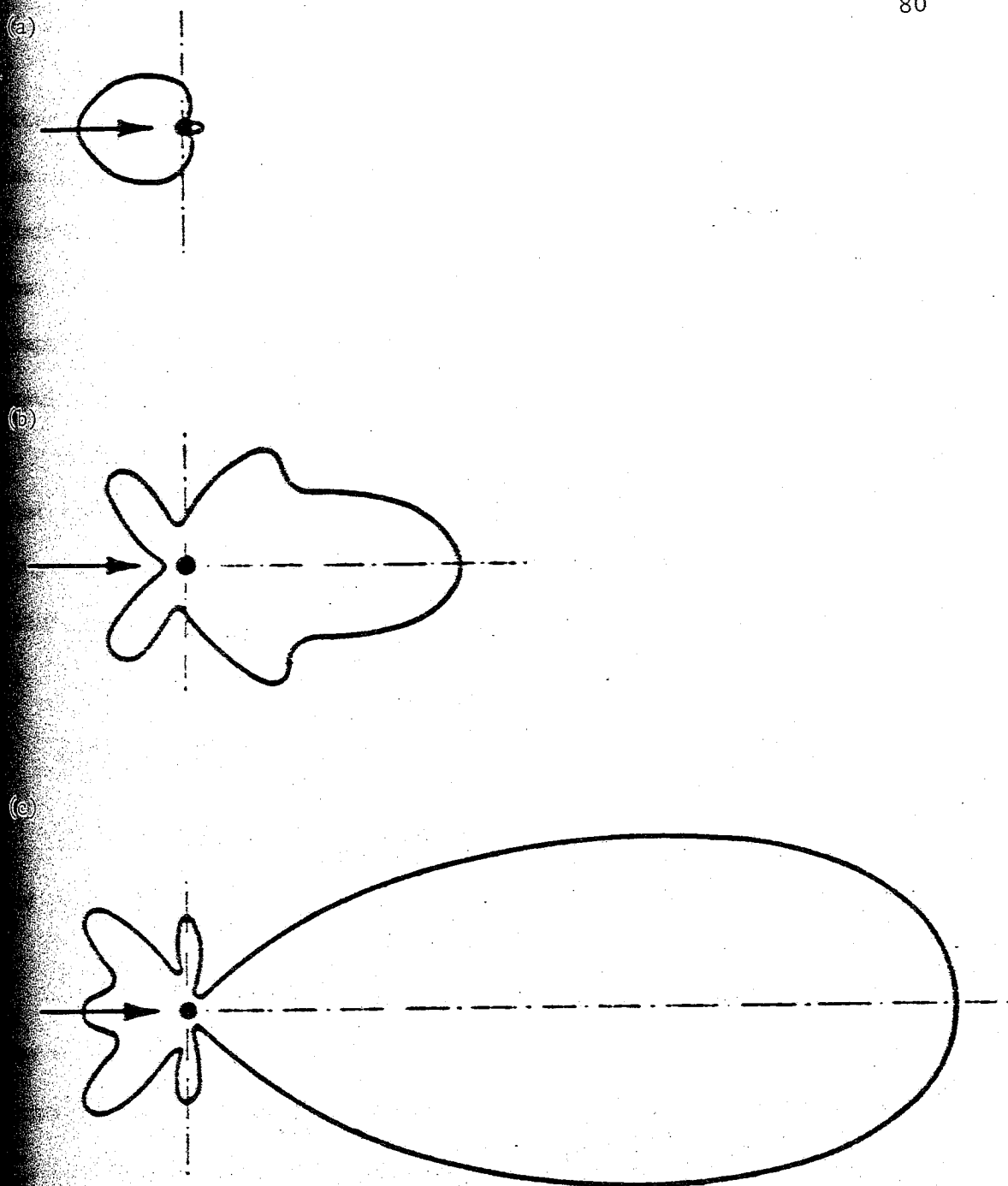


Figure 6. Scattered radial intensity for a sphere as in Figure 5, for the same cases (a) $ka = 1$ rad, (b) $ka = 3$, and (c) $ka = 5$. These plots were taken from Morse and Ingard (1968:420: Figure 8.4). The radius of intensity evaluation is unknown.

accordance with the discussion in Section 2.2.2. For both SCL and SSR, the condition $\rho_1 = 1000 \text{ mg/mm}^3 = 10^3 \cdot \rho_2$ resulted in a slightly diminished distribution for p_w' , significantly reduced \bar{u}_w' , and agreement to about 0.1% (for cylinder; 2% for sphere) for p_s' and \bar{u}_s' , as compared with the solutions calculated by RCL and RSR. All of these results agree with expectations.

A second means of checking the soft-object programs is to verify that the boundary conditions, Equations 20 or 46, are satisfied. Thus, programs SCL and SSR were temporarily modified to compute total variables in region 2 as the sum of the scattered and incident variables, or

$$p_2' = p_s' + p_i' \quad (88a)$$

$$\bar{u}_{r2}' = \bar{u}_{rs}' + \bar{u}_{ri}' \quad (88b)$$

and

$$\bar{u}_{\phi 2}' = \bar{u}_{\phi s}' + \bar{u}_{\phi i}' \quad (88c)$$

The values of these variables at the object boundary $r = a$ were compared with the corresponding values for the interior variables, namely p_w' , \bar{u}_{rw}' , $\bar{u}_{\phi w}'$, for a series of angular samples in ϕ . The matching of boundary values for pressure and radial velocity confirmed the satisfaction of the boundary conditions. It was also verified that tangential velocity is continuous only if $\rho_1 = \rho_2$, as can be shown using the wave equation (1b).

Finally, a very simple yet effective scheme for checking programs SCL and SSR is presented. Suppose that regions 1 and 2 have identical acoustic properties (i.e., $\rho_1 = \rho_2$ and $c_1 = c_2$). Then no impedance mismatch exists, so that the incident plane wave propagates undisturbed, represented by $p'_i = P$ in region 2 and $p'_w = P$ in region 1. Also, the scattered wave should be zero, i.e., $p'_s = 0$ in region 2. These relationships are readily verifiable.

Furthermore, the check can be extended to include the velocity \bar{u} through the use of the intensity, as follows. First, for a plane wave with pressure amplitude P , it is well known (see Equation 78) that

$$\langle |\bar{I}| \rangle = \frac{P^2}{2Z} \quad (89)$$

Because the incident wave is a simple plane wave, the velocity components u_x and u_y are in phase, so that Equation 84 holds exactly. Then the following readily verifiable relations hold true:

$$E_{a1} = \frac{\alpha_1 P^2}{Z_1} \quad (90a)$$

and

$$E_{a2} = \frac{\alpha_2 P^2}{Z_2} \quad (90b)$$

where $Z_1 = Z_2$ is the basis on which these equations are derived. Thus E_{a1} and E_{a2} should be constants, which are equal if $\alpha_1 = \alpha_2$. Of course, α_2 was made nonzero only for testing purposes; normally, $\alpha_2 = 0$ was used, because region 2 is assumed lossless. Now, both the pressure and the

intensity predictions were essentially verified, although not quite exactly, because the assignment $Z_2 = 1.000\ 001 \cdot Z_1 \cong Z_1$ was used to avoid computational difficulties which ensue for $Z_2 = Z_1$. This check supports correctness of all aspects of the computations all the way through to that of E_α , including calculating the radial and angular factors, combining them into the correct variables, and finally truncating properly.

Lastly, the plotting programs ISO and ISOLOS were checked with regard to correct values for F_{max} and F_{min} (see Section 3.2.2 for definition). Also, the approximate shapes and locations of a few contours were predicted from numerical data and compared with the actual plots.

3.2.2 Spatial distributions. As has been previously discussed (see Section 2.2.5), programs ISO and ISOLOS plot isomagnitude and, where appropriate, isophase contours for variables whose spatial distributions have been calculated analytically by programs SCL and SSR, for the cylindrical and spherical cases, respectively. More specifically, program ISO plots the wave variables $|p'|$, $|u'_r|$, and $|u'_\phi|$ as isomagnitude contours, and $\angle p'$, $\angle u'_r$, and $\angle u'_\phi$ as isophase contours. Program ISOLOS plots the estimated power-loss variables E_v and E_α as isomagnitude contours.

Both programs plot the total distributions of the aforementioned variables, using values on a polar grid. In region 1 of this grid, representing the cross sections of the object interiors, the quantities

\underline{p}'_w , \underline{u}'_{rw} , and $\underline{u}'_{\phi w}$ comprise the total solution for the wave variables. On the other hand, the quantities \underline{p}'_2 , \underline{u}'_{r2} , and $\underline{u}'_{\phi 2}$, as defined in Equations 88, are the total wave variables in region 2, representing the object exteriors. The power-loss variables E_{v1} , E_{v2} , E_{a1} , and E_{a2} are calculated using the total wave variables of the corresponding regions. A dashed circle represents the cylinder or sphere boundary, separating regions 1 and 2.

However, in spite of the capability of the programs to examine solutions both inside and outside the objects, this thesis focuses on spatial distributions solely within the objects, by means of the parameter choice $N_{r2} = 1$. This approach is in accordance with the assumption (see Section 1.2) that region 2 is made up of lossless material (recall the parameter selection $\tilde{\alpha}_2 = 0$ in Section 3.1).

The spatial distribution of a given variable is illustrated by plotting all contours along which the variable equals one of a set of N_L equally spaced values (the quantity N_L is the "number of levels"). In the case of isomagnitude contours of a nonnegative, real variable F_0 , these values are

$$F_{min} + \frac{1}{2}\Delta F, F_{min} + \frac{3}{2}\Delta F, \dots, F_{min} + \left[\frac{2N_L - 1}{2} \right] \Delta F$$

where

$$\Delta F \equiv \frac{F_{max} - F_{min}}{N_L} \quad (91)$$

is the increment between contours, and F_{min} and F_{max} represent the

minimum and maximum values of the plotted variable F_0 on the polar grid (including the interpolated center point). For isophase contours of a modular variable F_0 (with modulus 2π), the N_L contour values (in radians) are

$$0, \Delta F, 2\Delta F, \dots, (N_L - 1)\Delta F$$

where

$$\Delta F \equiv \frac{2\pi}{N_L} \quad (92)$$

This full range of angular values--which ignores the particular values of F_0 --is used for isophase contours, because of the meaninglessness of "minimum" and "maximum" with regard to modular variables. For both types of contours, the above contour values are assigned level numbers 1 through N_L ; the level number of each contour is displayed one space to the right of one randomly chosen point on the contour. It is important to note that the contours themselves are numbered, instead of the regions between the contours.

The following figures show groups of plots illustrating specific features and trends in the spatial distributions of the wave and power-loss variables. These single-page groupings are useful for comparative purposes, but the necessarily small size of the individual plots obscures many details. Therefore, full-size versions of every plot are supplied in the Appendix, in order to provide a detailed reference. Note that each group of plots illustrates a trend only for a single object shape (cylinder or sphere), and that all figures are presented

in cylinder/sphere pairs (on two separate pages). As a result, comparisons between object shapes, ceteris paribus, are performed using plots in identical locations on two successive pages.

Both small and full-size plots are identified at the left of each drawing by (in addition to the figure captions) notations of contour type (isomagnitude or isophase), object shape (cylinder or sphere), and variable (p' , \underline{u}'_r , \underline{u}'_ϕ , E_v , or E_α , indicated by "PRESSURE," "RAD VELOC," "TANG VELOC," "LOSS--VISC," or "LOSS--ABS," respectively). Also, values of the variables Z_r , $k_1\alpha$, α , ρ_1 , ρ_2 , c_1 , c_2 , f , N_{point} (the total number of contour points--limited to 5000), and N_L are displayed with all plots. Values of F_{min} and F_{max} appear only with isomagnitude plots, and values of η_1 and η_2 are noted only with plots of E_v .

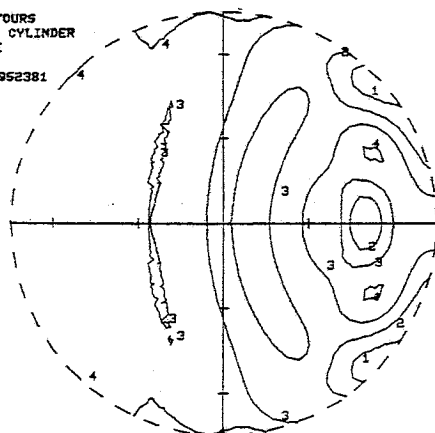
In some of the following plots, in which the contours are close together, it is difficult to discern the correspondence between level numbers and contours. However, this difficulty can generally be resolved by considering the spatial trends of the variables and by employing the "process of elimination" (there is a one-to-one correspondence between plotted contours and displayed level numbers). It may also be helpful to refer to the full-size versions of the plots provided in the Appendix.

The first set of plots, Figures 7 and 8, present typical examples of all six plots which can be produced by program ISO, namely isocontour drawings for the quantities $|p'|$, $\angle p'$, $|\underline{u}'_r|$, $\angle \underline{u}'_r$, $|\underline{u}'_\phi|$, and $\angle \underline{u}'_\phi$. Figure 7 represents the cylindrical case, and Figure 8 the spherical case. In both sets of plots, the (standard) object radius

ISO-MAGNITUDE CONTOURS
CROSS-SECTION OF CYLINDER
VARIABLE: PRESSURE

ZRAT [Z2/Z1] = .952381
AK1A = 9.97331
A = 2.5
RH01 = 1.
RH02 = 1.
C1 = 1.575
C2 = 1.5
F = 1.
P = 1.
NPT = 1170
NL = 4
RMIN = .842066
RMAX = 1.08232

INCIDENT WAVE
→

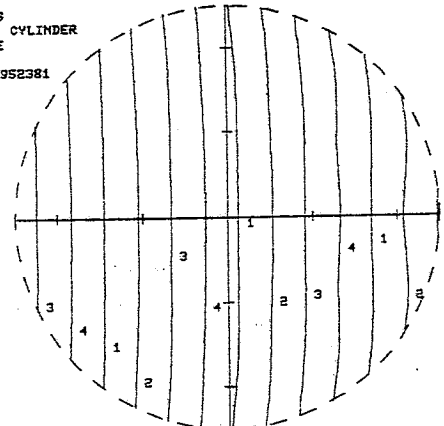


(a) See Figure 25.

ISO-PHASE CONTOURS
CROSS-SECTION OF CYLINDER
VARIABLE: PRESSURE

ZRAT [Z2/Z1] = .952381
AK1A = 9.97331
A = 2.5
RH01 = 1.
RH02 = 1.
C1 = 1.575
C2 = 1.5
F = 1.
P = 1.
NPT = 1381
NL = 4

INCIDENT WAVE
→

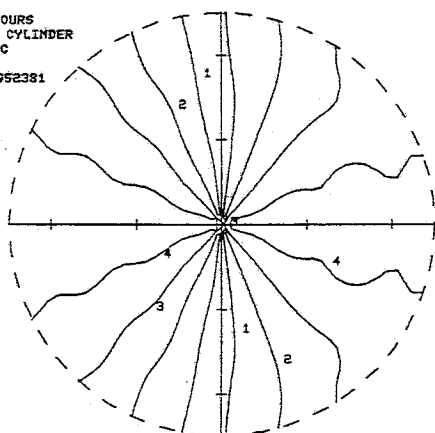


(b) See Figure 26.

ISO-MAGNITUDE CONTOURS
CROSS-SECTION OF CYLINDER
VARIABLE: RAD VELOC

ZRAT [Z2/Z1] = .952381
AK1A = 9.97331
A = 2.5
RH01 = 1.
RH02 = 1.
C1 = 1.575
C2 = 1.5
F = 1.
P = 1.
NPT = 901
NL = 4
RMIN = .000538
RMAX = .665739

INCIDENT WAVE
→

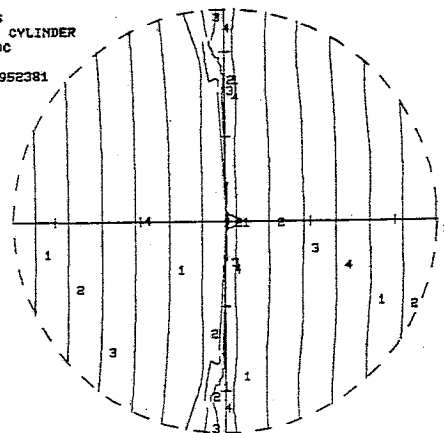


(c) See Figure 27.

ISO-PHASE CONTOURS
CROSS-SECTION OF CYLINDER
VARIABLE: RAD VELOC

ZRAT [Z2/Z1] = .952381
AK1A = 9.97331
A = 2.5
RH01 = 1.
RH02 = 1.
C1 = 1.575
C2 = 1.5
F = 1.
P = 1.
NPT = 1674
NL = 4

INCIDENT WAVE
→

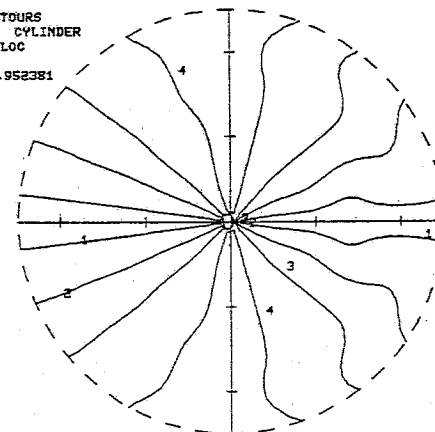


(d) See Figure 28.

ISO-MAGNITUDE CONTOURS
CROSS-SECTION OF CYLINDER
VARIABLE: TANG VELOC

ZRAT [Z2/Z1] = .952381
AK1A = 9.97331
A = 2.5
RH01 = 1.
RH02 = 1.
C1 = 1.575
C2 = 1.5
F = 1.
P = 1.
NPT = 911
NL = 4
RMIN = 0.
RMAX = .697265

INCIDENT WAVE
→

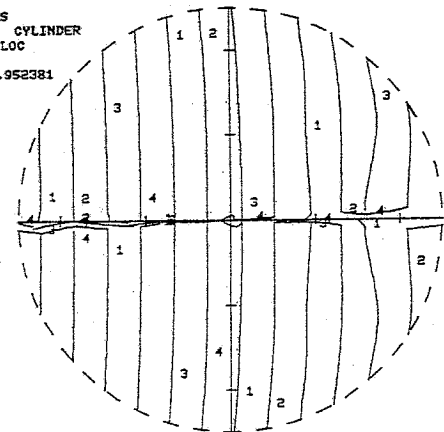


(e) See Figure 29.

ISO-PHASE CONTOURS
CROSS-SECTION OF CYLINDER
VARIABLE: TANG VELOC

ZRAT [Z2/Z1] = .952381
AK1A = 9.97331
A = 2.5
RH01 = 1.
RH02 = 1.
C1 = 1.575
C2 = 1.5
F = 1.
P = 1.
NPT = 1635
NL = 4

INCIDENT WAVE
→



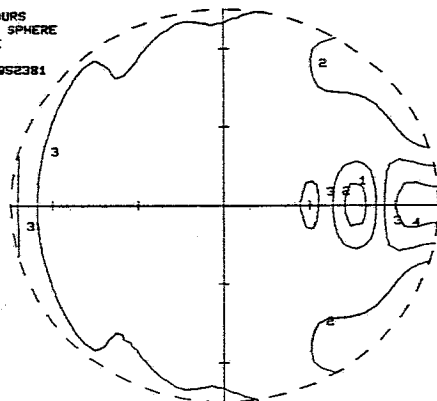
(f) See Figure 30.

Figure 7. Isomagnitude and isophase contours showing typical distributions of wave variables (pressure (p'), radial velocity (u'_r), and tangential velocity (u'_θ)) in cross section of cylinder (with c_1 5% higher than c_2 , and $k_1 a \cong 10$ rad).

ISOMAGNITUDE CONTOURS
CROSS-SECTION OF SPHERE
VARIABLE: PRESSURE

ZRAT [Z2/Z1] = .952381
AKIA = 9.97341
A = 2.5
RH01 = 1.
RH02 = 1.
C1 = 1.575
C2 = 1.5
F = 1.00001
P = 1.
NPT = 543
NL = 4
FMIN = .722333
FMAX = 1.20605

INCIDENT WAVE
→

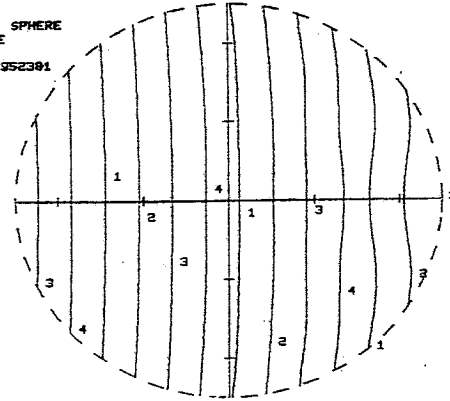


(a) See Figure 31.

ISOPHASE CONTOURS
CROSS-SECTION OF SPHERE
VARIABLE: PRESSURE

ZRAT [Z2/Z1] = .952381
AKIA = 9.97341
A = 2.5
RH01 = 1.
RH02 = 1.
C1 = 1.575
C2 = 1.5
F = 1.00001
P = 1.
NPT = 1389
NL = 4

INCIDENT WAVE
→

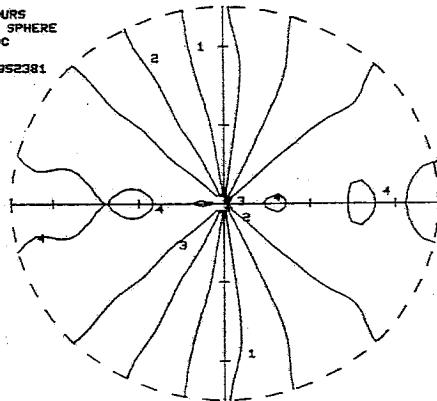


(b) See Figure 32.

ISOMAGNITUDE CONTOURS
CROSS-SECTION OF SPHERE
VARIABLE: RAD VELOC

ZRAT [Z2/Z1] = .952381
AKIA = 9.97341
A = 2.5
RH01 = 1.
RH02 = 1.
C1 = 1.575
C2 = 1.5
F = 1.00001
P = 1.
NPT = 833
NL = 4
FMIN = .002352
FMAX = .719871

INCIDENT WAVE
→

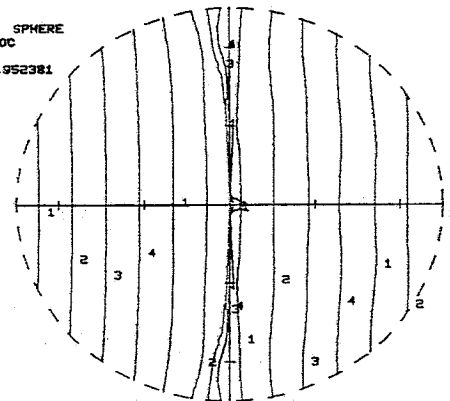


(c) See Figure 33.

ISOPHASE CONTOURS
CROSS-SECTION OF SPHERE
VARIABLE: RAD VELOC

ZRAT [Z2/Z1] = .952381
AKIA = 9.97341
A = 2.5
RH01 = 1.
RH02 = 1.
C1 = 1.575
C2 = 1.5
F = 1.00001
P = 1.
NPT = 1659
NL = 4

INCIDENT WAVE
→

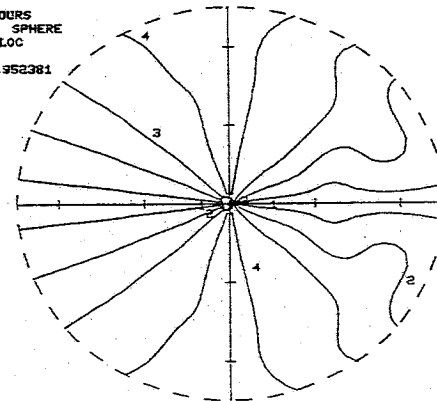


(d) See Figure 34.

ISOMAGNITUDE CONTOURS
CROSS-SECTION OF SPHERE
VARIABLE: TANG VELOC

ZRAT [Z2/Z1] = .952381
AKIA = 9.97341
A = 2.5
RH01 = 1.
RH02 = 1.
C1 = 1.575
C2 = 1.5
F = 1.00001
P = 1.
NPT = 929
NL = 4
FMIN = .0
FMAX = .63497

INCIDENT WAVE
→

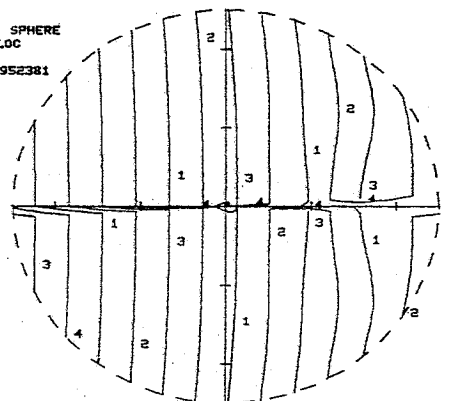


(e) See Figure 35.

ISOPHASE CONTOURS
CROSS-SECTION OF SPHERE
VARIABLE: TANG VELOC

ZRAT [Z2/Z1] = .952381
AKIA = 9.97341
A = 2.5
RH01 = 1.
RH02 = 1.
C1 = 1.575
C2 = 1.5
F = 1.00001
P = 1.
NPT = 1628
NL = 4

INCIDENT WAVE
→



(f) See Figure 36.

Figure 8. Isomagnitude and isophase contours showing typical distributions of wave variables in cross section of sphere (with c_1 5% higher than c_2 , and $k_1 a \cong 10$ rad).

($a = 2.5$ mm) is somewhat greater than the acoustic wavelength, as indicated by the value $k_1 a \cong 10$ rad. The impedance mismatch is moderate and is the result of a discrepancy in the acoustic velocity: c_1 (within the object) is 5% higher than c_2 (and also 5% higher than its "standard" value). The densities are matched and are set to the standard values. The dimensional units of the displayed parameters and constants can be determined from Tables 3 and 4. The units of the isomagnitude contour values (which can be calculated from N_L , F_{min} , and F_{max}) are kN/mm^2 for $|p'|$, and mm/us for $|u'_x|$ and $|u'_\phi|$.

As regards the interpretation of the plots, first suppose that the impedance mismatch did not exist, so that the interior pressure wave p'_w would be merely a continuation of the incident plane wave p'_i . In this case, for the isomagnitude plot of $|p'|$, the pressure amplitude would be P at all points, resulting in $F_{min} = F_{max} = P$ ($= 1 \text{ kN/mm}^2$). No contours would be drawn, because $|p'_w|$ would take on a single value throughout the region, instead of on sets of lines. The isophase contours for $\angle p'_w$ would be straight, evenly spaced vertical lines. In the cases in Figures 7 and 8, the velocity mismatch results in areas where the interior pressure wave has a magnitude above or below the incident pressure amplitude P , as indicated by $F_{min} < P$ and $F_{max} > P$. The range of values F_{min} through F_{max} is greater in the spherical case, as is almost always true. The isophase contours possess the general characteristics discussed above for the case of no mismatch, but differ somewhat in two ways: first, a slight "downstream" (to the right) "bowing" is observed in almost all lines, and is most pronounced in the

central portion of the objects. Second, some more random phase distortion is observed on the right side of the object, as shown by "wavy" phase contours. This distortion generally is more prominent in the spherical case, other things being equal, and usually occurs in the regions of greater nonuniformity of magnitude. The situations in which these phenomena occur and their significance will be considered later in detail.

Attention is now turned to the particle velocity plots. The isomagnitude plots for $|\underline{u}'_r|$ and $|\underline{u}'_\phi|$ show essentially radial contours, with strong angular dependence. Each particle velocity component is large at the angle where it is aligned with the longitudinal (horizontal, in this case) particle movement of the incident wave, and is small at directions orthogonal to this movement. Thus the radial velocity amplitude is greatest along the horizontal axis, where the tangential velocity has minimum amplitude, and vice versa along the vertical axis. Note that $F_{min} = 0$ for $|\underline{u}'_\phi|$, as required by symmetry at the horizontal axis; on the other hand, F_{min} is relatively small (as compared with F_{max}) but nonzero for $|\underline{u}'_r|$.

These isomagnitude contours for particle velocity show primarily the angular dependence of the (arbitrary) velocity components and obscure the effects of the acoustic-velocity mismatch. Thus it seems that plotting \underline{u}'_r and \underline{u}'_ϕ is not a good way to elucidate these effects. The ideal alternative would perhaps be to plot the amplitude of the magnitude of the particle velocity vector \bar{u} . However, such a quantity does not in general exist, because $|\bar{u}|$ is not "simple harmonic" (unless

the components, say u_r and u_ϕ , are in phase—see discussion in Section 2.4). Owing to this difficulty, no additional plots of particle velocity will be presented.

The "distortion" around the center in the plots of $|u_r'|$ and $|u_\phi'|$ deserves special mention: it occurs partly because the discrete polar grid performs poorly in representing converging radial lines. Also, a more general and recurring problem contributes to this distortion: the process of interpolation in "guessing" a value for the missing center sample frequently results in anomalous curves in this area. This "strangeness" in the contours should be ignored.

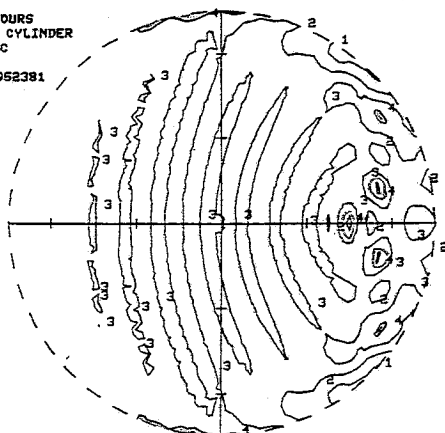
Finally, the isophase contours for $\angle u_r'$ and $\angle u_\phi'$ are considered. They are quite similar to the curves for $\angle p'$. The "garbage" along the vertical axis with $\angle u_r'$ and along the horizontal axis with $\angle u_\phi'$ owes to the very low magnitudes of the velocity components in those areas, and is of no significance. Also note the symmetry-dependent phase reversal of $\angle u_\phi'$ at the horizontal axis.

Figures 9 and 10 compare (for the cylinder and sphere, respectively) the two estimates of power loss per unit volume E_v and E_α for three different cases. The first and second examples entail relatively large spheres ($\alpha = 5$ mm) and thus high $k_1\alpha$, whereas a much smaller sphere ($\alpha = 0.25$ mm) is used in the third example. A moderate velocity mismatch (c_1 5% higher than c_2) is imposed in the first and third instances, and a large density mismatch (ρ_1 20% higher than ρ_2) is considered in the second case. These selections are intended as a representative sample of the many possible situations. The dimensional

ISO-MAGNITUDE CONTOURS
CROSS-SECTION OF CYLINDER
VARIABLE: LOSS-VISC

ZRAT C22/Z11 = .952381
AK1A = 19.9466
A = 5.
RH01 = 1.
RH02 = 1.
C1 = 1.575
C2 = 1.5
F = 1.
P = 1.
NPT = 2245
NL = 4
FRIN = .001854
FRAX = .004015
ETAT = .000989
ETAT2 = 0.

INCIDENT WAVE

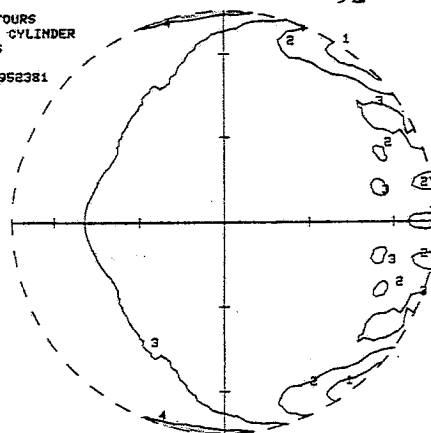


(a) See Figure 37.

ISO-MAGNITUDE CONTOURS
CROSS-SECTION OF CYLINDER
VARIABLE: LOSS-ABS

ZRAT C22/Z11 = .952381
AK1A = 19.9466
A = 5.
RH01 = 1.
RH02 = 1.
C1 = 1.575
C2 = 1.5
F = 1.
P = 1.
NPT = 553
NL = 4
FRIN = .00205
FRAX = .004
ALF1 = .005
ALF2 = 0.

INCIDENT WAVE

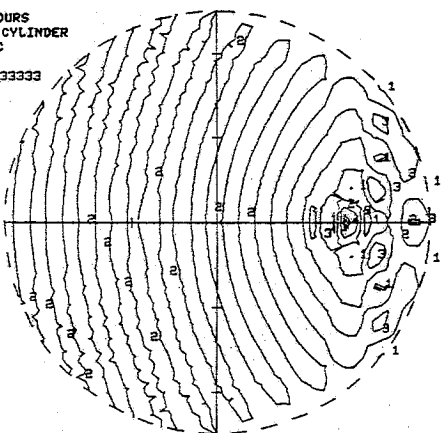


(b) See Figure 38.

ISO-MAGNITUDE CONTOURS
CROSS-SECTION OF CYLINDER
VARIABLE: LOSS-VISC

ZRAT C22/Z11 = .833333
AK1A = 20.944
A = 5.
RH01 = 1.2
RH02 = 1.
C1 = 1.5
C2 = 1.5
F = 1.
P = 1.
NPT = 2801
NL = 4
FRIN = .001813
FRAX = .005874
ETAT = .001025
ETAT2 = 0.

INCIDENT WAVE

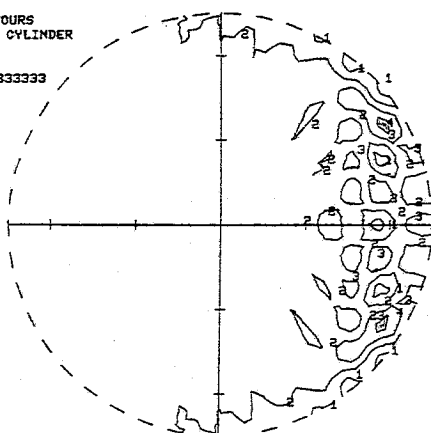


(c) See Figure 39.

ISO-MAGNITUDE CONTOURS
CROSS-SECTION OF CYLINDER
VARIABLE: LOSS-ABS

ZRAT C22/Z11 = .833333
AK1A = 20.944
A = 5.
RH01 = 1.2
RH02 = 1.
C1 = 1.5
C2 = 1.5
F = 1.
P = 1.
NPT = 368
NL = 4
FRIN = .002633
FRAX = .004106
ALF1 = .005
ALF2 = 0.

INCIDENT WAVE

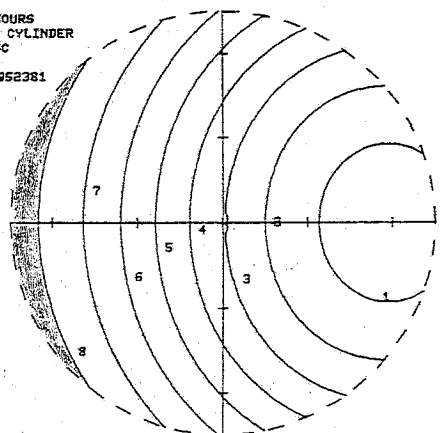


(d) See Figure 40.

ISO-MAGNITUDE CONTOURS
CROSS-SECTION OF CYLINDER
VARIABLE: LOSS-VISC

ZRAT C22/Z11 = .952381
AK1A = .997331
A = .25
RH01 = 1.
RH02 = 1.
C1 = 1.575
C2 = 1.5
F = 1.
P = 1.
NPT = 1113
NL = 3
FRIN = .002337
FRAX = .003347
ETAT = .000959
ETAT2 = 0.

INCIDENT WAVE

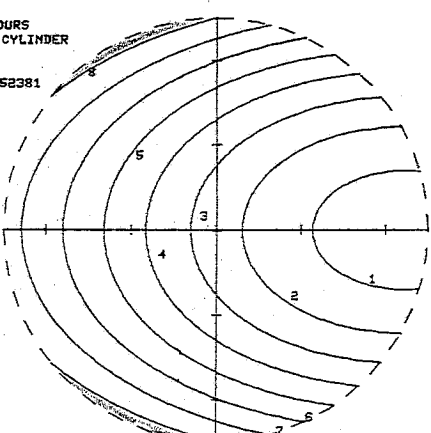


(e) See Figure 41.

ISO-MAGNITUDE CONTOURS
CROSS-SECTION OF CYLINDER
VARIABLE: LOSS-ABS

ZRAT C22/Z11 = .952381
AK1A = .997331
A = .25
RH01 = 1.
RH02 = 1.
C1 = 1.575
C2 = 1.5
F = 1.
P = 1.
NPT = 1253
NL = 3
FRIN = .00312
FRAX = .003315
ALF1 = .005
ALF2 = 0.

INCIDENT WAVE



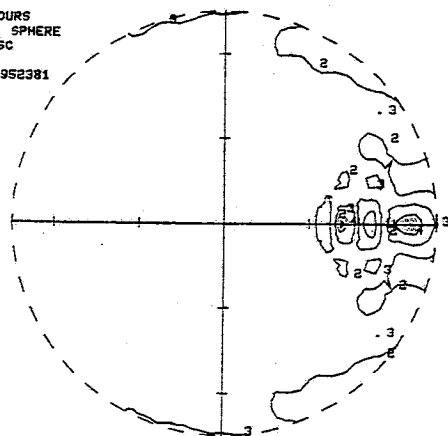
(f) See figure 42.

Figure 9. A comparison between two estimates of power loss (per unit volume), viscous (E_v) and absorptive (E_a), for three representative cases, in cylinder.

ISOMAGNITUDE CONTOURS
CROSS-SECTION OF SPHERE
VARIABLE: LOSS-VISC

ZRAT [Z2/Z1] = .952381
AKIA = 19.9468
A = 5.
RH01 = 1.
RH02 = 1.
C1 = 1.575
C2 = 1.5
F = 1.00001
P = 1.
NPT = 556
NL = 4
FMIN = .000987
FMAX = .005224
ETAL = .000989
ETAR = 0.

INCIDENT WAVE



(a) See Figure 43.

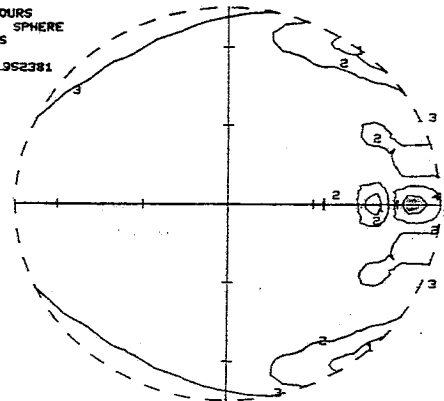
ISOMAGNITUDE CONTOURS
CROSS-SECTION OF SPHERE
VARIABLE: LOSS-ABS

ZRAT [Z2/Z1] = .952381
AKIA = 19.9468
A = 5.
RH01 = 1.
RH02 = 1.
C1 = 1.575
C2 = 1.5
F = 1.00001
P = 1.
NPT = 515
NL = 4

FMIN = .001638
FMAX = .0044

ALF1 = .005
ALF2 = 0.

INCIDENT WAVE



(b) See Figure 44.

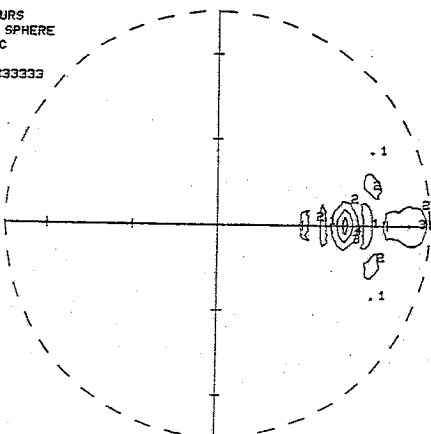
ISOMAGNITUDE CONTOURS
CROSS-SECTION OF SPHERE
VARIABLE: LOSS-VISC

ZRAT [Z2/Z1] = .833333
AKIA = 20.9442
A = 5.
RH01 = 1.2
RH02 = 1.
C1 = 1.5
C2 = 1.5
F = 1.00001
P = 1.
NPT = 331
NL = 4

FMIN = .000026
FMAX = .013744

ETAL = .001025
ETAR = 0.

INCIDENT WAVE



(c) See Figure 45.

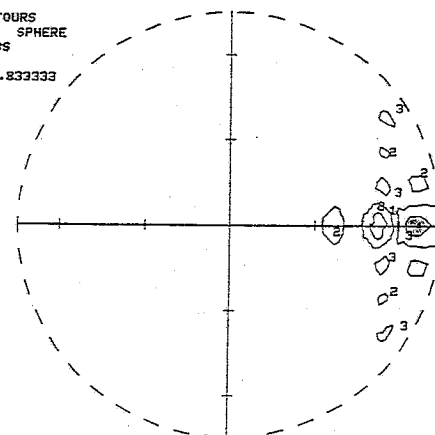
ISOMAGNITUDE CONTOURS
CROSS-SECTION OF SPHERE
VARIABLE: LOSS-ABS

ZRAT [Z2/Z1] = .833333
AKIA = 20.9442
A = 5.
RH01 = 1.2
RH02 = 1.
C1 = 1.5
C2 = 1.5
F = 1.00001
P = 1.
NPT = 293
NL = 4

FMIN = .000316
FMAX = .006289

ALF1 = .005
ALF2 = 0.

INCIDENT WAVE

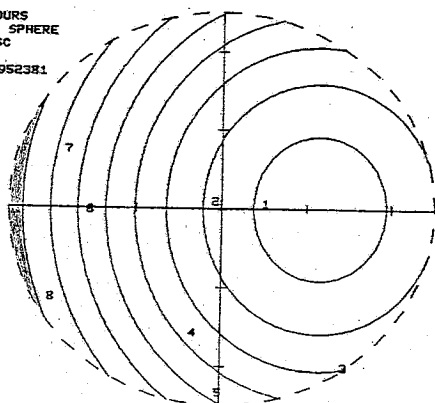


(d) See Figure 46.

ISOMAGNITUDE CONTOURS
CROSS-SECTION OF SPHERE
VARIABLE: LOSS-VISC

ZRAT [Z2/Z1] = .952381
AKIA = .997341
A = .25
RH01 = 1.
RH02 = 1.
C1 = 1.575
C2 = 1.5
F = 1.00001
P = 1.
NPT = 1220
NL = 8
FMIN = .002921
FMAX = .003207
ETAL = .000989
ETAR = 0.

INCIDENT WAVE



(e) See Figure 47.

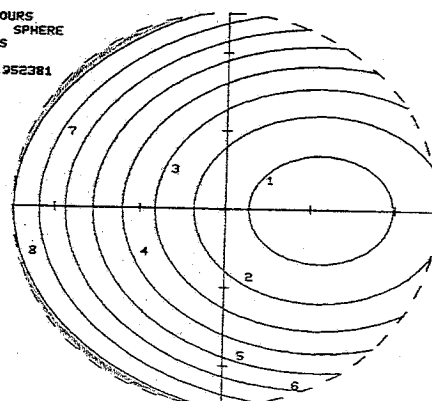
ISOMAGNITUDE CONTOURS
CROSS-SECTION OF SPHERE
VARIABLE: LOSS-ABS

ZRAT [Z2/Z1] = .952381
AKIA = .997341
A = .25
RH01 = 1.
RH02 = 1.
C1 = 1.575
C2 = 1.5
F = 1.00001
P = 1.
NPT = 1411
NL = 8

FMIN = .003141
FMAX = .003271

ALF1 = .005
ALF2 = 0.

INCIDENT WAVE



(f) See Figure 48.

Figure 10. Viscous and absorptive power loss in sphere, shown for three cases.

units of the contour values are MW/mm^3 . Three important criteria upon which the estimates can be compared are the magnitudes, sizes, and locations of "hot spots." These areas of relatively high heating are identified on the "hotter" side of contours with high level numbers (i.e., those near and including N_L). The degree of heating in these hot spots is dependent on F_{max} . Thus very hot spots are found inside contours with the highest level numbers (N_L), on (isomagnitude) plots of E_v or E_α with relatively high values for F_{max} . However, it must be borne in mind that contour values can be similar even if level numbers are different and values for N_L are the same, if values for F_{max} and/or F_{min} differ between two plots. Thus level numbers alone should not be used in comparing the magnitudes of hot spots.

On the basis of the previous criteria, this author considers the first pair of plots (on each figure) to be a fair "match," the second pair a poor match, and the third pair a good match. Thus the estimates seem to agree best for smaller objects (or lower $k_1 a$) and lower mismatches; these generalizations hold for both cylindrical and spherical objects. In almost all instances, F_{max} is higher and F_{min} is lower for the viscosity estimate E_v than the corresponding values for the generalized absorption estimate E_α . Moreover, a greater degree of spatial nonuniformity occurs in plots of E_v .

It is thought that the narrower F_{max} range of E_α and its lesser spatial diversity result from (undesirable) phase cancellation in the product $p|\bar{u}|$ used in the estimate. This error occurs from the application of the absorption estimate to situations in which standing waves

are present; the absorption equations (77) and (82) are strictly accurate only with travelling waves. The presence of standing waves is readily verifiable in the first and second cylindrical cases, as indicated by the curved, equally spaced "bands" in the plots of E_{v1} (recall from Equation 76 that E_{v1} is proportional to $|p'_v|^2$, so that a banded pattern of $|p'_v|$ is suggested).

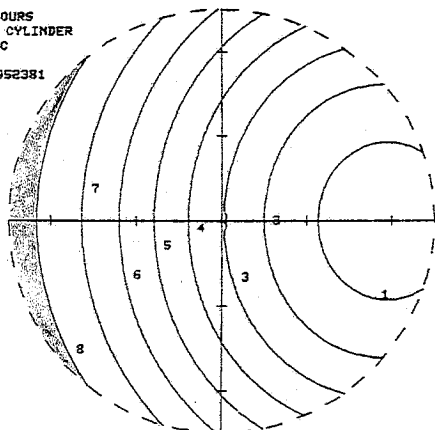
The effects of object size and impedance mismatch on viscous power loss E_{v1} are explored in the next eight figures. The first two, Figures 11 and 12, show isomagnitude plots of E_v for six radius values (for the cylinder and sphere, respectively), illustrating the significance of this parameter and, more generally, of the quantity $k_1 a$. There is a moderate velocity mismatch, with c_1 5% higher than c_2 , whereas ρ_1 and ρ_2 are equal and are set to the standard values. It is readily seen that F_{max} increases (and F_{min} decreases) with increasing a (or $k_1 a$), for both the cylinder and the sphere, indicating increasing nonuniformity with larger objects, especially with the sphere. The values given for maximum E_v can be compared with a uniform $E_v \cong 0.0034 \text{ MW/mm}^3$ which results with no impedance mismatch, for objects of all sizes. Observe that F_{max} is near this value for smaller objects of both shapes, but increases to about 130% of the value for cylinders of radius 10 mm (for which $k_1 a \cong 40 \text{ rad}$) and to about 220% for spheres of the same radius.

As regards the locations of hot spots, most heating occurs at the "upstream" (left) boundary of both cylinders and spheres of small radii. For larger radii, both objects exhibit more spatial diversity,

ISO-MAGNITUDE CONTOURS
CROSS-SECTION OF CYLINDER
VARIABLE: LOSS-VISC

ZRAT [Z2/Z1] = .952381
AK1A = .997331
A = .25
RH01 = 1.
RH02 = 1.
C1 = 1.575
C2 = 1.5
F = 1.
P = 1.
NPT = 1113
NL = 8
FMIN = .002897
FMAX = .003347
ETA1 = .000989
ETA2 = 0.

INCIDENT WAVE
→

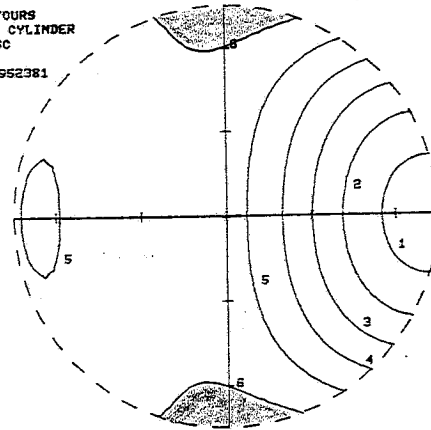


(a) See Figure 41.

ISO-MAGNITUDE CONTOURS
CROSS-SECTION OF CYLINDER
VARIABLE: LOSS-VISC

ZRAT [Z2/Z1] = .952381
AK1A = 1.99466
A = .5
RH01 = 1.
RH02 = 1.
C1 = 1.575
C2 = 1.5
F = 1.
P = 1.
NPT = 704
NL = 6
FMIN = .002582
FMAX = .003429
ETA1 = .000989
ETA2 = 0.

INCIDENT WAVE
→

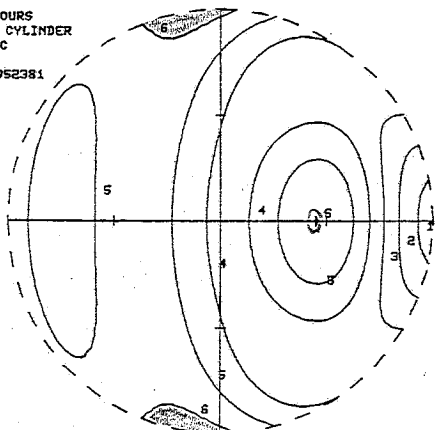


(b) See Figure 49.

ISO-MAGNITUDE CONTOURS
CROSS-SECTION OF CYLINDER
VARIABLE: LOSS-VISC

ZRAT [Z2/Z1] = .952381
AK1A = 3.98932
A = 2.5
RH01 = 1.
RH02 = 1.
C1 = 1.575
C2 = 1.5
F = 1.
P = 1.
NPT = 1049
NL = 5
FMIN = .002422
FMAX = .003529
ETA1 = .000989
ETA2 = 0.

INCIDENT WAVE
→

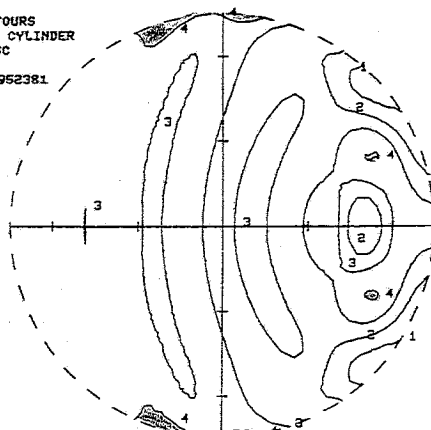


(c) See Figure 50.

ISO-MAGNITUDE CONTOURS
CROSS-SECTION OF CYLINDER
VARIABLE: LOSS-VISC

ZRAT [Z2/Z1] = .952381
AK1A = 9.97331
A = 2.5
RH01 = 1.
RH02 = 1.
C1 = 1.575
C2 = 1.5
F = 1.
P = 1.
NPT = 1262
NL = 4
FMIN = .00225
FMAX = .003718
ETA1 = .000989
ETA2 = 0.

INCIDENT WAVE
→

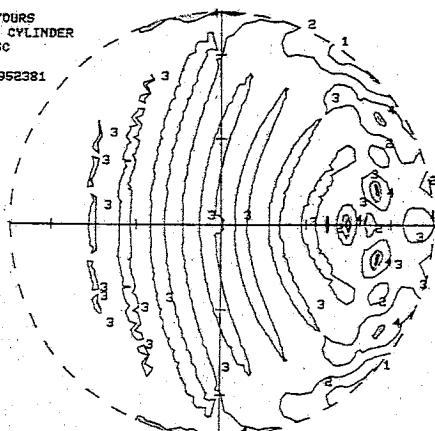


(d) See Figure 51.

ISO-MAGNITUDE CONTOURS
CROSS-SECTION OF CYLINDER
VARIABLE: LOSS-VISC

ZRAT [Z2/Z1] = .952381
AK1A = 19.9466
A = 10.
RH01 = 1.
RH02 = 1.
C1 = 1.575
C2 = 1.5
F = 1.
P = 1.
NPT = 2245
NL = 3
FMIN = .001254
FMAX = .004015
ETA1 = .000989
ETA2 = 0.

INCIDENT WAVE
→

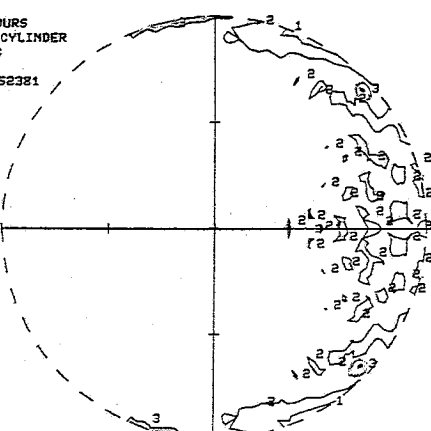


(e) See Figure 37.

ISO-MAGNITUDE CONTOURS
CROSS-SECTION OF CYLINDER
VARIABLE: LOSS-VISC

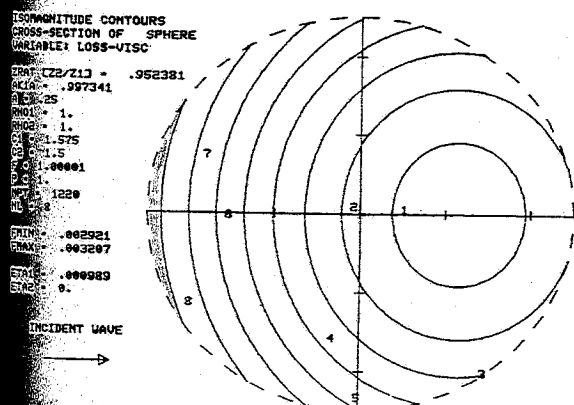
ZRAT [Z2/Z1] = .952381
AK1A = 39.8932
A = 10.
RH01 = 1.
RH02 = 1.
C1 = 1.575
C2 = 1.5
F = 1.
P = 1.
NPT = 730
NL = 3
FMIN = .001421
FMAX = .004375
ETA1 = .000989
ETA2 = 0.

INCIDENT WAVE
→

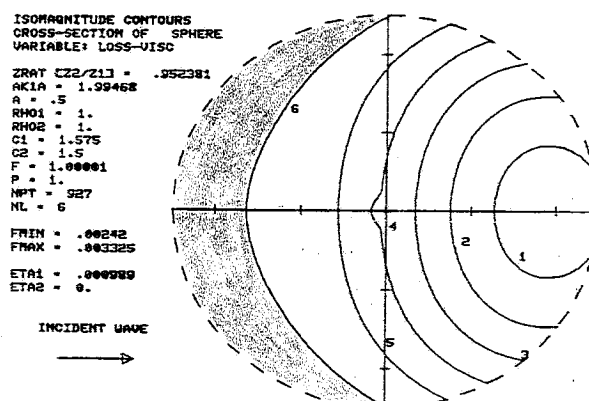


(f) See Figure 52.

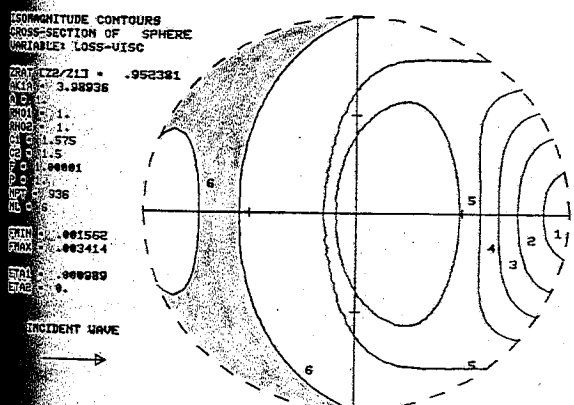
Figure 11. Illustration of dependence of viscous power loss (E_v) in cylinder on $k_1 a$ (i.e., relation between object size and acoustic wavelength). Six radius values are considered, for which $k_1 a$ ranges from about 1 to 40 rad. A 5% velocity mismatch ($c_1 > c_2$) is used in all cases.



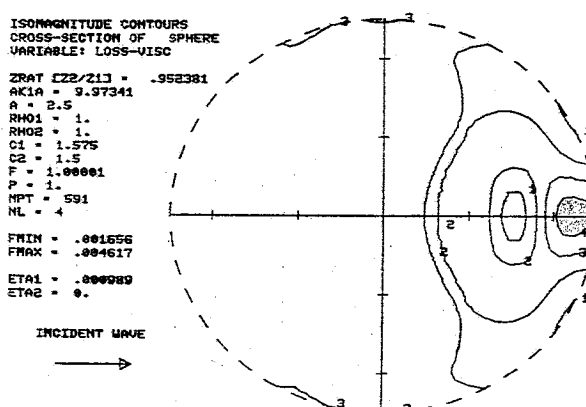
(a) See Figure 47.



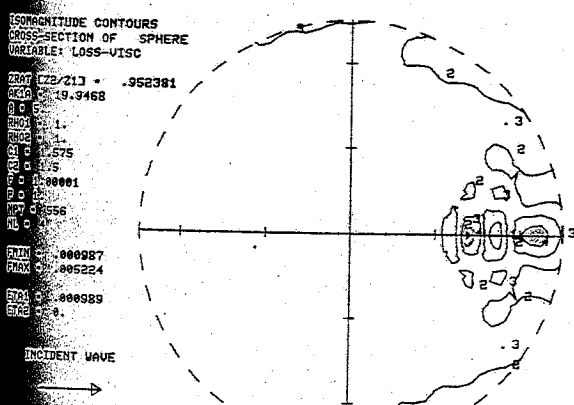
(b) See Figure 53.



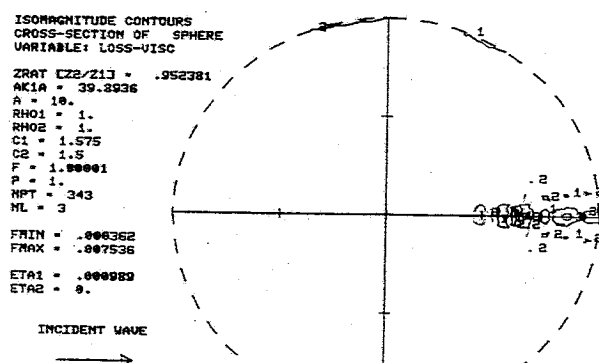
(c) See Figure 54.



(d) See Figure 55.



(e) See Figure 43.



(f) See Figure 56.

Figure 12. Dependence of E_v in sphere on $k_1 a$, again shown for $k_1 a$ ranging from approximately 1 to 40 rad, and a 5% velocity mismatch ($c_1 > c_2$).

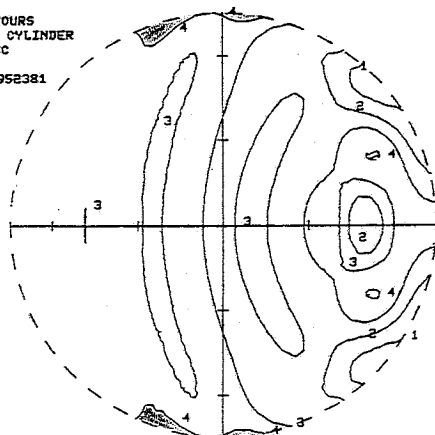
including "focused-looking" hot spots inside the "downstream" (right) halves. In addition, hot spots are seen at the "side" (top and bottom) boundaries of larger cylinders. Finally, note that for the largest objects ($\alpha = 10$ mm), the plot resolution is rather poor, owing both to an insufficient polar-grid point density and also to the necessity of using only three contour levels, in order to maintain $N_{point} \leq 5000$, as previously mentioned.

The importance of the acoustic-velocity mismatch is examined in Figures 13 and 14, in which isomagnitude plots of E_v are shown for four values of c_1 . The first two cases (describing the relatively "rigid-object" situation, for which $c_1 > c_2$) entail c_1 being a moderate 5% and a much more extreme 20% higher than c_2 . Similarly, the second pair of plots ($c_1 < c_2$) uses the values c_1 5% and 20% lower than c_2 . All other parameters besides c_1 are set to standard values (which means equal densities ($\rho_1 = \rho_2$)). First, it should be noted that changes in c_1 are manifested primarily with regard to the impedance mismatch, upon which attention is presently centered, and secondarily as changes in the quantity $k_1\alpha$, the importance of which was studied in the previous figure set. Thus a 5% increase in c_1 (above c_2 , set to the standard value) results in a 4.8% decrease in the impedance ratio Z_p , as calculated using Equation 23, and in the quantity $k_1\alpha$, according to Equation 19a. In work related to this thesis, it has been found that increases in the impedance mismatch, as reflected by Z_p being further (either larger or smaller) from the no-mismatch value $Z_p = 1$, generally result in increases in F_{max} and

ISO-MAGNITUDE CONTOURS
CROSS-SECTION OF CYLINDER
VARIABLE: LOSS-VISC

ZRAT $[Z_2/Z_1] = .952381$
AKIA = 9.97331
A = 2.5
RH01 = 1.
RH02 = 1.
C1 = 1.575
C2 = 1.5
P = 1.
NPT = 1262
NL = 4
FMIN = .00225
FMAX = .003713
ETA1 = .000989
ETA2 = 0.

INCIDENT WAVE

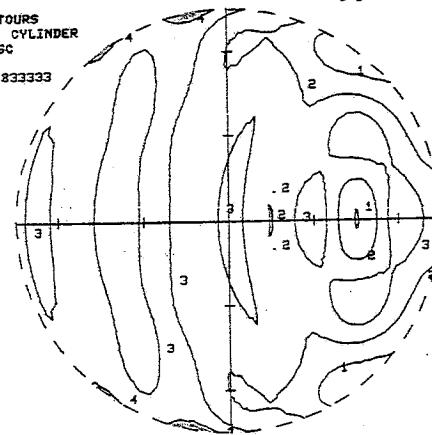


(a) See Figure 51.

ISO-MAGNITUDE CONTOURS
CROSS-SECTION OF CYLINDER
VARIABLE: LOSS-VISC

ZRAT $[Z_2/Z_1] = .833333$
AKIA = 8.72665
A = 2.5
RH01 = 1.
RH02 = 1.
C1 = 1.8
C2 = 1.5
P = 1.
NPT = 1439
NL = 4
FMIN = .00067
FMAX = .004529
ETA1 = .001477
ETA2 = 0.

INCIDENT WAVE

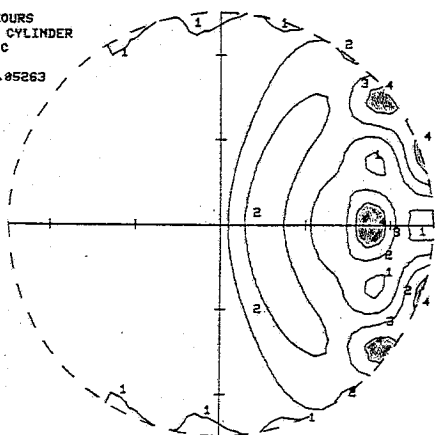


(b) See Figure 57.

ISO-MAGNITUDE CONTOURS
CROSS-SECTION OF CYLINDER
VARIABLE: LOSS-VISC

ZRAT $[Z_2/Z_1] = 1.05263$
AKIA = 11.0231
A = 2.5
RH01 = 1.
RH02 = 1.
C1 = 1.425
C2 = 1.5
P = 1.
NPT = 931
NL = 4
FMIN = .002837
FMAX = .004959
ETA1 = .000732
ETA2 = 0.

INCIDENT WAVE

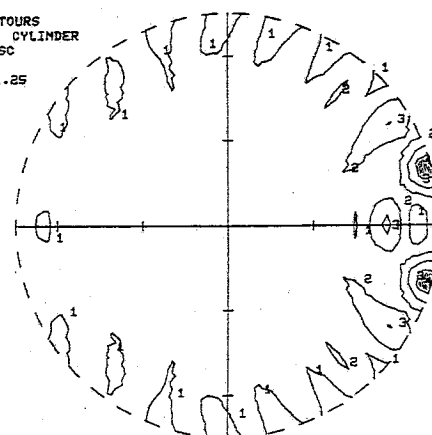


(c) See Figure 58.

ISO-MAGNITUDE CONTOURS
CROSS-SECTION OF CYLINDER
VARIABLE: LOSS-VISC

ZRAT $[Z_2/Z_1] = 1.25$
AKIA = 13.09
A = 2.5
RH01 = 1.
RH02 = 1.
C1 = 1.2
C2 = 1.5
P = 1.
NPT = 802
NL = 4
FMIN = .000109
FMAX = .018337
ETA1 = .000437
ETA2 = 0.

INCIDENT WAVE



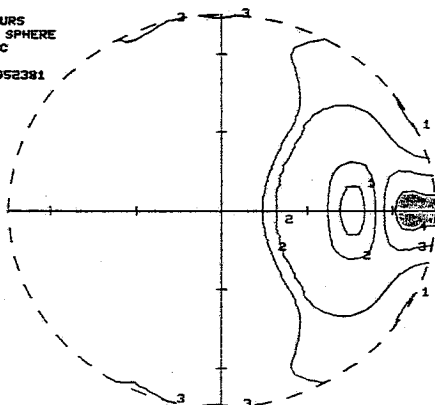
(d) See Figure 59.

Figure 13. Dependence of viscous power loss (E_v) in cylinder on the velocity mismatch, shown for c_1 5% and 20% higher and lower than c_2 (and $k_1 a \cong 10$ rad).

ISOMAGNITUDE CONTOURS
CROSS-SECTION OF SPHERE
VARIABLE: LOSS-VISC

ZRAT $[Z_2/Z_1] = .952381$
AK1A = 9.97341
A = 2.5
RH01 = 1.
RH02 = 1.
C1 = 1.575
C2 = 1.5
F = 1.00001
P = 1.
NPT = 591
NL = 4
FMIN = .001656
FMAX = .004617
ETA1 = .000989
ETA2 = 0.

INCIDENT WAVE
→



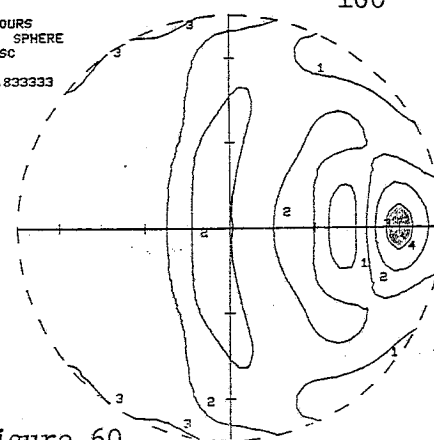
(a) See Figure 55.

ISOMAGNITUDE CONTOURS
CROSS-SECTION OF SPHERE
VARIABLE: LOSS-VISC

ZRAT $[Z_2/Z_1] = .833333$
AK1A = 8.72673
A = 2.5
RH01 = 1.
RH02 = 1.
C1 = 1.3
C2 = 1.5
F = 1.00001
P = 1.
NPT = 1044
NL = 4

FMIN = .000317
FMAX = .005638
ETA1 = .001477
ETA2 = 0.

INCIDENT WAVE
→

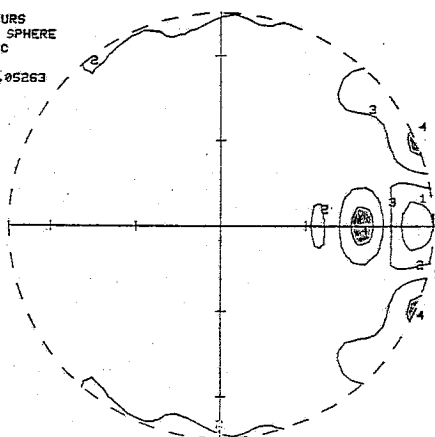


(b) See Figure 60.

ISOMAGNITUDE CONTOURS
CROSS-SECTION OF SPHERE
VARIABLE: LOSS-VISC

ZRAT $[Z_2/Z_1] = 1.05263$
AK1A = 11.0232
A = 2.5
RH01 = 1.
RH02 = 1.
C1 = 1.425
C2 = 1.5
F = 1.00001
P = 1.
NPT = 415
NL = 4
FMIN = .000998
FMAX = .00688
ETA1 = .000732
ETA2 = 0.

INCIDENT WAVE
→



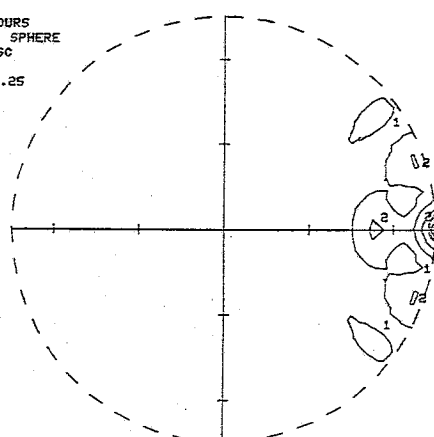
(c) See Figure 61.

ISOMAGNITUDE CONTOURS
CROSS-SECTION OF SPHERE
VARIABLE: LOSS-VISC

ZRAT $[Z_2/Z_1] = 1.25$
AK1A = 13.0901
A = 2.5
RH01 = 1.
RH02 = 1.
C1 = 1.2
C2 = 1.5
F = 1.00001
P = 1.
NPT = 317
NL = 4

FMIN = .000054
FMAX = .102932
ETA1 = .000437
ETA2 = 0.

INCIDENT WAVE
→



(d) See Figure 62.

Figure 14. Dependence of E_v in sphere on the velocity mismatch, shown for values of $c_1 \pm 5\%$ and $\pm 20\%$ with respect to c_2 (and $k_1 a \cong 10$ rad).

in spatial "peakedness" and complexity. As regards $k_1 a$, the previous figures (11 and 12) demonstrate that increases in $k_1 a$ generally elicit increases in F_{max} , with larger increases for the sphere. Now, both of the previous factors affect E_{v1} indirectly by means of the pressure p'_w . However, Equation 80 shows that E_{v1} is not only proportional to $|p'_w|^2$, but also inversely proportional to the characteristic acoustic impedance $Z_1 \equiv \rho_1 c_1$ (where the quantity $\eta_1 k_1^2 / 2Z_1$, or α_1 by Equation 81a, is held constant). Thus a 5% increase in c_1 uniformly decreases E_{v1} by 4.8%, affecting F_{max} but not the spatial distribution. In summary, a change in c_1 affects E_{v1} indirectly, by means of Z_r and $k_1 a$, and directly, by "inverse proportionality."

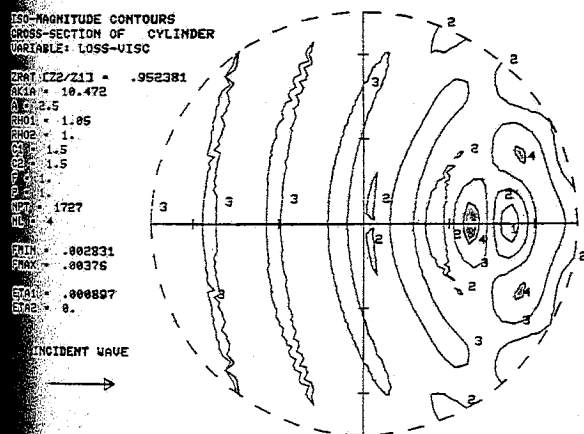
It is now appropriate to demonstrate the above statements by application to Figures 13 and 14. First, effects on F_{max} are considered. In the situation $c_1 > c_2$ and for both object shapes, the expected increase in F_{max} , when c_1 is raised from 1.575 to 1.8 mm/ μ s, is blunted by the effects of the decrease in $k_1 a$ and the uniform inverse-proportional decrease in E_{v1} . Thus F_{max} increases only 22% with the cylinder and 23% with the sphere. On the other hand, when c_1 is lowered in the situation $c_1 < c_2$ from 1.425 to 1.2 mm/ μ s, all three factors act to increase F_{max} , resulting in a 270% increase with the cylinder and a phenomenal 14-fold increase with the sphere. (Another factor supporting the greater increases in F_{max} , in the latter situation of $c_1 < c_2$, is the larger fractional change in Z_r when c_1 is decreased a given percentage, rather than increased.) It is also seen that the degree of spatial nonuniformity tends to parallel the

magnitude of F_{max} .

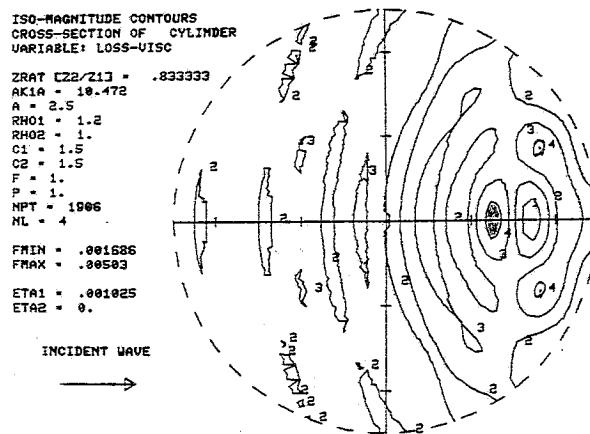
In addition, some generalizations are possible concerning the locations of hot spots. In the former situation ($c_1 > c_2$), "focused" hot spots are mainly found within the downstream halves of both the cylinder and the sphere, and/or at the side boundaries of the cylinder. As for the situation $c_1 < c_2$, the hottest spots are primarily located at the downstream boundaries of both objects.

Another obvious and instructive arrangement of parameters is an impedance mismatch owing to density, instead of acoustic velocity. Thus, in Figures 15 and 16, four different (nonstandard) values are used for the interior density ρ_1 , with all other parameters set to standard values. Similar to the choices for c_1 in the previous figures (13 and 14), the situation $\rho_1 > \rho_2$ is studied using ρ_1 5% and 20% higher than ρ_2 (standard), while the values ρ_1 5% and 20% lower than ρ_2 provide information about the complementary situation ($\rho_1 < \rho_2$). The important difference in this case, as compared with previous changes in c_1 , is that the quantity $k_1 \alpha$ is unaffected by changes in ρ_1 , while the impedance ratio Z_r is affected by ρ_1 exactly as it is by c_1 . In addition, E_{v1} is inversely proportional to ρ_1 , just as to c_1 . Therefore, this case merely excludes the effects of changes in $k_1 \alpha$, which have been manifested in the previous two figure sets.

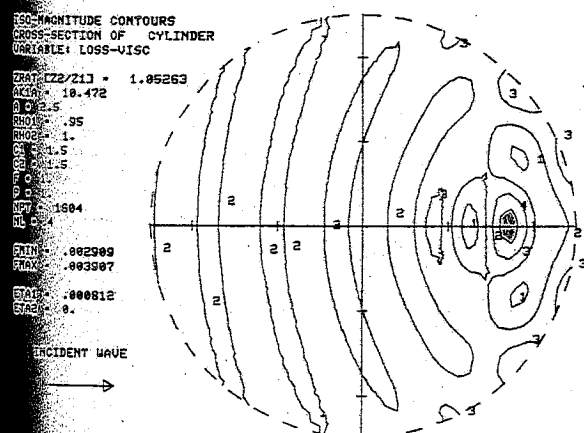
Again, effects on F_{max} of changes in ρ_1 are first examined. When ρ_1 is increased from 1.05 to 1.2 mg/mm³ for the situation $\rho_1 > \rho_2$, the increased impedance mismatch tends to increase F_{max} . However, this



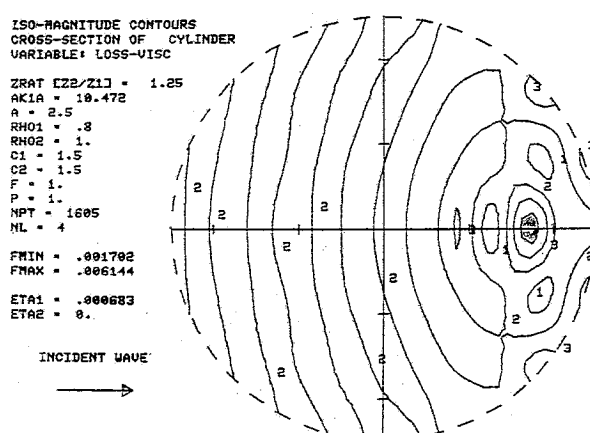
(a) See Figure 63.



(b) See Figure 64.

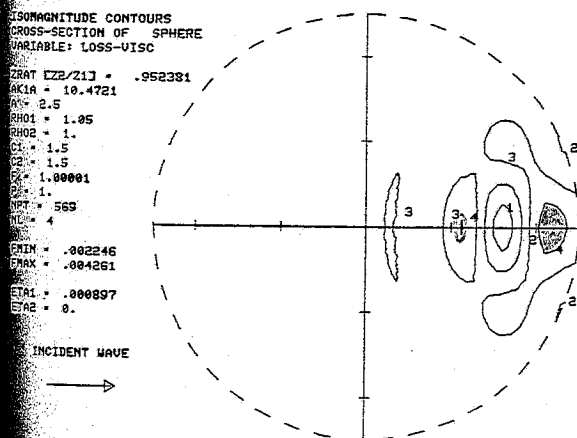


(c) See Figure 65.

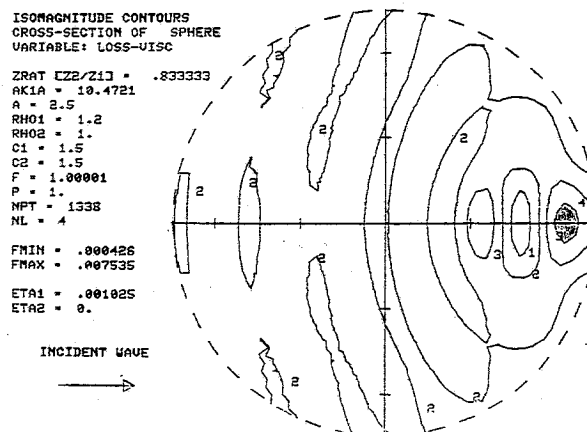


(d) See Figure 66.

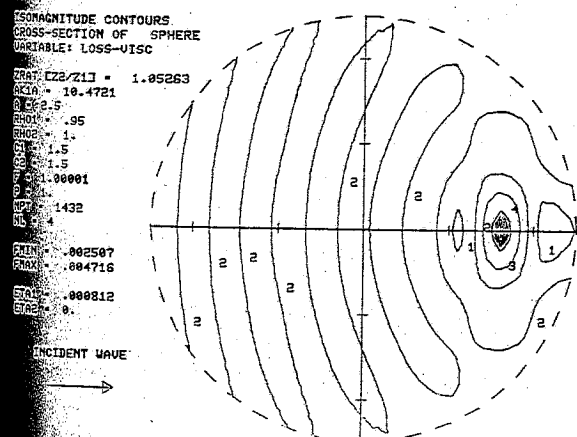
Figure 15. Dependence of viscous power loss (E_v) in cylinder on the density mismatch, shown for ρ_1 5% and 20% greater and less than ρ_2 (and $k_1 a \cong 10$ rad).



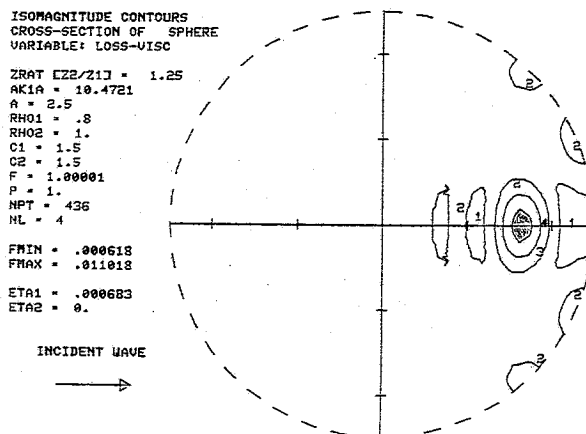
(a) See Figure 67.



(b) See Figure 68.



(c) See Figure 69.



(d) See Figure 70.

Figure 16. Dependence of E_v in sphere on the density mismatch, shown for $\rho_1 \pm 5\%$ and $\pm 20\%$ with respect to ρ_2 (and $k_1 a \cong 10$ rad).

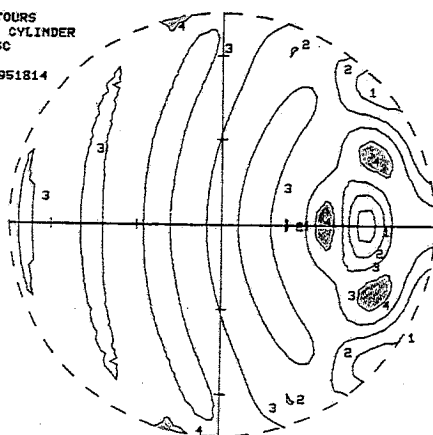
increase is now countered only by the uniform inverse-proportional decrease in E_{v1} , and not also by a decrease in $k_1 a$, as was the case when using c_1 . Therefore, it is not surprising that F_{max} increases by 34% with the cylinder and 77% with the sphere, as compared with 22% and 23% in the previous case using c_1 . Conversely, in the situation $\rho_1 < \rho_2$, the decrease in ρ_1 from 0.95 to 0.8 mg/mm³ also tends to increase F_{max} , but now this increase is reinforced only by the uniform inverse-proportional increase in E_{v1} , and not also by an increase in $k_1 a$, as was previously the case. These factors help to explain why the increases in F_{max} in this situation are 57% and 230% for the cylinder and the sphere, respectively, versus 270% and 1400% increases in Figures 13 and 14. Lastly, in all these cases for which the impedance mismatch owes to density, "focused" hot spots are consistently found within the downstream halves of objects of both shapes.

The last set of viscous-power-loss plots, Figures 17 and 18, are perhaps a more realistic combination of the situations studied in Figures 13 through 16. Impedance mismatches of approximately $\pm 5\%$ and $\pm 20\%$ are again considered, but are now realized through contributions from both ρ_1 and c_1 . Thus for both object shapes, the relatively "rigid-object" situation ($Z_1 > Z_2$) is examined for the case in which c_1 and ρ_1 are each 2.5% higher than c_2 and ρ_2 , respectively, so that Z_1 is 5.1% above Z_2 (standard), and also for the case of c_1 and ρ_1 each being 10% higher than the standard values, so that Z_1 is 21% above Z_2 . Conversely, the relatively "soft-object" situation ($Z_1 < Z_2$) is studied for the complementary cases in which c_1 , ρ_1 , and Z_1 are

ISO-MAGNITUDE CONTOURS
CROSS-SECTION OF CYLINDER
VARIABLE: LOSS-VISC

ZRAT E_2/Z_1 = .951814
AK1A = 10.2156
A = 2.5
RH01 = 1.025
RH02 = 1.
C1 = 1.5375
C2 = 1.5
F = 1.
P = 1.
NPT = 1579
NL = 4
FMIN = .002815
FMAX = .003627
ETA1 = .000943
ETA2 = 0.

INCIDENT WAVE

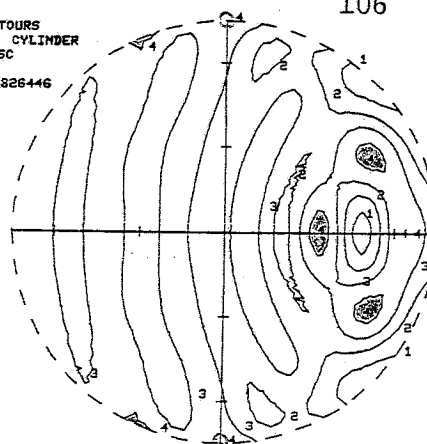


(a) See Figure 71.

ISO-MAGNITUDE CONTOURS
CROSS-SECTION OF CYLINDER
VARIABLE: LOSS-VISC

ZRAT E_2/Z_1 = .828446
AK1A = 9.51908
A = 2.5
RH01 = 1.1
RH02 = 1.
C1 = 1.65
C2 = 1.5
F = 1.
P = 1.
NPT = 1679
NL = 4
FMIN = .00117
FMAX = .004311
ETA1 = .001251
ETA2 = 0.

INCIDENT WAVE

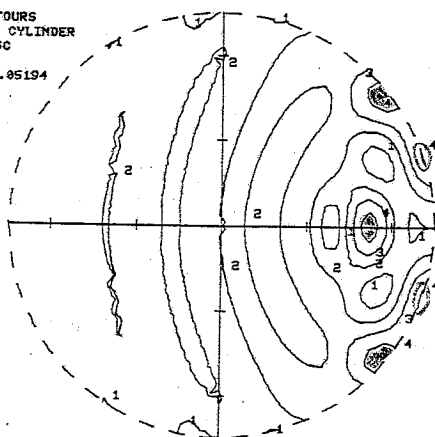


(b) See Figure 72.

ISO-MAGNITUDE CONTOURS
CROSS-SECTION OF CYLINDER
VARIABLE: LOSS-VISC

ZRAT E_2/Z_1 = 1.05194
AK1A = 10.7405
A = 2.5
RH01 = .975
RH02 = 1.
C1 = 1.4625
C2 = 1.5
F = 1.
P = 1.
NPT = 1401
NL = 4
FMIN = .002998
FMAX = .00426
ETA1 = .000772
ETA2 = 0.

INCIDENT WAVE

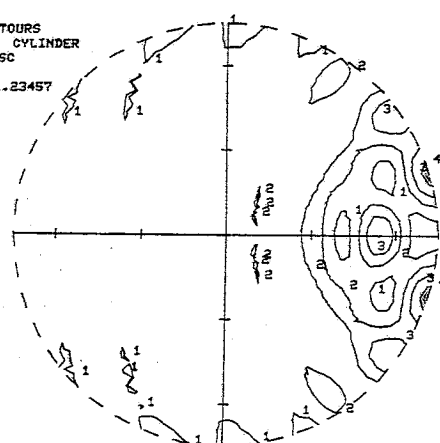


(c) See Figure 73.

ISO-MAGNITUDE CONTOURS
CROSS-SECTION OF CYLINDER
VARIABLE: LOSS-VISC

ZRAT E_2/Z_1 = 1.23457
AK1A = 11.6355
A = 2.5
RH01 = .9
RH02 = 1.
C1 = 1.35
C2 = 1.5
F = 1.
P = 1.
NPT = 918
NL = 4
FMIN = .001768
FMAX = .004494
ETA1 = .00056
ETA2 = 0.

INCIDENT WAVE



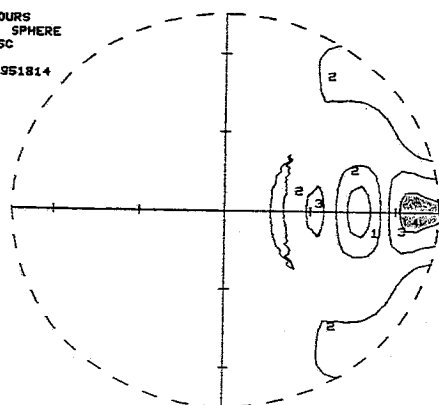
(d) See Figure 74.

Figure 17. Dependence of viscous power loss (E_v) in cylinder on a "blended" impedance mismatch, owing to equal contributions from velocity and density. Four cases are considered, for which Z_1 is about 5% and 20% above and below Z_2 (and $k_1 a \cong 10$ rad).

ISOMAGNITUDE CONTOURS
CROSS-SECTION OF SPHERE
VARIABLE: LOSS-VISC

ZRAT [Z2/Z1] = .951814
AKIA = 10.2167
A = 2.5
RH01 = 1.025
RH02 = 1.
C1 = 1.5375
C2 = 1.5
F = 1.00001
P = 1.
NPT = 491
NL = 4
FMIN = .001939
FMAX = .004561
ETA1 = .000943
ETA2 = 0.

INCIDENT WAVE

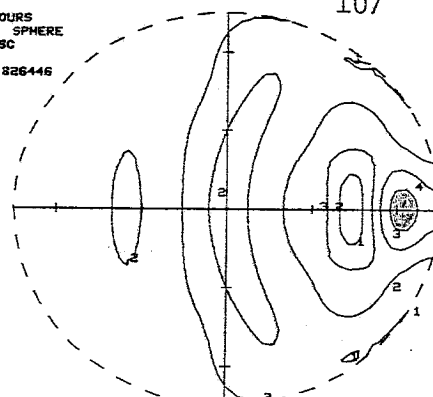


(a) See Figure 75.

ISOMAGNITUDE CONTOURS
CROSS-SECTION OF SPHERE
VARIABLE: LOSS-VISC

ZRAT [Z2/Z1] = .826446
AKIA = 9.52007
A = 2.5
RH01 = 1.1
RH02 = 1.
C1 = 1.65
C2 = 1.5
F = 1.00001
P = 1.
NPT = 1037
NL = 4
FMIN = .000266
FMAX = .00686
ETA1 = .001251
ETA2 = 0.

INCIDENT WAVE

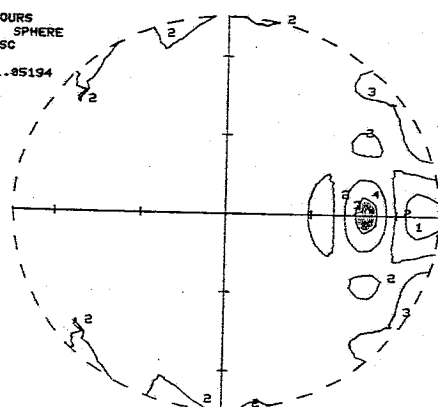


(b) See Figure 76.

ISOMAGNITUDE CONTOURS
CROSS-SECTION OF SPHERE
VARIABLE: LOSS-VISC

ZRAT [Z2/Z1] = 1.05194
AKIA = 10.7406
A = 2.5
RH01 = .975
RH02 = 1.
C1 = 1.4625
C2 = 1.5
F = 1.00001
P = 1.
NPT = 508
NL = 4
FMIN = .001253
FMAX = .005622
ETA1 = .000772
ETA2 = 0.

INCIDENT WAVE

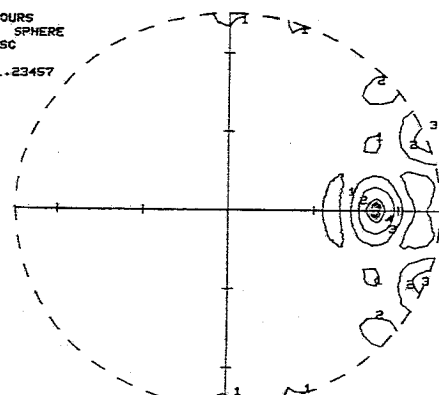


(c) See Figure 77.

ISOMAGNITUDE CONTOURS
CROSS-SECTION OF SPHERE
VARIABLE: LOSS-VISC

ZRAT [Z2/Z1] = 1.23457
AKIA = 11.6356
A = 2.5
RH01 = .9
RH02 = 1.
C1 = 1.35
C2 = 1.5
F = 1.00001
P = 1.
NPT = 468
NL = 4
FMIN = .00001
FMAX = .021648
ETA1 = .00056
ETA2 = 0.

INCIDENT WAVE



(d) See Figure 78.

Figure 18. Dependence of E_v in sphere on a combined impedance mismatch owing equally to velocity and density, shown for $Z_1 \pm 5\%$ and $\pm 20\%$ with respect to Z_2 (and $k_1 a \cong 10$ rad).

lower than c_2 , ρ_2 , and Z_2 by the same respective percentages. All parameters besides c_1 and ρ_1 possess standard values.

Thus, each of these plots can be grouped with two corresponding plots from the previous four figures, all of which have similar impedance mismatches and the same object shapes (e.g., Figures 13a, 15a, and 17a comprise a (cylinder) group for which Z_1 is 5% higher than the standard value). For all three plots, similar values of Z_1 produce similar impedance-mismatch effects owing to similar values of Z_r and also cause similar "inverse-proportional" results. The difference lies solely with the quantity $k_1 a$, which is affected only by c_1 and not by ρ_1 . Since all plots in a group of similar values of Z_1 have different values for c_1 , the values for $k_1 a$ also are all different. It is readily verified that for most of these groups, if the plots are ranked in order of increasing $k_1 a$ (or decreasing c_1), then the corresponding values of F_{max} will also be ranked in increasing order. This finding is consistent with that of Figures 11 and 12; the analyses differ in that the former is based on smaller increments in $k_1 a$. Also note that values of F_{max} again tend to be higher in the spherical cases (Figure 18) than in the corresponding cylindrical cases (Figure 17).

As concerns that distribution of heating in these "combination" figures, all plots (of both object shapes) exhibit hot spots within the downstream halves. In addition, hot spots are found in the cylinder at the side boundaries for the situation $Z_1 < Z_2$, and at the downstream boundary for $Z_1 > Z_2$.

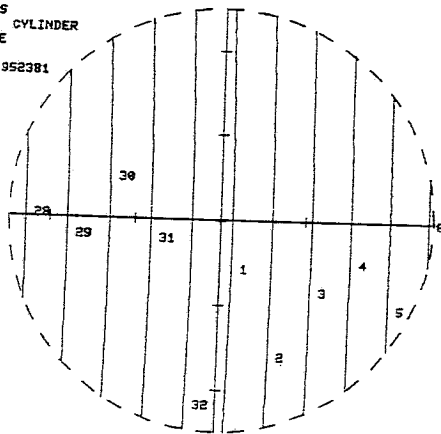
For the remainder of this section, attention is turned to pressure isophase contours. Although heating is the main topic of this thesis, the programs used to obtain this information can also be used to permit some generalizations (see Section 4) about experimental alternatives for pressure measurement, for which purpose $\angle p'$ is examined. The next six figures, 19 through 24, involve exactly the same cases as the previous figures, 11 through 16 (the cases of Figures 17 and 18 are excluded, however). But now, isophase contours for $\angle p'$ are presented, instead of isomagnitude contours for E_v . These plots are evaluated with regard to two properties mentioned earlier with regard to $\angle p'_w$ in Figures 7 and 8: "bowing" and "random" phase distortion, or "wavy" isophase contours--simply termed "distortion" hereafter.

In the first set of curves, Figures 19 and 20, for the cylinder and sphere, respectively, the radius a again takes on six different values, so that the quantity $k_1 a$ varies from about 1 to 40 rad. The velocity c_1 is set 5% higher than c_2 . The reader is again advised to ignore plot anomalies at the centers of the objects. As regards bowing, the significant features of these plots are a steady increase in bowing with increasing $k_1 a$, as shown by the isophase contours curving relatively more (especially near the center) per given distance, and a strong similarity between the cylinder and the sphere as to the extent of bowing for a given $k_1 a$. Distortion is found primarily within the downstream halves of both objects, where the pressure magnitude tends to be least uniform; is somewhat more extensive for the sphere; and generally becomes more severe as $k_1 a$ increases.

ISO-PHASE CONTOURS
CROSS-SECTION OF CYLINDER
VARIABLE: PRESSURE

ZRAT [Z2/Z1] = .952381
AKIA = .997331
A = .25
RH01 = 1.
RH02 = 1.
C1 = 1.575
C2 = 1.5
F = 1.
P = 1.
NPT = 1177
NL = 32

INCIDENT WAVE
→

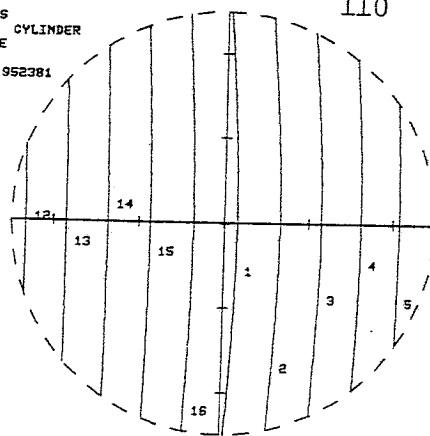


(a) See Figure 79.

ISO-PHASE CONTOURS
CROSS-SECTION OF CYLINDER
VARIABLE: PRESSURE

ZRAT [Z2/Z1] = .952381
AKIA = 1.99466
A = .5
RH01 = 1.
RH02 = 1.
C1 = 1.575
C2 = 1.5
F = 1.
P = 1.
NPT = 1127
NL = 16

INCIDENT WAVE
→

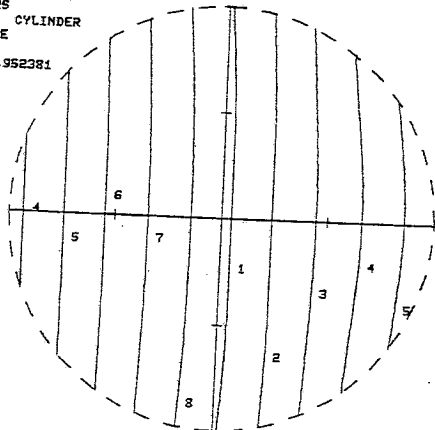


(b) See Figure 80.

ISO-PHASE CONTOURS
CROSS-SECTION OF CYLINDER
VARIABLE: PRESSURE

ZRAT [Z2/Z1] = .952381
AKIA = 3.98932
A = 1.
RH01 = 1.
RH02 = 1.
C1 = 1.575
C2 = 1.5
F = 1.
P = 1.
NPT = 1121
NL = 8

INCIDENT WAVE
→

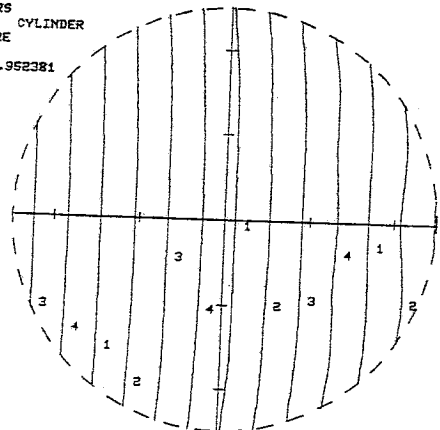


(c) See Figure 81.

ISO-PHASE CONTOURS
CROSS-SECTION OF CYLINDER
VARIABLE: PRESSURE

ZRAT [Z2/Z1] = .952381
AKIA = 9.97331
A = 2.5
RH01 = 1.
RH02 = 1.
C1 = 1.575
C2 = 1.5
F = 1.
P = 1.
NPT = 1381
NL = 4

INCIDENT WAVE
→

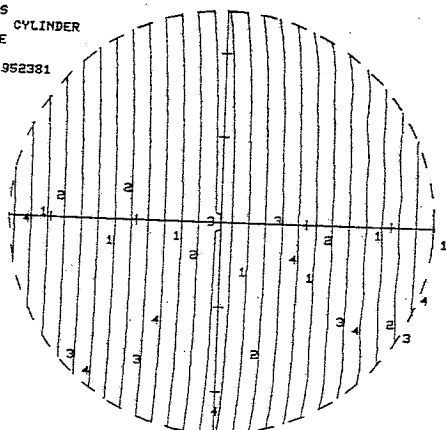


(d) See Figure 26.

ISO-PHASE CONTOURS
CROSS-SECTION OF CYLINDER
VARIABLE: PRESSURE

ZRAT [Z2/Z1] = .952381
AKIA = 19.9466
A = 5.
RH01 = 1.
RH02 = 1.
C1 = 1.575
C2 = 1.5
F = 1.
P = 1.
NPT = 2706
NL = 4

INCIDENT WAVE
→

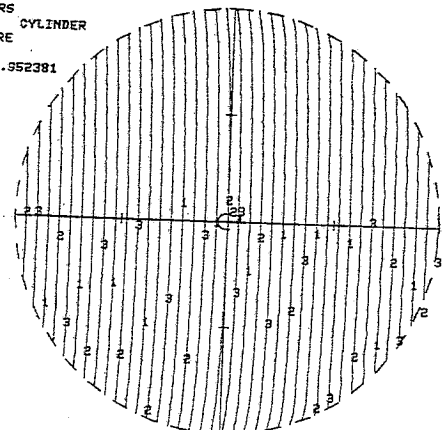


(e) See Figure 82.

ISO-PHASE CONTOURS
CROSS-SECTION OF CYLINDER
VARIABLE: PRESSURE

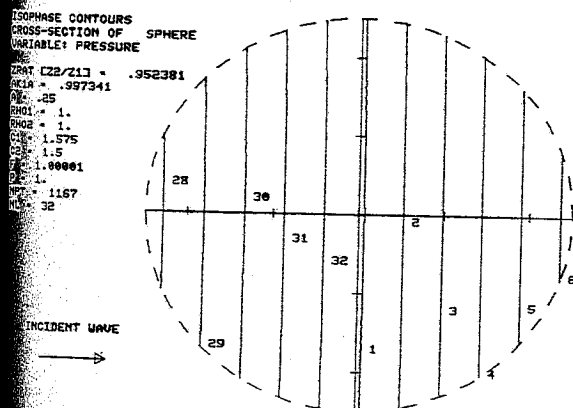
ZRAT [Z2/Z1] = .952381
AKIA = 39.8932
A = 10.
RH01 = 1.
RH02 = 1.
C1 = 1.575
C2 = 1.5
F = 1.
P = 1.
NPT = 4041
NL = 3

INCIDENT WAVE
→

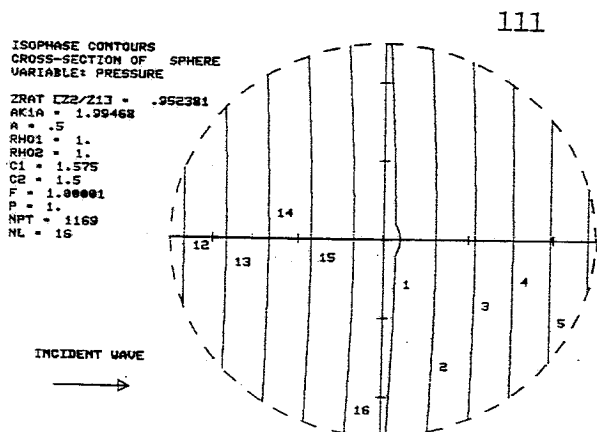


(f) See Figure 83.

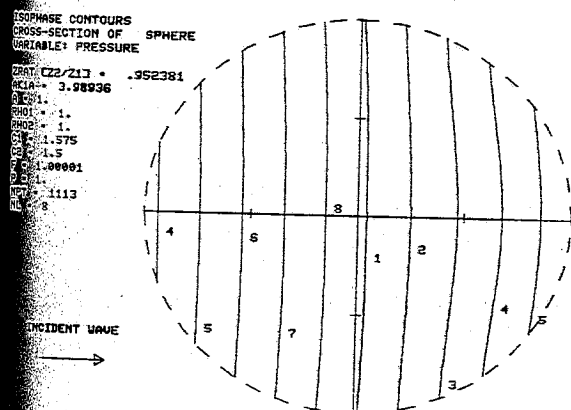
Figure 19. Isophase contours showing dependence of pressure phase ($\angle p'$) in cylinder on the wave product $k_1 a$. Six radius values are considered, for which $k_1 a$ ranges from about 1 to 40 rad. A 5% velocity mismatch ($c_1 > c_2$) is used in all cases.



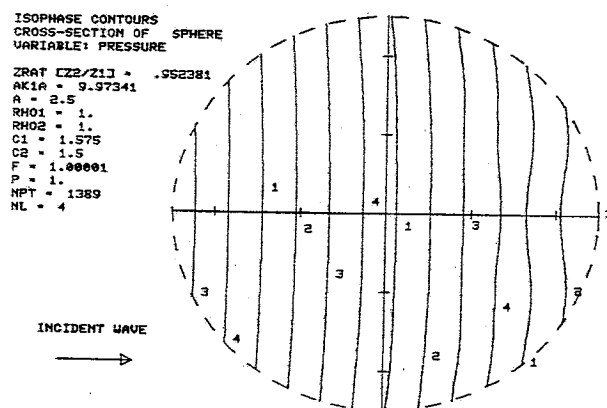
(a) See Figure 84.



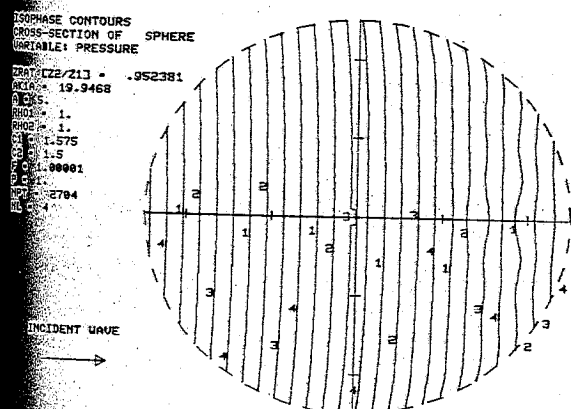
(b) See Figure 85.



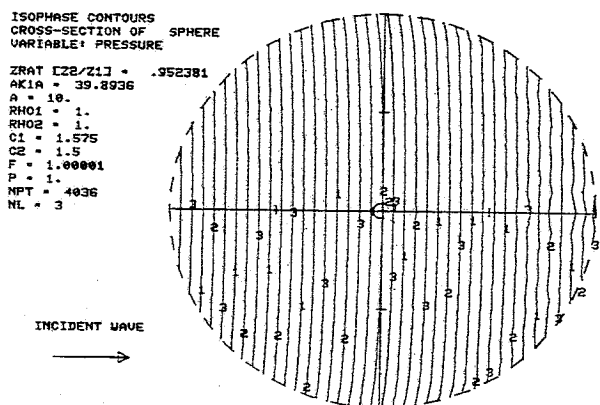
(c) See Figure 86.



(d) See Figure 32.



(e) See Figure 87.



(f) See Figure 88.

Figure 20. Dependence of $\angle p'$ in sphere on $k_1 a$, shown for $k_1 a$ ranging from approximately 1 to 40 rad, and a 5% velocity mismatch ($c_1 > c_2$).

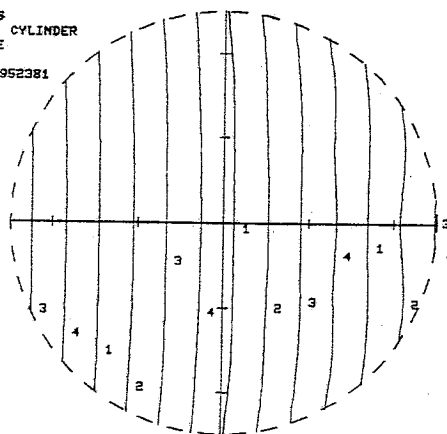
Figures 21 and 22 explore the importance of an impedance mismatch owing to acoustic velocity. For each object shape, four values for c_1 are used, with all other parameters set to standard values. It is observed that downstream (to the right) bowing occurs in the situation $c_1 < c_2$, and upstream (to the left) bowing for $c_1 > c_2$; furthermore, bowing is more pronounced with larger velocity mismatches. Distortion, too, is more extreme in the latter situation, especially with the sphere, and again is located within the downstream halves of both objects.

The final set of plots, Figures 23 and 24, present pressure isophase contours for a series of purely density-based impedance mismatches, analogous to the previous velocity mismatches. Thus ρ_1 is set to four different (nonstandard) values, with all other parameter values standard. No bowing is seen in any of the plots, strongly suggesting that this phenomenon is the result of refraction; the previous figures also support this explanation. On the other hand, distortion occurs for the density mismatches in a manner similar to that of the previous velocity mismatches. Therefore, it seems likely that distortion owes primarily to the more general impedance mismatch. The small discrepancies in the degree of distortion between the two sets of plots probably are caused, at least in part, by differences in $k_1 a$.

ISO-PHASE CONTOURS
CROSS-SECTION OF CYLINDER
VARIABLE: PRESSURE

ZRAT [Z2/Z1] = .952381
AKIA = 9.97331
A = 2.5
RH01 = 1.
RH02 = 1.
C1 = 1.575
C2 = 1.5
F = 1.
P = 1.
NPT = 1381
NL = 4

INCIDENT WAVE
→

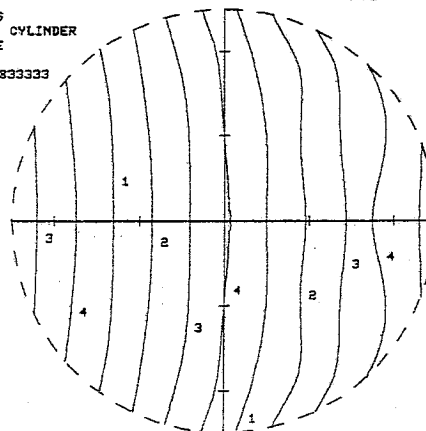


(a) See Figure 26.

ISO-PHASE CONTOURS
CROSS-SECTION OF CYLINDER
VARIABLE: PRESSURE

ZRAT [Z2/Z1] = .833333
AKIA = 8.72665
A = 2.5
RH01 = 1.
RH02 = 1.
C1 = 1.8
C2 = 1.5
F = 1.
P = 1.
NPT = 1213
NL = 4

INCIDENT WAVE
→

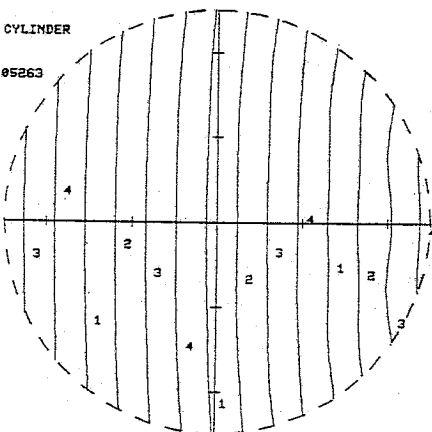


(b) See Figure 89.

ISO-PHASE CONTOURS
CROSS-SECTION OF CYLINDER
VARIABLE: PRESSURE

ZRAT [Z2/Z1] = 1.05263
AKIA = 11.0231
A = 2.5
RH01 = 1.
RH02 = 1.
C1 = 1.425
C2 = 1.5
F = 1.
P = 1.
NPT = 1527
NL = 4

INCIDENT WAVE
→

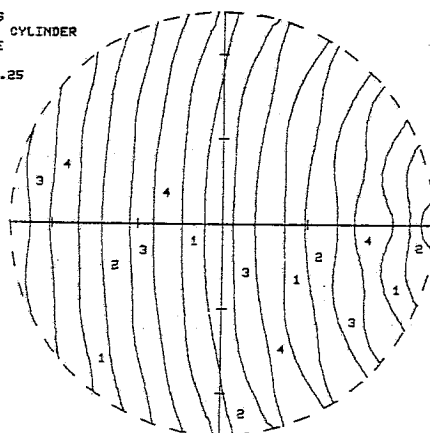


(c) See Figure 90.

ISO-PHASE CONTOURS
CROSS-SECTION OF CYLINDER
VARIABLE: PRESSURE

ZRAT [Z2/Z1] = 1.25
AKIA = 13.09
A = 2.5
RH01 = 1.
RH02 = 1.
C1 = 1.2
C2 = 1.5
F = 1.
P = 1.
NPT = 1811
NL = 4

INCIDENT WAVE
→



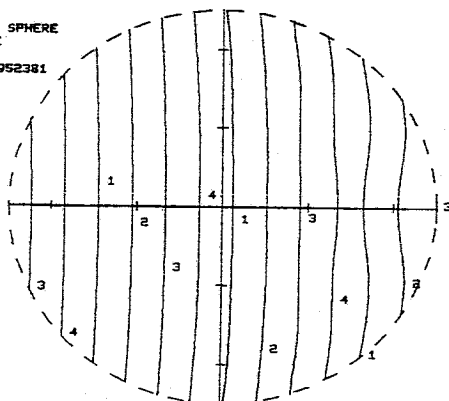
(d) See Figure 91.

Figure 21. Dependence of pressure phase ($\angle p'$) in cylinder on the velocity mismatch, shown for c_1 5% and 20% higher and lower than c_2 (and $k_1 a \cong 10$ rad).

ISOPHASE CONTOURS
CROSS-SECTION OF SPHERE
VARIABLE: PRESSURE

ZRAT [Z2/Z1] = .952381
AK1A = 3.97341
A = 2.5
RH01 = 1.
RH02 = 1.
C1 = 1.575
C2 = 1.5
F = 1.00001
P = 1.
NPT = 1389
NL = 4

INCIDENT WAVE
→

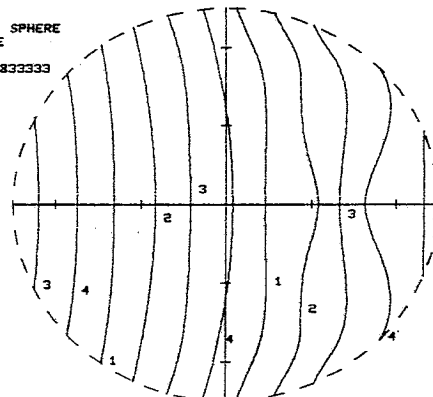


(a) See Figure 32.

ISOPHASE CONTOURS
CROSS-SECTION OF SPHERE
VARIABLE: PRESSURE

ZRAT [Z2/Z1] = .833333
AK1A = 3.72673
A = 2.5
RH01 = 1.
RH02 = 1.
C1 = 1.3
C2 = 1.5
F = 1.00001
P = 1.
NPT = 1227
NL = 4

INCIDENT WAVE
→

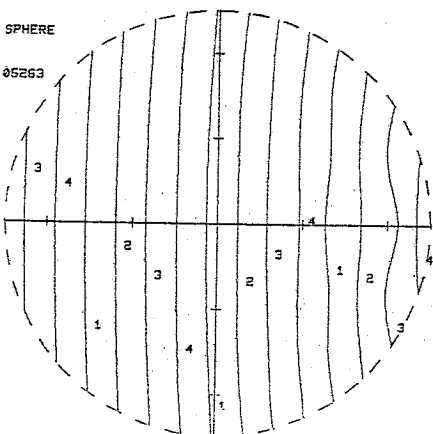


(b) See Figure 92.

ISOPHASE CONTOURS
CROSS-SECTION OF SPHERE
VARIABLE: PRESSURE

ZRAT [Z2/Z1] = 1.05263
AK1A = 11.0232
A = 2.5
RH01 = 1.
RH02 = 1.
C1 = 1.425
C2 = 1.5
F = 1.00001
P = 1.
NPT = 1531
NL = 4

INCIDENT WAVE
→

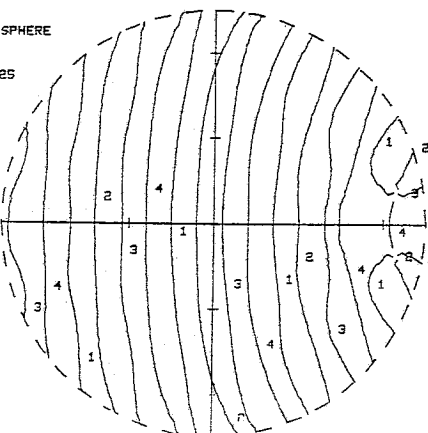


(c) See Figure 93.

ISOPHASE CONTOURS
CROSS-SECTION OF SPHERE
VARIABLE: PRESSURE

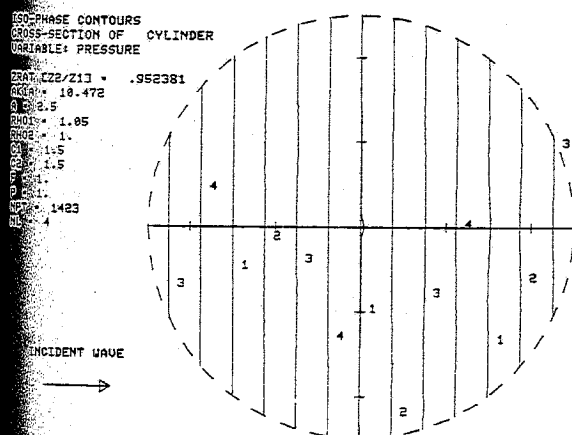
ZRAT [Z2/Z1] = 1.25
AK1A = 13.0901
A = 2.5
RH01 = 1.
RH02 = 1.
C1 = 1.2
C2 = 1.5
F = 1.00001
P = 1.
NPT = 1783
NL = 4

INCIDENT WAVE
→

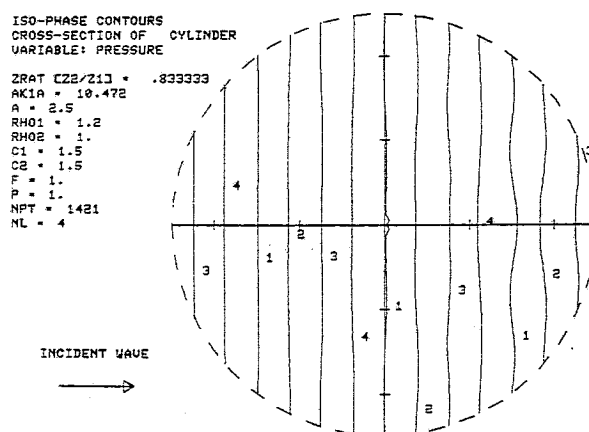


(d) See Figure 94.

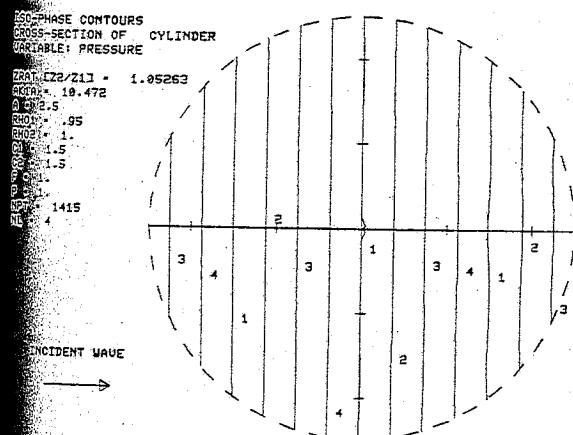
Figure 22. Dependence of $\Delta p'$ in sphere on the velocity mismatch, shown for values of $c_1 \pm 5\%$ and $\pm 20\%$ with respect to c_2 (and $k_1 a \cong 10$ rad).



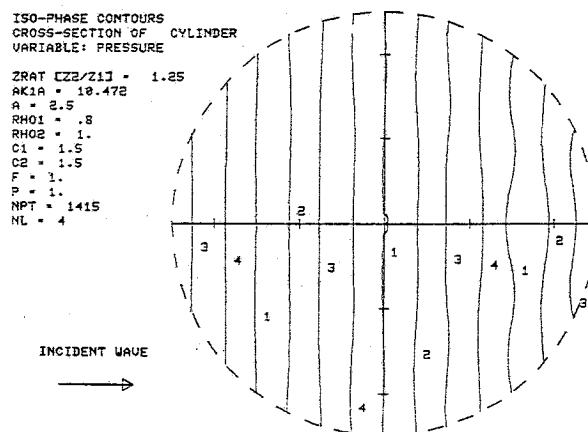
(a) See Figure 95.



(b) See Figure 96.



(c) See Figure 97.



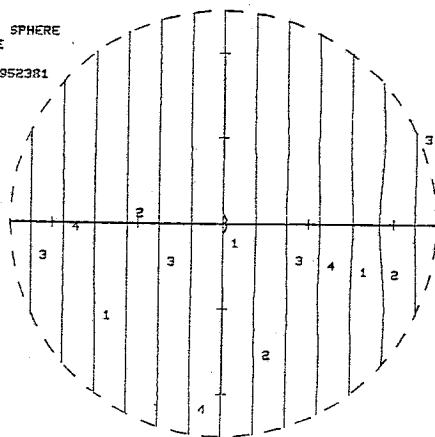
(d) See Figure 98.

Figure 23. Dependence of pressure phase ($\angle p'$) in cylinder on the density mismatch, shown for ρ_1 5% and 20% greater and less than ρ_2 (and $k_1 a \cong 10$ rad).

ISOPHASE CONTOURS
CROSS-SECTION OF SPHERE
VARIABLE: PRESSURE

ZRAT [Z2/Z1] = .952381
AKIA = 10.4721
A = 2.5
RH01 = 1.05
RH02 = 1.
C1 = 1.5
C2 = 1.5
F = 1.00001
P = 1.
NPT = 1419
NL = 4

INCIDENT WAVE
→

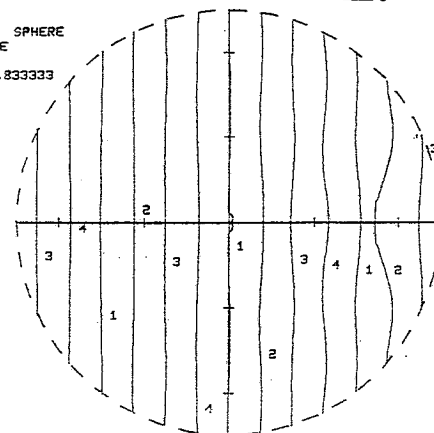


(a) See Figure 99.

ISOPHASE CONTOURS
CROSS-SECTION OF SPHERE
VARIABLE: PRESSURE

ZRAT [Z2/Z1] = .833333
AKIA = 10.4721
A = 2.5
RH01 = 1.2
RH02 = 1.
C1 = 1.5
C2 = 1.5
F = 1.00001
P = 1.
NPT = 1421
NL = 4

INCIDENT WAVE
→

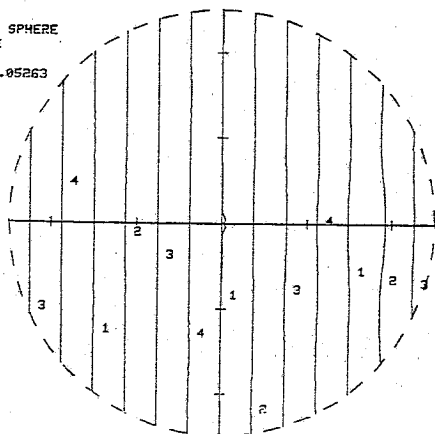


(b) See Figure 100.

ISOPHASE CONTOURS
CROSS-SECTION OF SPHERE
VARIABLE: PRESSURE

ZRAT [Z2/Z1] = 1.05263
AKIA = 10.4721
A = 2.5
RH01 = .95
RH02 = 1.
C1 = 1.5
C2 = 1.5
F = 1.00001
P = 1.
NPT = 1419
NL = 4

INCIDENT WAVE
→

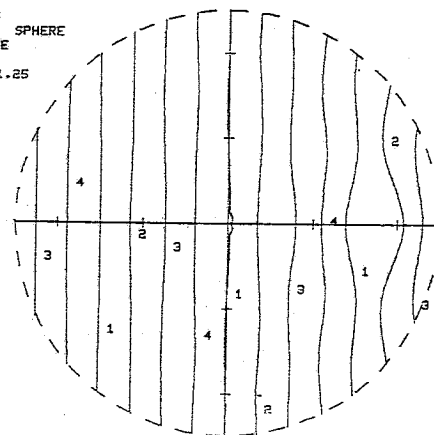


(c) See Figure 101.

ISOPHASE CONTOURS
CROSS-SECTION OF SPHERE
VARIABLE: PRESSURE

ZRAT [Z2/Z1] = 1.25
AKIA = 10.4721
A = 2.5
RH01 = .8
RH02 = 1.
C1 = 1.5
C2 = 1.5
F = 1.00001
P = 1.
NPT = 1423
NL = 4

INCIDENT WAVE
→



(d) See Figure 102.

Figure 24. Dependence of $\langle p' \rangle$ in sphere on the density mismatch, shown for $\rho_1 \pm 5\%$ and $\pm 20\%$ with respect to ρ_2 (and $k_1 a \cong 10$ rad).

4. DISCUSSION AND CONCLUSIONS

One of the original aims of this thesis was to apply numerical methods to solving wave problems. Once such a method is successfully used for simple problems, such as the soft- and rigid-object problems solved in Sections 2.2, it could, presumably, be extended to solve more complex problems, for which analytical solutions are not known or cannot be found. It is unfortunate that the general method-of-lines approach used in the package FORSIM suffers from both instability and inefficiency in solving for the steady-state solution of a two-dimensional hyperbolic differential equation. The general nature of this approach, and its implementation, is well suited to the expansion of the problem to include three dimensions and two coordinate systems, and to account for a temperature distribution, as well. Thus, in the search for a new numerical approach which alleviates the former problems of instability and inefficiency, it must be remembered that flexibility is an important feature, so that the numerical method can be truly useful in tackling more complex wave problems. Such flexibility may not be available in packages specifically designed for solving hyperbolic problems. The FORSIM manual (Carver et al., 1978:29-30) discusses this issue further, and describes other available packages.

Turning attention to the results found analytically, it is interesting to compare the plots of estimated viscous power loss in spheres, presented in Section 3.2.2, with illustrations of loss in spheres owing to electromagnetic (microwave) radiation, provided by Kritikos and Schwan (1975). One minor difficulty with this comparison is the

polarization of the incident electromagnetic wave, resulting in distinct "E-" and "H-plane" cross sections of the sphere. This issue is irrelevant with longitudinal acoustic waves, so that the angle θ of the cross-section plane is arbitrary. Nevertheless, hot-spot locations in the two problems are significantly similar (heating in the E- and H-planes is not markedly different, in general). In particular, for lower values of $k_1 a$, both types of radiation result in strikingly similar solutions, with maximum heating at the upstream boundary. For higher values of $k_1 a$, for which the solutions are more complex, some agreement is still seen: maximum heating occurs in areas within the downstream halves of spheres, again for acoustic and electromagnetic irradiation. However, these "focused" hot spots are located nearer to the center of the sphere, in the case of electromagnetic waves.

The trends in the dependence of heating on object shape and parameter values can be summarized as follows. Maximum heating and spatial nonuniformity are usually more extreme with the sphere than with the cylinder, ceteris paribus; this very consistent finding probably owes to the sphere being circular, and thus best suited for "focusing," in all cross sections, as opposed to the single circular cross section of the cylinder. Also, higher values of $k_1 a$ and larger impedance mismatches generally contribute to extremes in heating. The worst case presented, in terms of highest maximum E_y , is Figure 14d, in which F_{max} is more than 30 times higher than the uniform heating with a plane wave of the same amplitude as the incident wave. The latter case occurs with a sphere, where $k_1 a = 13.1$ rad and the impedance

ratio $Z_r = 1.25$. However, even more extreme situations can be predicted, based on the previously stated trends (higher $k_1\alpha$ and/or Z_r further from unity). The usual location of hot spots in both the cylinder and the sphere is at the upstream boundary for lower values of $k_1\alpha$, and within the downstream halves or at the downstream boundary for higher values. In addition, heating is often found at the side boundaries of the cylinder, for higher $k_1\alpha$.

Finally, it is desired to compare the performance of two types of pressure detectors, based on information provided by the earlier figures. The first, a thermal detector, measures temperature and permits estimation of heat generation and thus pressure, assuming viscous power loss is proportional to the square of the pressure. The second type is a piezoelectric transducer, which measures pressure much more directly than does a thermal detector, but suffers from errors being introduced by phase-averaging of pressure across the face of the transducer. For simplicity, both devices are assumed to be disc-shaped, the plane of which is oriented normal to the propagation direction of the incident wave.

It is obvious that both devices will give nonspecific--basically meaningless--results if they are situated in an area of high nonuniformity of magnitude, in particular the downstream halves of a cylinder or a sphere for which $k_1\alpha$ is rather high and/or the impedance mismatch is large. In such an area, the piezoelectric transducer suffers from the additional difficulty of being subjected to significant "random" phase distortion. If, on the other hand, the detectors are located in the

central or upstream portions of the object interiors, the magnitude and phase distortion will be significantly reduced. Here, a distinction is seen between the detectors: the main potential error lies with the piezoelectric transducer, which may be affected by phase "bowing," most pronounced near the centers of the objects. As can be inferred from Figures 19 through 24, the piezoelectric transducer will perform best in situations where it is much smaller than the object diameter, so that the phase is relatively constant across the transducer face, and where velocity mismatches and $k_1 a$ are as low as possible.

REFERENCES

1. Carver, M. B., et al., The FORSIM VI Simulation Package for the Automated Solution of Arbitrarily Defined Partial and/or Ordinary Differential Equations. Chalk River, Ontario: Chalk River Nuclear Laboratories, February 1978, no. AECL-5821.
2. Chan, A. K., R. A. Sigelmann, and A. W. Guy, "Calculations of Therapeutic Heat Generated by Ultrasound in Fat-Muscle-Bone Layers," IEEE Transactions on Biomedical Engineering, vol. BME-21, no. 4, pp. 280-284, July 1974.
3. Control Data Corp., Math Science Library. Minneapolis, Minn.: CDC Publication No. 60327500, 1973.
4. Frizzell, L. A., "Ultrasonic Heating of Tissues." Unpublished Doctor's dissertation, Dept. of Electrical Engineering, University of Rochester, 1975, pp. 88-99.
5. Goss, S. A., R. L. Johnston, and F. Dunn, "Comprehensive compilation of empirical ultrasonic properties of mammalian tissues," Journal of the Acoustical Society of America, vol. 64, no. 2, pp. 423-457, August 1978.
6. Hildebrand, F. B., Advanced Calculus for Applications. Englewood Cliffs, N.J.: Prentice-Hall, Inc., 1962.
7. Johnston, R. L., et al., "Elements of Tissue Characterization--Part I: Ultrasonic Propagation Properties," Ultrasonic Tissue Characterization II, ed. M. Linzer. National Bureau of Standards, Spec. Publ. 525, pp. 19-27. Washington: U.S. Government Printing Office, 1979.
8. Kinsler, L. E., and A. R. Frey, Fundamentals of Acoustics. 2nd ed. New York: John Wiley & Sons, 1962.
9. Kritikos, H. N., and H. P. Schwan, "Hot Spots Generated in Conducting Spheres by Electromagnetic Waves and Biological Implications," IEEE Transactions on Biomedical Engineering, vol. BME-19, no. 1, pp. 53-58, January 1972.
10. _____, "The Distribution of Heating Potential Inside Lossy Spheres," IEEE Transactions on Biomedical Engineering, vol. BME-22, no. 6, pp. 457-463, November 1975.
11. _____, "Formation of Hot Spots in Multilayer Spheres," IEEE Transactions on Biomedical Engineering, vol. BME-23, no. 2, pp. 168-172, March 1976.

12. Kritikos, H. N., and H. P. Schwan, "Potential Temperature Rise Induced by Electromagnetic Field in Brain Tissues," IEEE Transactions on Biomedical Engineering, vol. BME-26, no. 1, pp. 29-33, January 1979.
13. Morse, P. M., Vibration and Sound. 1st ed. New York: McGraw-Hill Book Co., Inc., 1936.
14. _____ and K. U. Ingard, Theoretical Acoustics. New York: McGraw-Hill Book Co., Inc., 1968.
15. O'Brien, W. D., Jr., "The Relationship Between Collagen and Ultrasonic Attenuation and Velocity in Tissue," Ultrasonics International 1977 Conference Proceedings, sponsored by the journal Ultrasonics. Surrey, England: IPC Business Press Limited, 1977, pp. 194-204.

APPENDIX

The following plots, Figures 25 through 102, are full-size versions of the plots previously presented in groups in Figures 7 through 24, and are provided for closer inspection. The ordering is the same as for the grouped plots, according to a left-to-right, then down-the-page sequence. However, each plot which is included in more than one grouping is repeated here only for its first respective occurrence.

ISO-MAGNITUDE CONTOURS
CROSS-SECTION OF CYLINDER
VARIABLE: PRESSURE

ZRAT [Z2/Z1] = .952381

AK1A = 9.97331

A = 2.5

RH01 = 1.

RH02 = 1.

C1 = 1.575

C2 = 1.5

F = 1.

P = 1.

NPT = 1170

NL = 4

FMIN = .842006

FMAX = 1.08232

INCIDENT WAVE:



Figure 25. Pressure isomagnitude contours in cross section of cylinder, with c_1 5% greater than c_2 , and $k_1 \alpha \cong 10$ rad.

ISO-PHASE CONTOURS
CROSS-SECTION OF CYLINDER
VARIABLE: PRESSURE

ZRAT [Z2/Z1] = .952381

AK1A = 9.97331

A = 2.5

RH01 = 1.

RH02 = 1.

C1 = 1.575

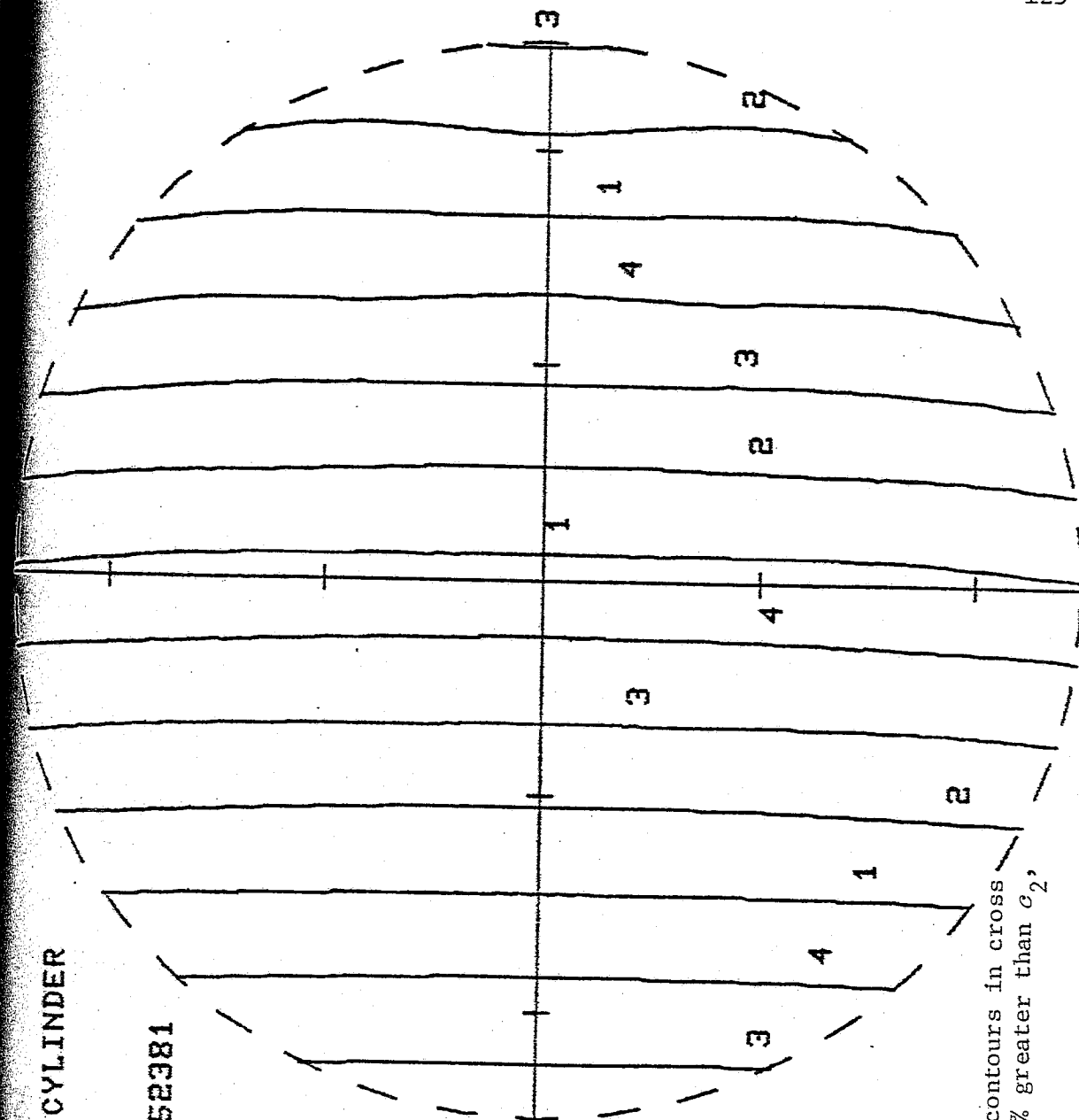
C2 = 1.5

F = 1.

P = 1.

NPT = 1381

NL = 4



INCIDENT WAVE



Figure 26. Pressure isophase contours in cross section of cylinder, with c_1 5% greater than c_2 , and $k_1 \alpha \approx 10$ rad.

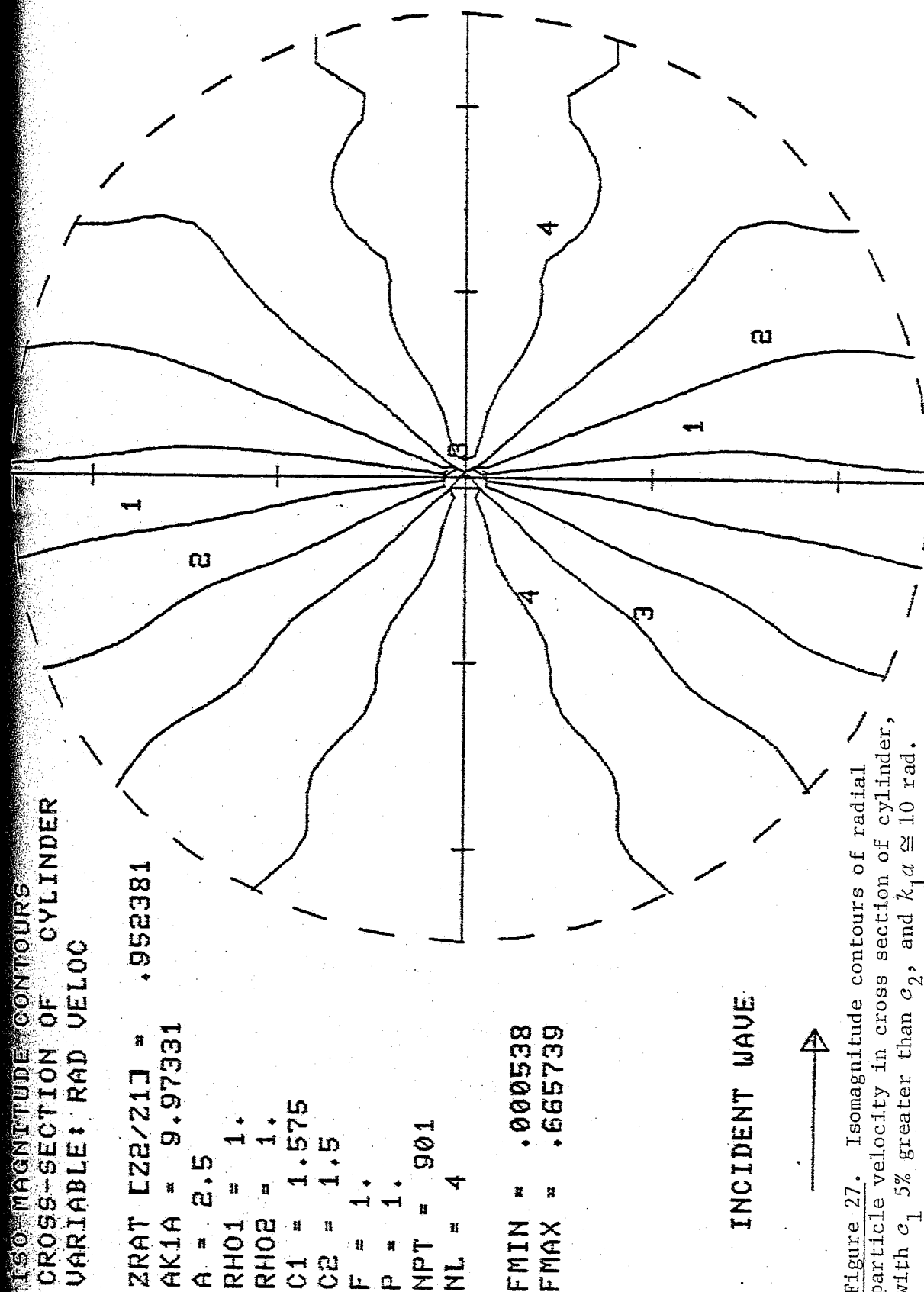


Figure 27. Isomagnitude contours of radial particle velocity in cross section of cylinder, with c_1 5% greater than c_2 , and $k_1 a \approx 10$ rad.

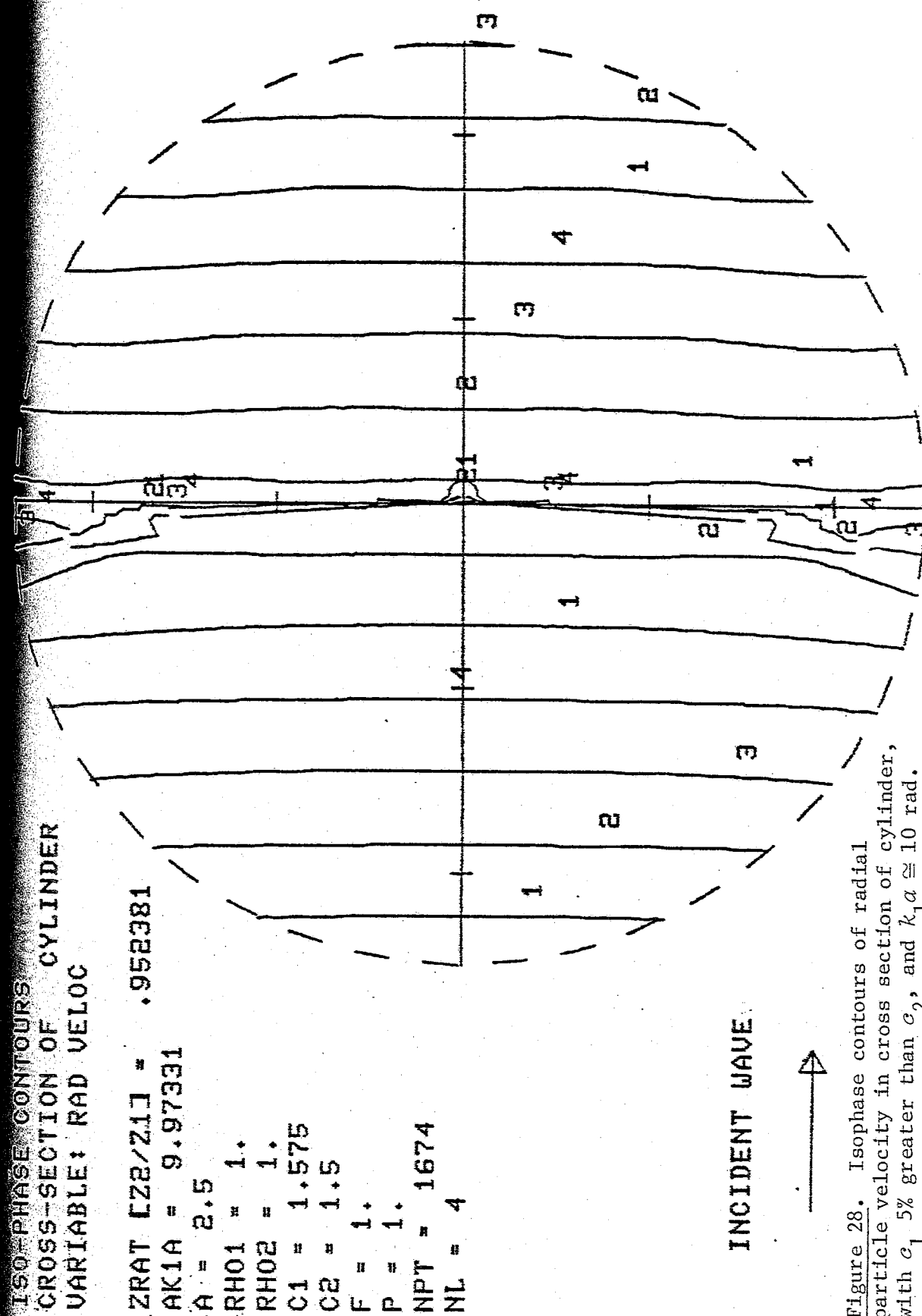


Figure 28. Isophase contours of radial particle velocity in cross section of cylinder, with c_1 5% greater than c_2 , and $k_1 a \approx 10$ rad.

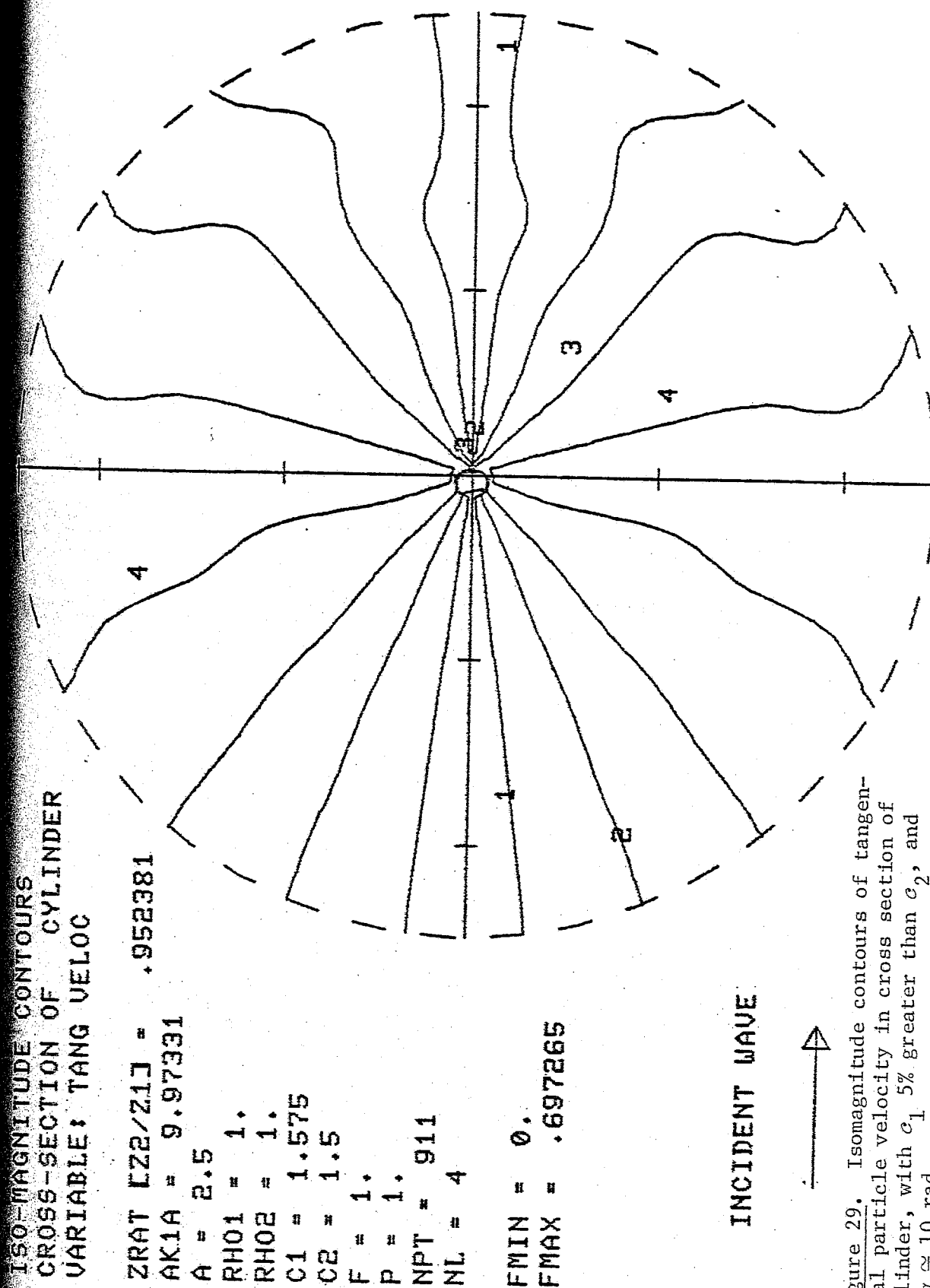


Figure 29. Isomagnitude contours of tangential particle velocity in cross section of cylinder, with c_1 5% greater than c_2 , and $k_1 \alpha \approx 10$ rad.

ISO-PHASE CONTOURS
CROSS-SECTION OF CYLINDER
VARIABLE: TANG VELOC

ZRAT [Z2/Z1] = .952381

AK1A = 9.97331

A = 2.5

RHO1 = 1.

RHO2 = 1.

C1 = 1.575

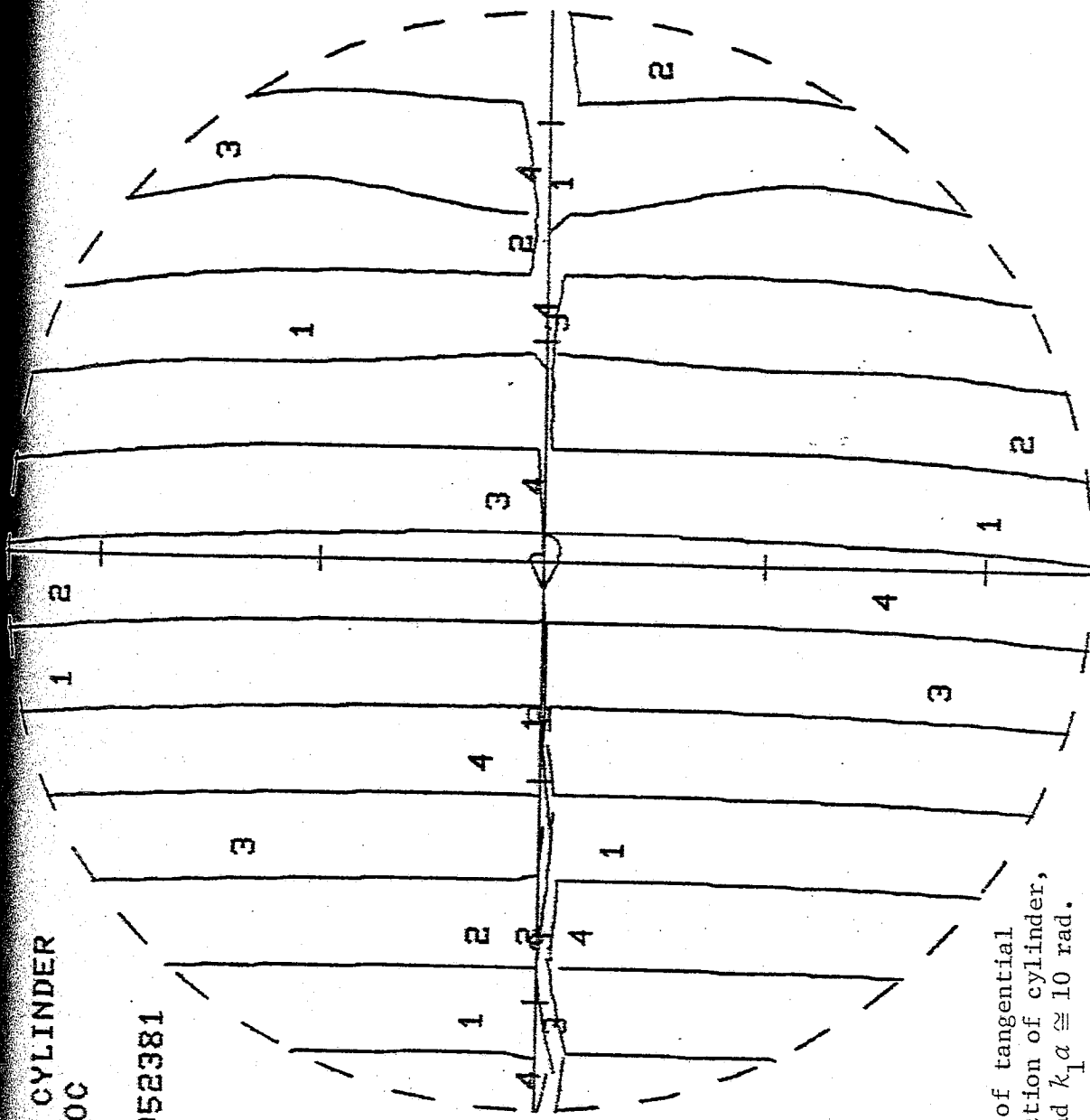
C2 = 1.5

F = 1.

P = 1.

NPT = 1635

NL = 4



INCIDENT WAVE



Figure 30. Isophase contours of tangential particle velocity in cross section of cylinder, with α_1 5% greater than α_2 , and $k_1 \alpha \approx 10$ rad.

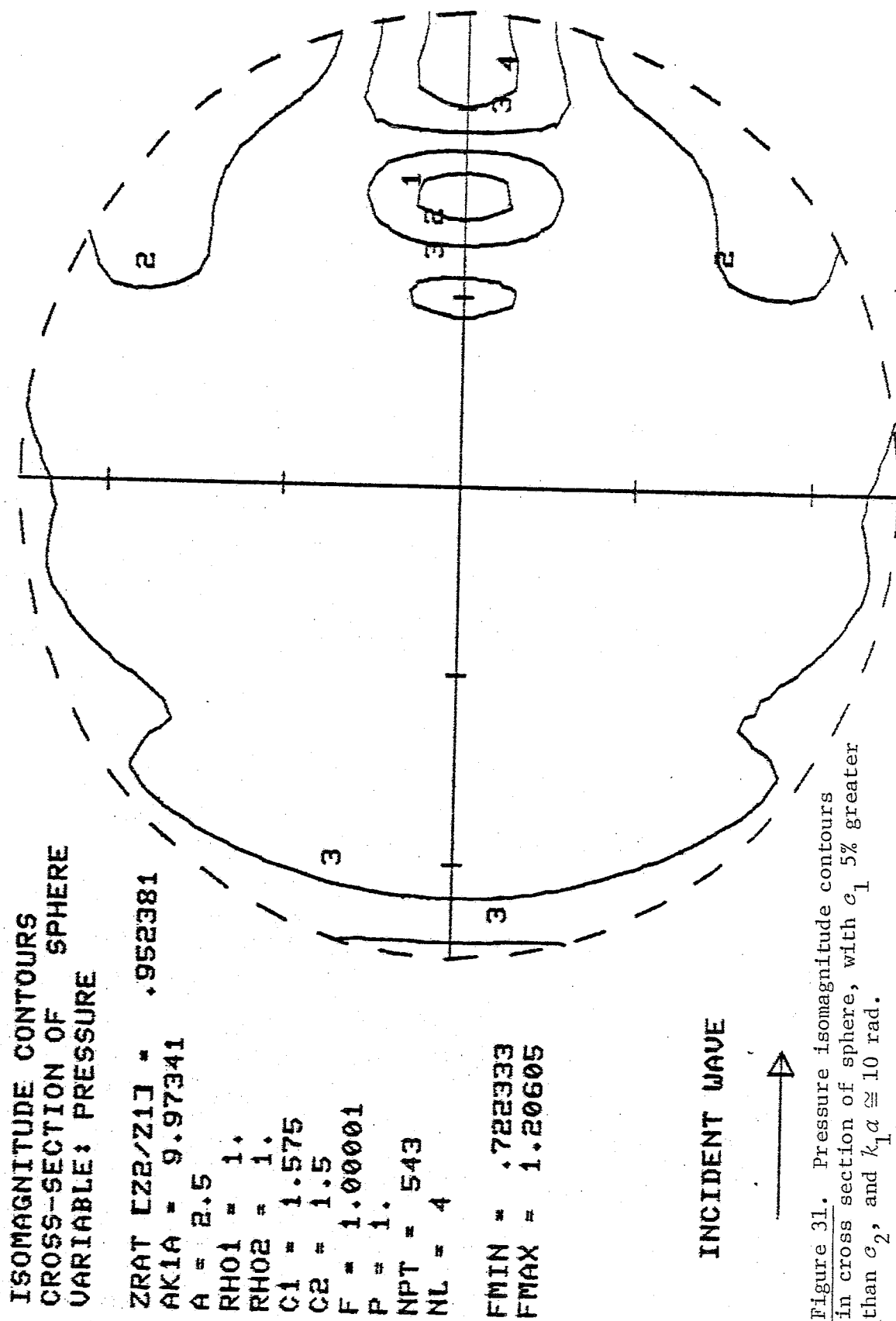


Figure 31. Pressure isomagnitude contours in cross section of sphere, with c_1 5% greater than c_2 , and $k_1 a \cong 10$ rad.

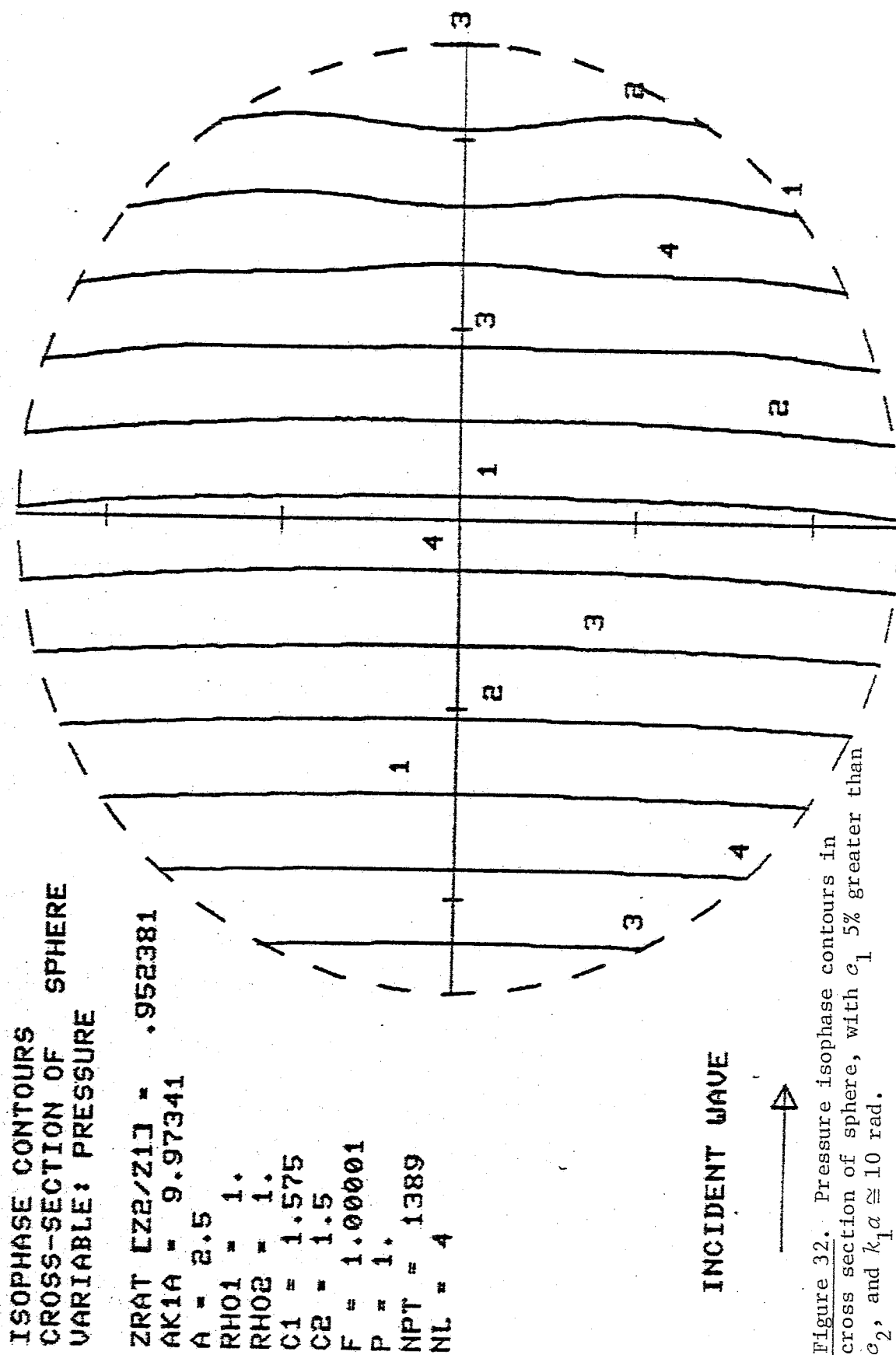


Figure 32. Pressure isophase contours in cross section of sphere, with c_1 5% greater than c_2 , and $k_1 a \approx 10$ rad.

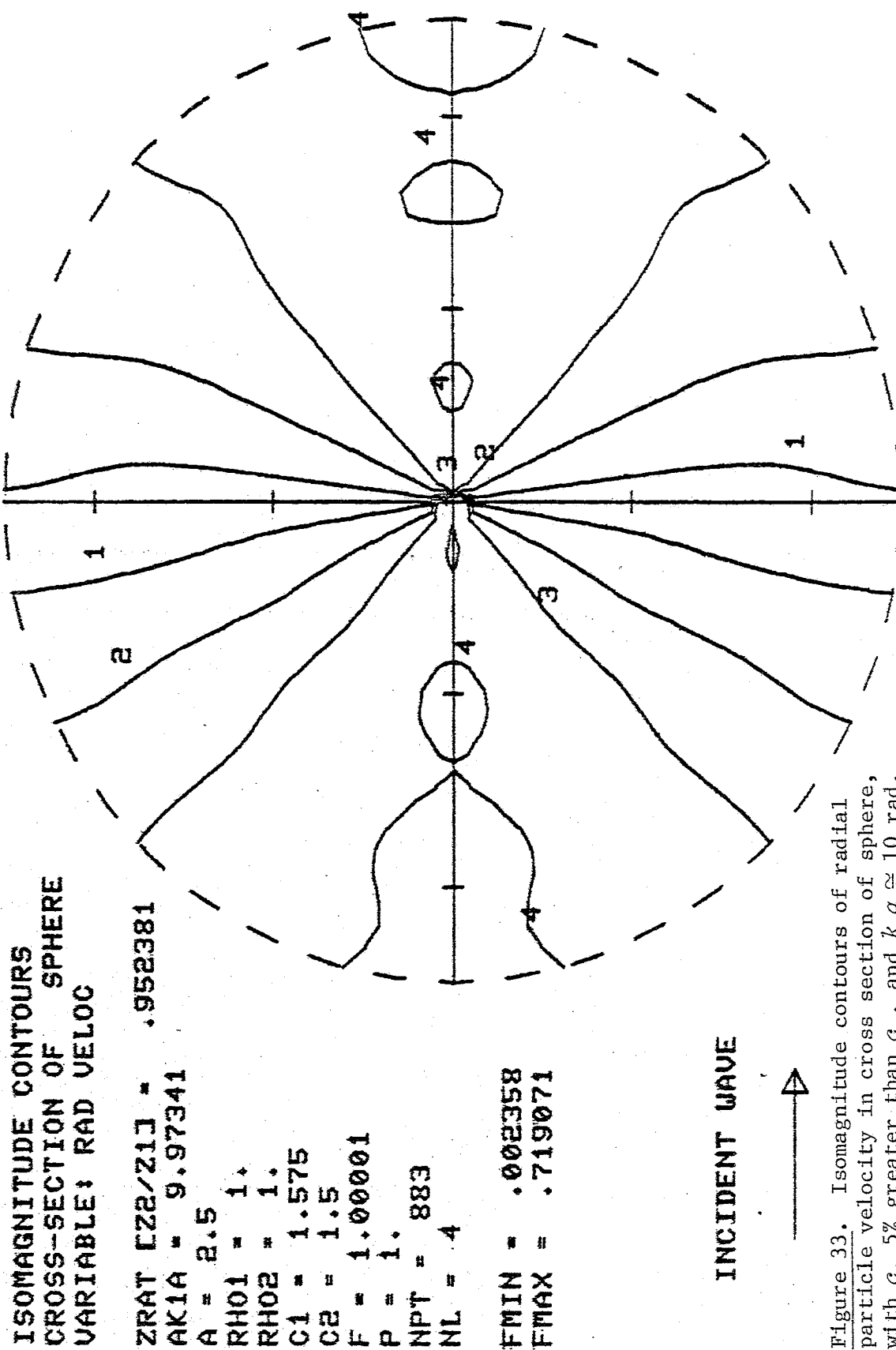
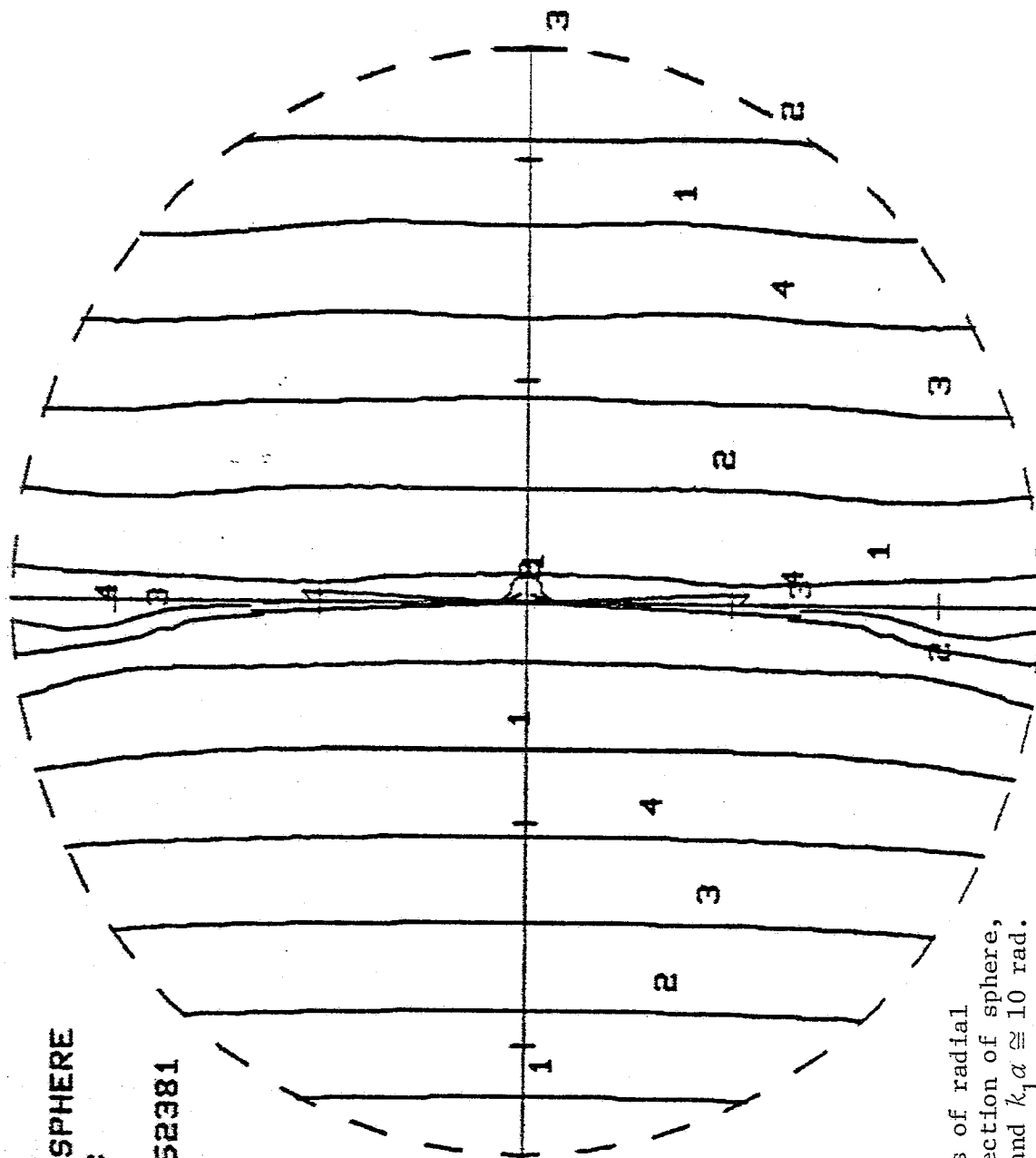


Figure 33. Isomagnitude contours of radial particle velocity in cross section of sphere, with c_1 5% greater than c_2 , and $k_1 a \approx 10$ rad.

ISOPHASE CONTOURS
CROSS-SECTION OF SPHERE
VARIABLE: RAD VELOC

ZRAT [Z2/Z1] = .952381
AK1A = 9.97341
A = 2.5
RH01 = 1.
RH02 = 1.
C1 = 1.575
C2 = 1.5
F = 1.00001
P = 1.
NPT = 1659
NL = 4



INCIDENT WAVE



Figure 34. Isophase contours of radial particle velocity in cross section of sphere, with c_1 5% greater than c_2 , and $k_1 \alpha \approx 10$ rad.

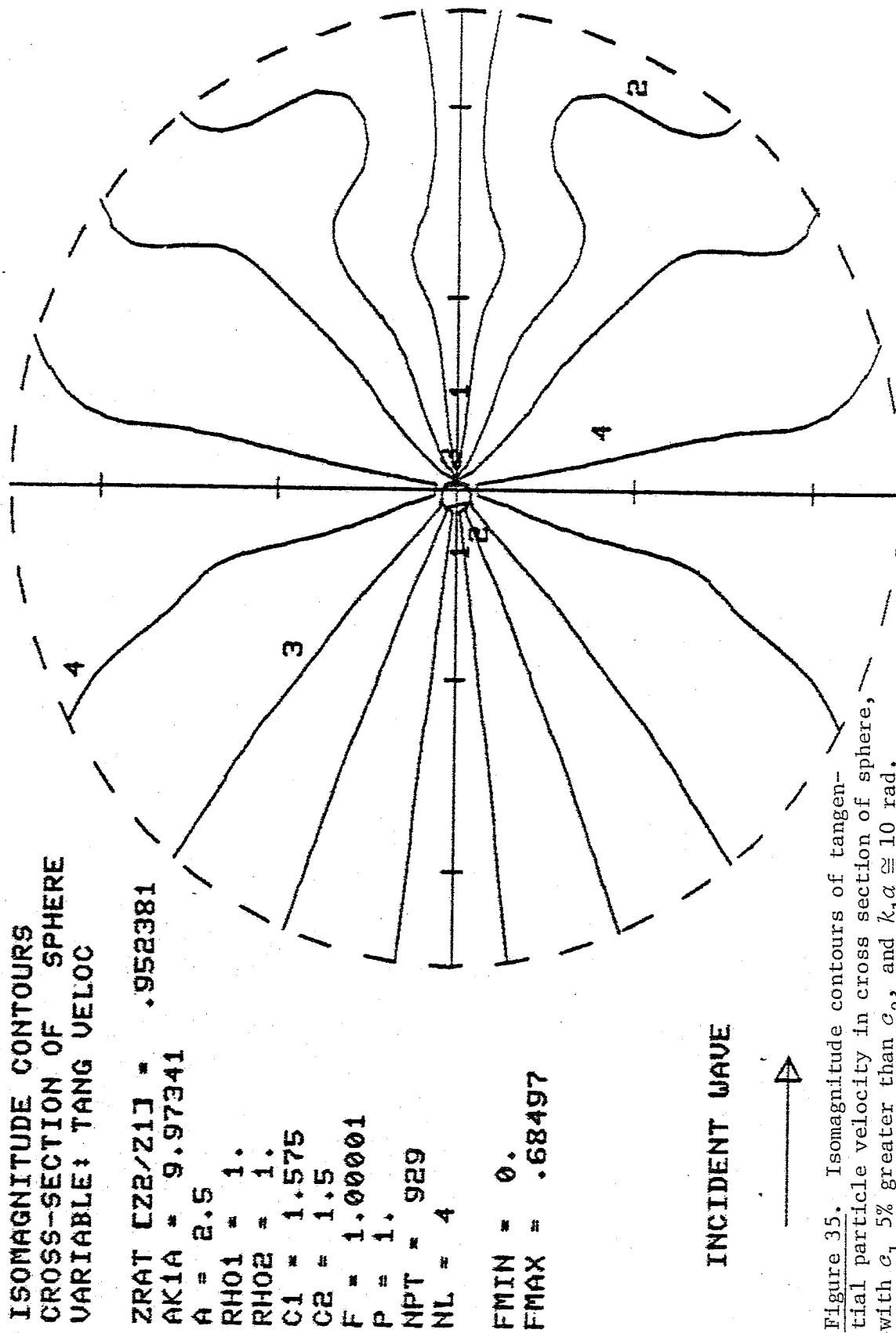


Figure 35. Isomagnitude contours of tangential particle velocity in cross section of sphere, with c_1 5% greater than c_2 , and $k_1 \alpha \approx 10$ rad.

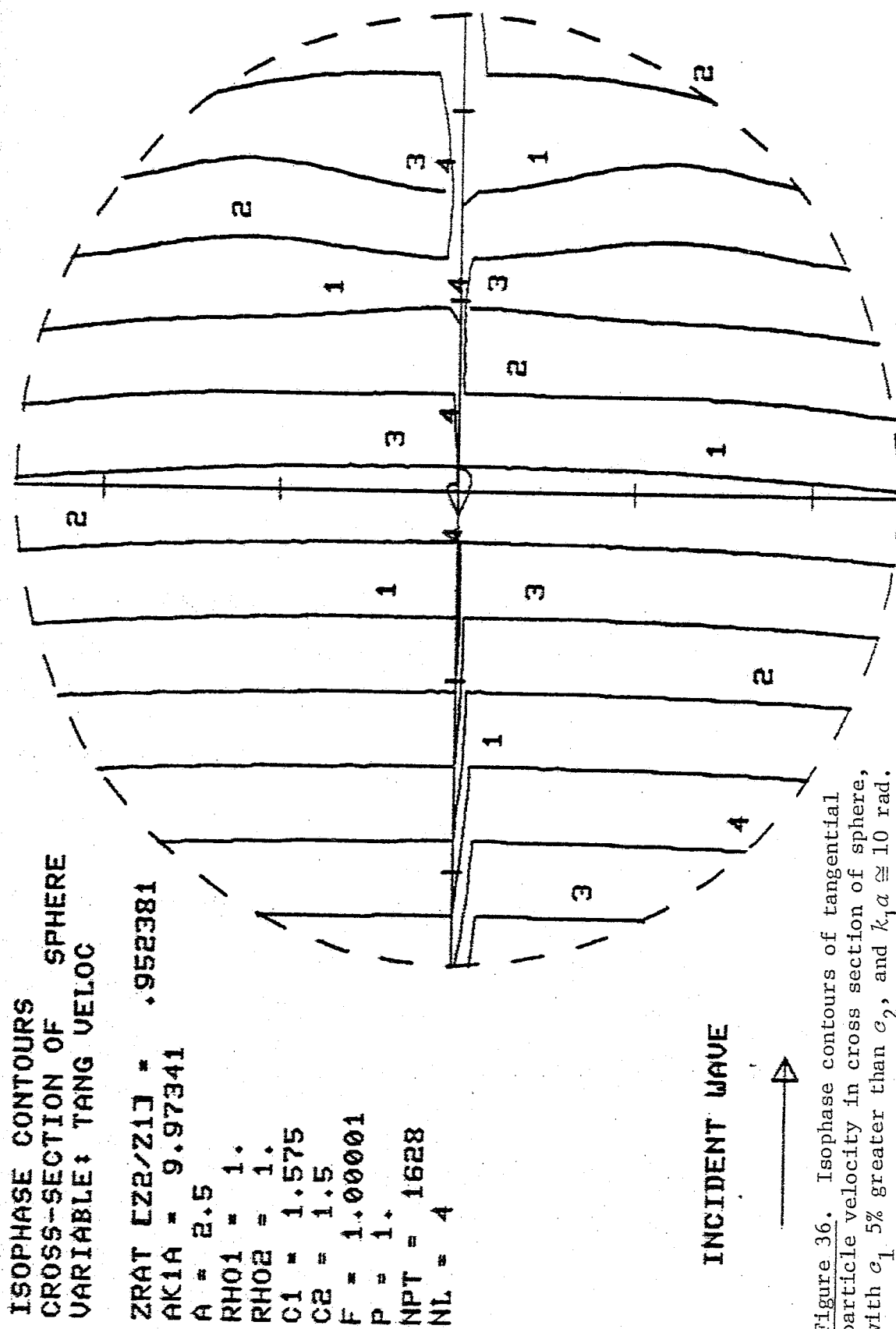


Figure 36. Isophase contours of tangential particle velocity in cross section of sphere, with c_1 5% greater than c_2 , and $k_1 a \approx 10$ rad.

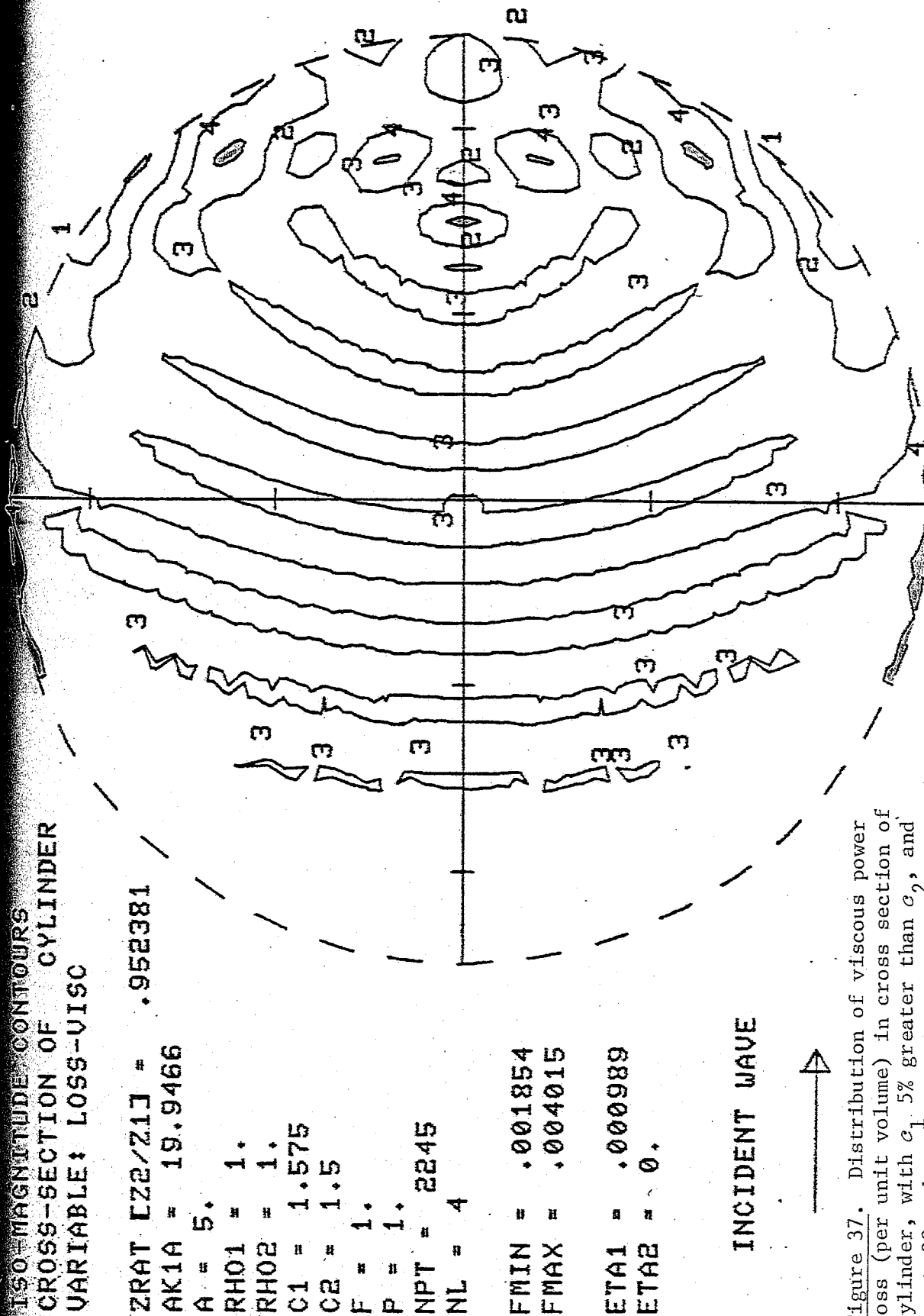


Figure 37. Distribution of viscous power loss (per unit volume) in cross section of cylinder, with c_1 5% greater than c_2 , and $k_1 a \approx 20$ rad.

ISO-MAGNITUDE CONTOURS
CROSS-SECTION OF CYLINDER
VARIABLE: LOSS-ABS

ZRAT [Z2/Z1] = .952381

AK1A = 19.9466

A = 5.

RH01 = 1.

RH02 = 1.

C1 = 1.575

C2 = 1.5

F = 1.

P = 1.

NPT = 553

NL = 4

FMIN = .00205

FMAX = .004

ALF1 = .005

ALF2 = 0.

INCIDENT WAVE



Figure 38. Distribution of absorptive power loss (per unit volume) in cross section of cylinder, with c_1 5% greater than c_2 , and $k_1 a \approx 20$ rad.

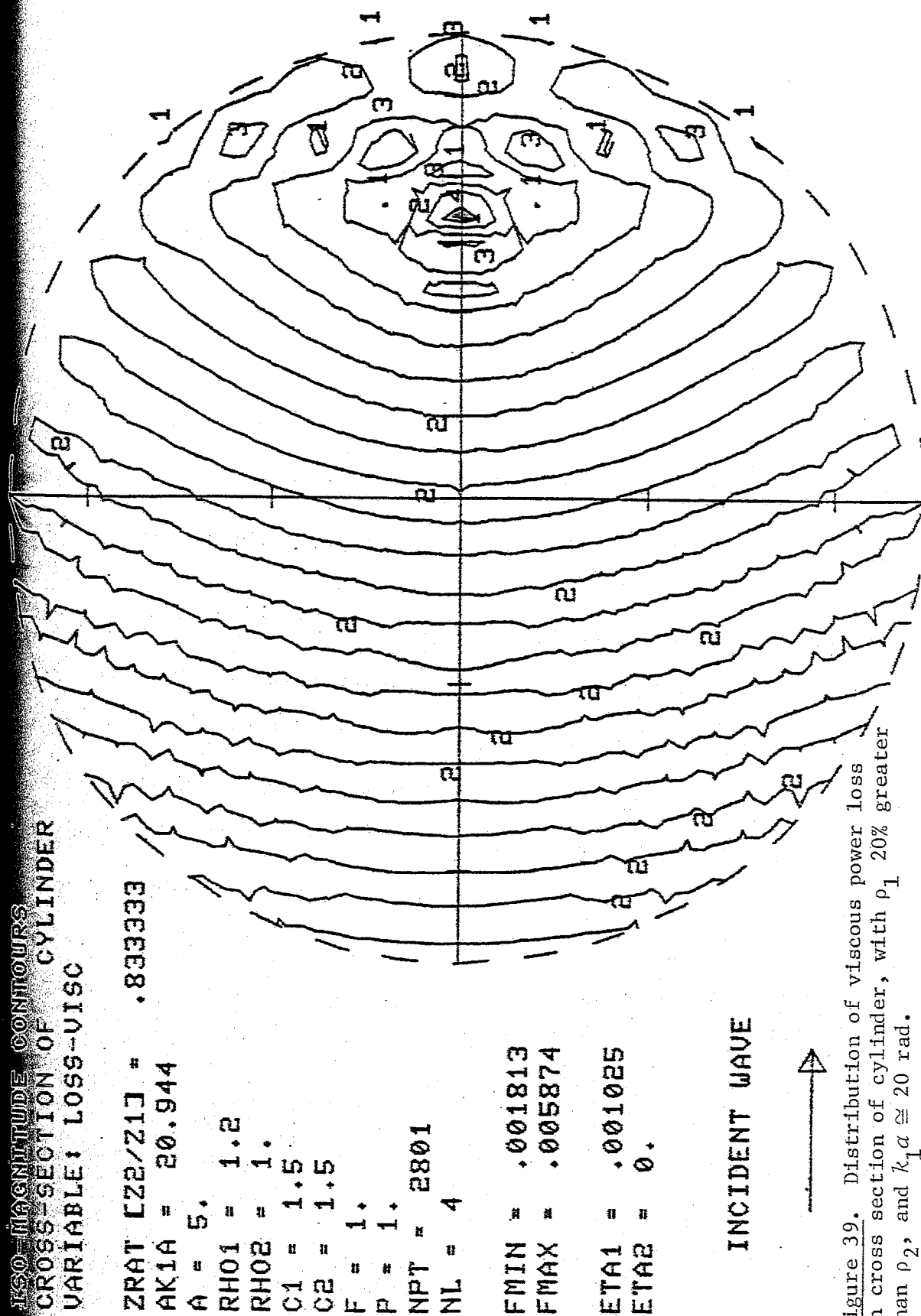


Figure 39. Distribution of viscous power loss in cross section of cylinder, with ρ_1 20% greater than ρ_2 , and $k_1\alpha \approx 20$ rad.

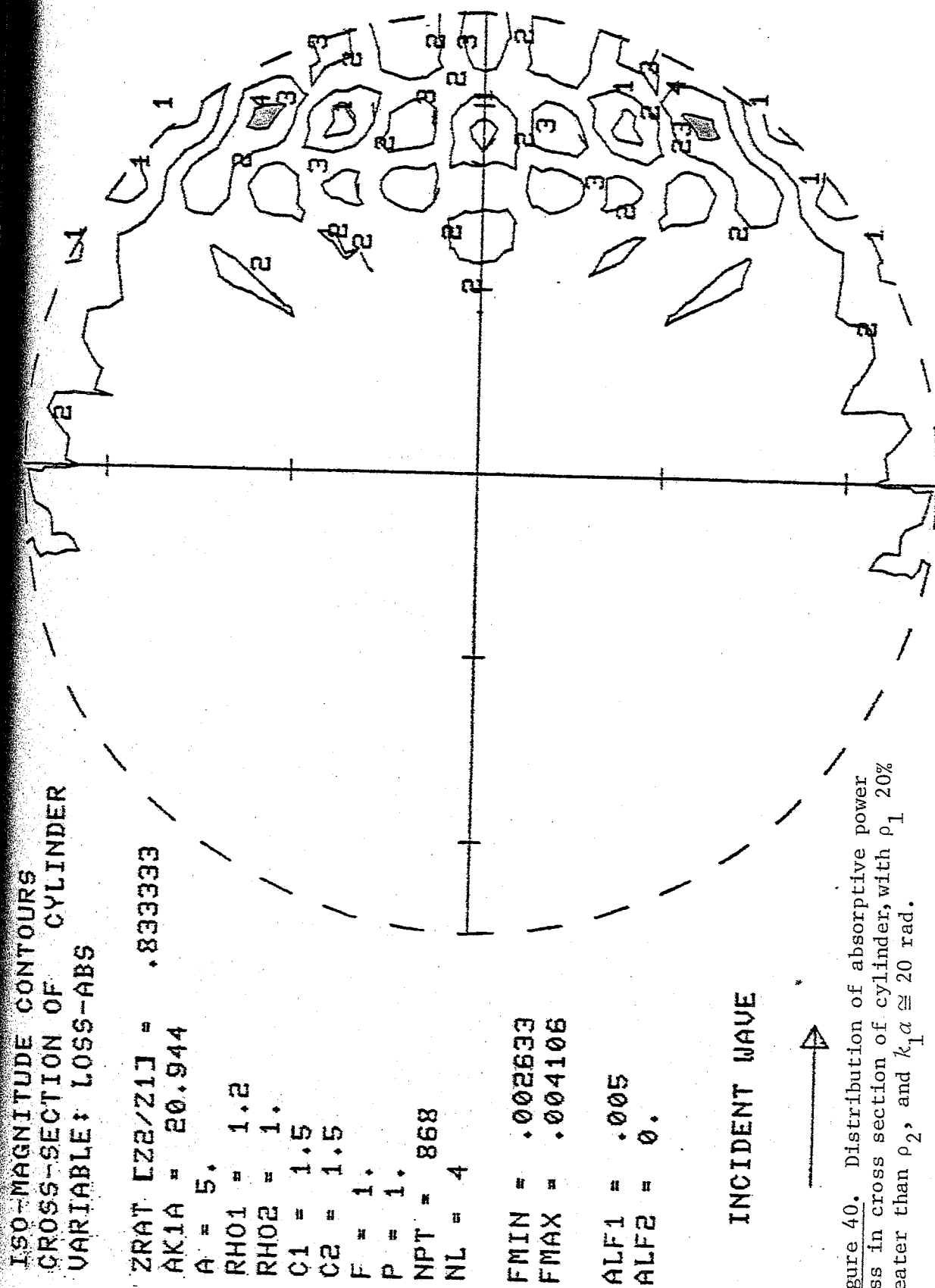


Figure 40. Distribution of absorptive power loss in cross section of cylinder, with ρ_1 20% greater than ρ_2 , and $k_1 a \approx 20$ rad.

ISO-MAGNITUDE CONTOURS
CROSS-SECTION OF CYLINDER
VARIABLE: LOSS-VISC

ZRAT [Z2/Z1] = .952381

AK1A = .997331

A = .25

RHO1 = 1.

RHO2 = 1.

C1 = 1.575

C2 = 1.5

F = 1.

P = 1.

NPT = 1113

NL = 8

FMIN = .002897

FMAX = .003347

ETA1 = .000989

ETA2 = 0.

INCIDENT WAVE



Figure 41. Distribution of viscous power loss in cross section of cylinder, with c_1 5% greater than c_2 , and $k_1 a \approx 1$ rad.

ISO-MAGNITUDE CONTOURS
CROSS-SECTION OF CYLINDER
VARIABLE: LOSS-ABS

ZRAT [Z2/Z1] = .952381

AK1A = .997331

A = .25

RHO1 = 1.

RHO2 = 1.

C1 = 1.575

C2 = 1.5

F = 1.

P = 1.

NPT = 1253

NL = 8

FMIN = .00312

FMAX = .003315

ALF1 = .005

ALF2 = 0.

INCIDENT WAVE

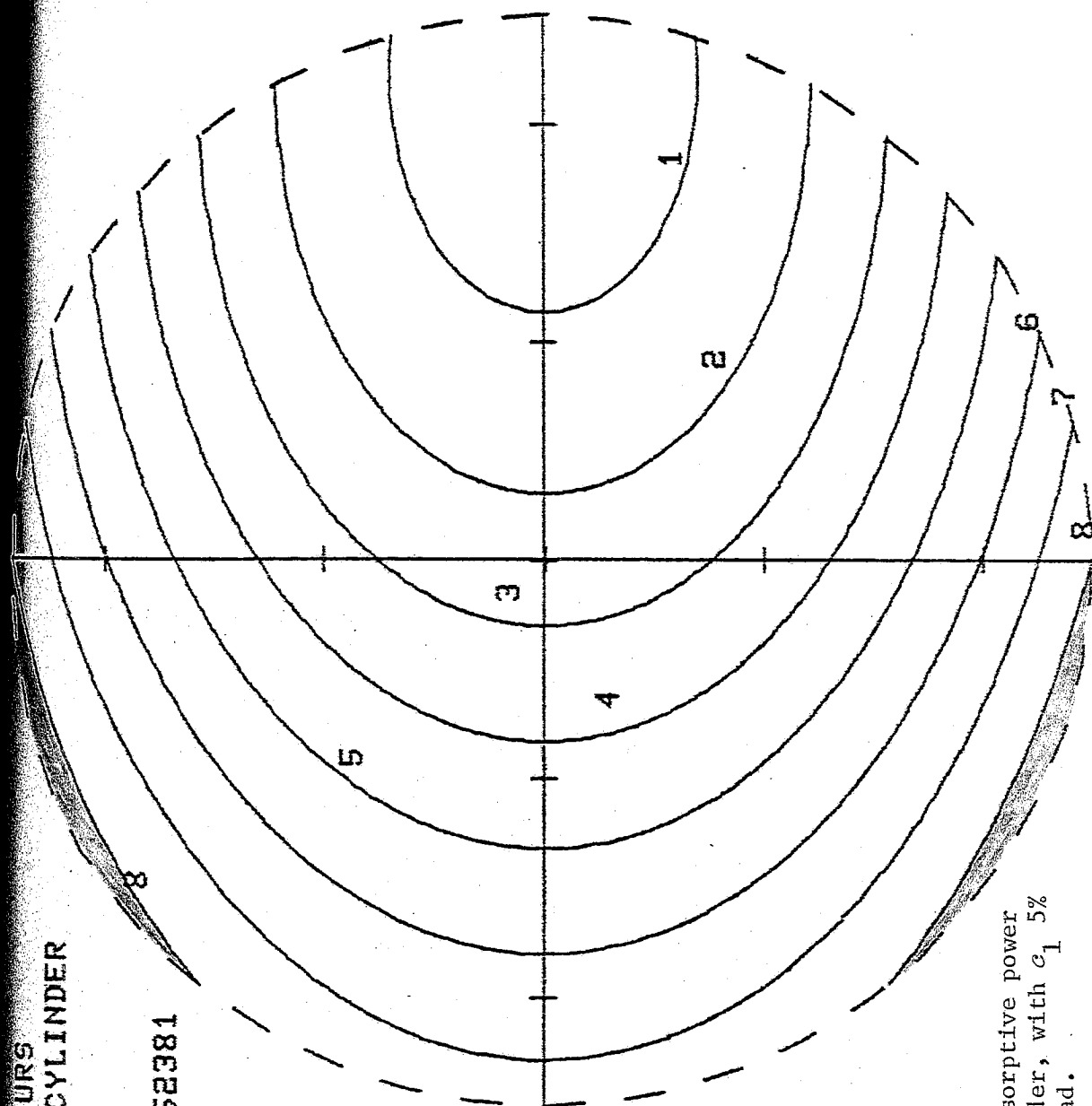


Figure 42. Distribution of absorptive power loss in cross section of cylinder, with c_1 5% greater than c_2 , and $k_1 a \cong 1$ rad.

ISOMAGNITUDE CONTOURS
CROSS-SECTION OF SPHERE
VARIABLE: LOSS-VISC

ZRAT EZ2/Z1J = .952381

AK1A = 19.9468

A = 5.

RHO1 = 1.

RHO2 = 1.

C1 = 1.575

C2 = 1.5

F = 1.00001

P = 1.

NPT = 556

NL = 4

FMIN = .000987

FMAX = .005224

ETA1 = .000989

ETA2 = 0.

INCIDENT WAVE

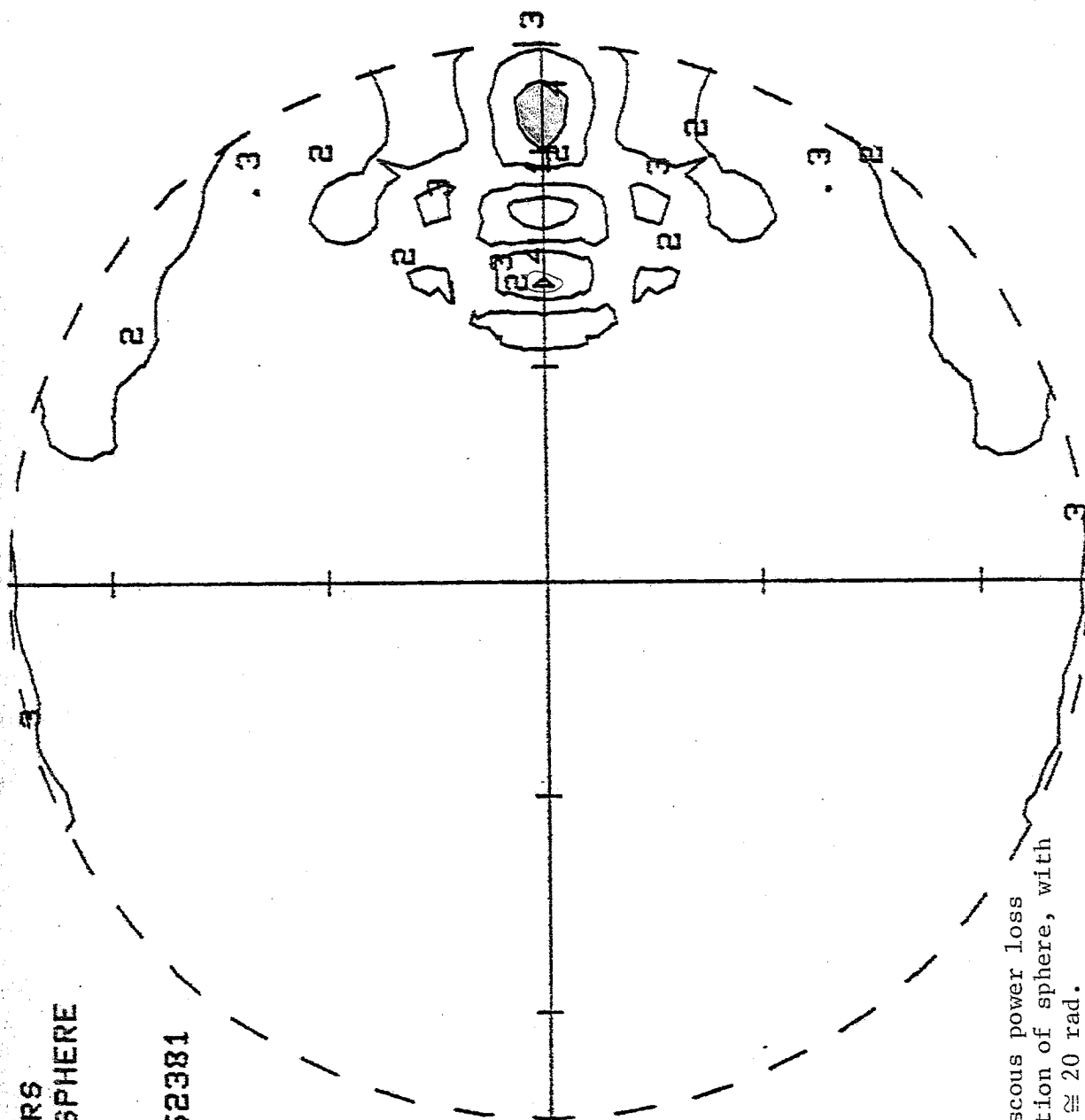


Figure 43. Distribution of viscous power loss (per unit volume) in cross section of sphere, with c_1 5% greater than c_2 , and $k_1 a \approx 20$ rad.

ISOMAGNITUDE CONTOURS
CROSS-SECTION OF SPHERE
VARIABLE: LOSS-ABS

ZRAT LZ2/Z17 = .952381

AK1A = 19.9468

A = 5.

RHO1 = 1.

RHO2 = 1.

C1 = 1.575

C2 = 1.5

F = 1.00001

P = 1.

NPT = 515

NL = 4

FMIN = .001638

FMAX = .0044

ALF1 = .005

ALF2 = 0.

INCIDENT WAVE

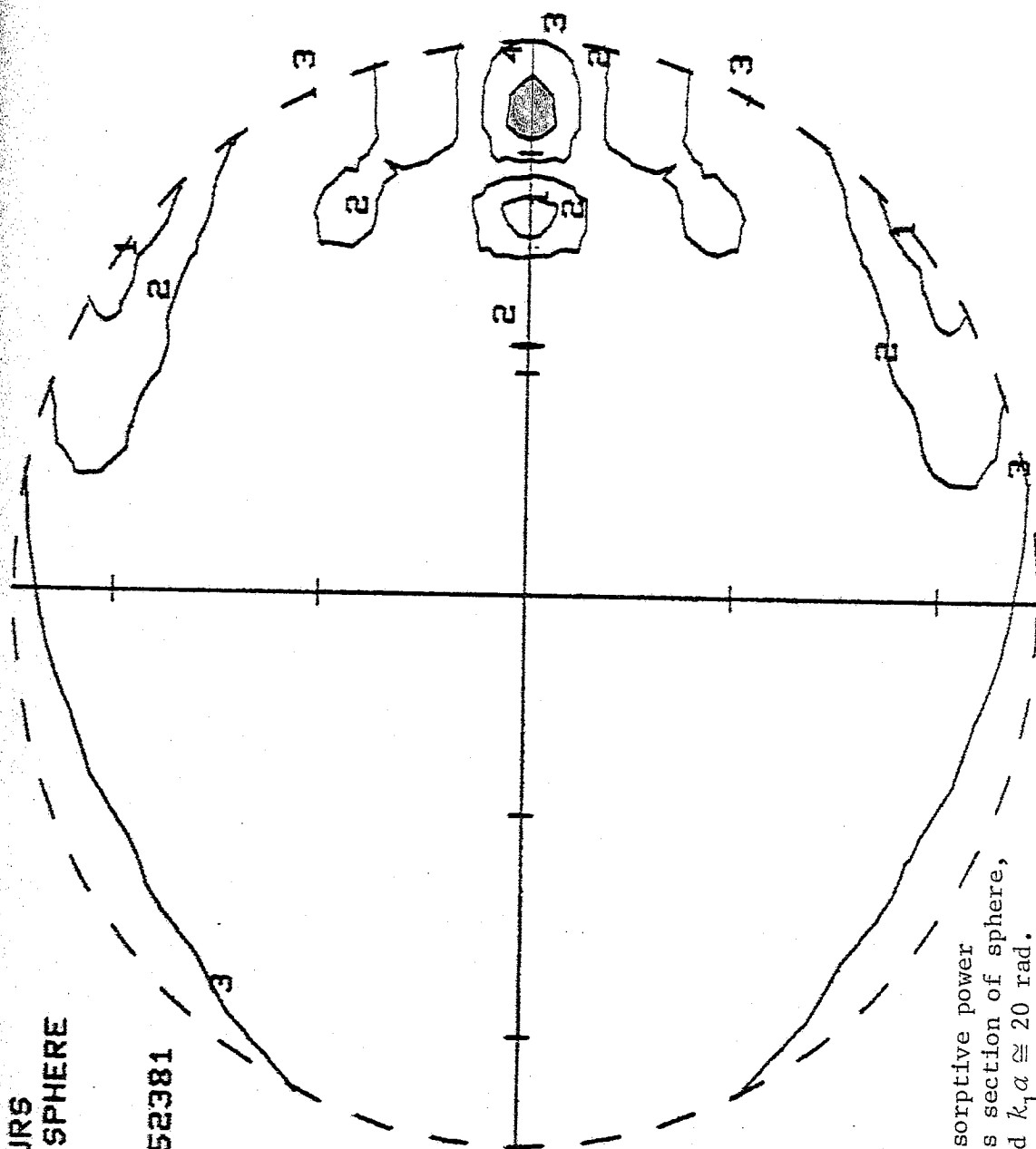


Figure 44. Distribution of absorptive power loss (per unit volume) in cross section of sphere, with c_1 5% greater than c_2 , and $k_1 \alpha \approx 20$ rad.

ISOMAGNITUDE CONTOURS
CROSS-SECTION OF SPHERE
VARIABLE: LOSS-VISC

ZRAT [Z2/Z1] = .833333

AK1A = 20.9442

A = 5.

RHO1 = 1.2

RHO2 = 1.

C1 = 1.5

C2 = 1.5

F = 1.00001

P = 1.

NPT = 331

NL = 4

FMIN = .000026

FMAX = .013744

ETA1 = .001025

ETA2 = 0.

INCIDENT WAVE



Figure 45. Distribution of viscous power loss in cross section of sphere, with ρ_1 20% greater than ρ_2 , and $k_1 a \approx 20$ rad.

ISOMAGNITUDE CONTOURS
CROSS-SECTION OF SPHERE
VARIABLE: LOSS-ABS

ZRAT [Z2/Z1] = .833333

AK1A = 20.9442

A = 5.

RHO1 = 1.2

RHO2 = 1.

C1 = 1.5

C2 = 1.5

F = 1.00001

P = 1.

NPT = 293

NL = 4

FMIN = .000316

FMAX = .006289

ALF1 = .005

ALF2 = 0.

INCIDENT WAVE:

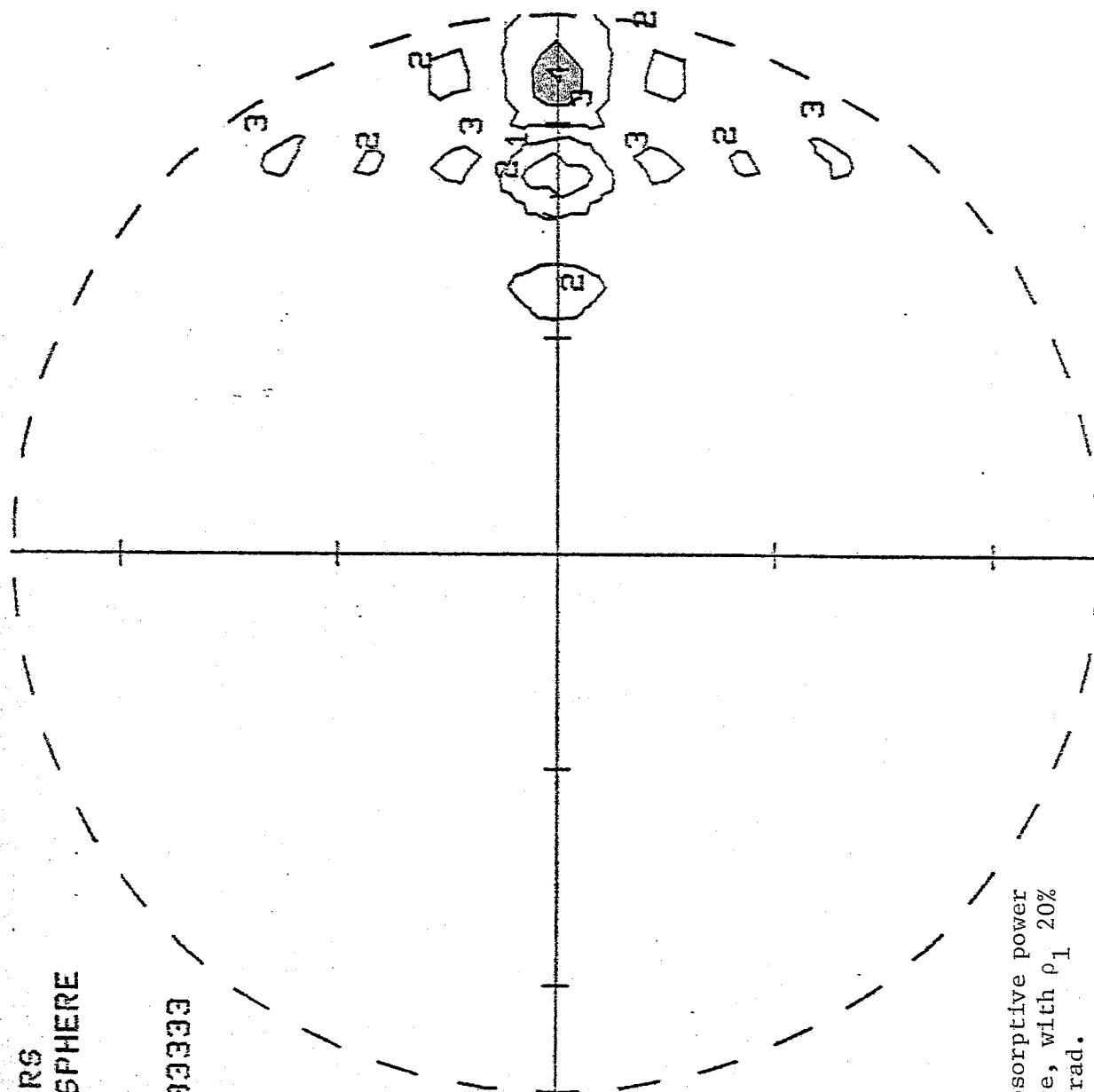


Figure 46. Distribution of absorptive power loss in cross section of sphere, with ρ_1 20% greater than ρ_2 , and $k_1 a \approx 20$ rad.

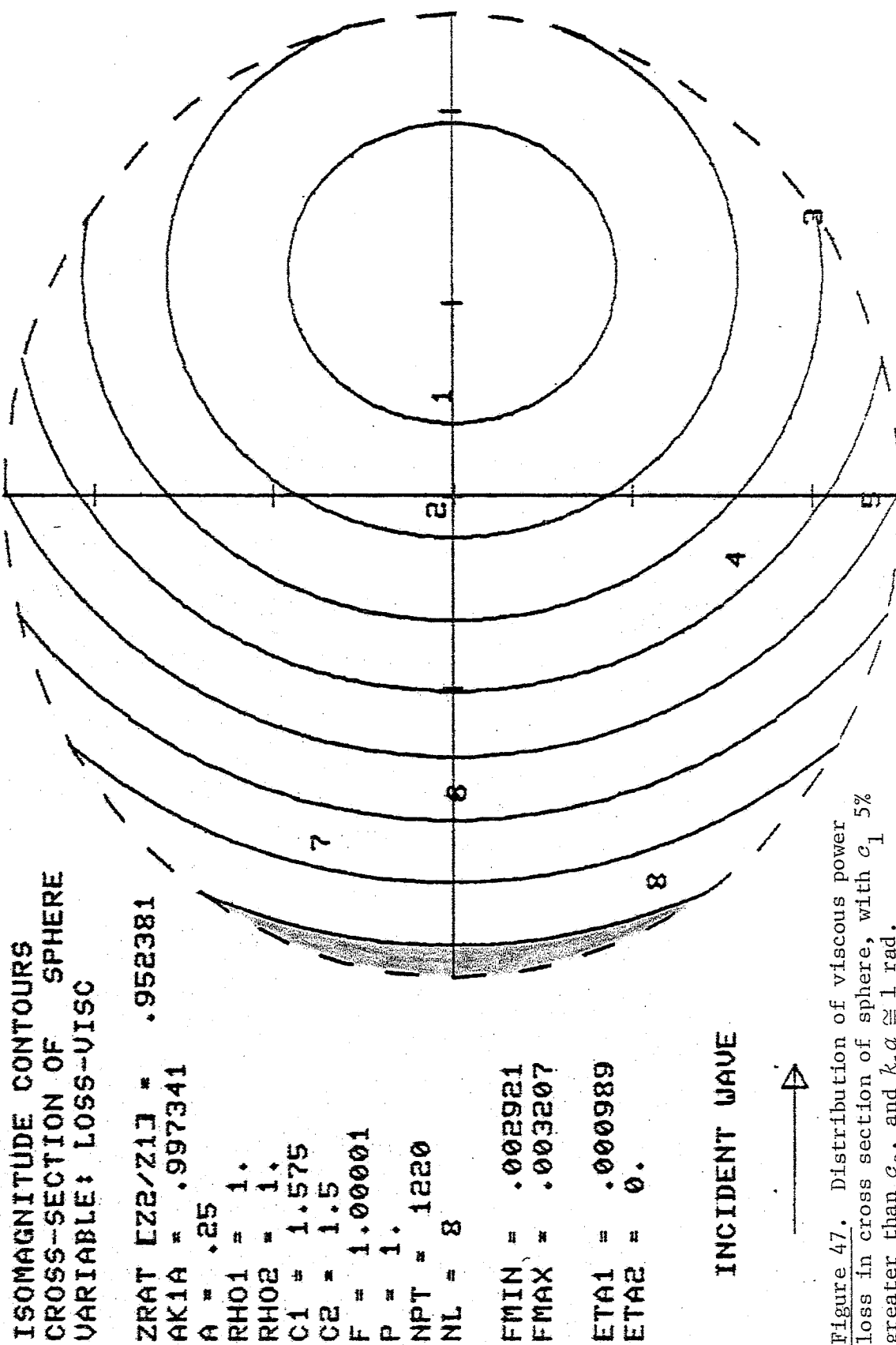


Figure 47. Distribution of viscous power loss in cross section of sphere, with c_1 5% greater than c_2 , and $k_1 a \cong 1$ rad.

ISOMAGNITUDE CONTOURS
CROSS-SECTION OF SPHERE
VARIABLE: LOSS-ABS

ZRAT [Z2/Z1] = .952381
AK1A = .997341
A = .25
RH01 = 1.
RH02 = 1.
C1 = 1.575
C2 = 1.5
F = 1.00001
P = 1.
NPT = 1411
NL = 8

FMIN = .003141
FMAX = .003271
ALF1 = .005
ALF2 = 0.

INCIDENT WAVE

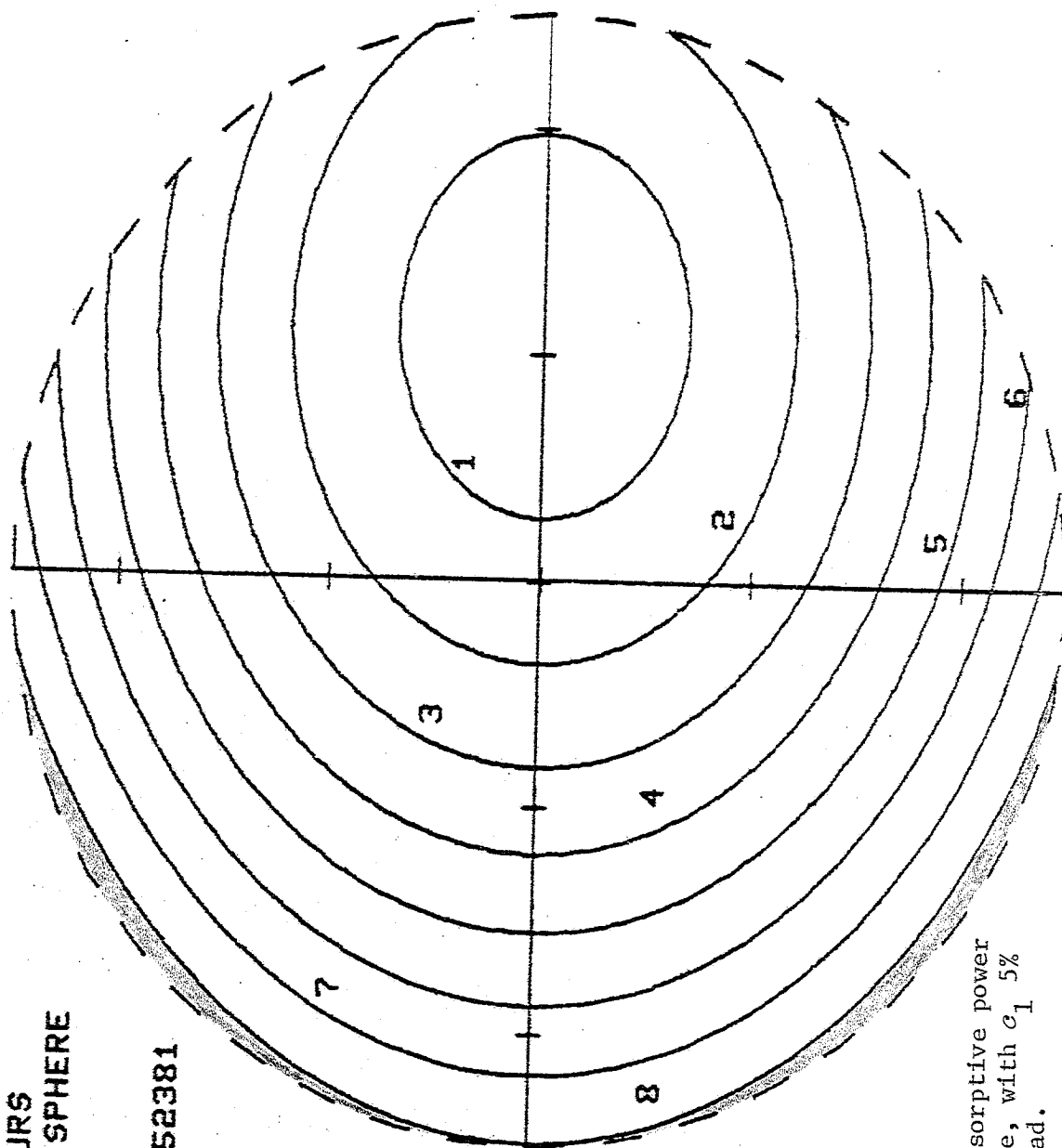


Figure 48. Distribution of absorptive power loss in cross section of sphere, with α_1 5% greater than α_2 , and $k_1 \alpha \cong 1$ rad.

ISO-MAGNITUDE CONTOURS
CROSS-SECTION OF CYLINDER
VARIABLE: LOSS-VISC

ZRAT [Z2/Z1] = .952381

AK1A = 1.99466

A = .5

RHO1 = 1.

RHO2 = 1.

C1 = 1.575

C2 = 1.5

F = 1.

P = 1.

NPT = 704

NL = 6

FMIN = .002582

FMAX = .003429

ETA1 = .000989

ETA2 = 0.

INCIDENT WAVE

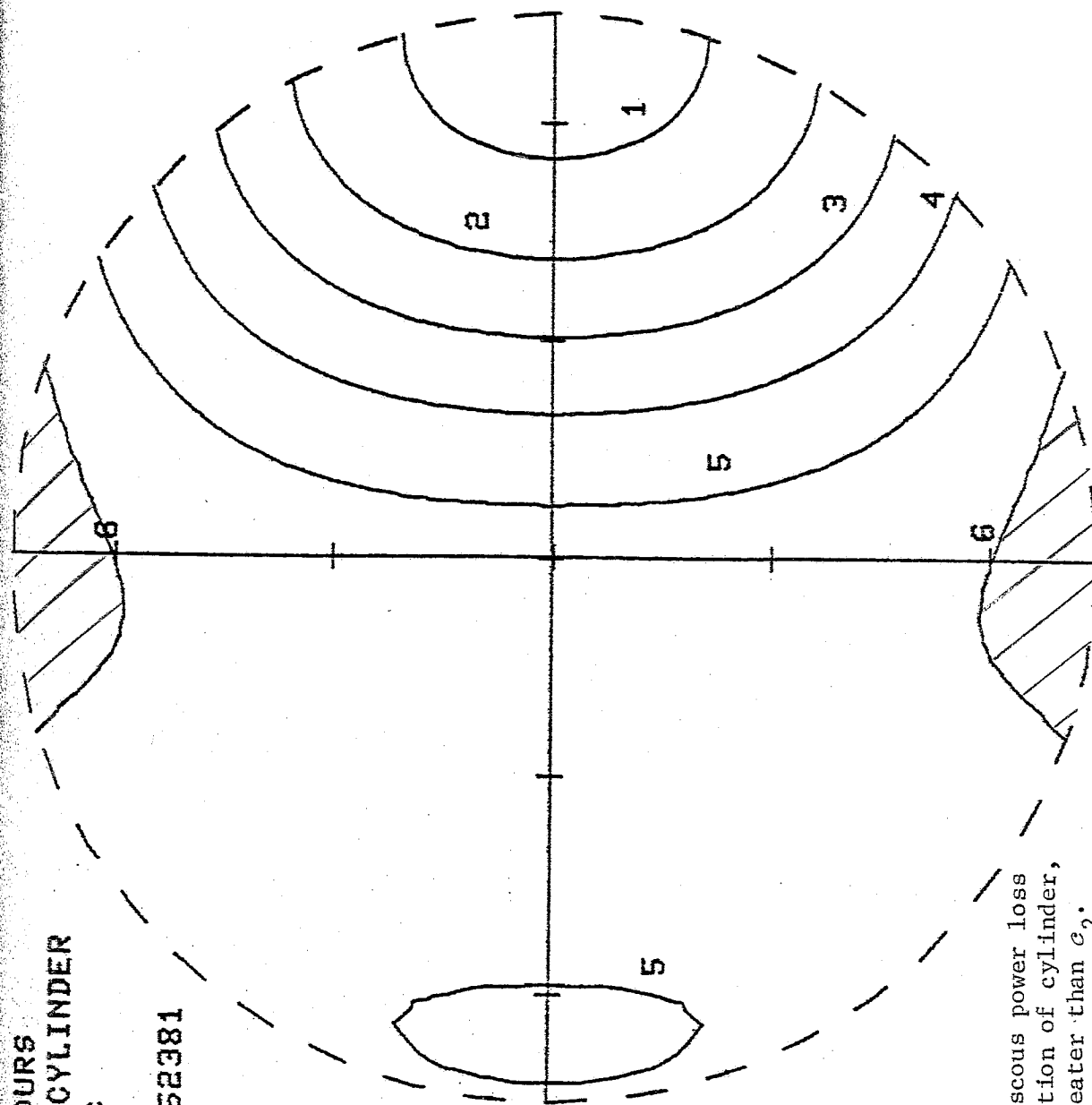


Figure 49. Distribution of viscous power loss (per unit volume) in cross section of cylinder, with $k_1 a \approx 2$ rad, and c_1 5% greater than c_2 .

ISO-MAGNITUDE CONTOURS
CROSS-SECTION OF CYLINDER
VARIABLE: LOSS-VISC

ZRAT [Z2/Z1] = .952381

AK1A = 3.98932

A = 1.

RHO1 = 1.

RHO2 = 1.

C1 = 1.575

C2 = 1.5

F = 1.

P = 1.

NPT = 1049

NL = 6

FMIN = .002422

FMAX = .003529

ETA1 = .000989

ETA2 = 0.

INCIDENT WAVE

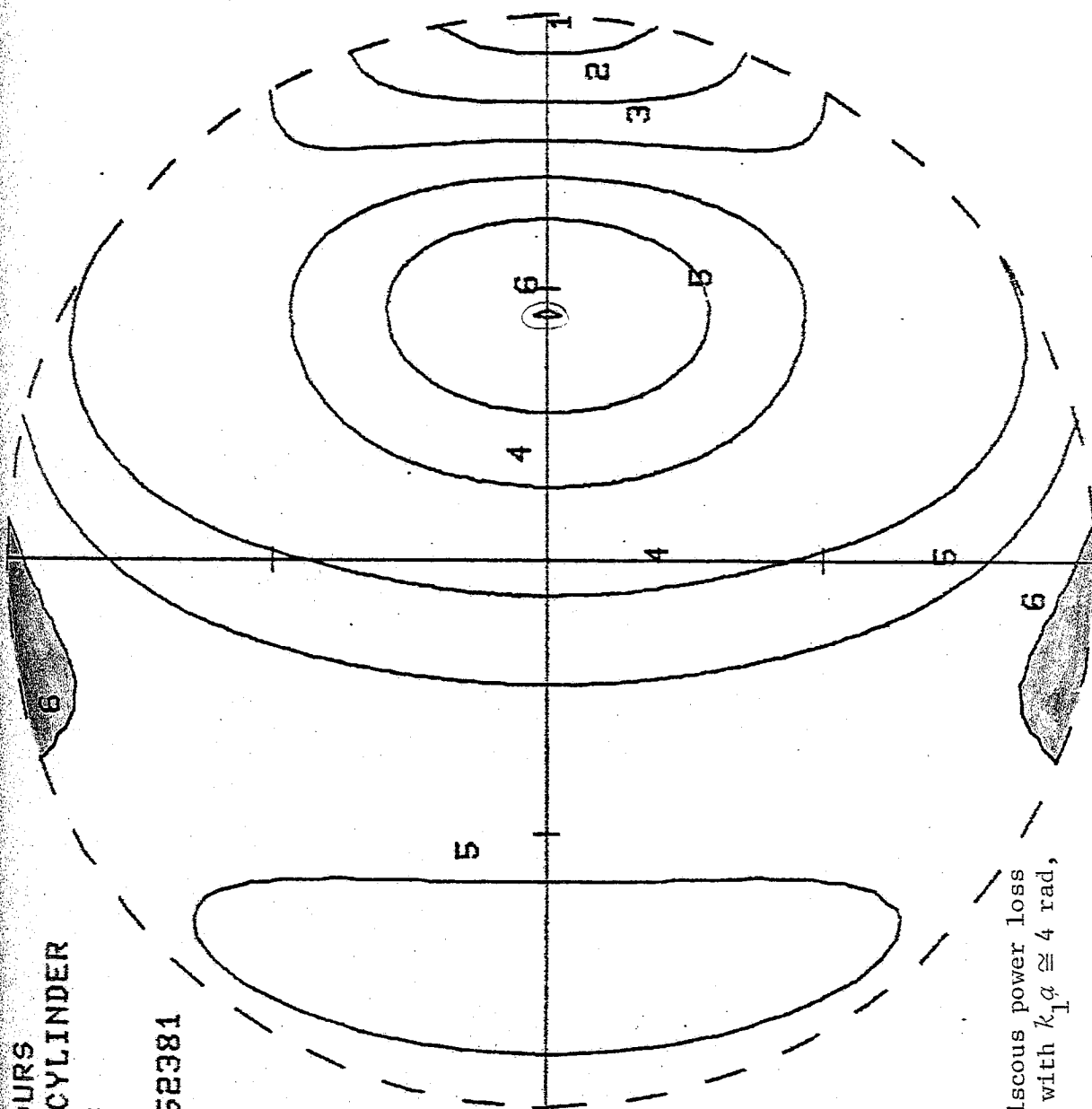


Figure 50. Distribution of viscous power loss in cross section of cylinder, with $k_1 a \cong 4$ rad, and α_1 5% greater than α_2 .

ISO-MAGNITUDE CONTOURS
CROSS-SECTION OF CYLINDER
VARIABLE: LOSS-VISC

ZRAT CZ2/Z11 = .952381

AK1A = 9.97331

A = 2.5

RH01 = 1.

RH02 = 1.

C1 = 1.575

C2 = 1.5

F = 1.

P = 1.

NPT = 1262

NL = 4

FMIN = .00225

FMAX = .003718

ETA1 = .000989

ETA2 = 0.

INCIDENT WAVE

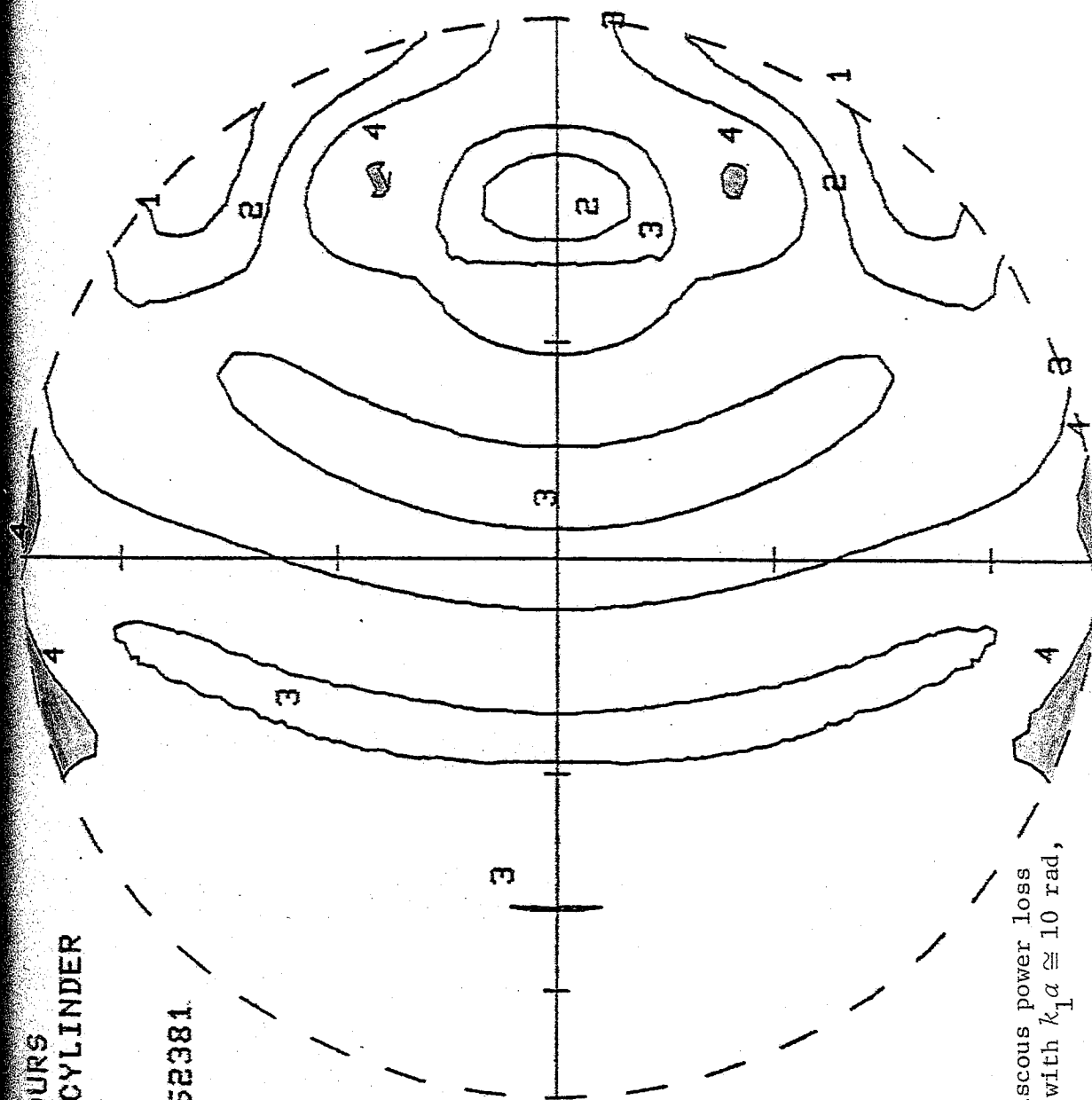


Figure 51. Distribution of viscous power loss in cross section of cylinder, with $k_1 a \approx 10$ rad, and c_1 5% greater than c_2 .

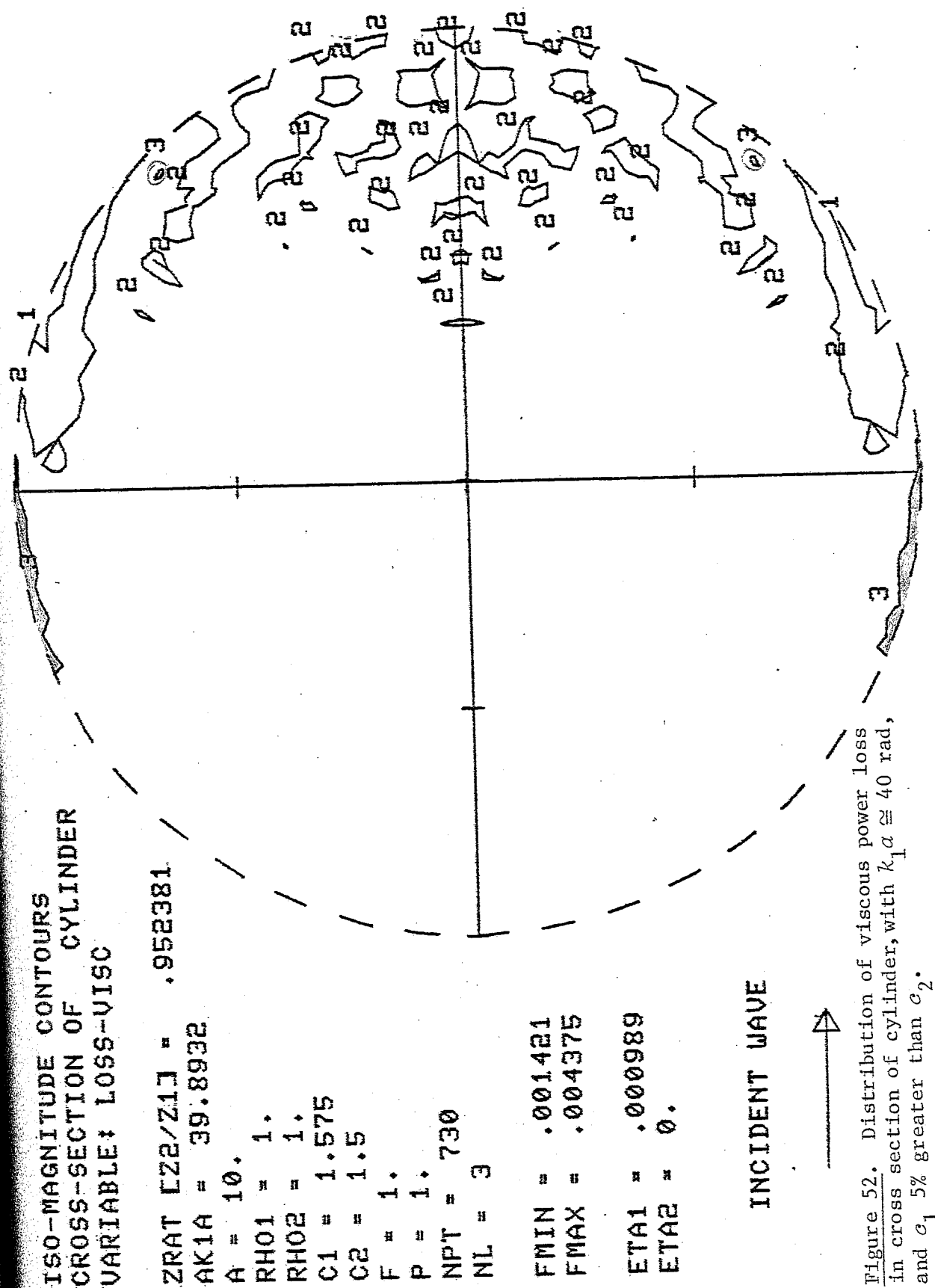


Figure 52. Distribution of viscous power loss in cross section of cylinder, with $k_1 a \approx 40$ rad, and c_1 5% greater than c_2 .

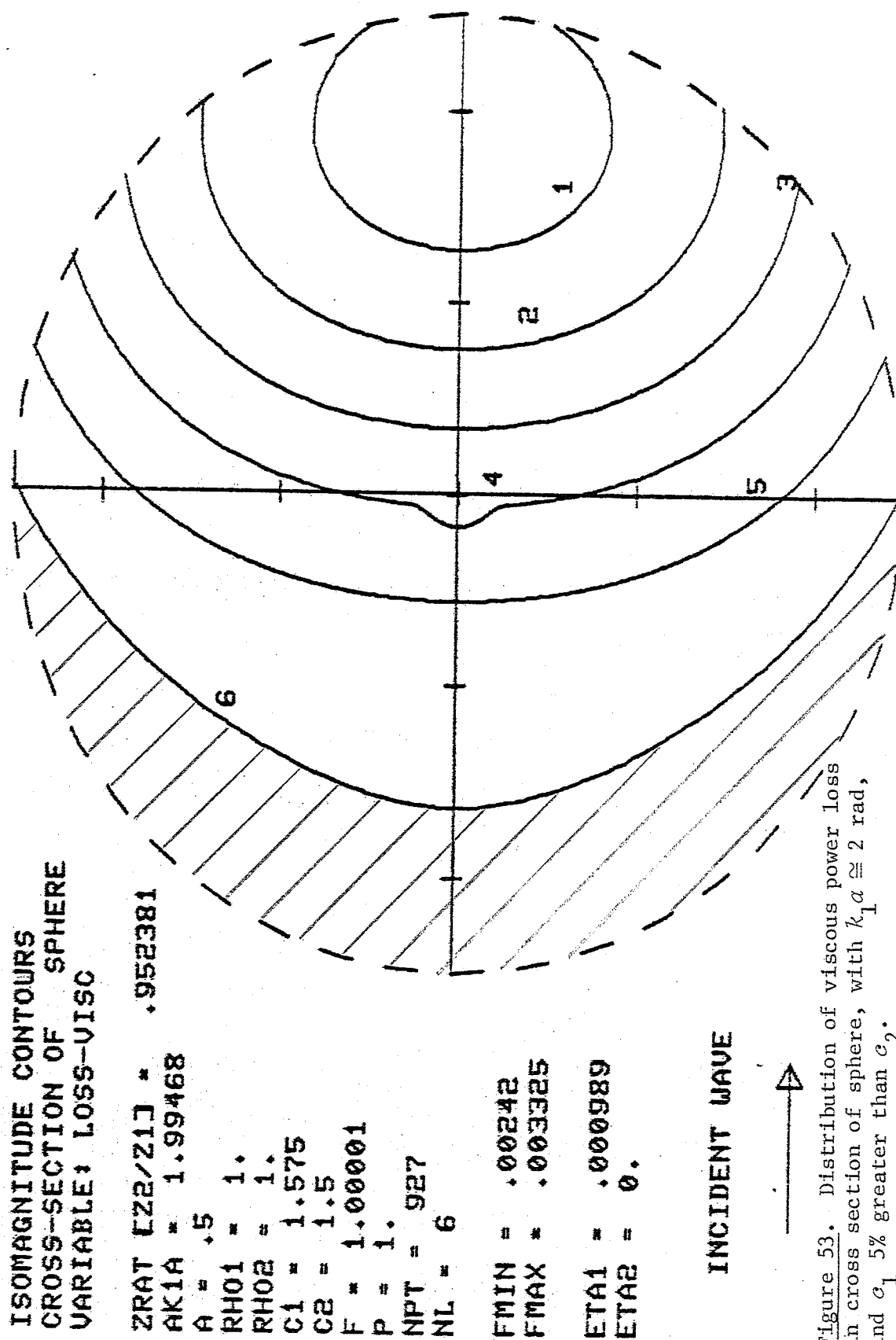


Figure 53. Distribution of viscous power loss in cross section of sphere, with $k_1 a \cong 2$ rad, and c_1 5% greater than c_2 .

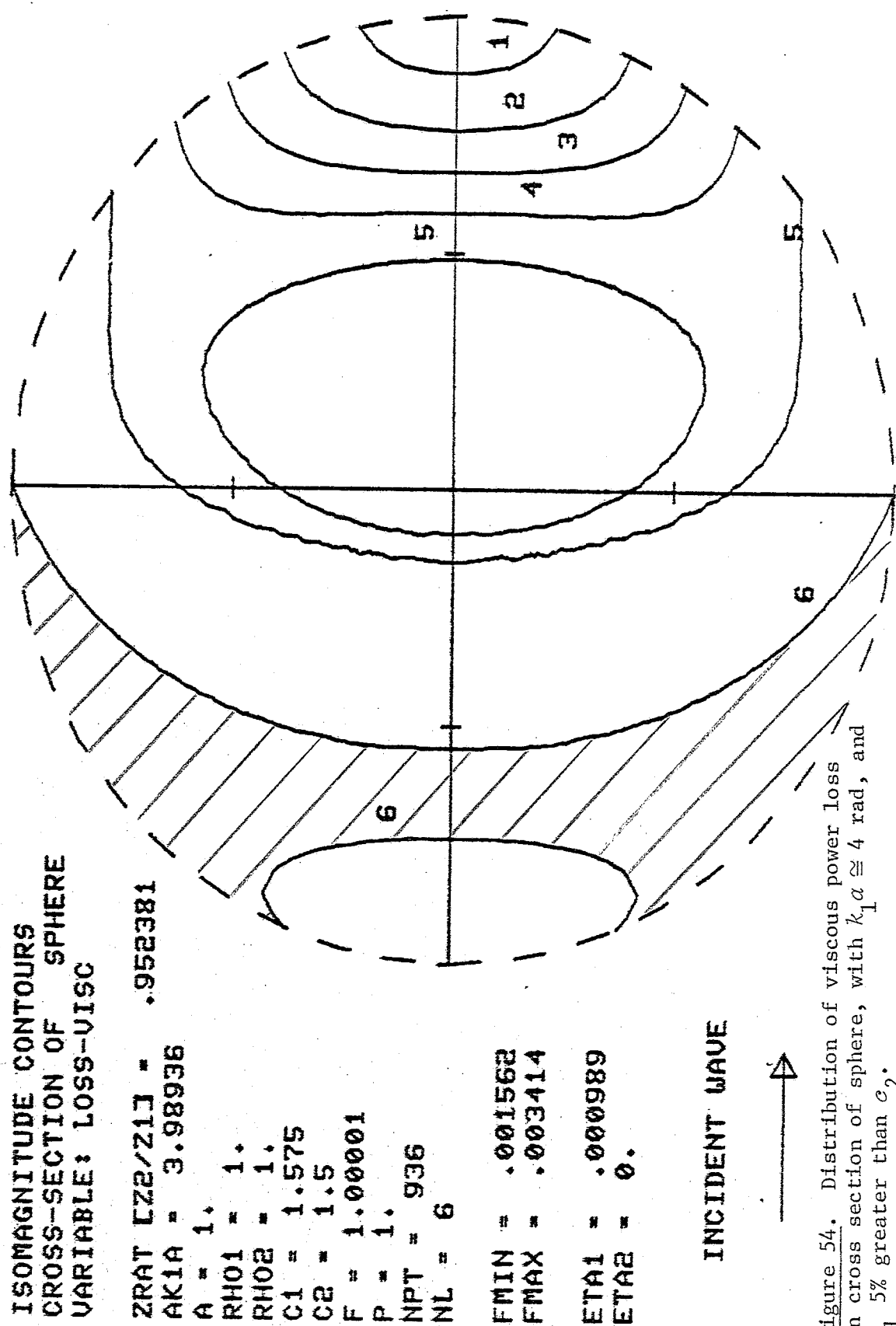


Figure 54. Distribution of viscous power loss in cross section of sphere, with $k_1 a \cong 4$ rad, and c_1 5% greater than c_2 .

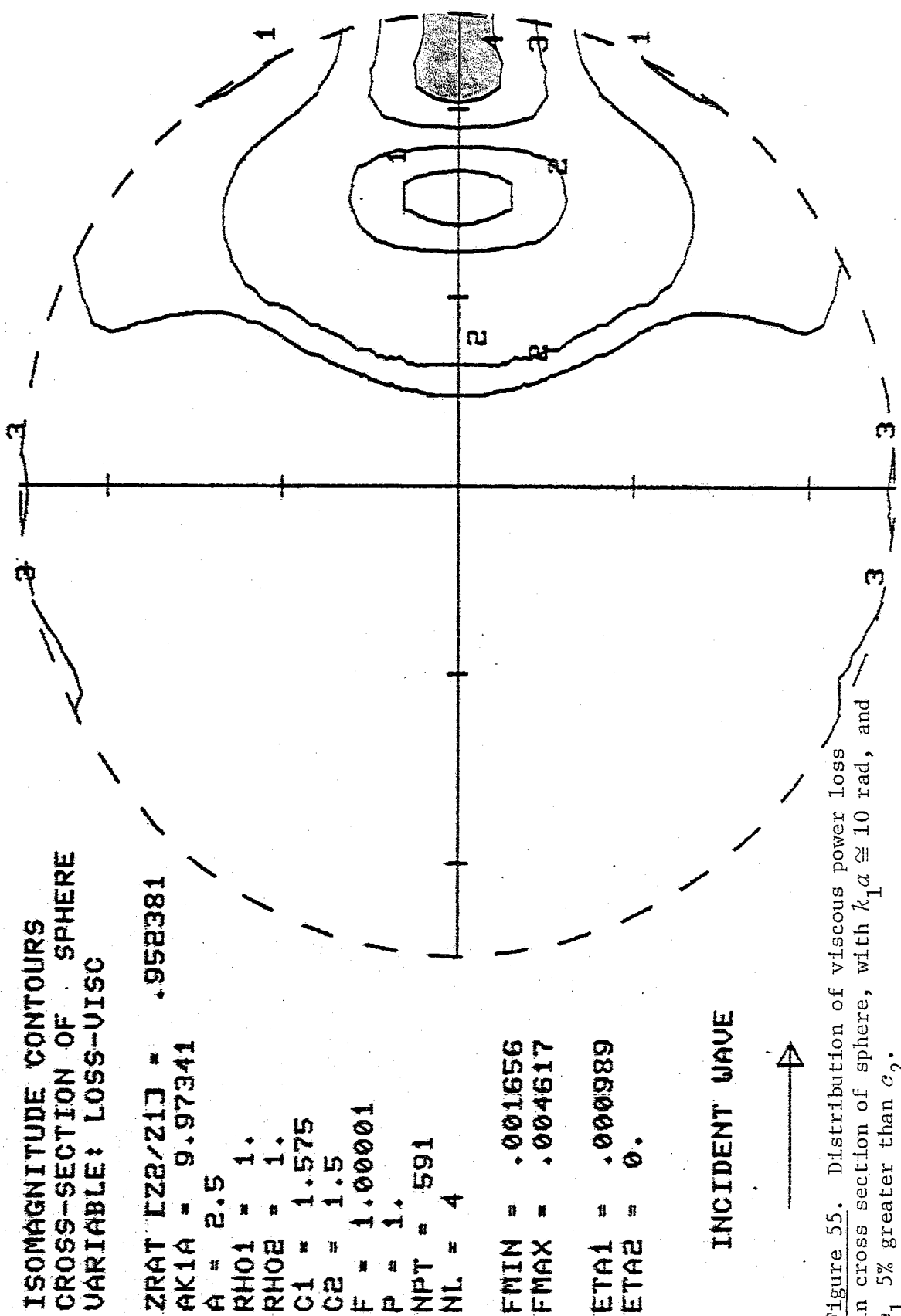


Figure 55. Distribution of viscous power loss in cross section of sphere, with $k_1 a \approx 10$ rad, and c_1 5% greater than c_2 .

ISOMAGNITUDE CONTOURS
CROSS-SECTION OF SPHERE
VARIABLE: LOSS-VISC

ZRAT [Z2/Z1] = .952381

AK1A = 39.8936

A = 10.

RHO1 = 1.

RHO2 = 1.

C1 = 1.575

C2 = 1.5

F = 1.00001

P = 1.

NPT = 343

NL = 3

FMIN = .000362

FMAX = .007536

ETA1 = .000989

ETA2 = 0.

INCIDENT WAVE

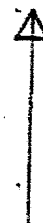


Figure 56. Distribution of viscous power loss in cross section of sphere, with $k_1 a \approx 40$ rad, and c_1 5% greater than c_2 .

ISO-MAGNITUDE CONTOURS
CROSS-SECTION OF CYLINDER
VARIABLE: LOSS-VISC

ZRAT [Z2/Z1] = .833333

AK1A = 8.72665

A = 2.5

RH01 = 1.

RH02 = 1.

C1 = 1.8

C2 = 1.5

F = 1.

P = 1.

NPT = 1439

NL = 4

FMIN = .00067

FMAX = .004529

ETA1 = .001477

ETA2 = 0.

INCIDENT WAVE

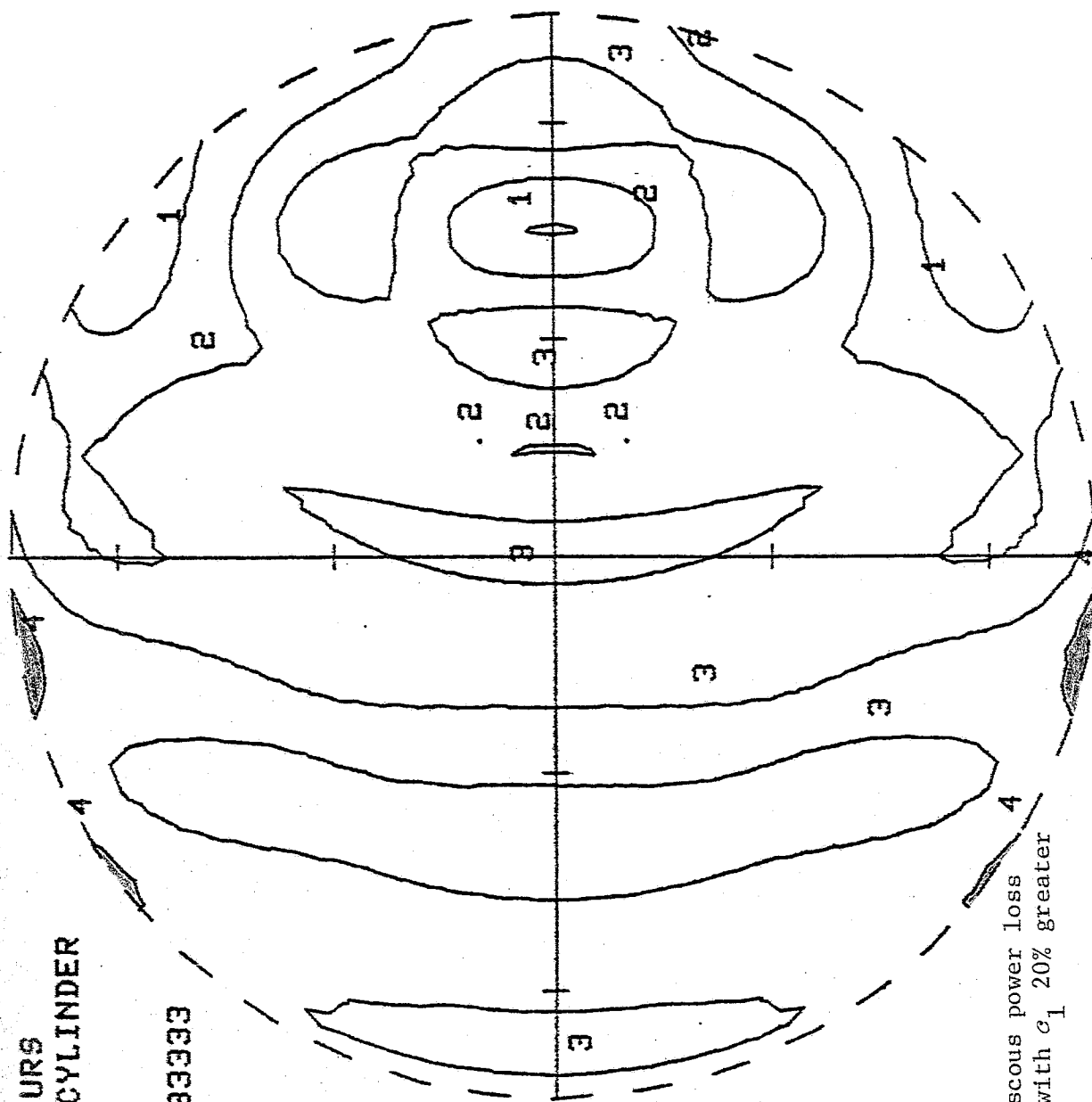


Figure 57. Distribution of viscous power loss in cross section of cylinder, with c_1 20% greater than c_2 , and $k_1 \alpha \approx 10$ rad.

ISO-MAGNITUDE CONTOURS
CROSS-SECTION OF CYLINDER
VARIABLE: LOSS-VISC

ZRAT [Z2/Z1] = 1.05263

AK1A = 11.0231

A = 2.5

RHO1 = 1.

RHO2 = 1.

C1 = 1.425

C2 = 1.5

F = 1.

P = 1.

NPT = 931

NL = 4

FMIN = .002837

FMAX = .004959

ETA1 = .000732

ETA2 = 0.

INCIDENT WAVE

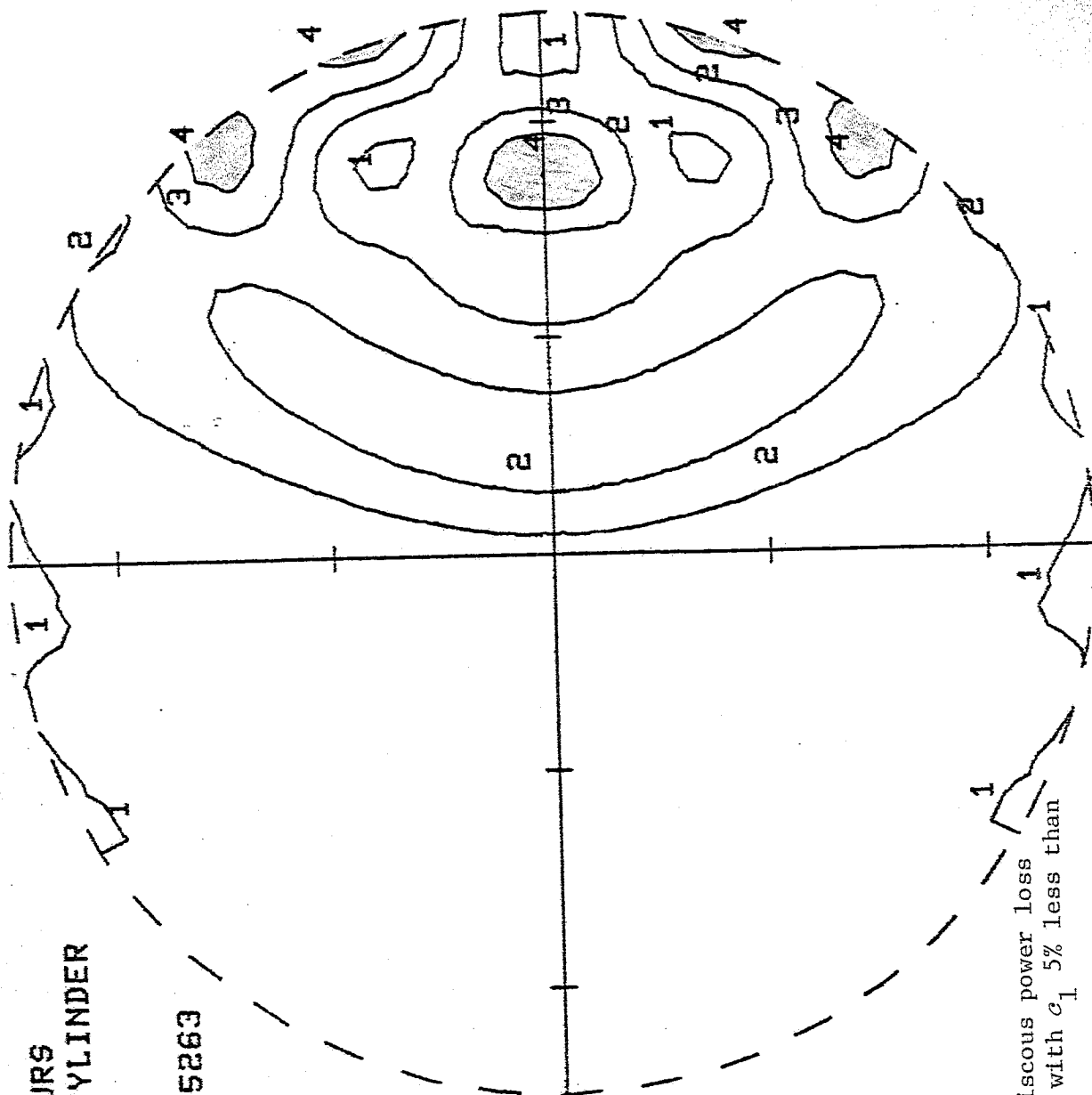


Figure 58. Distribution of viscous power loss in cross section of cylinder, with c_1 5% less than c_2 , and $k_1 \alpha \approx 10$ rad.

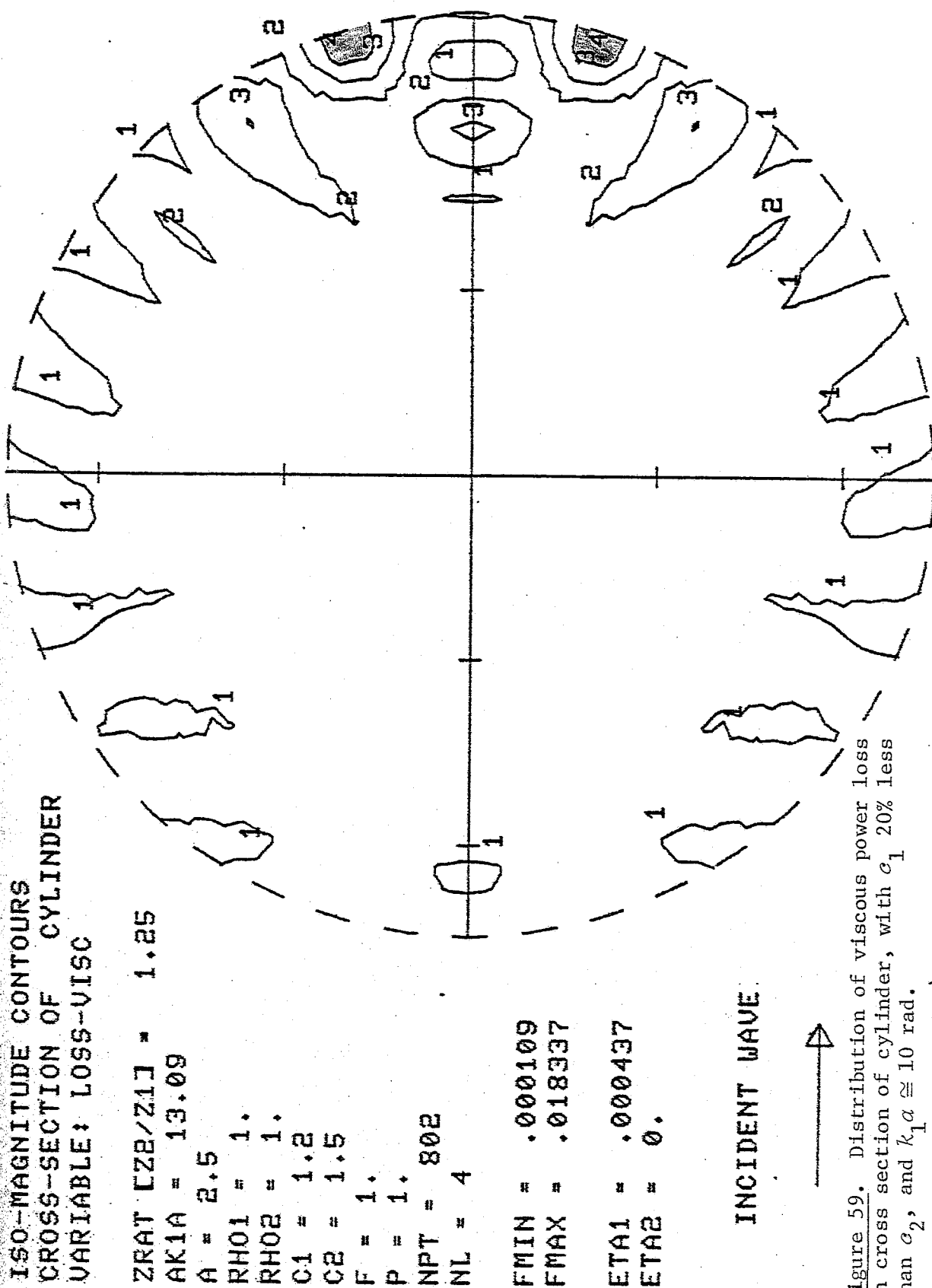


Figure 59. Distribution of viscous power loss in cross section of cylinder, with c_1 20% less than c_2 , and $k_1 a \approx 10$ rad.

ISOMAGNITUDE CONTOURS
CROSS-SECTION OF SPHERE
VARIABLE: LOSS-VISC

ZRAT CZ2/Z11 = .833333

AK1A = 8.72673

A = 2.5

RHO1 = 1.

RHO2 = 1.

C1 = 1.8

C2 = 1.5

F = 1.00001

P = 1.

NPT = 1044

NL = 4

FMIN = .000317

FMAX = .005698

ETA1 = .001477

ETA2 = 0.

INCIDENT WAVE

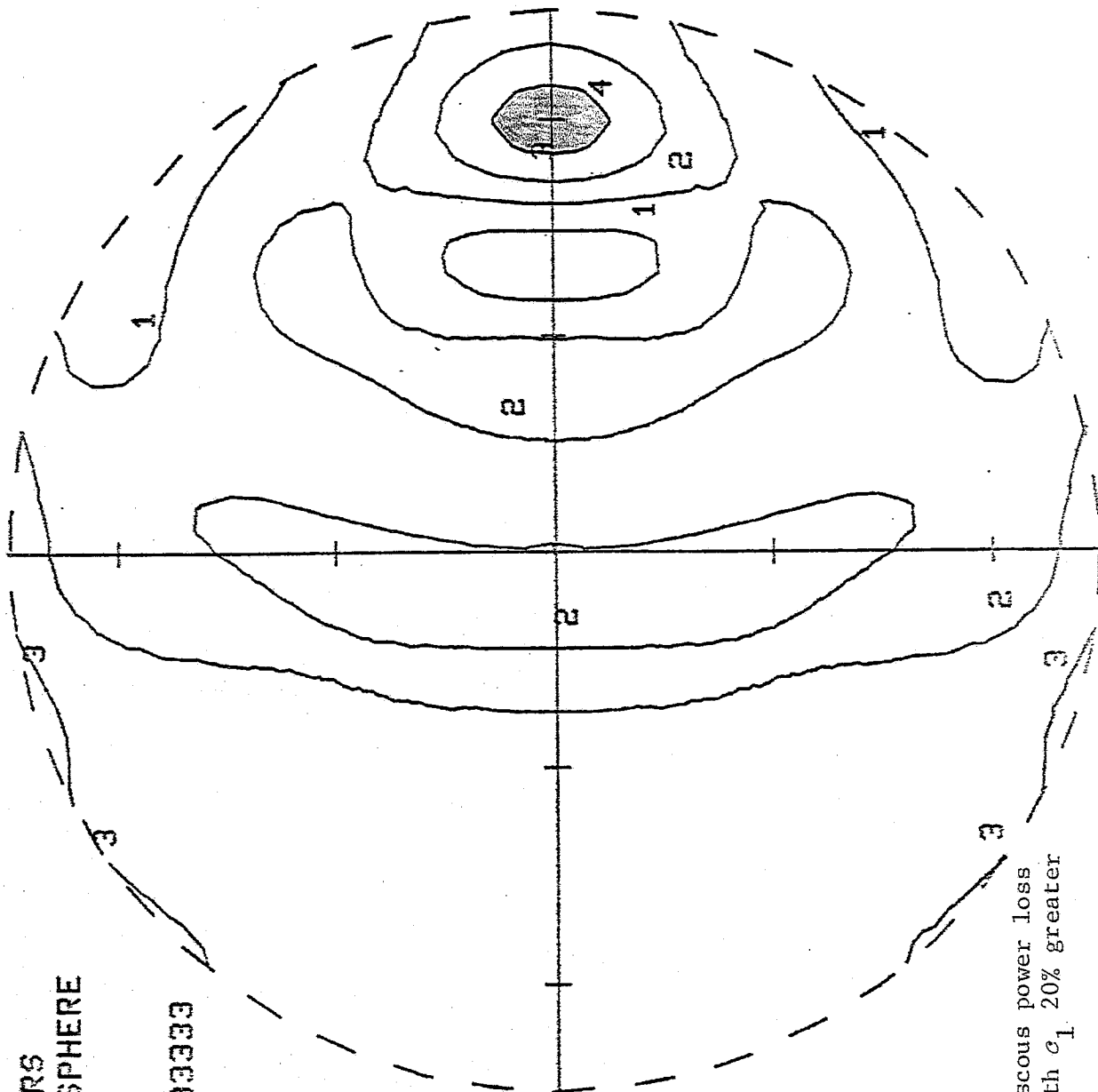


Figure 60. Distribution of viscous power loss in cross section of sphere, with c_1 20% greater than c_2 , and $k_1 a \approx 10$ rad.

ISOMAGNITUDE CONTOURS
CROSS-SECTION OF SPHERE
VARIABLE: LOSS-VISC

ZRAT [Z2/Z1] = 1.05263

AK1A = 11.0232

A = 2.5

RHO1 = 1.

RHO2 = 1.

C1 = 1.425

C2 = 1.5

F = 1.00001

P = 1.

NPT = 415

NL = 4

FMIN = .000998

FMAX = .00688

ETA1 = .000732

ETA2 = 0.

INCIDENT WAVE



Figure 61. Distribution of viscous power loss in cross section of sphere, with σ_1 5% less than σ_2 , and $k_1 a \cong 10$ rad.

ISOMAGNITUDE CONTOURS
CROSS-SECTION OF SPHERE
VARIABLE: LOSS-VISC

ZRAT [Z2/Z1] = 1.25

AK1A = 13.0901

A = 2.5

RHO1 = 1.

RHO2 = 1.

C1 = 1.2

C2 = 1.5

F = 1.00001

P = 1.

NPT = 317

NL = 4

FMIN = .000054

FMAX = .102932

ETA1 = .000437

ETA2 = 0.

INCIDENT WAVE:



Figure 62. Distribution of viscous power loss in cross section of sphere, with c_1 20% less than c_2 , and $k_1 a \approx 10$ rad.

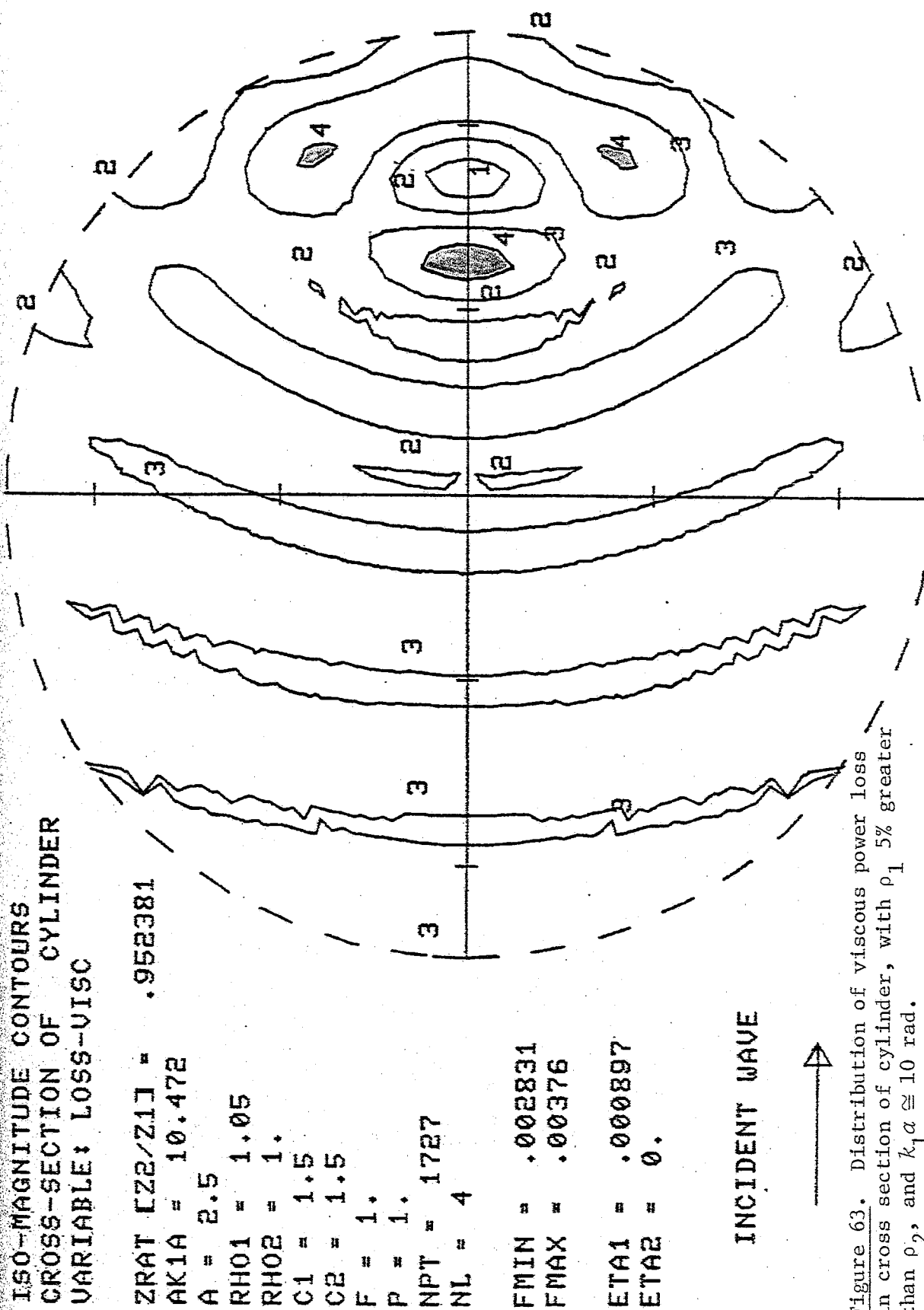


Figure 63. Distribution of viscous power loss in cross section of cylinder, with ρ_1 5% greater than ρ_2 , and $k_1 \alpha \approx 10$ rad.

ISO-MAGNITUDE CONTOURS
CROSS-SECTION OF CYLINDER
VARIABLE: LOSS-VISC

ZRAT LZ2/Z1] = .833333

AK1A = 10.472

A = 2.5

RHO1 = 1.2

RHO2 = 1.

C1 = 1.5

C2 = 1.5

F = 1.

P = 1.

NPT = 1906

NL = 4

FMIN = .001686

FMAX = .00503

ETA1 = .001025

ETA2 = 0.

INCIDENT WAVE

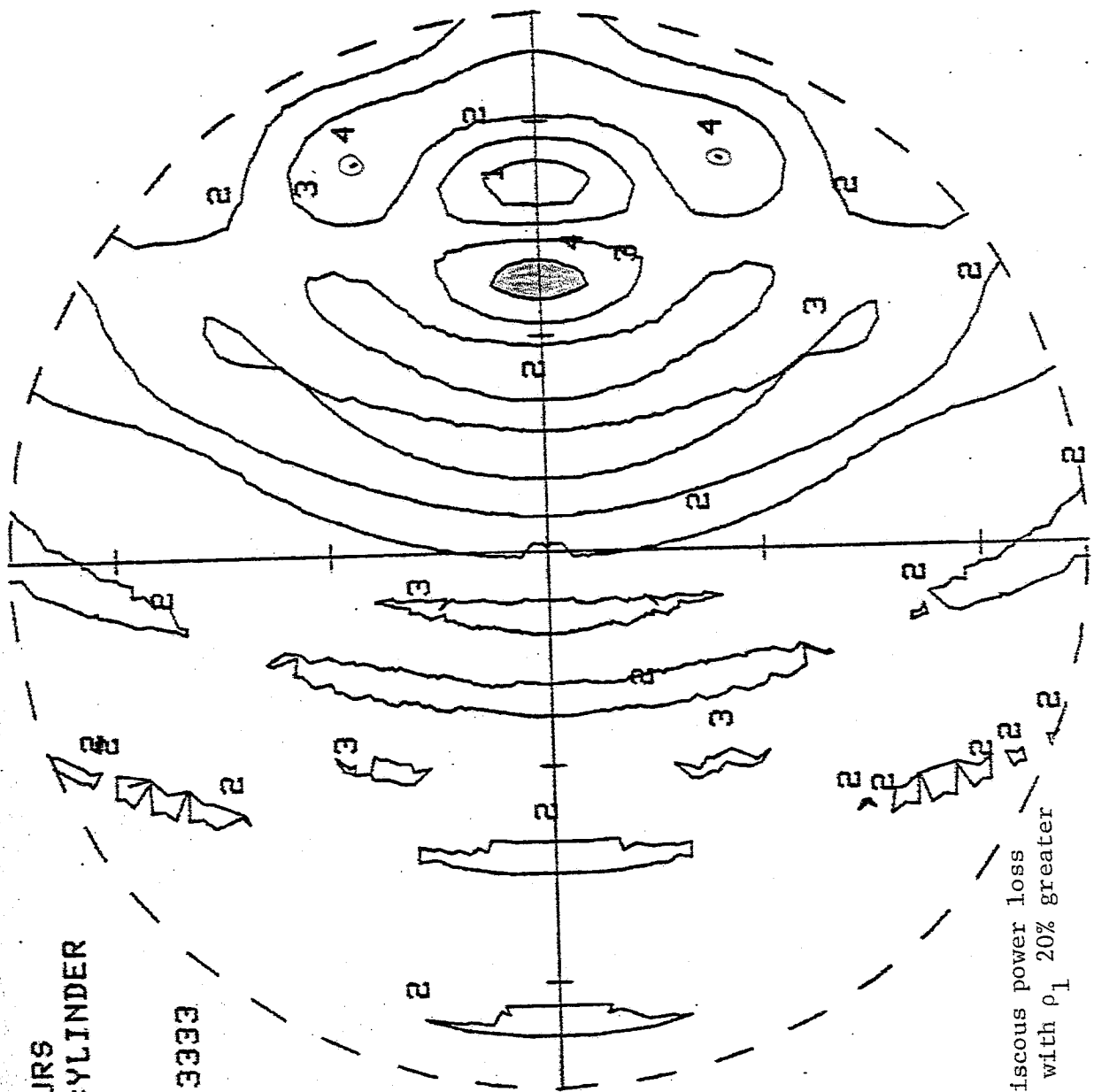


Figure 64. Distribution of viscous power loss in cross section of cylinder, with ρ_1 20% greater than ρ_2 , and $k_1 a \approx 10$ rad.

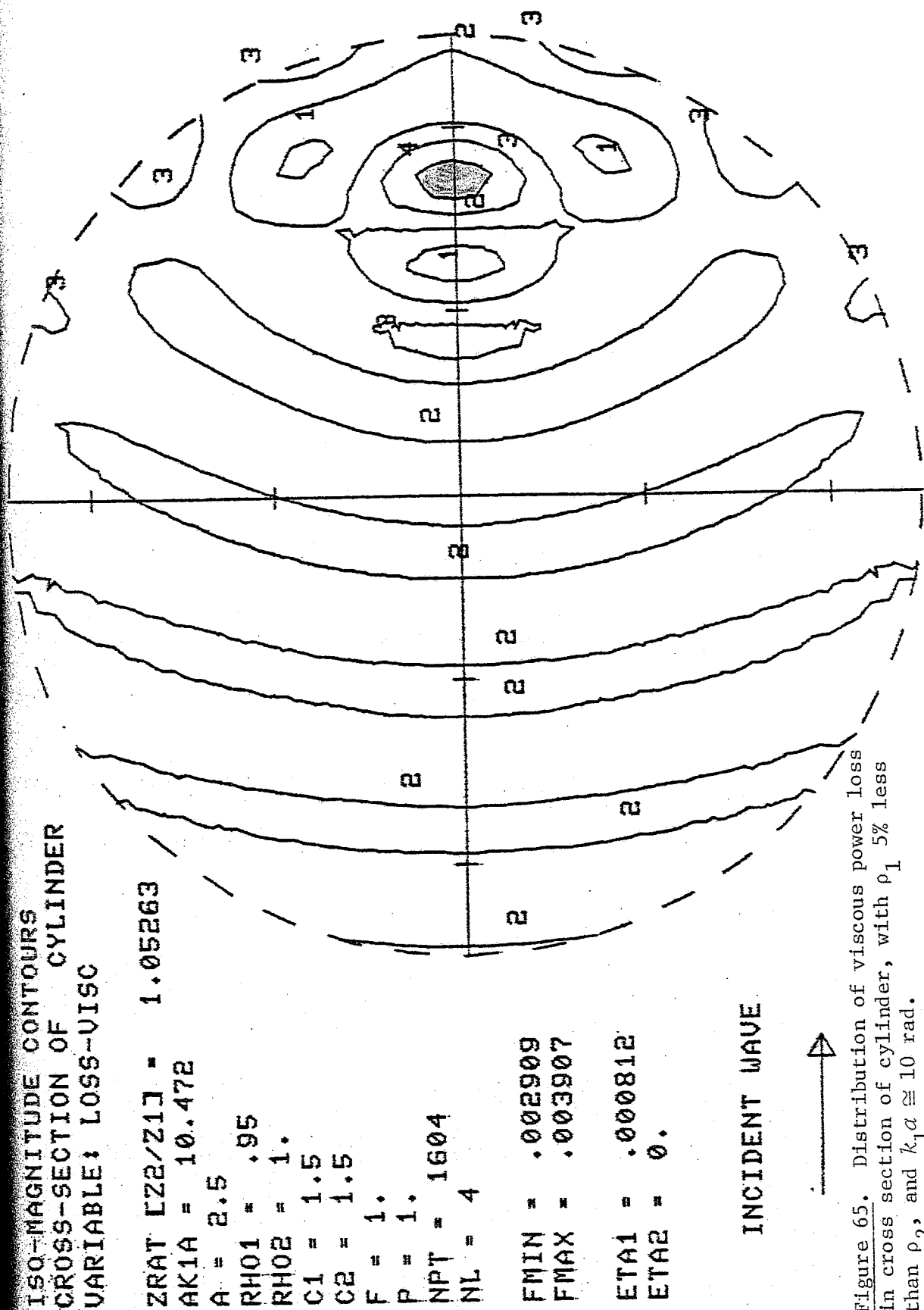


Figure 65. Distribution of viscous power loss in cross section of cylinder, with ρ_1 5% less than ρ_2 , and $k_1 a \approx 10$ rad.

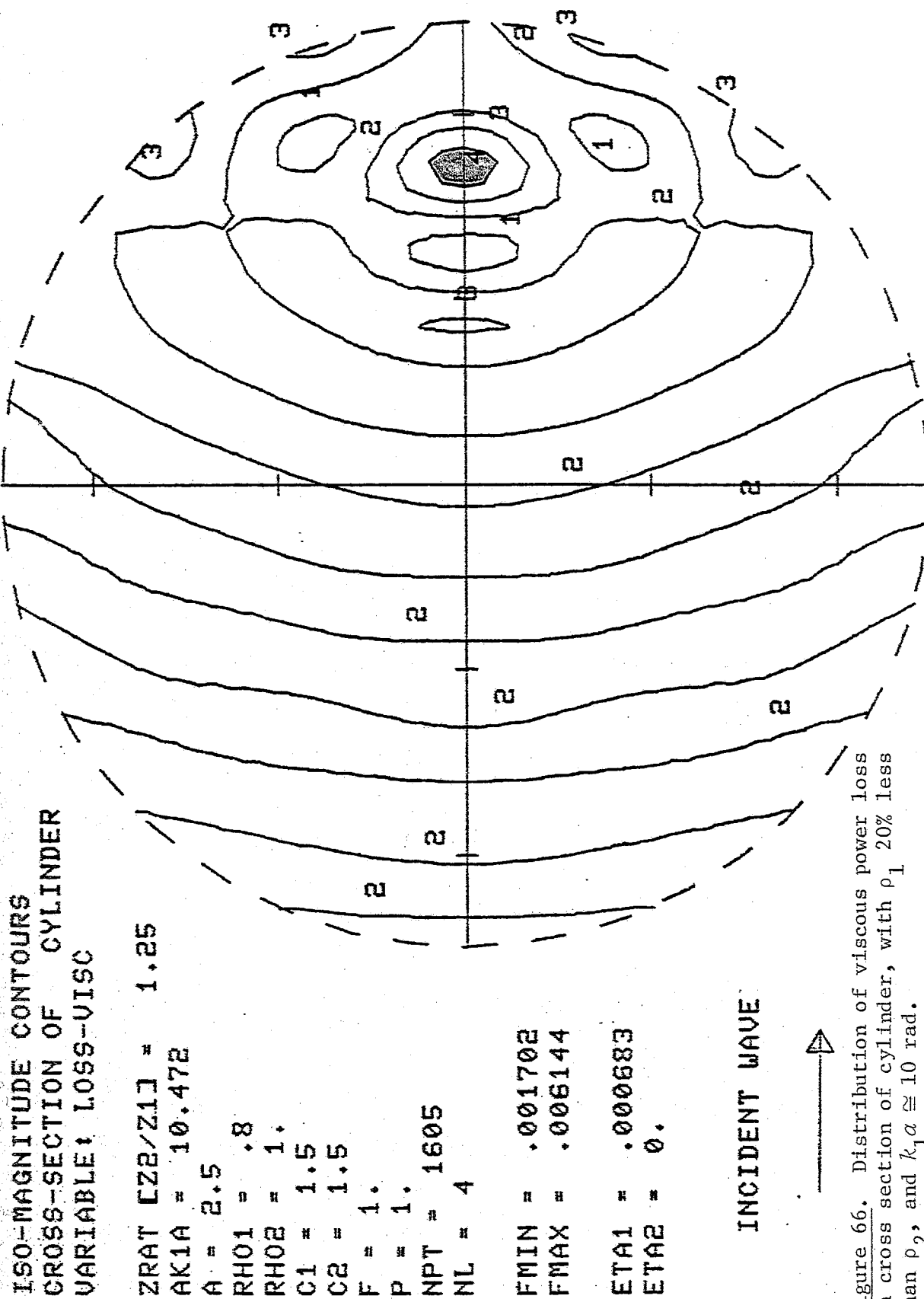


Figure 66. Distribution of viscous power loss in cross section of cylinder, with ρ_1 20% less than ρ_2 , and $k_1 \alpha \approx 10$ rad.

ISOMAGNITUDE CONTOURS
CROSS-SECTION OF SPHERE
VARIABLE: LOSS-VISC

ZRAT CZ2/Z17 = .952381

AK1A = 10.4721

A = 2.5

RHO1 = 1.05

RHO2 = 1.

C1 = 1.5

C2 = 1.5

F = 1.00001

P = 1.

NPT = 569

NL = 4

FMIN = .002246

FMAX = .004261

ETA1 = .000897

ETA2 = 0.

INCIDENT WAVE

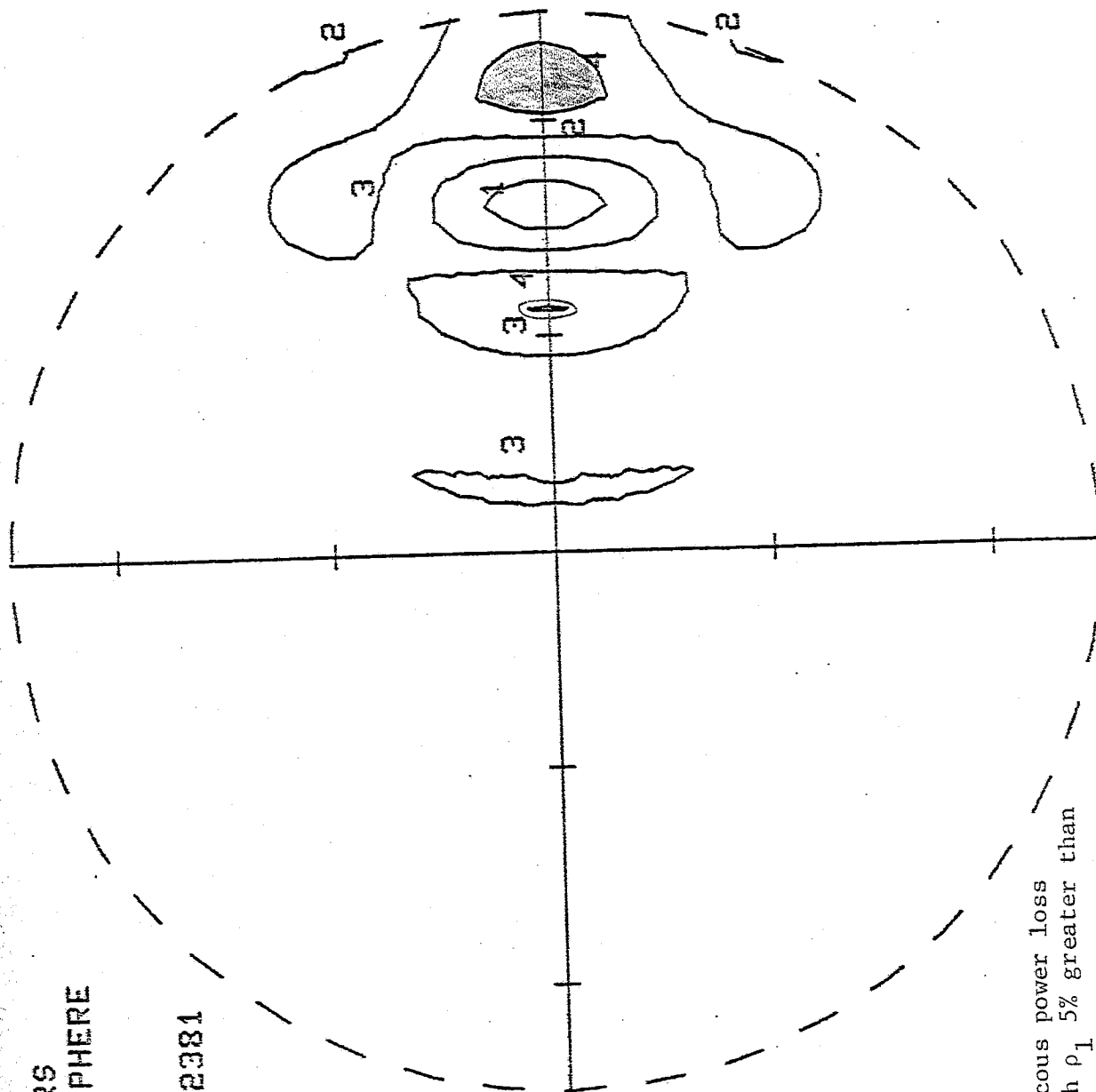


Figure 67. Distribution of viscous power loss in cross section of sphere, with ρ_1 5% greater than ρ_2 , and $k_1 a \approx 10$ rad.

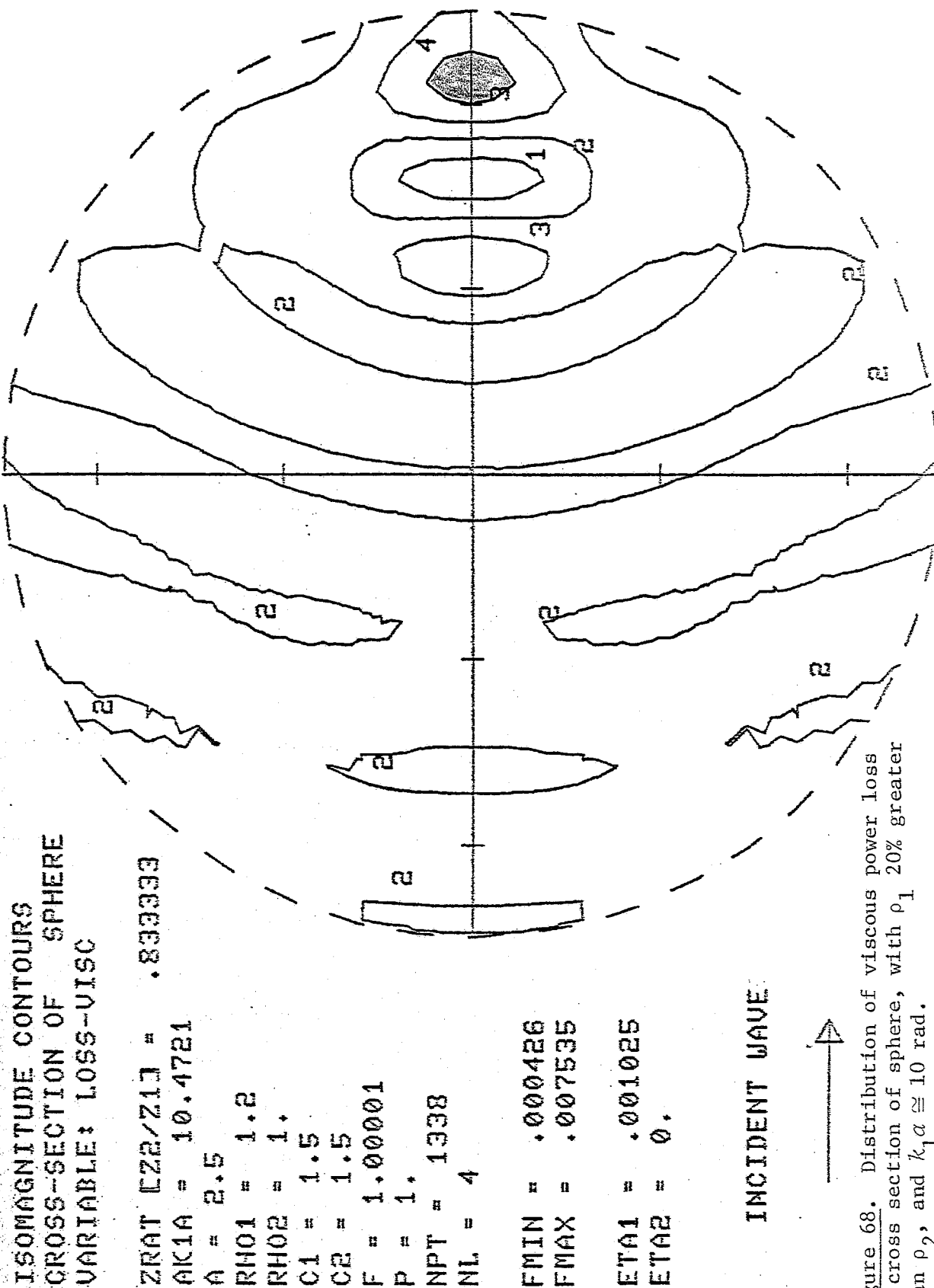


Figure 68. Distribution of viscous power loss in cross section of sphere, with ρ_1 20% greater than ρ_2 , and $k_1 a \approx 10$ rad.

ISOMAGNITUDE CONTOURS
CROSS-SECTION OF SPHERE
VARIABLE: LOSS-VISC

ZRAT LZ2/Z1J = 1.05263

AK1A = 10.4721

A = 2.5

RHO1 = .95

RHO2 = 1.

C1 = 1.5

C2 = 1.5

F = 1.00001

P = 1.

NPT = 1432

NL = 4

FMIN = .002507

FMAX = .004716

ETA1 = .000812

ETA2 = 0.

INCIDENT WAVE

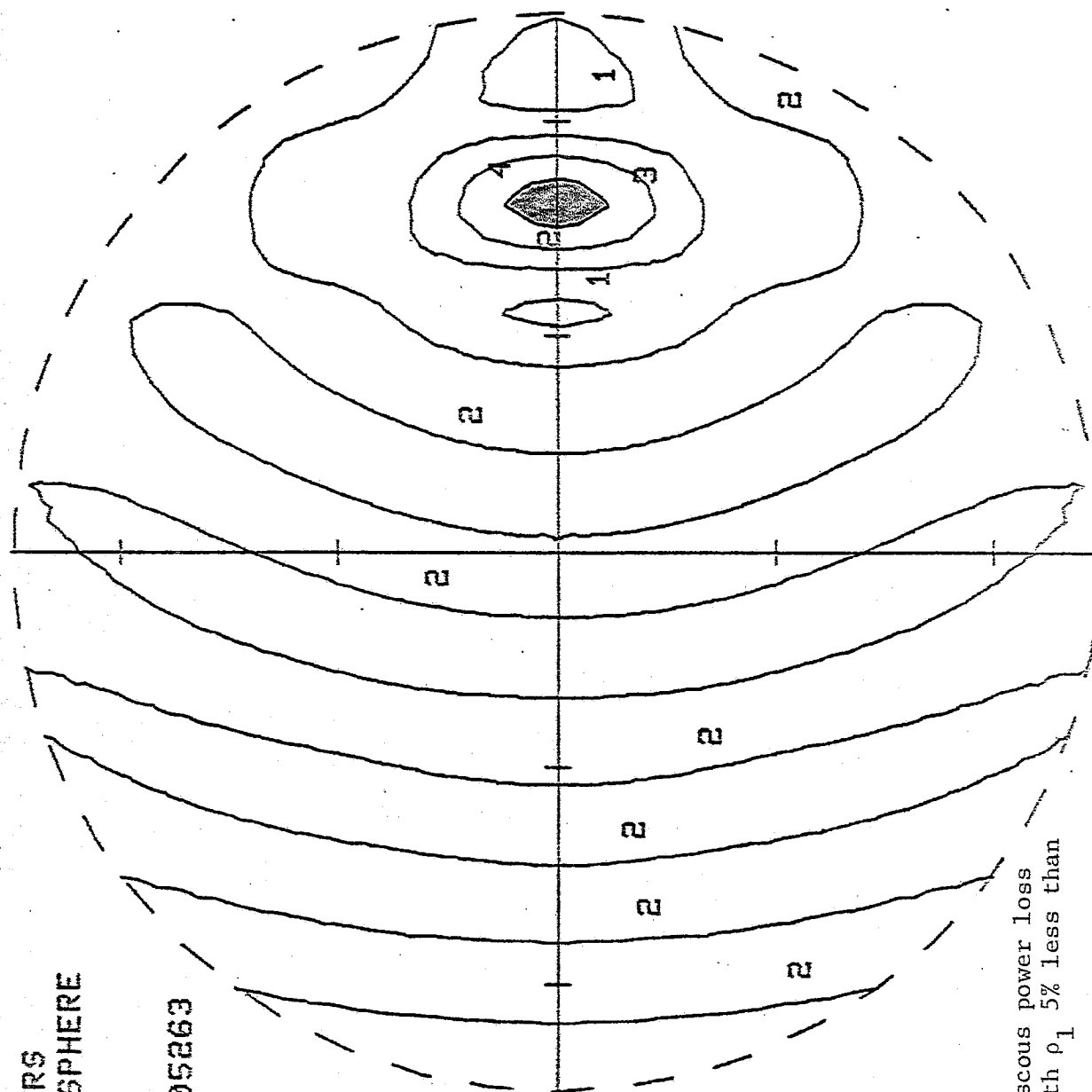


Figure 69. Distribution of viscous power loss in cross section of sphere, with ρ_1 5% less than ρ_2 , and $k_1 a \cong 10$ rad.

ISOMAGNITUDE CONTOURS
CROSS-SECTION OF SPHERE
VARIABLE: LOSS-VISC

ZRAT Z_{22}/Z_{11} = 1.25

AK1A = 10.4721

A = 2.5

RH01 = .8

RH02 = 1.

C1 = 1.5

C2 = 1.5

F = 1.00001

P = 1.

NPT = 436

NL = 4

FMIN = .000618

FMAX = .011018

ETA1 = .000683

ETA2 = 0.

INCIDENT WAVE

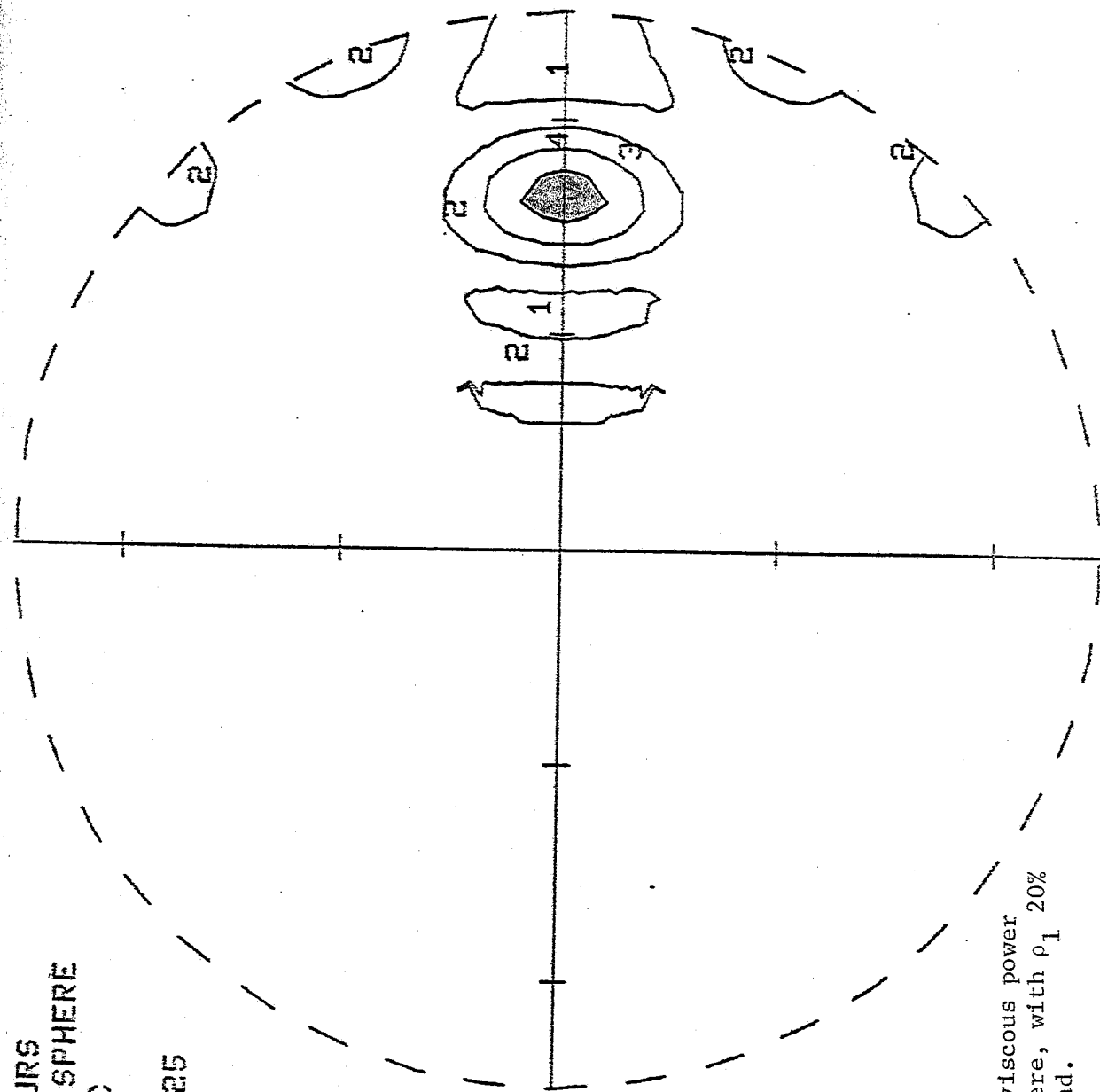


Figure 70. Distribution of viscous power loss in cross section of sphere, with ρ_1 20% less than ρ_2 , and $k_1 a \approx 10$ rad.

ISO-MAGNITUDE CONTOURS
CROSS-SECTION OF CYLINDER
VARIABLE: LOSS-VISC

ZRAT [Z2/Z1] = .951814

AK1A = 10.2166

A = 2.5

RHO1 = 1.025

RHO2 = 1.

C1 = 1.5375

C2 = 1.5

F = 1.

P = 1.

NPT = 1570

NL = 4

FMIN = .002615

FMAX = .003627

ETA1 = .000943

ETA2 = 0.

INCIDENT WAVE

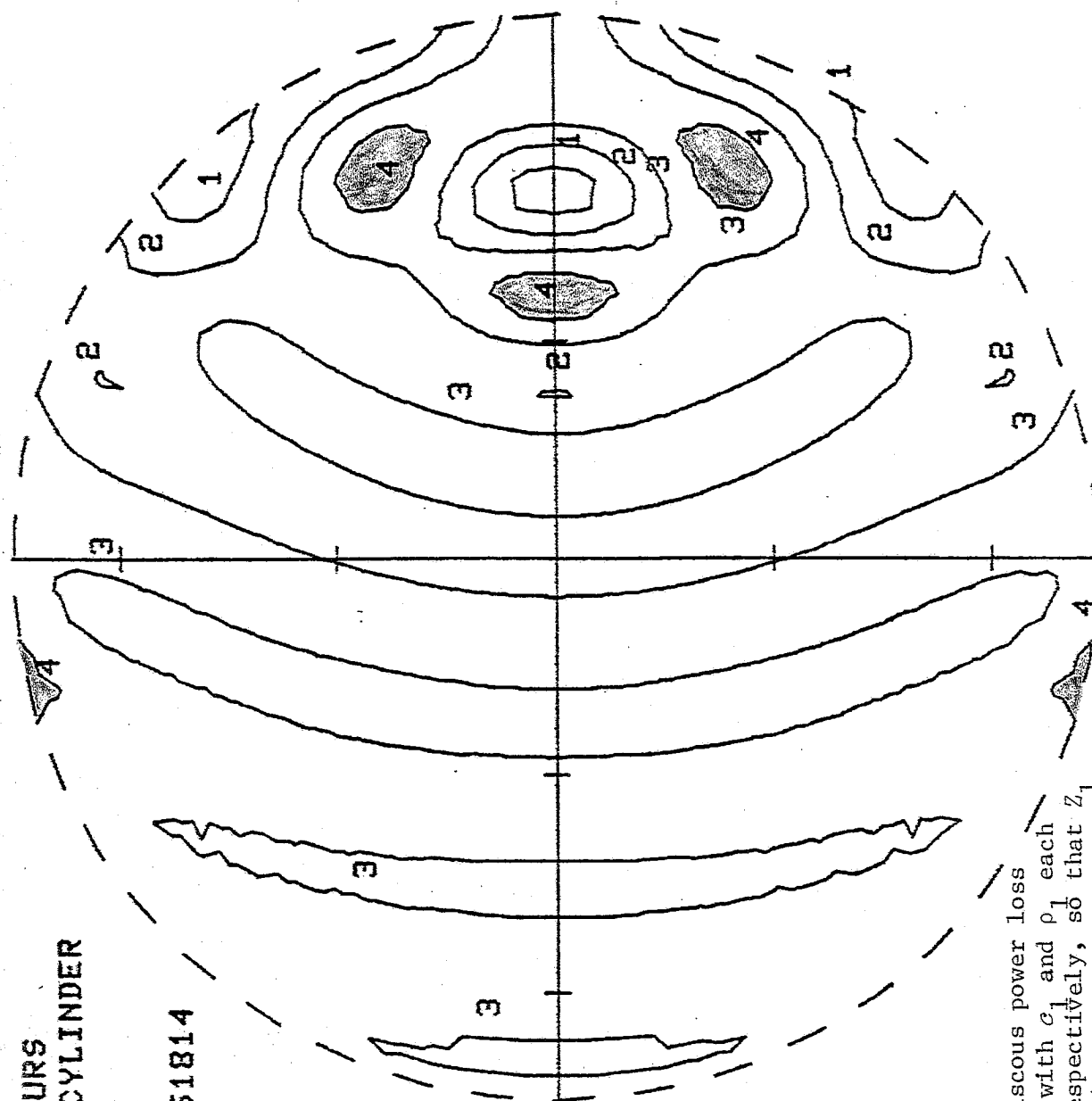


Figure 71. Distribution of viscous power loss in cross section of cylinder, with c_1 and ρ_1 each 2.5% greater than c_2 and ρ_2 respectively, so that Z_1 is 5.1% greater than Z_2 ; also, $k_1 a \approx 10$ rad.

ISO-MAGNITUDE CONTOURS
CROSS-SECTION OF CYLINDER
VARIABLE: LOSS-UIISC

ZRAT [Z2/Z1] = .826446

AK1A = 9.51998

A = 2.5

RH01 = 1.1

RH02 = 1.

C1 = 1.65

C2 = 1.5

F = 1.

P = 1.

NPT = 1679

NL = 4

FMIN = .00117

FMAX = .004311

ETA1 = .001251

ETA2 = 0.

INCIDENT WAVE

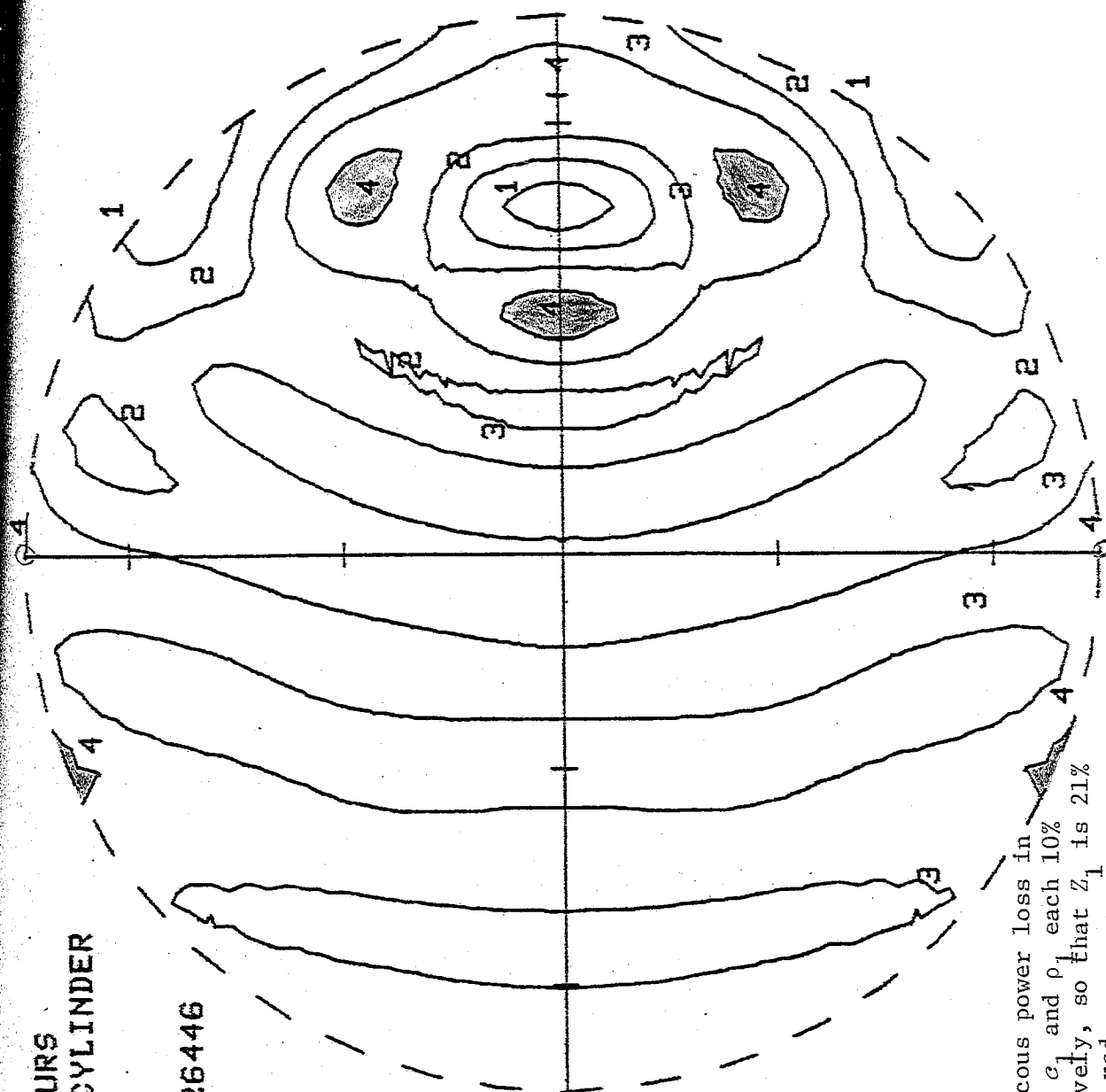


Figure 72. Distribution of viscous power loss in cross section of cylinder, with c_1 and ρ_1 each 10% greater than c_2 and ρ_2 respectively, so that Z_1 is 21% greater than Z_2 ; also, $k_1 \alpha \approx 10$ rad.

ISO-MAGNITUDE CONTOURS
CROSS-SECTION OF CYLINDER
VARIABLE: LOSS-VISC

ZRAT CZ2/Z1 = 1.05194

AK1A = 10.7405

A = 2.5

RHO1 = .975

RHO2 = 1.

C1 = 1.4625

C2 = 1.5

F = 1.

P = 1.

NPT = 1401

NL = 4

FMIN = .002998

FMAX = .00426

ETA1 = .000772

ETA2 = 0.

INCIDENT WAVE

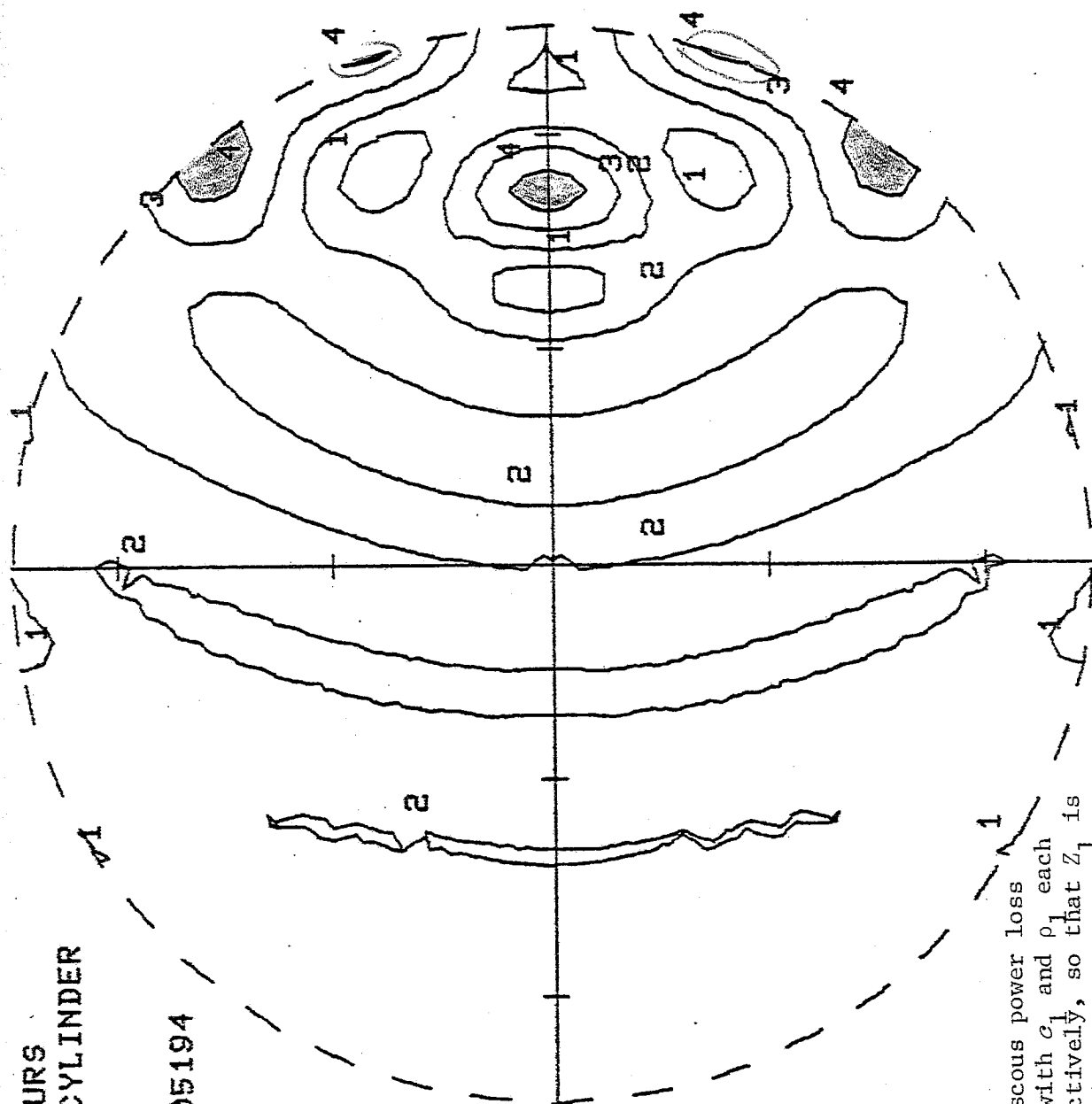


Figure 73. Distribution of viscous power loss in cross-section of cylinder, with c_1 and ρ_1 each 2.5% less than c_2 and ρ_2 respectively, so that Z_1 is 5.1% less than Z_2 ; also, $k_1 a \approx 10$ rad.

ISO-MAGNITUDE CONTOURS
CROSS-SECTION OF CYLINDER
VARIABLE: LOSS-VISC

ZRAT [Z2/Z1] = 1.23457

AK1A = 11.6355

A = 2.5

RHO1 = .9

RHO2 = 1.

C1 = 1.35

C2 = 1.5

F = 1.

P = 1.

NPT = 918

NL = 4

FMIN = .001768

FMAX = .009494

ETA1 = .00056

ETA2 = 0.

INCIDENT WAVE

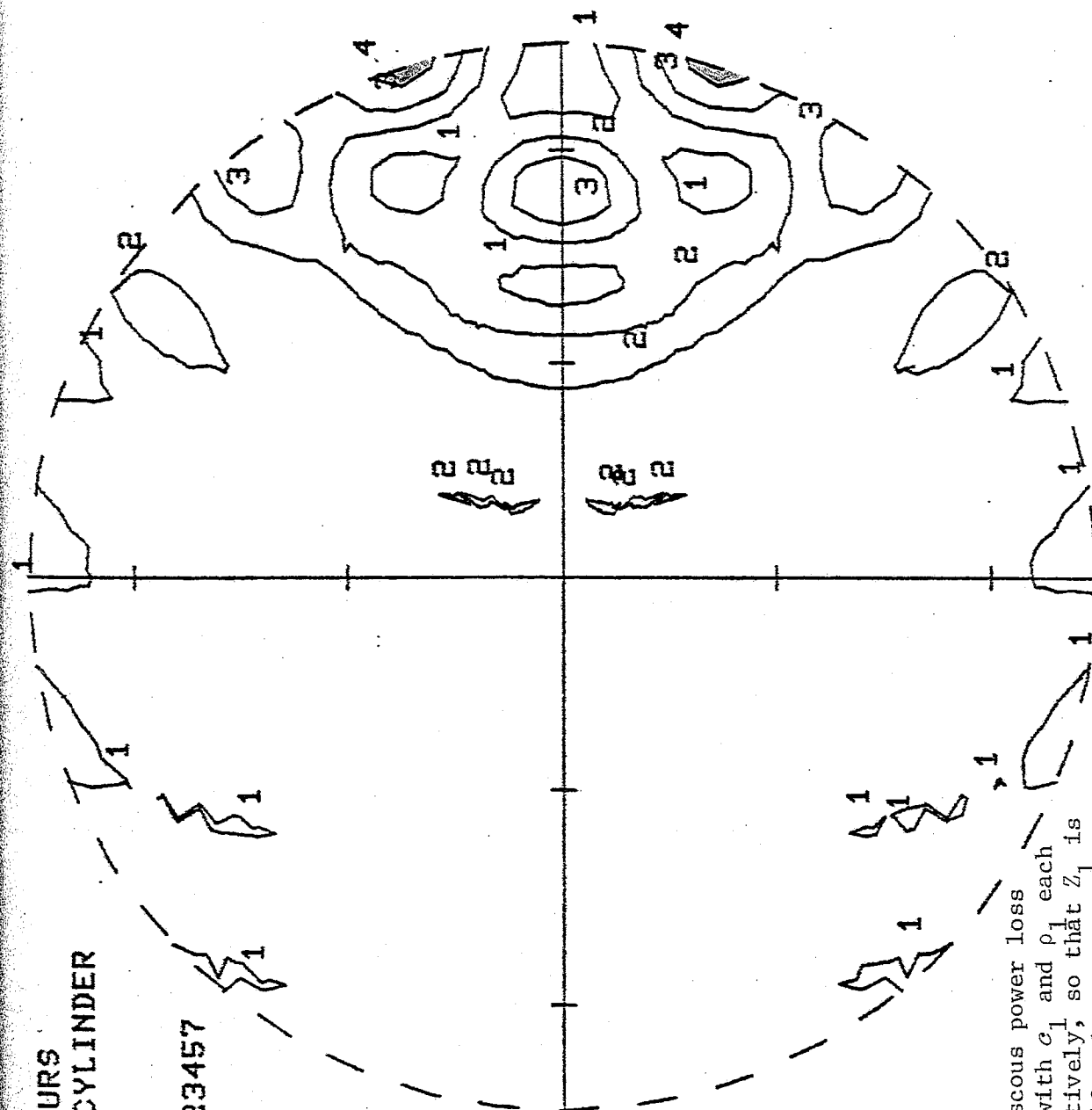


Figure 74. Distribution of viscous power loss in cross section of cylinder, with c_1 and ρ_1 each 10% less than c_2 and ρ_2 respectively, so that Z_1 is 21% less than Z_2 ; also, $k_1 a \approx 10$ rad.

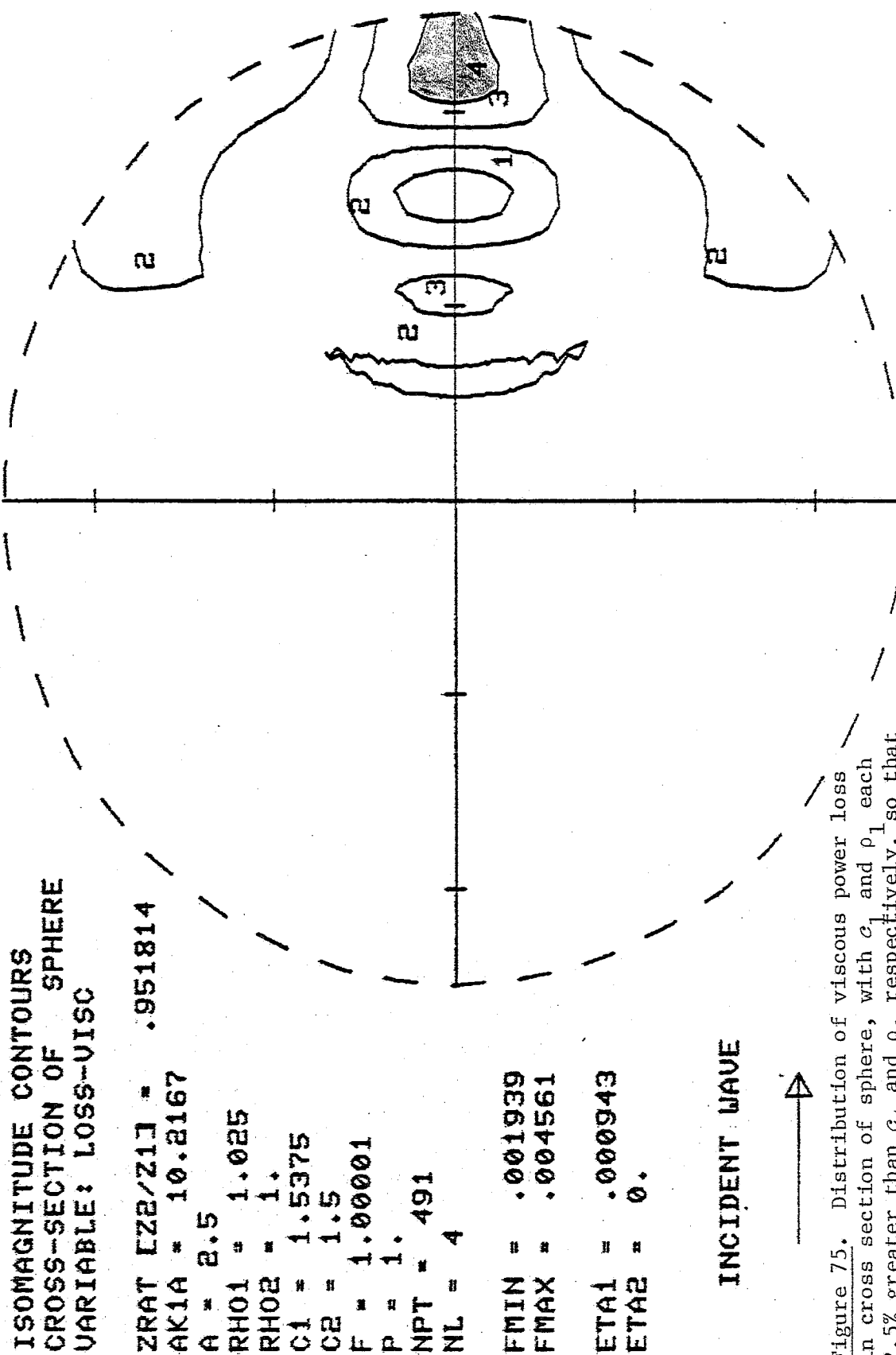


Figure 75. Distribution of viscous power loss in cross section of sphere, with c_1 and ρ_1 each 2.5% greater than c_2 and ρ_2 respectively, so that Z_1 is 5.1% greater than Z_2 ; also, $k_1 a \approx 10$ rad.

ISOMAGNITUDE CONTOURS
CROSS-SECTION OF SPHERE
VARIABLE: LOSS-VISC

ZRAT L22/Z1J = .826446

AK1A = 9.52007

A = 2.5

RHO1 = 1.1

RHO2 = 1.

C1 = 1.65

C2 = 1.5

F = 1.00001

P = 1.

NPT = 1037

NL = 4

FMIN = .000266

FMAX = .00686

ETA1 = .001251

ETA2 = 0.

INCIDENT WAVE

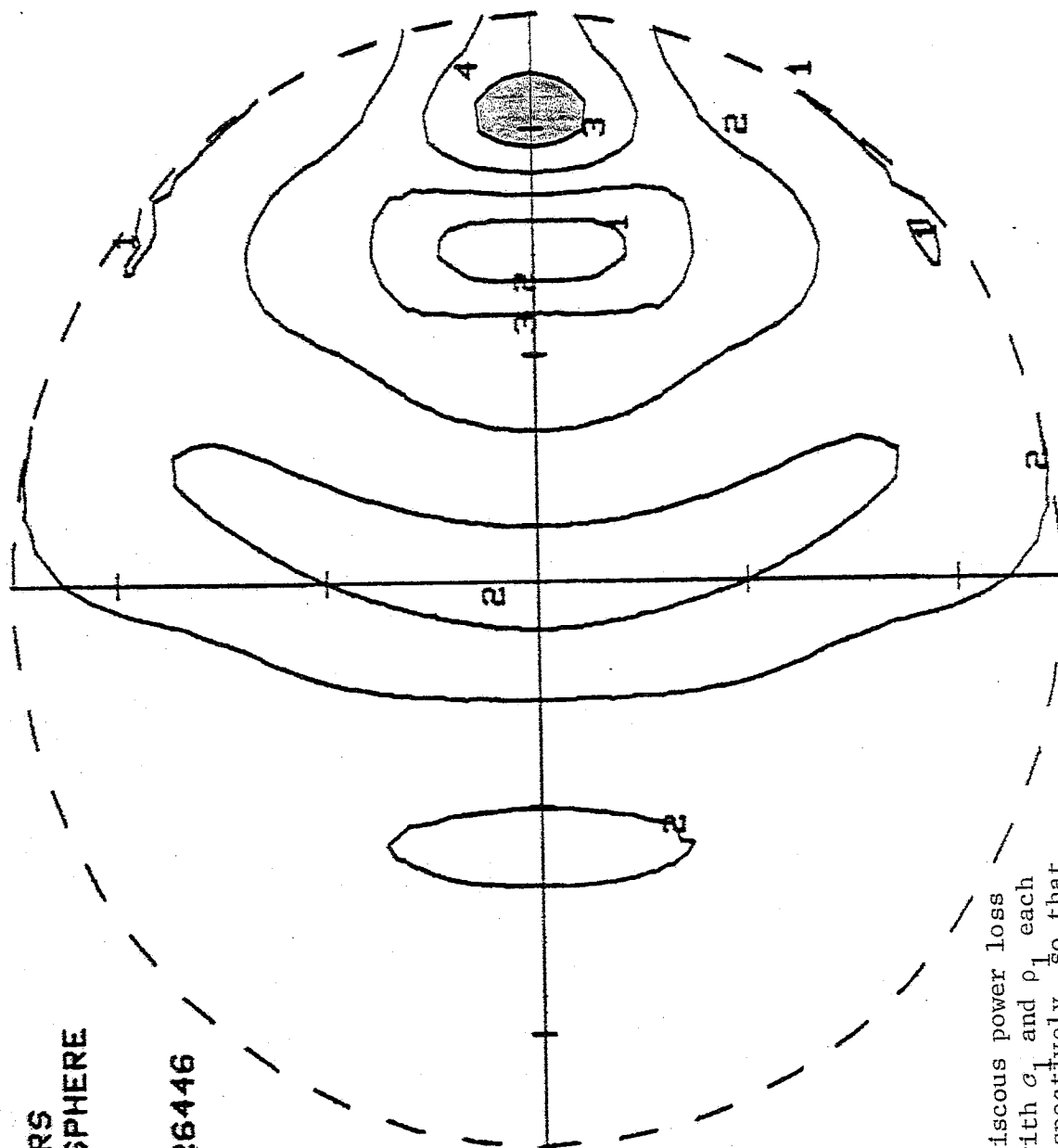


Figure 76. Distribution of viscous power loss in cross section of sphere, with c_1 and ρ_1 each 10% greater than c_2 and ρ_2 respectively, so that Z_1 is 21% greater than Z_2 ; also, $k_1 a \approx 10$ rad.

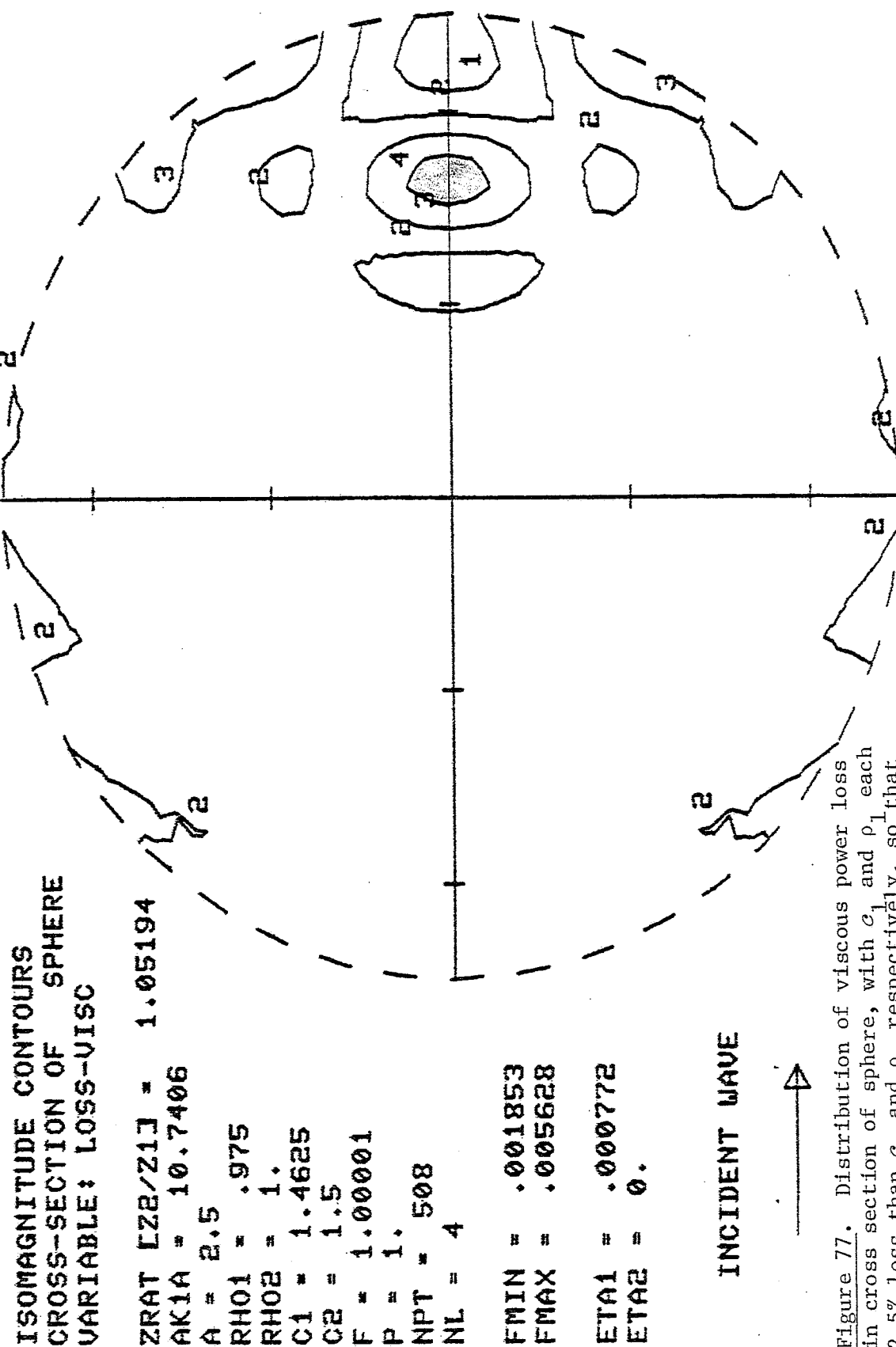


Figure 77. Distribution of viscous power loss in cross section of sphere, with c_1 and ρ_1 each 2.5% less than c_2 and ρ_2 respectively, so that Z_1 is 5.1% less than Z_2 ; also, $k_1 \alpha \cong 10$ rad.

ISOMAGNITUDE CONTOURS
CROSS-SECTION OF SPHERE
VARIABLE: LOSS-UISC

ZRAT LZ2/Z11 = 1.23457

AK1A = 11.6356

A = 2.5

RHO1 = .9

RHO2 = 1.

C1 = 1.35

C2 = 1.5

F = 1.00001

P = 1.

NPT = 468

NL = 4

FMIN = .00001

FMAX = .021648

ETA1 = .00056

ETA2 = 0.

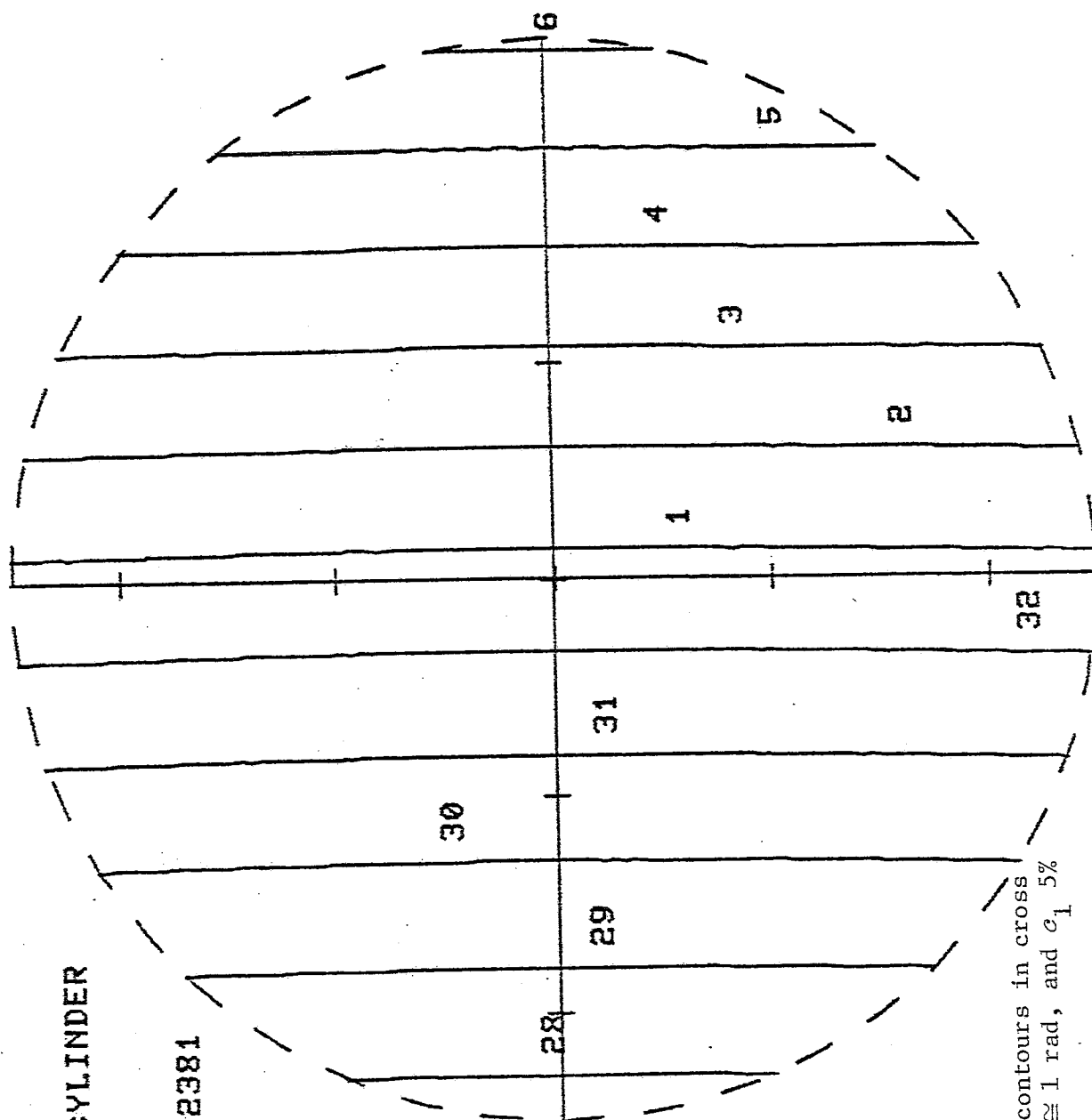
INCIDENT WAVE



Figure 78. Distribution of viscous power loss in cross section of sphere, with c_1 and ρ_1 each 10% less than c_2 and ρ_2 respectively, so that Z_1 is 21% less than Z_2 ; also, $k_1 a \approx 10$ rad.

ISO-PHASE CONTOURS
CROSS-SECTION OF CYLINDER
VARIABLE: PRESSURE

ZRAT [Z2/Z1] = .952381
AK1A = .997331
A = .25
RH01 = 1.
RH02 = 1.
C1 = 1.575
C2 = 1.5
F = 1.
P = 1.
NPT = 1177
NL = 32

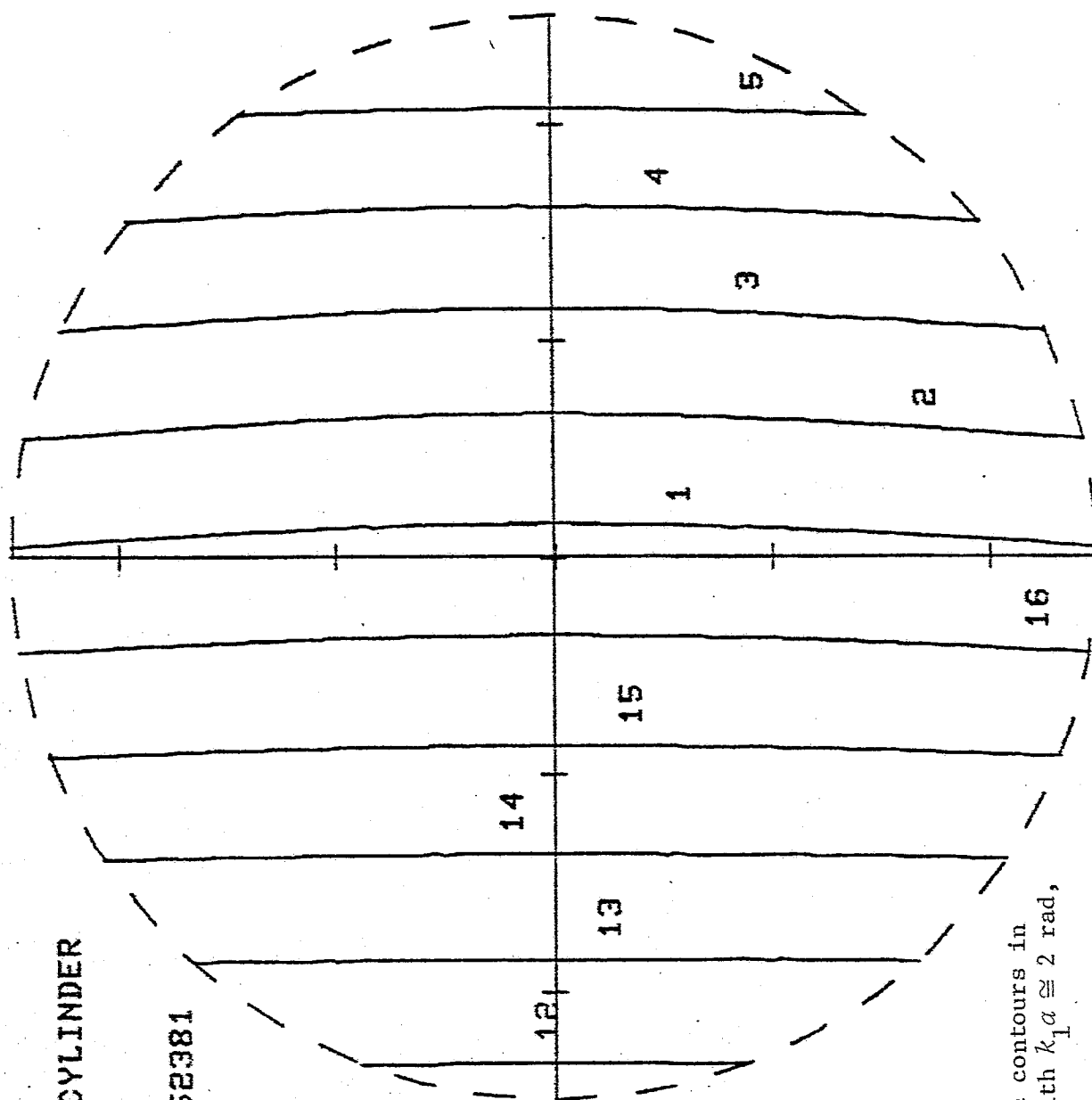


INCIDENT WAVE

Figure 79. Pressure isophase contours in cross section of cylinder, with $k_1 a \approx 1$ rad, and c_1 5% greater than c_2 .

ISO-PHASE CONTOURS
CROSS-SECTION OF CYLINDER
VARIABLE: PRESSURE

ZRAT [Z2/Z1] = .952381
AK1A = 1.99466
A = .5
RH01 = 1.
RH02 = 1.
C1 = 1.575
C2 = 1.5
F = 1.
P = 1.
NPT = 1127
NL = 16



INCIDENT WAVE



Figure 80. Pressure isophase contours in cross section of cylinder, with $k_1 a \cong 2$ rad, and c_1 5% greater than c_2 .

ISO-PHASE CONTOURS
CROSS-SECTION OF CYLINDER
VARIABLE: PRESSURE

ZRAT [Z2/Z1] = .952381

AK1A = 3.98932

A = 1.

RH01 = 1.

RH02 = 1.

C1 = 1.575

C2 = 1.5

F = 1.

P = 1.

NPT = 1121

NL = 8

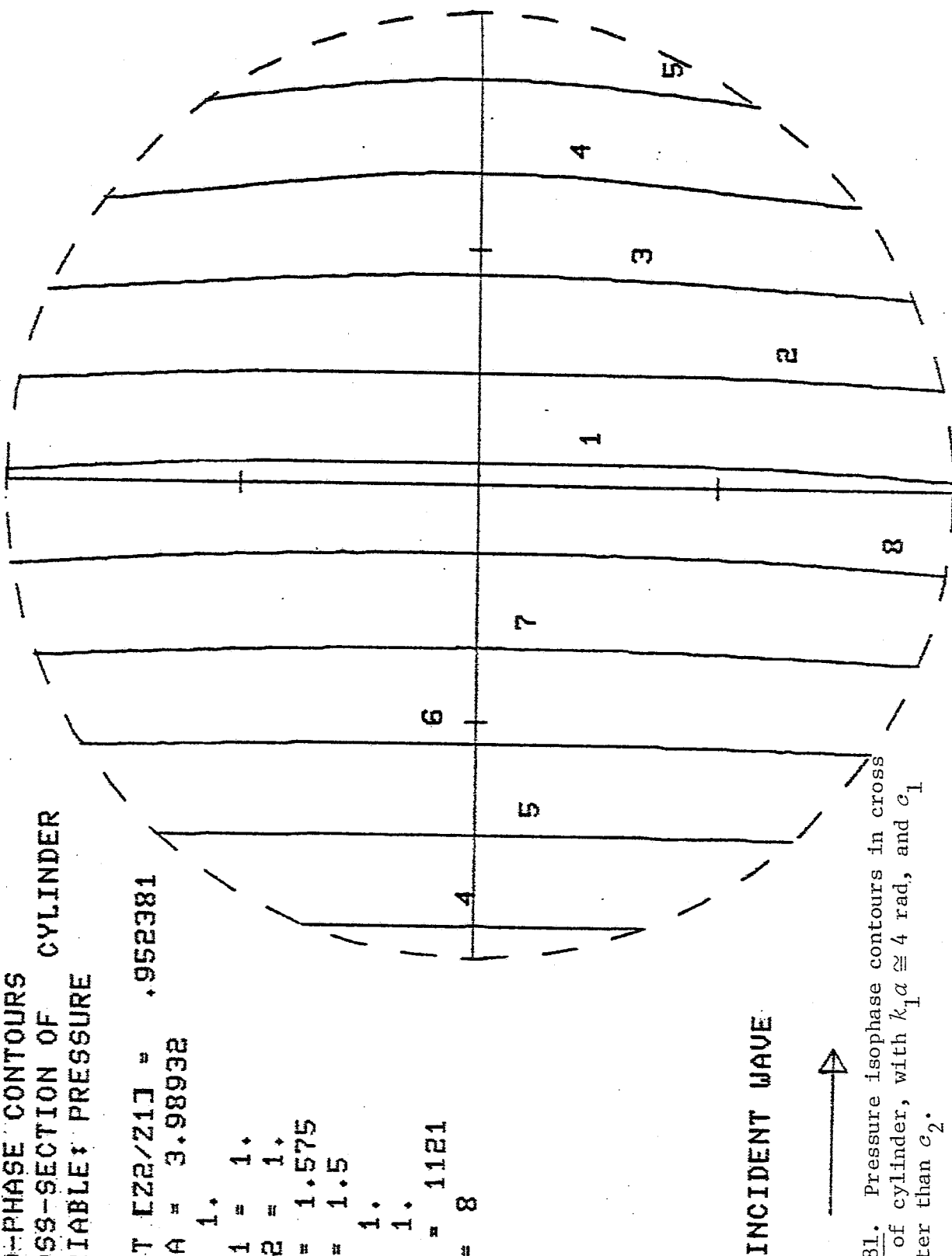
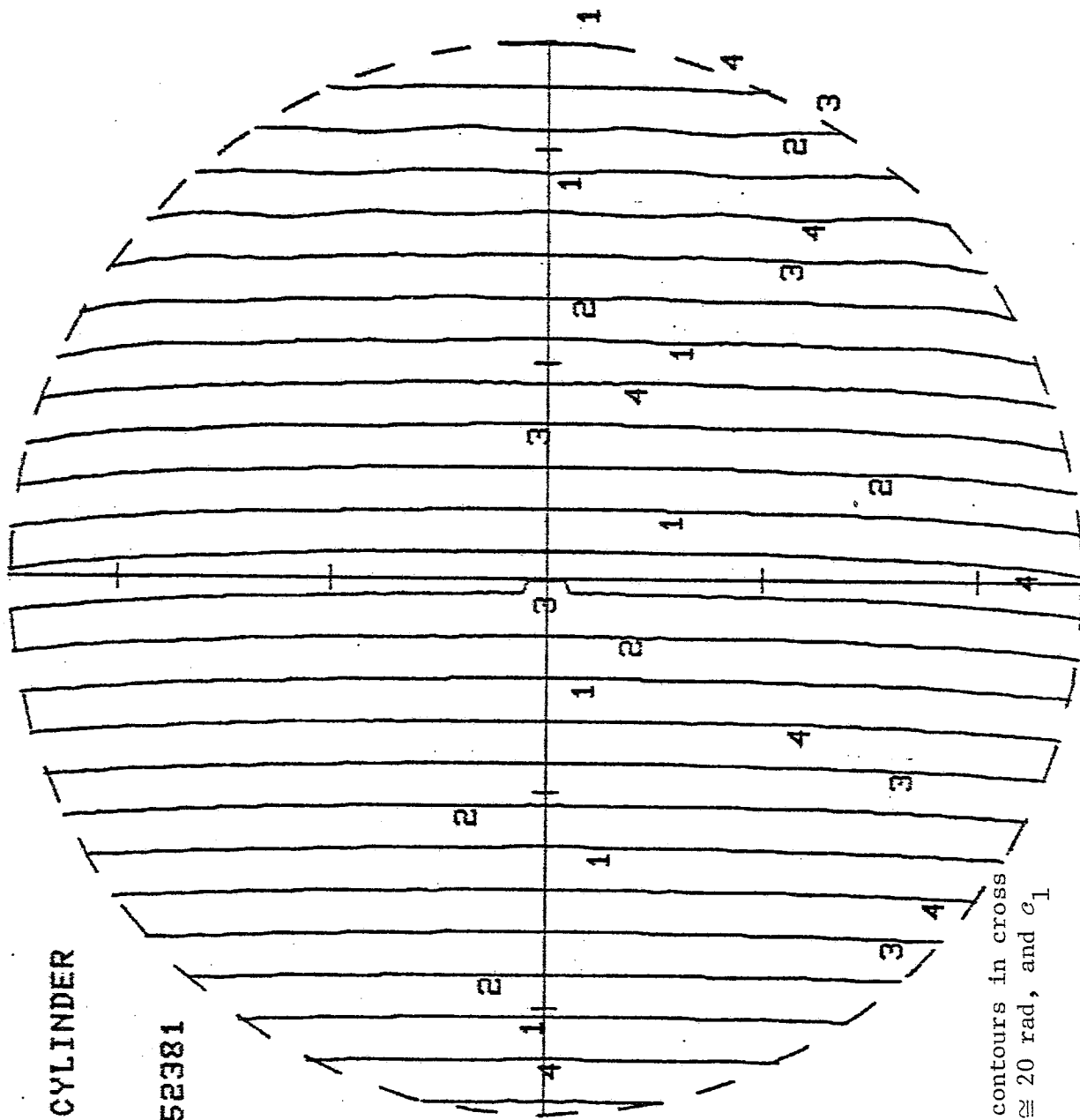


Figure 81. Pressure isophase contours in cross section of cylinder, with $k_1 \alpha \approx 4$ rad, and c_1 5% greater than c_2 .

ISO-PHASE CONTOURS
CROSS-SECTION OF CYLINDER
VARIABLE: PRESSURE

ZRAT [Z2/Z1] = .952381
AK1A = 19.9466
A = 5.
RH01 = 1.
RH02 = 1.
C1 = 1.575
C2 = 1.5
F = 1.
P = 1.
NPT = 2706
NL = 4



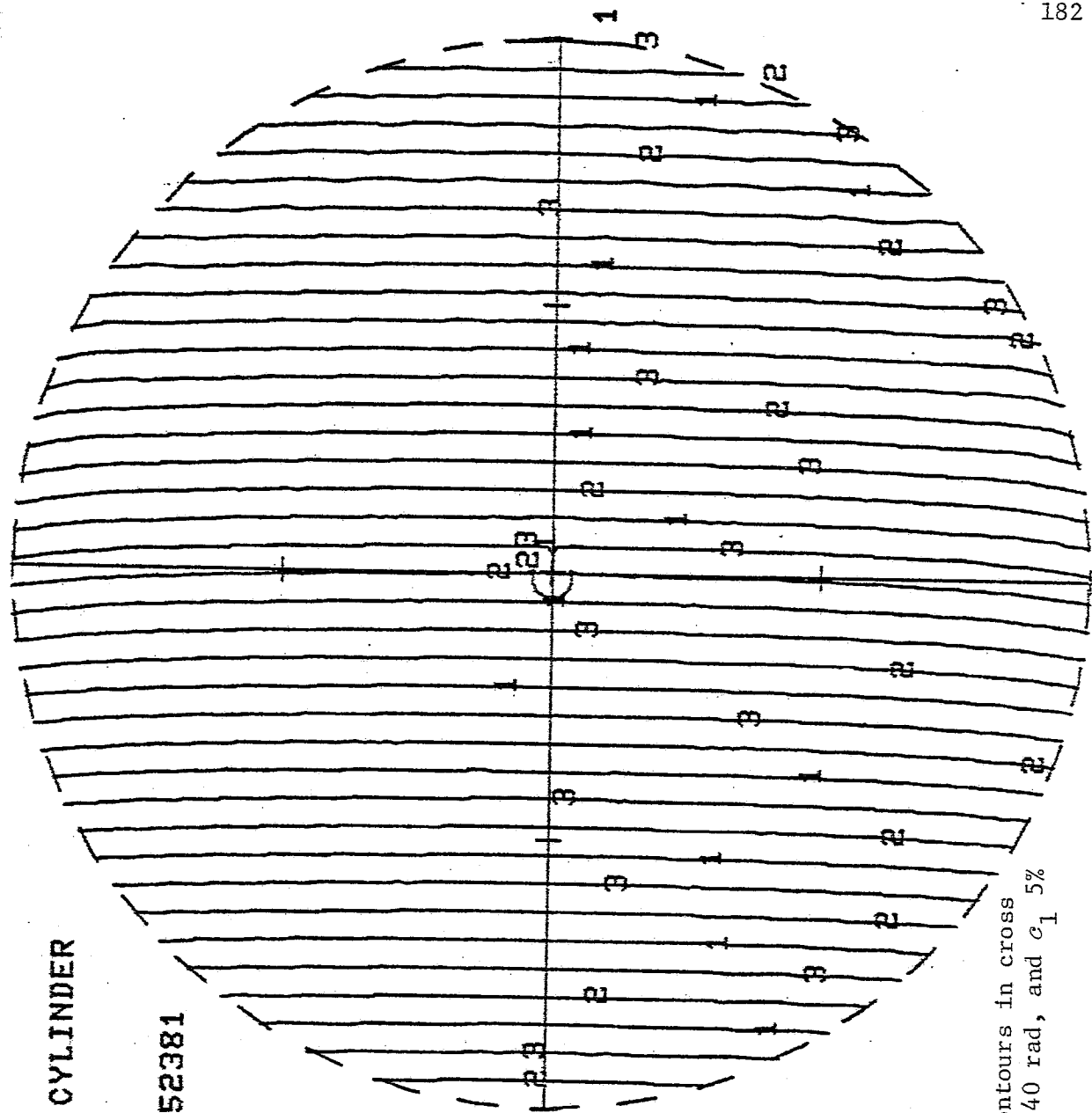
INCIDENT WAVE



Figure 82. Pressure isophase contours in cross section of cylinder, with $k_1 a \approx 20$ rad, and c_1 5% greater than c_2 .

ISO-PHASE CONTOURS
CROSS-SECTION OF CYLINDER
VARIABLE: PRESSURE

ZRAT CZ2/Z1J = .952381
AK1A = 39.8932
A = 10.
RH01 = 1.
RH02 = 1.
C1 = 1.575
C2 = 1.5
F = 1.
P = 1.
NPT = 4041
NL = 3



INCIDENT WAVE



Figure 83. Pressure isophase contours in cross section of cylinder, with $k_1 \alpha \cong 40$ rad, and c_1 5% greater than c_2 .

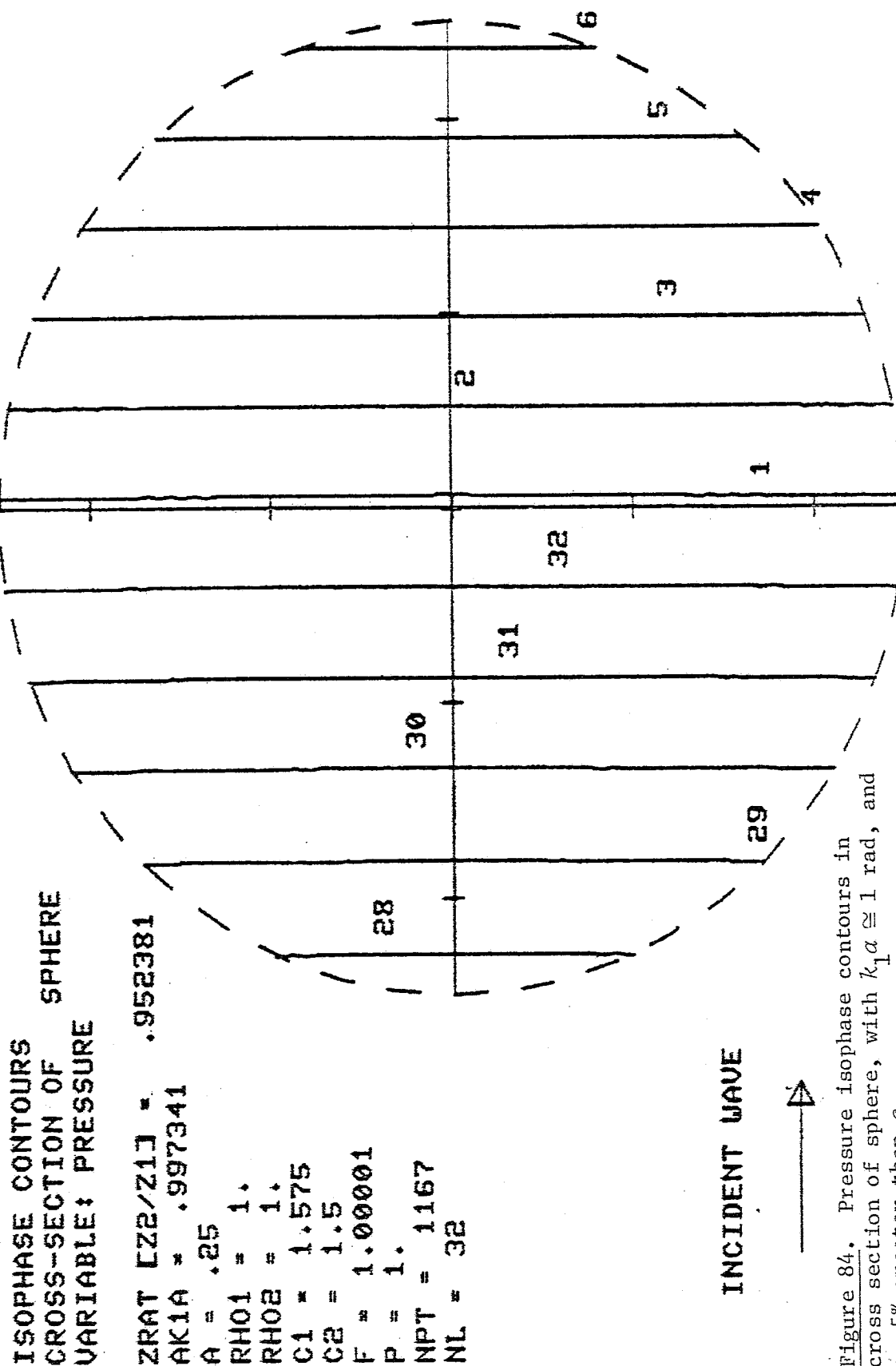
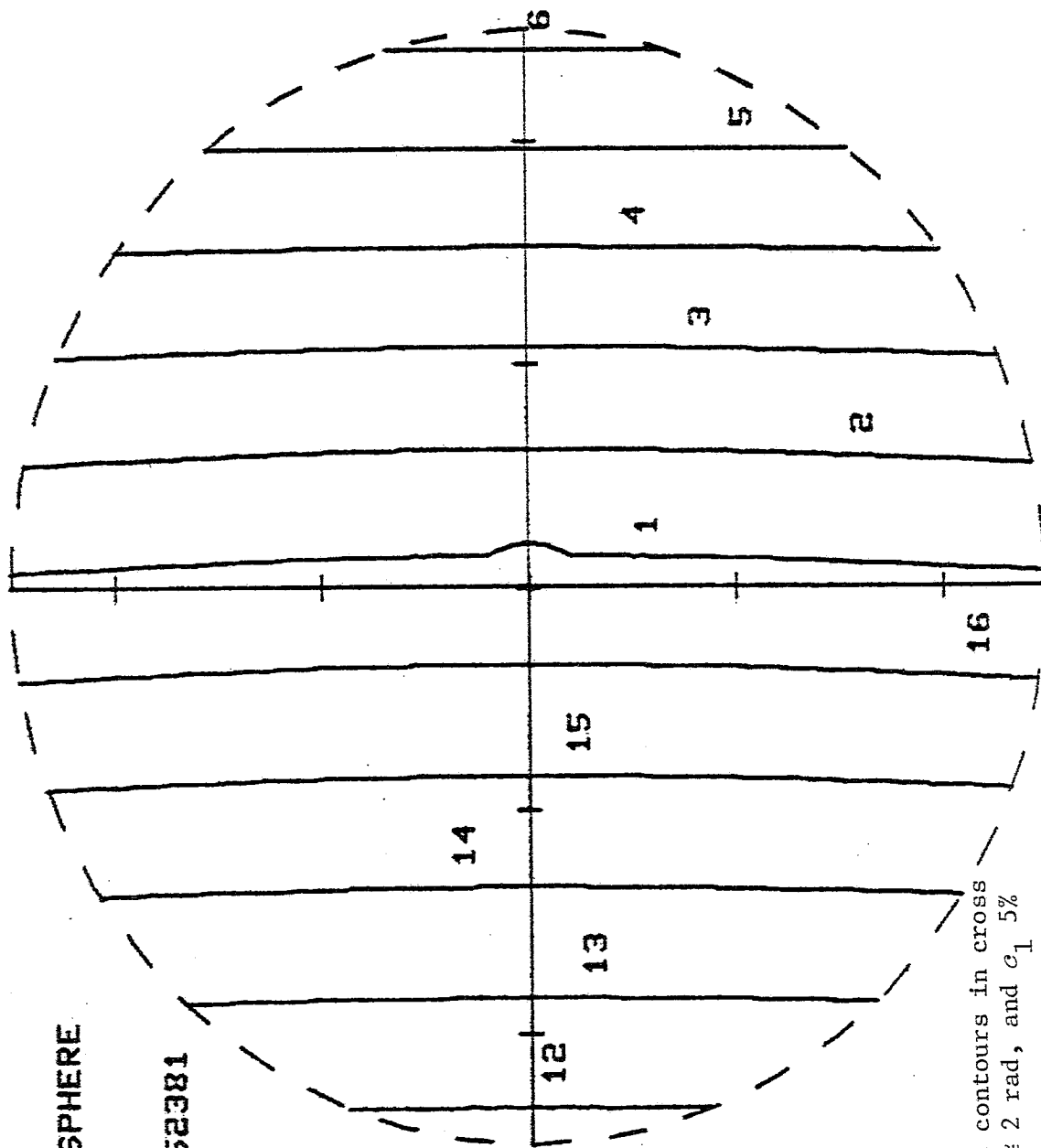


Figure 84. Pressure isophase contours in cross section of sphere, with $k_1 a \cong 1$ rad, and c_1 5% greater than c_2 .

ISOPHASE CONTOURS
CROSS-SECTION OF SPHERE
VARIABLE: PRESSURE

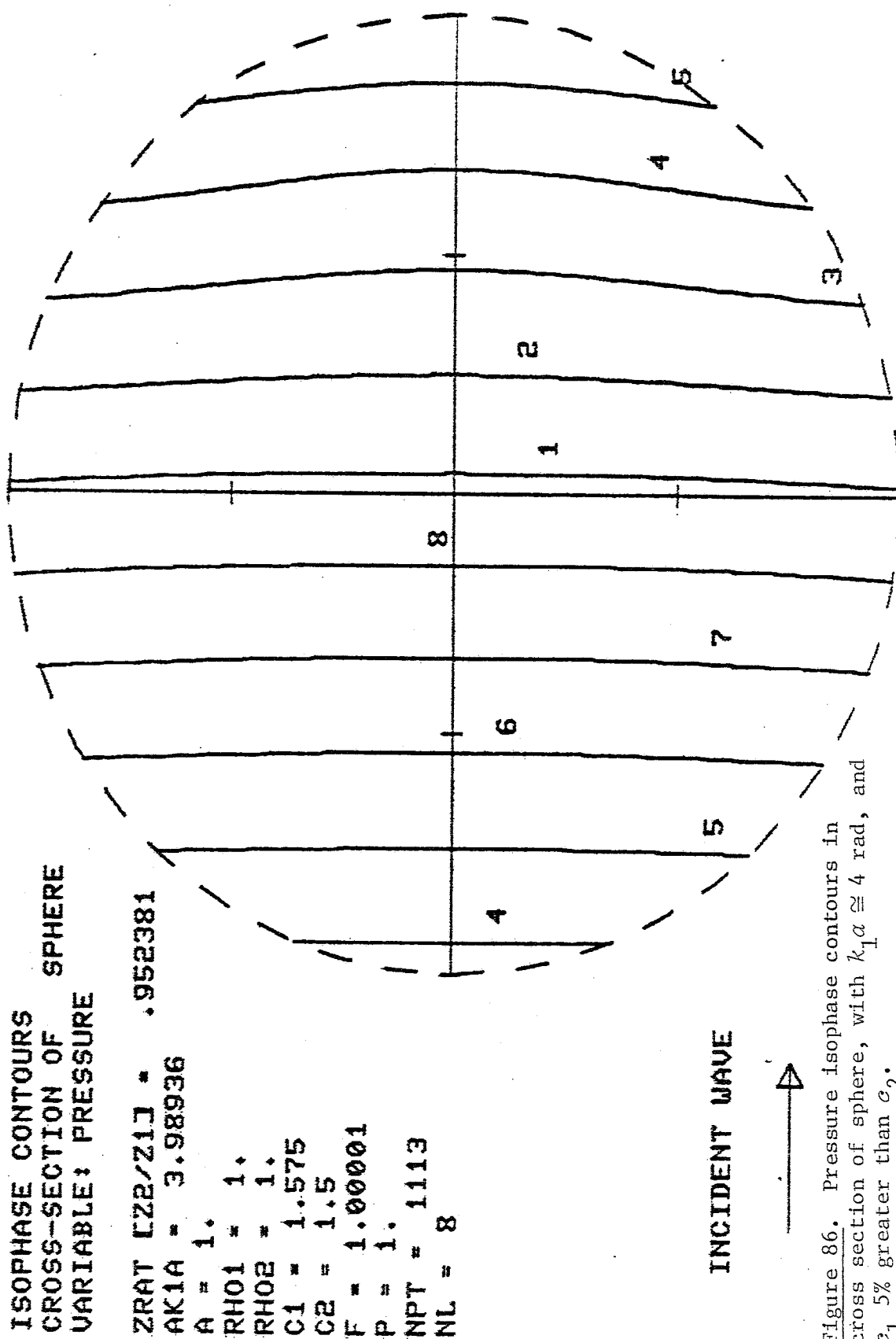
ZRAT LZ2/Z1J = .952381
AK1A = 1.99468
A = .5
RH01 = 1.
RH02 = 1.
C1 = 1.575
C2 = 1.5
F = 1.00001
P = 1.
NPT = 1169
NL = 16



INCIDENT WAVE

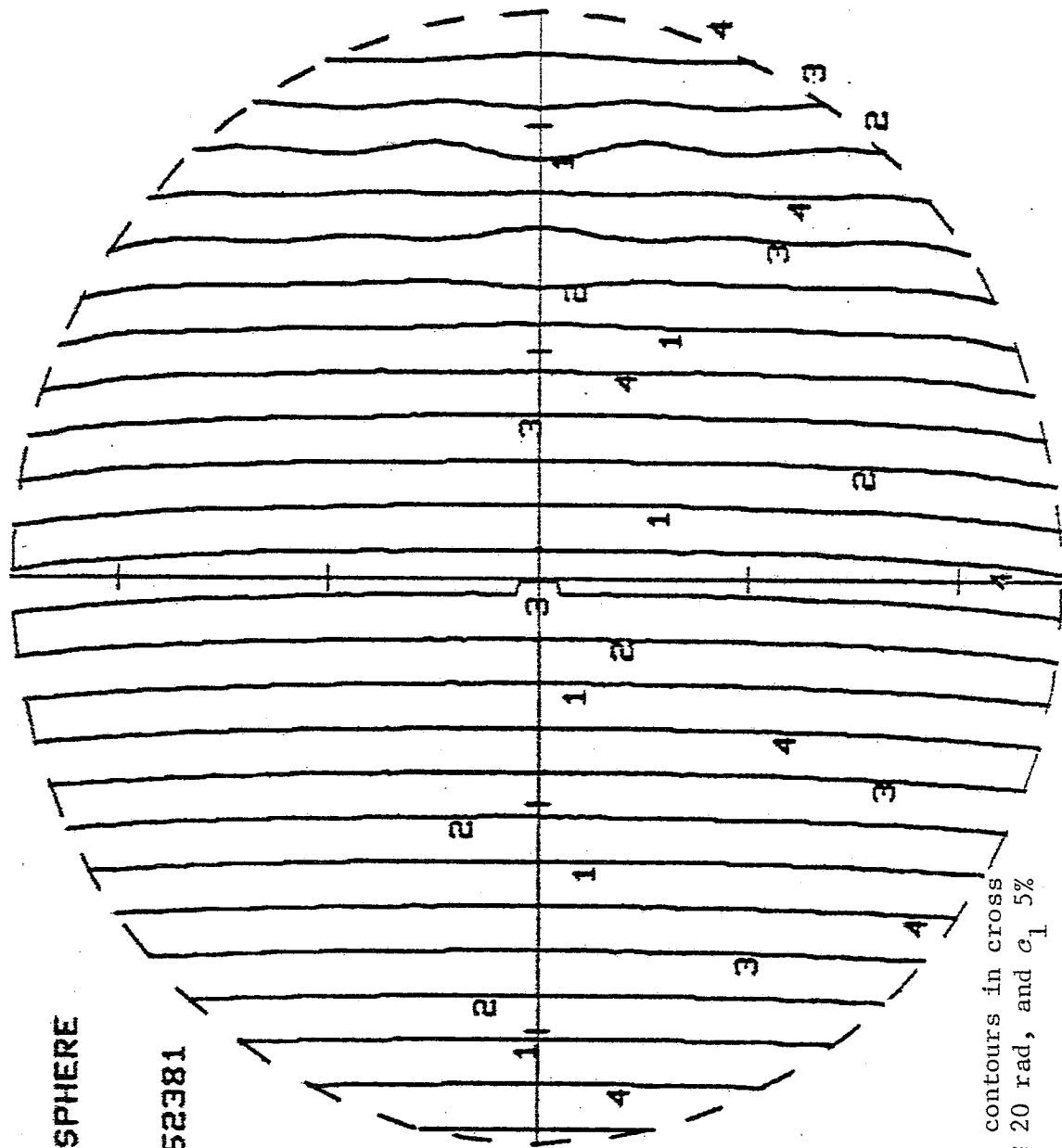


Figure 85. Pressure isophase contours in cross section of sphere, with $k_1 a \approx 2$ rad, and c_1 5% greater than c_2 .



ISOPHASE CONTOURS
CROSS-SECTION OF SPHERE
VARIABLE: PRESSURE

ZRAT [Z2/Z1] = .952381
AK1A = 19.9468
A = 5.
RH01 = 1.
RH02 = 1.
C1 = 1.575
C2 = 1.5
F = 1.00001
P = 1.
NPT = 2704
NL = 4



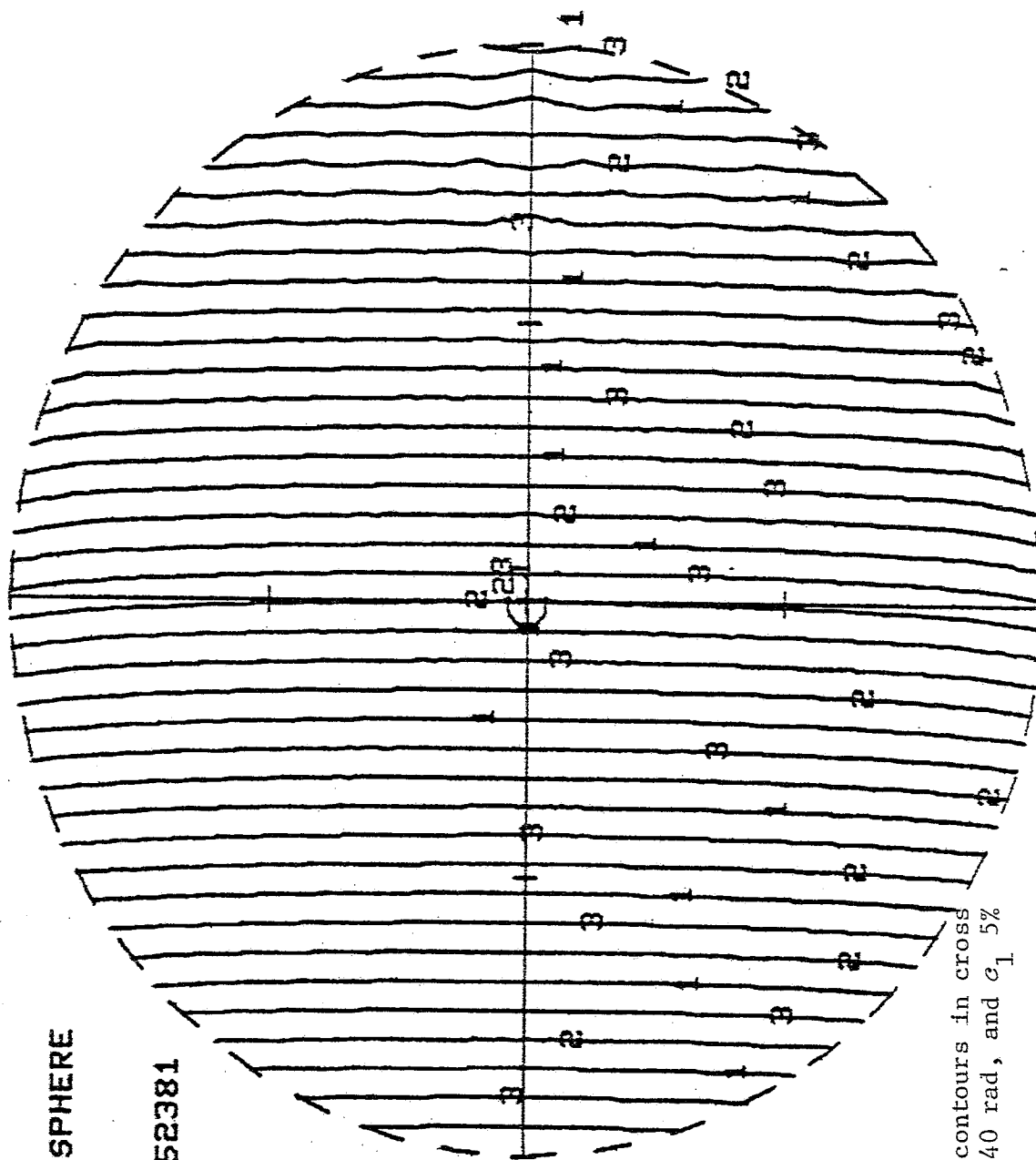
INCIDENT WAVE



Figure 87. Pressure isophase contours in cross section of sphere, with $k_1 a \approx 20$ rad, and c_1 5% greater than c_2 .

ISOPHASE CONTOURS
CROSS-SECTION OF SPHERE
VARIABLE: PRESSURE

ZRAT [Z2/Z1] = .952381
AK1A = 39.8936
A = 10.
RH01 = 1.
RH02 = 1.
C1 = 1.575
C2 = 1.5
F = 1.00001
P = 1.
NPT = 4036
NL = 3



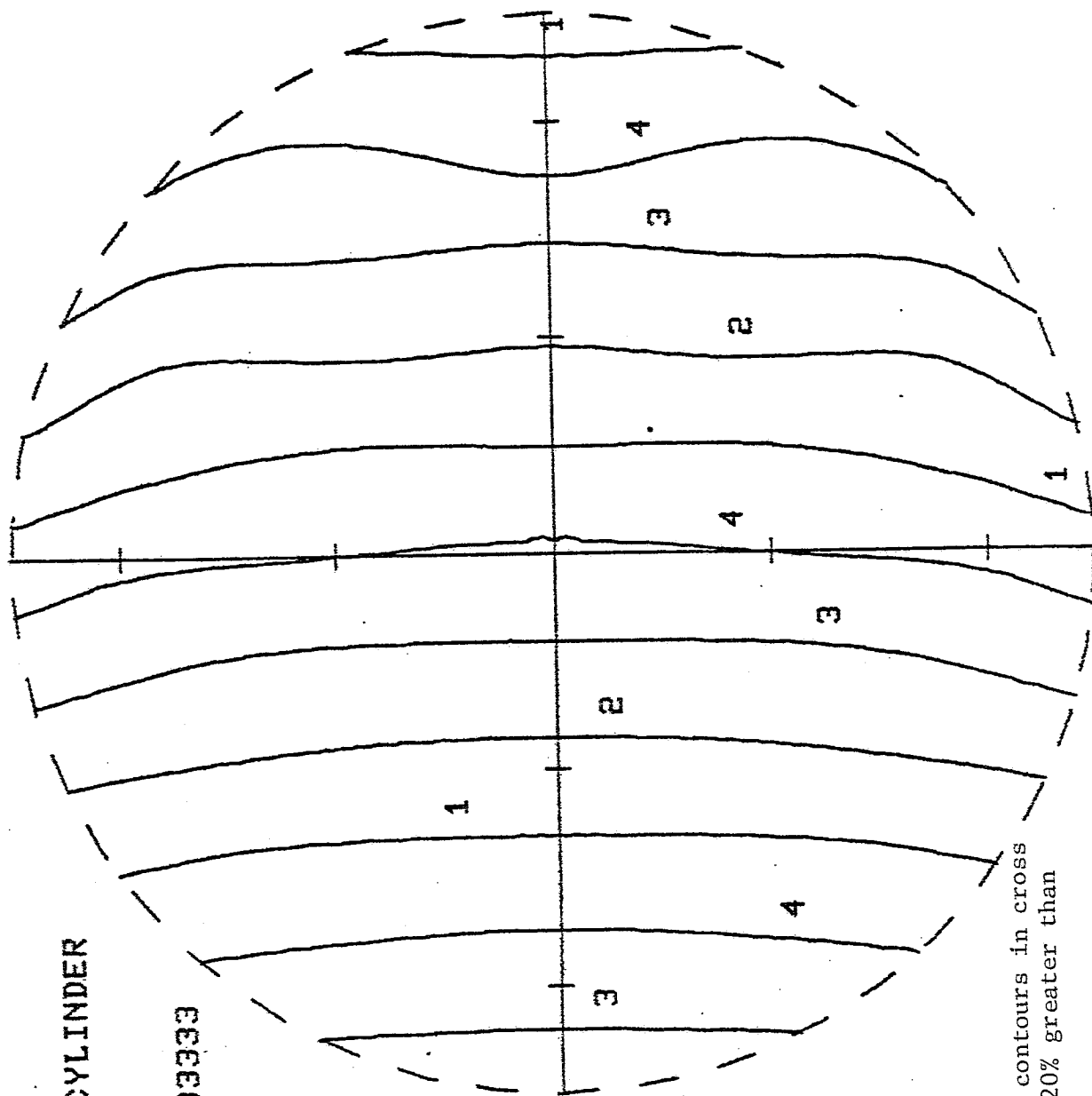
INCIDENT WAVE



Figure 88. Pressure isophase contours in cross section of sphere, with $k_1 \alpha \approx 40$ rad, and c_1 5% greater than c_2 .

ISO-PHASE CONTOURS
CROSS-SECTION OF CYLINDER
VARIABLE: PRESSURE

ZRAT [Z2/Z1] = .833333
AK1A = 8.72665
A = 2.5
RH01 = 1.
RH02 = 1.
C1 = 1.8
C2 = 1.5
F = 1.
P = 1.
NPT = 1213
NL = 4



INCIDENT WAVE

Figure 89. Pressure isophase contours in cross section of cylinder, with c_1 20% greater than c_2 , and $k_1 a \approx 10$ rad.

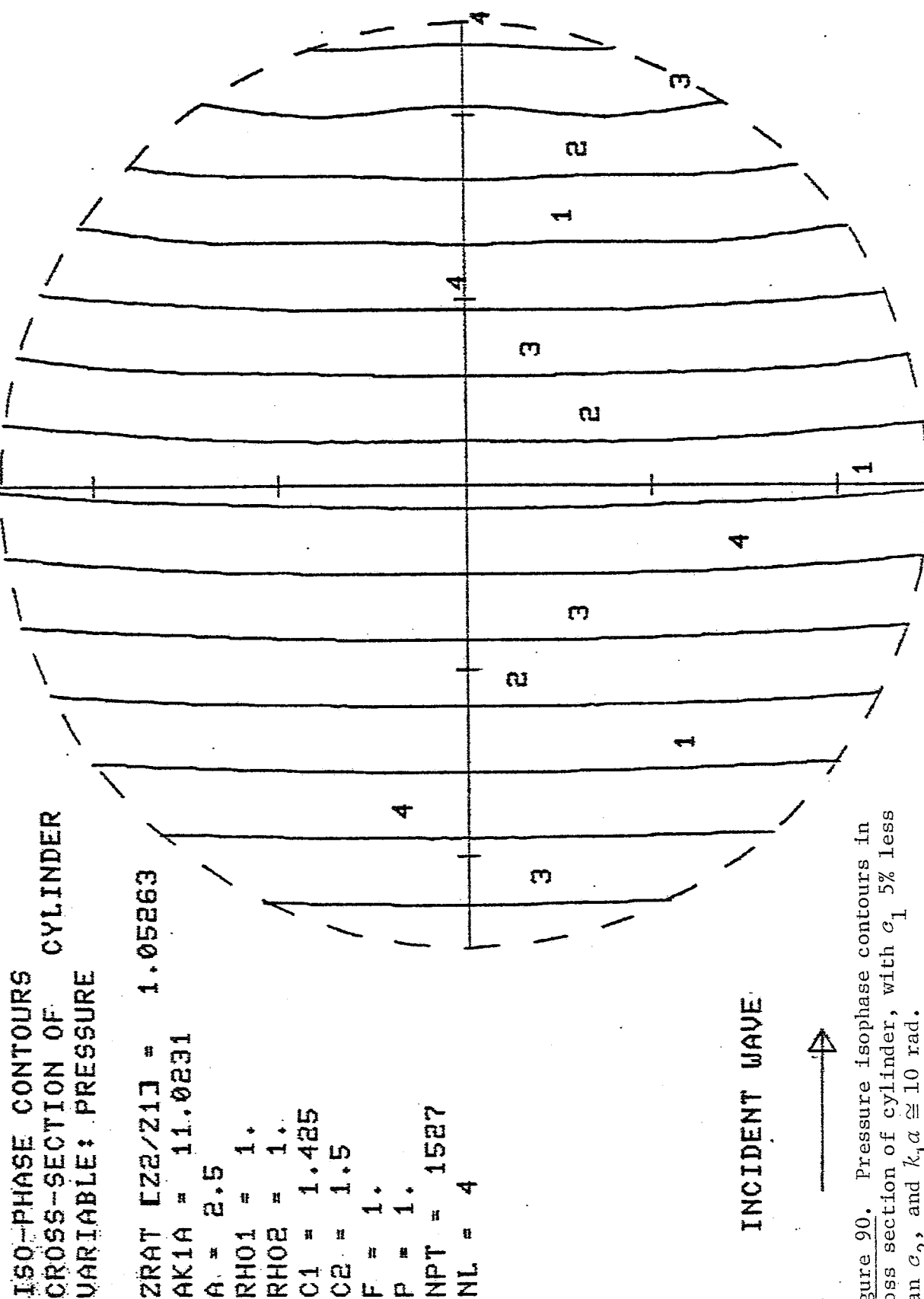


Figure 90. Pressure isophase contours in cross section of cylinder, with c_1 5% less than c_2 , and $k_1 a \approx 10$ rad.

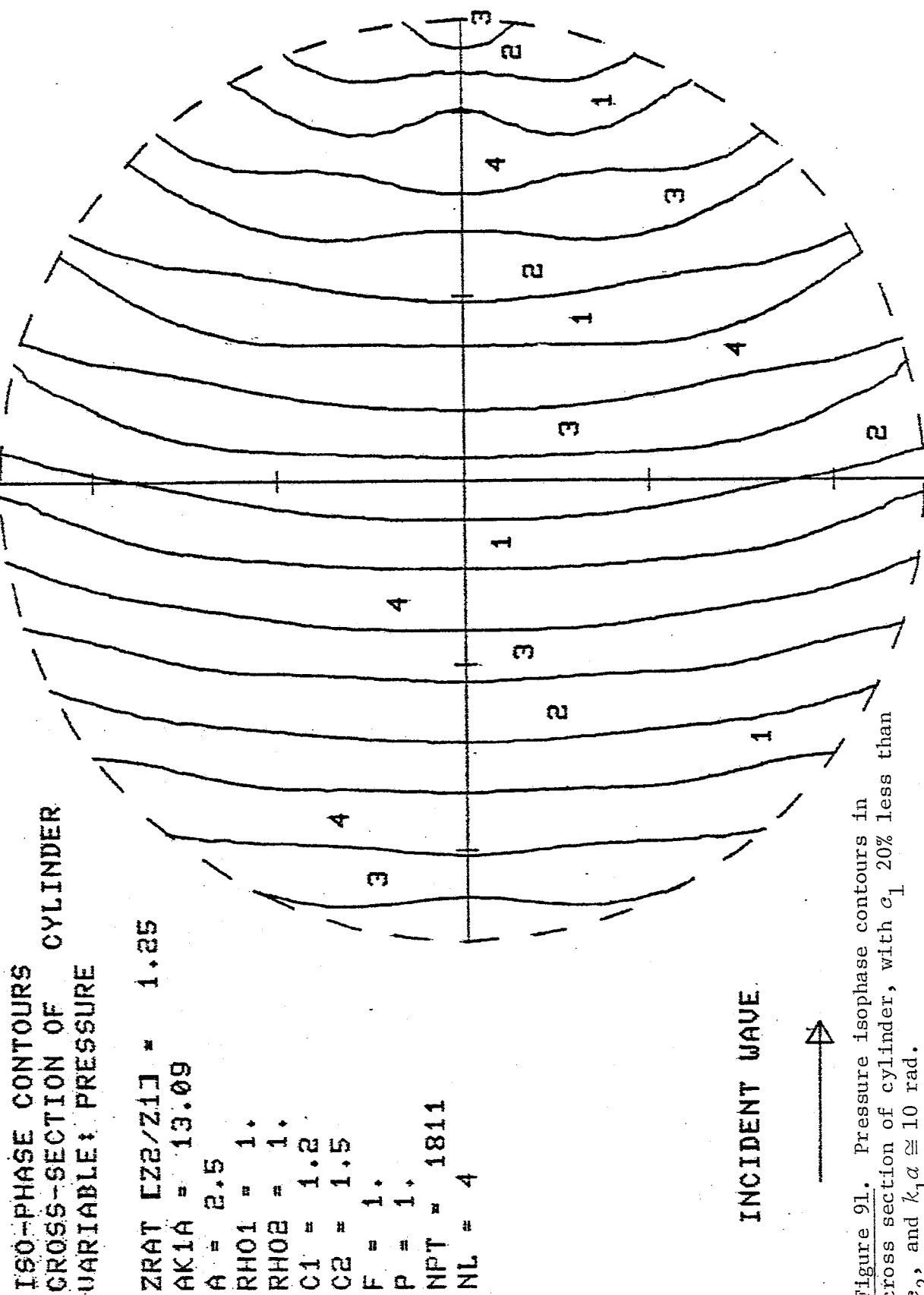
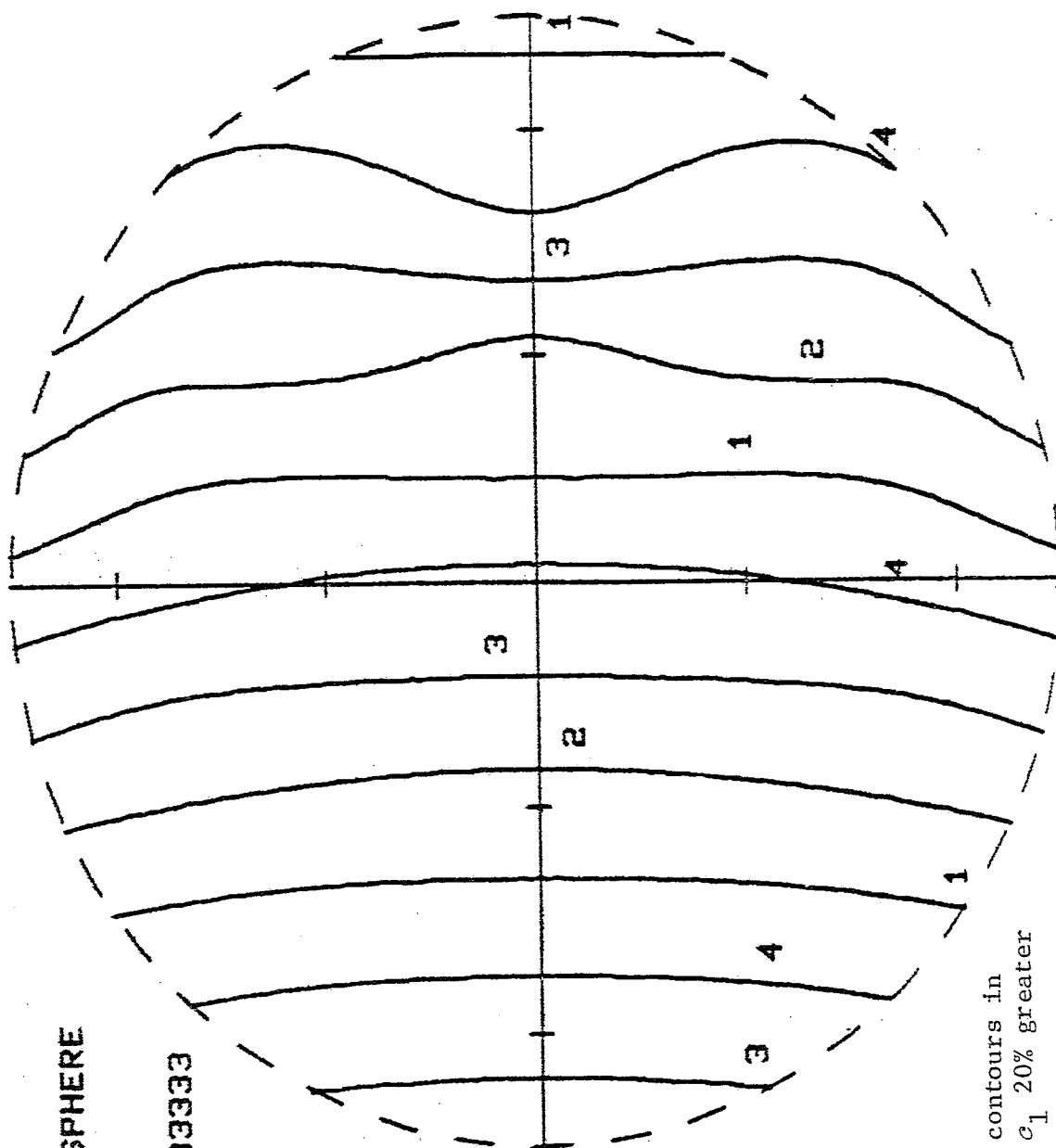


Figure 91. Pressure isophase contours in cross section of cylinder, with c_1 20% less than c_2 , and $k_1 a \approx 10$ rad.

ISOPHASE CONTOURS
CROSS-SECTION OF SPHERE
VARIABLE: PRESSURE

ZRAT [Z2/Z1] = .833333
AK1A = 8.72673
A = 2.5
RH01 = 1.
RH02 = 1.
C1 = 1.8
C2 = 1.5
F = 1.00001
P = 1.
NPT = 1227
NL = 4



INCIDENT WAVE

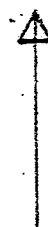
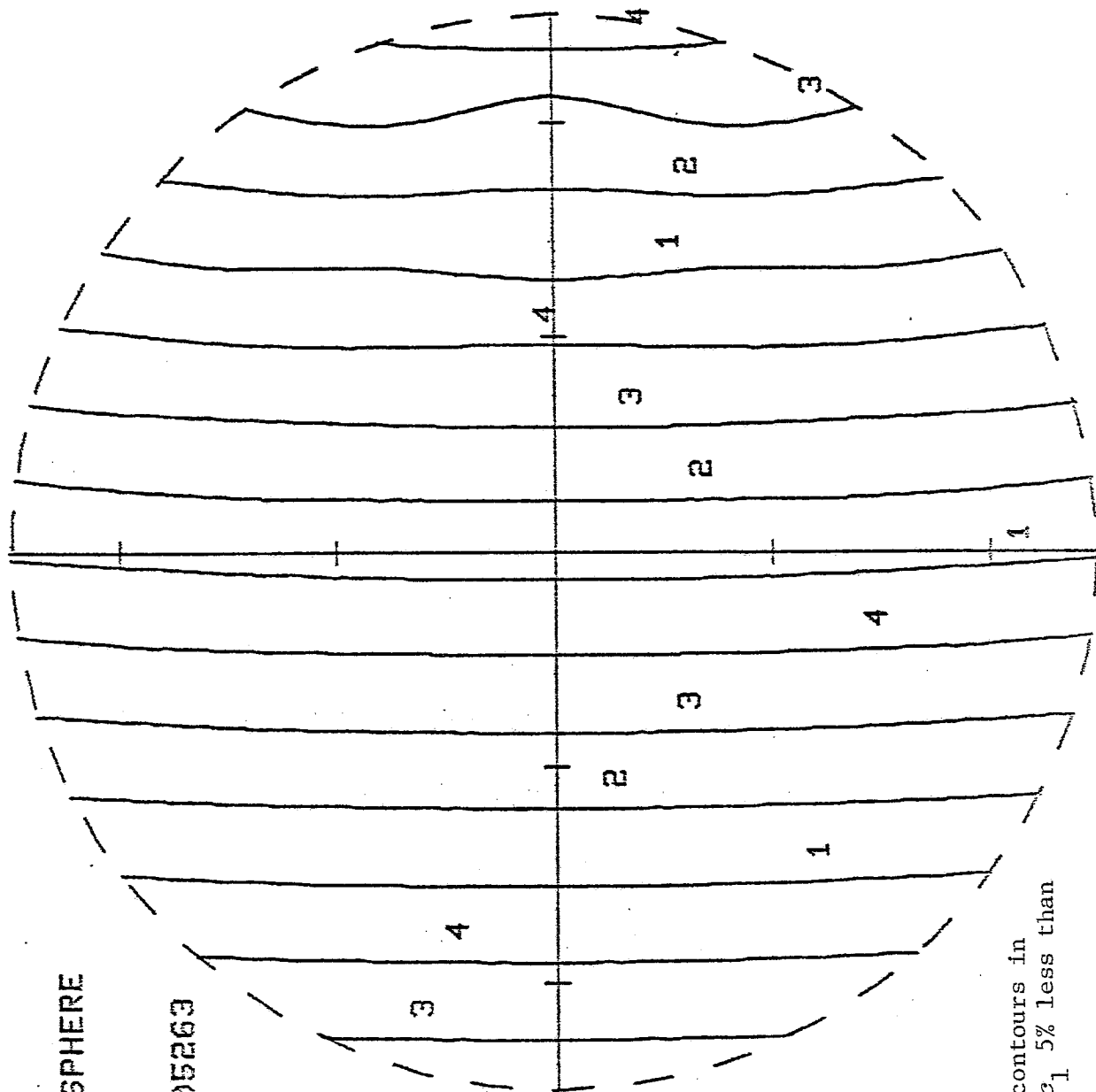


Figure 92. Pressure isophase contours in cross section of sphere, with c_1 20% greater than c_2 , and $k_1 \alpha \approx 10$ rad.

ISOPHASE CONTOURS
CROSS-SECTION OF SPHERE
VARIABLE: PRESSURE

ZRAT C22/Z17 = 1.05263
AK1A = 11.0232
A = 2.5
RHO1 = 1.
RHO2 = 1.
C1 = 1.425
C2 = 1.5
F = 1.00001
P = 1.
NPT = 1531
NL = 4



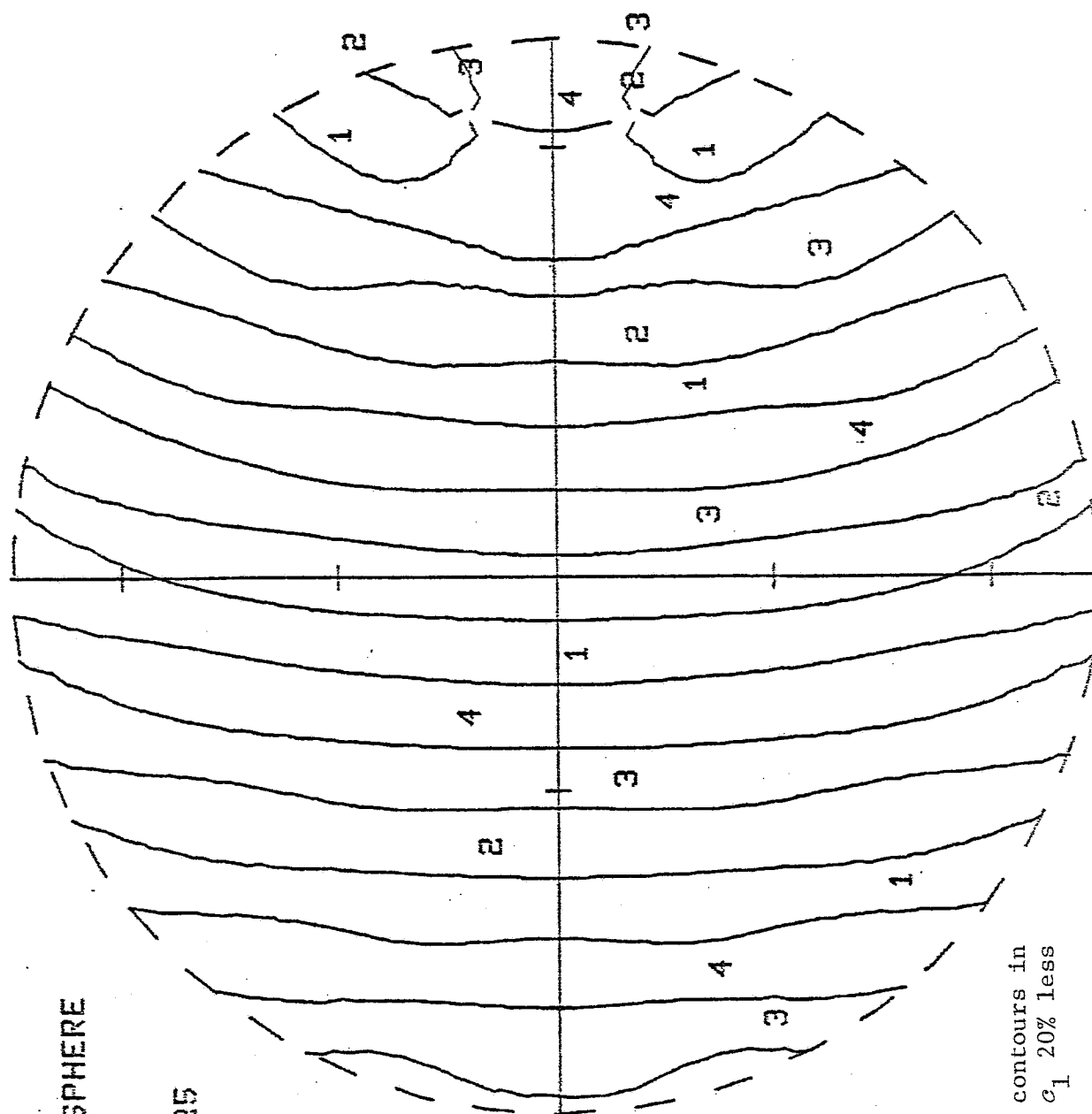
INCIDENT WAVE



Figure 93. Pressure isophase contours in cross section of sphere, with c_1 5% less than c_2 , and $k_1 a \approx 10$ rad.

ISOPHASE CONTOURS
CROSS-SECTION OF SPHERE
VARIABLE: PRESSURE

ZRAT [Z2/Z1] = 1.25
AK1A = 13.0901
A = 2.5
RH01 = 1.
RH02 = 1.
C1 = 1.2
C2 = 1.5
F = 1.00001
P = 1.
NPT = 1783
NL = 4



INCIDENT WAVE



Figure 94. Pressure isophase contours in cross section of sphere, with c_1 20% less than c_2 , and $k_1 a \approx 10$ rad.

ISO-PHASE CONTOURS
CROSS-SECTION OF CYLINDER
VARIABLE: PRESSURE

ZRAT [Z2/Z1] = .952381

AK1A = 10.472

A = 2.5

RH01 = 1.05

RH02 = 1.

C1 = 1.5

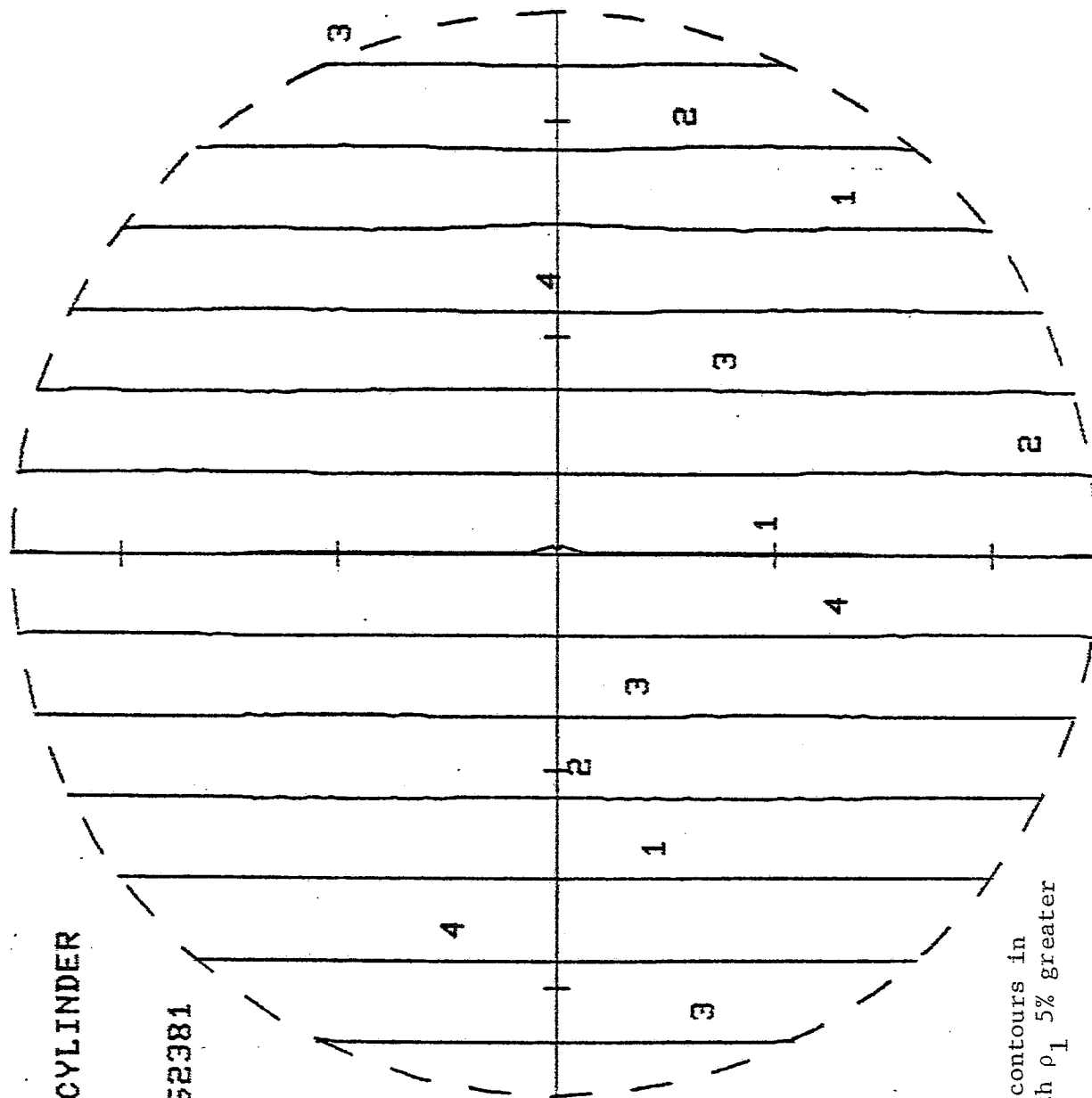
C2 = 1.5

F = 1.

P = 1.

NPT = 1423

NL = 4



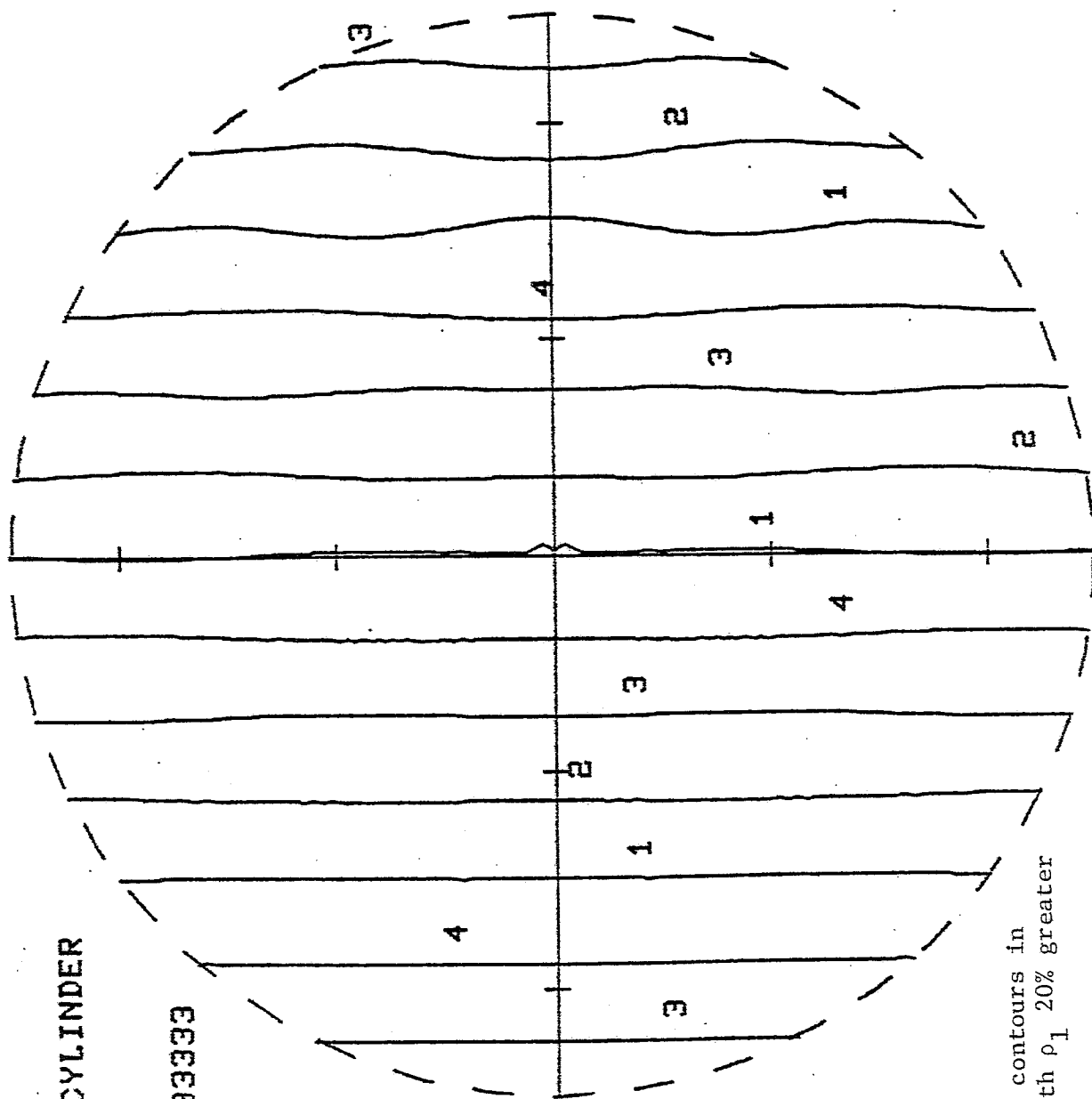
INCIDENT WAVE



Figure 95. Pressure isophase contours in cross section of cylinder, with ρ_1 5% greater than ρ_2 , and $k_1 a \approx 10$ rad.

ISO-PHASE CONTOURS
CROSS-SECTION OF CYLINDER
VARIABLE: PRESSURE

ZRAT CZ22/Z17 = .833333
AK1A = 10.472
A = 2.5
RH01 = 1.2
RH02 = 1.
C1 = 1.5
C2 = 1.5
F = 1.
P = 1.
NPT = 1421
NL = 4



INCIDENT WAVE



Figure 96. Pressure isophase contours in cross section of cylinder, with ρ_1 20% greater than ρ_2 , and $k_1 \alpha \approx 10$ rad.

ISO-PHASE CONTOURS
CROSS-SECTION OF CYLINDER
VARIABLE: PRESSURE

ZRAT [Z2/Z1] = 1.05263

AK1A = 10.472

A = 2.5

RHO1 = .95

RHO2 = 1.

C1 = 1.5

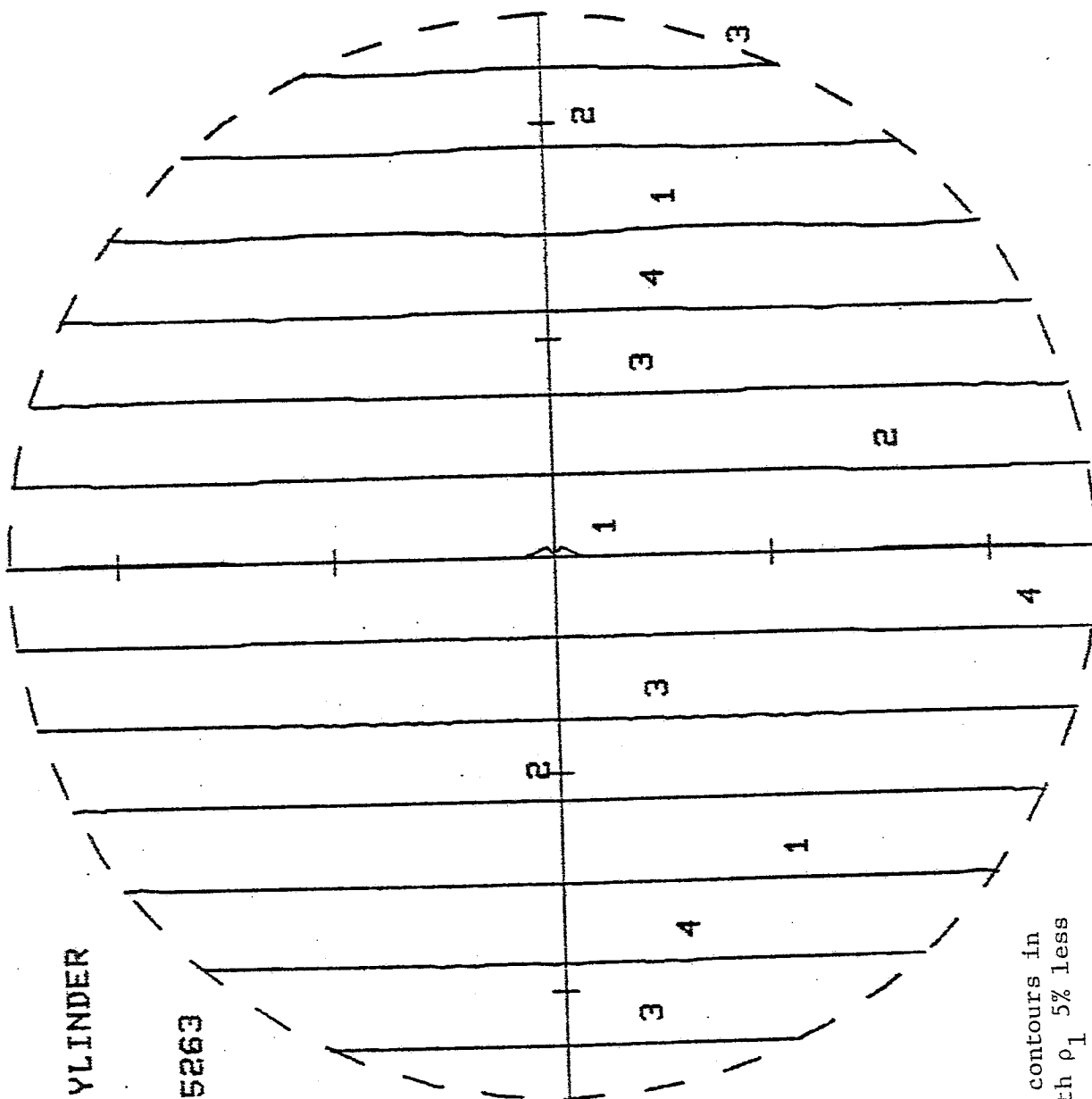
C2 = 1.5

F = 1.

P = 1.

NPT = 1415

NL = 4



INCIDENT WAVE



Figure 97. Pressure isophase contours in cross section of cylinder, with ρ_1 5% less than ρ_2 , and $k_1 a \approx 10$ rad.

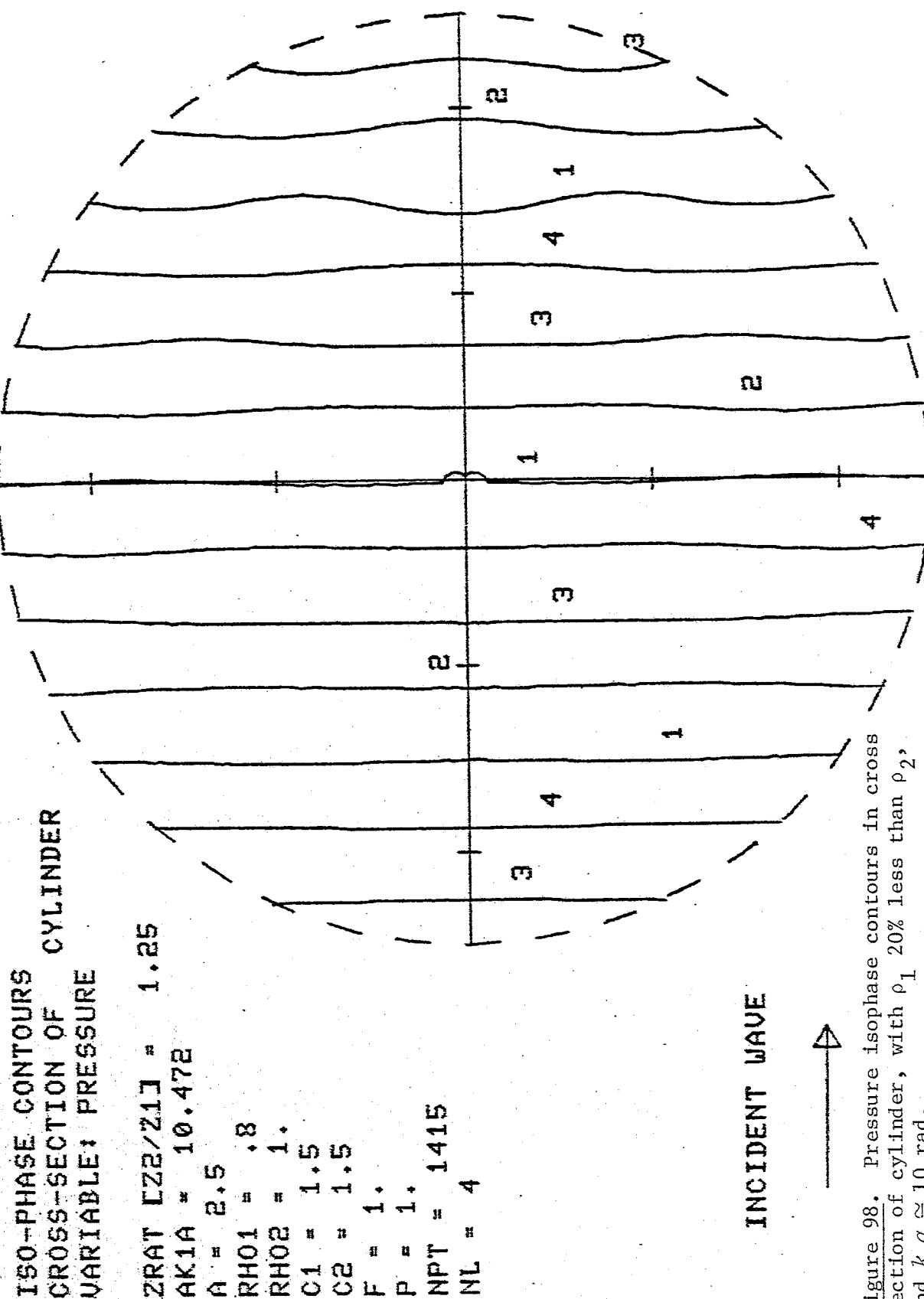
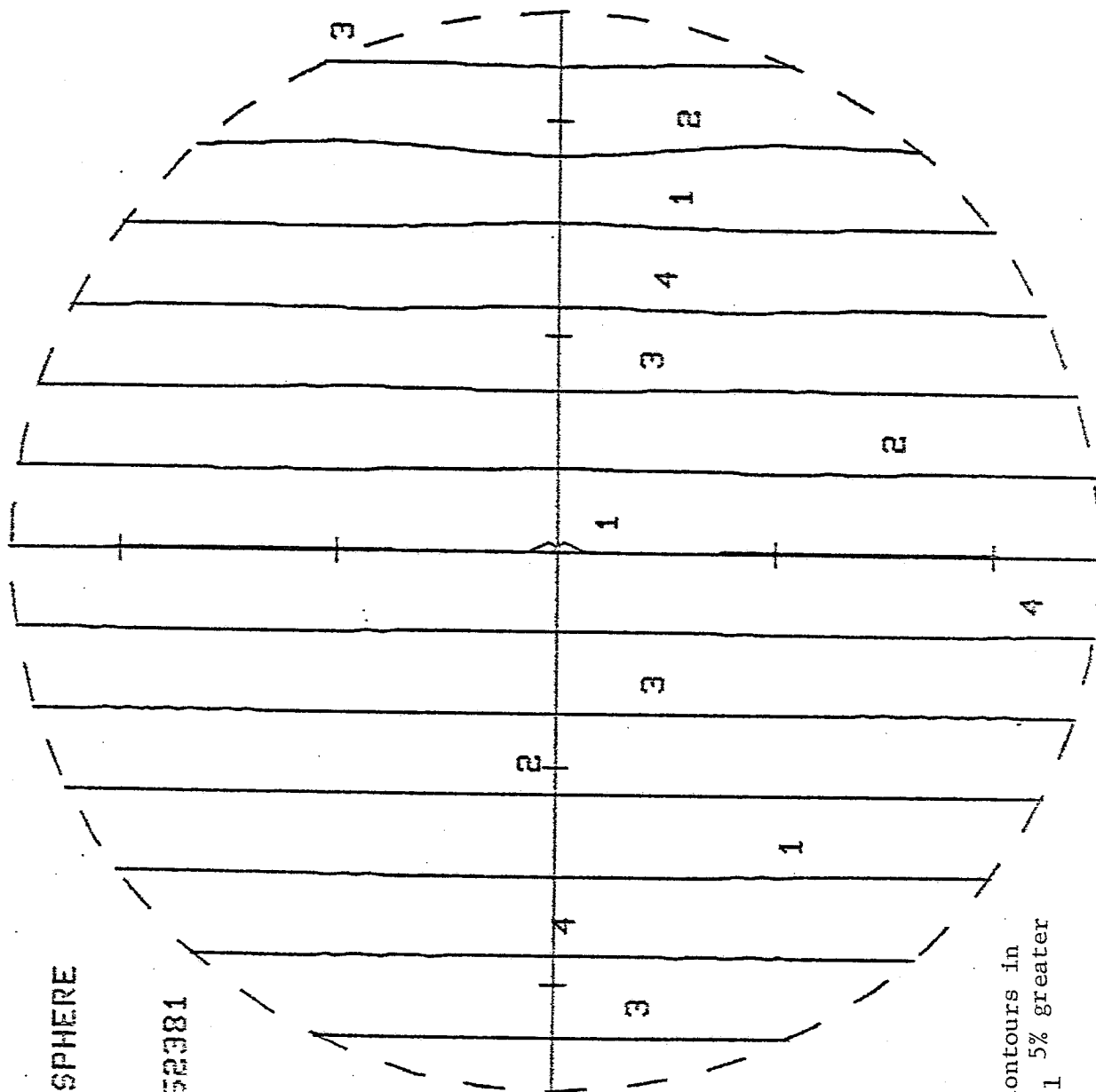


Figure 98. Pressure isophase contours in cross section of cylinder, with ρ_1 20% less than ρ_2 , and $k_1 a \approx 10$ rad.

ISOPHASE CONTOURS
CROSS-SECTION OF SPHERE
VARIABLE: PRESSURE

ZRAT [Z2/Z1] = .952381
AK1A = 10.4721
A = 2.5
RH01 = 1.05
RH02 = 1.
C1 = 1.5
C2 = 1.5
F = 1.000001
P = 1.
NPT = 1419
NL = 4



INCIDENT WAVE



Figure 99. Pressure isophase contours in cross section of sphere, with ρ_1 5% greater than ρ_2 , and $k_1 \alpha \cong 10$ rad.

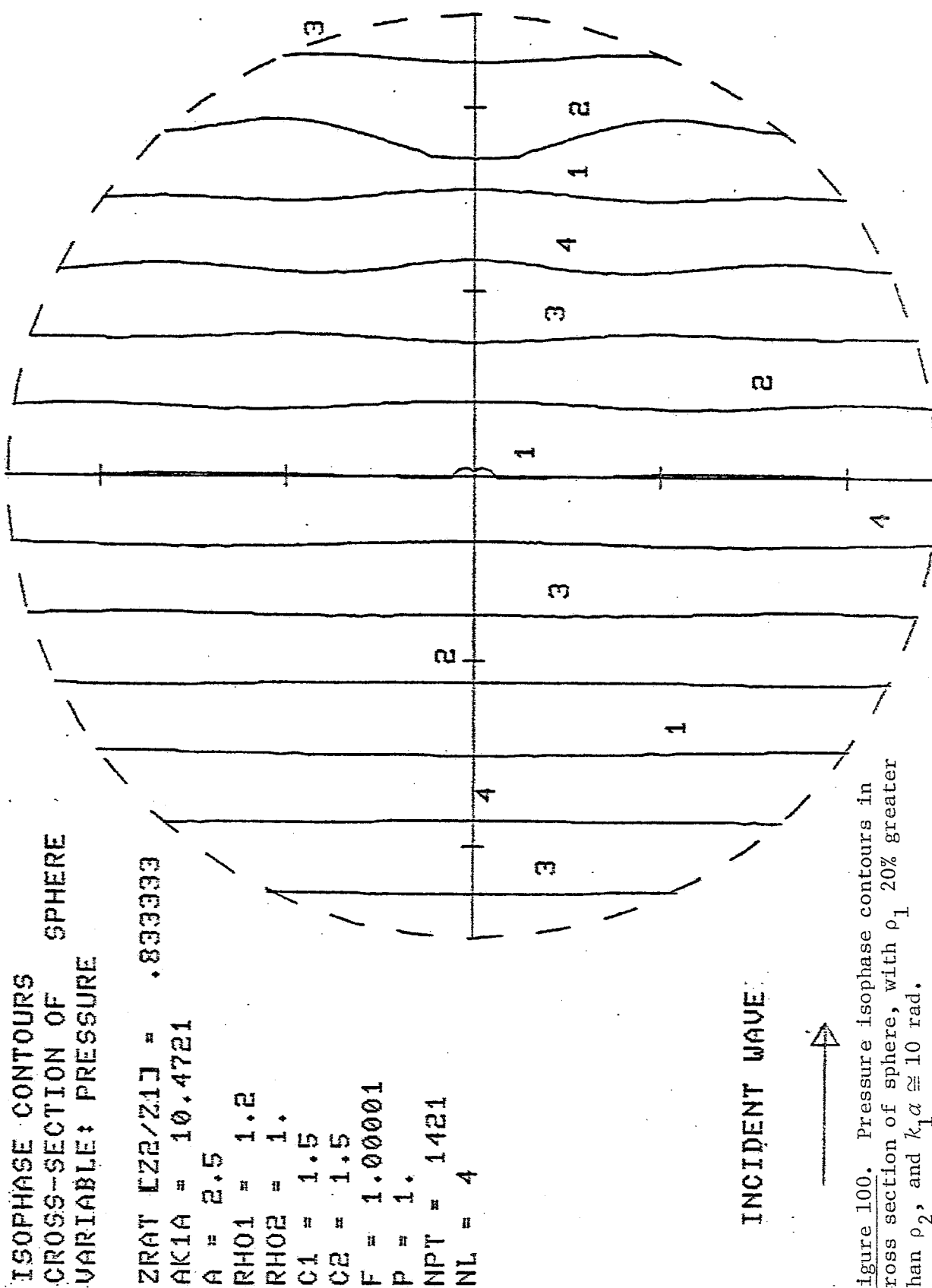


Figure 100. Pressure isophase contours in cross section of sphere, with ρ_1 20% greater than ρ_2 , and $k_1 \alpha \approx 10$ rad.

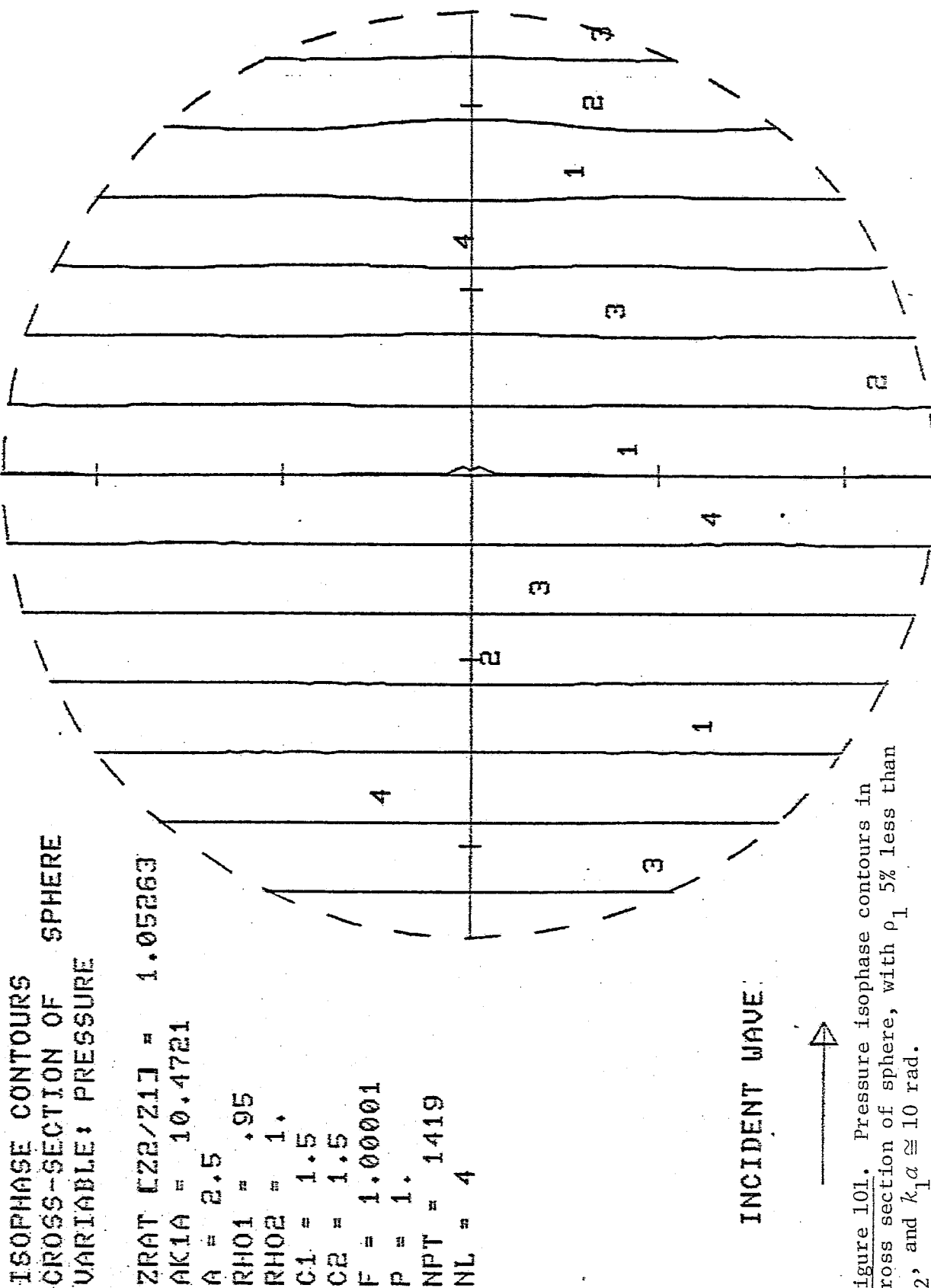


Figure 101. Pressure isophase contours in cross section of sphere, with ρ_1 5% less than ρ_2 , and $k_1 a \approx 10$ rad.

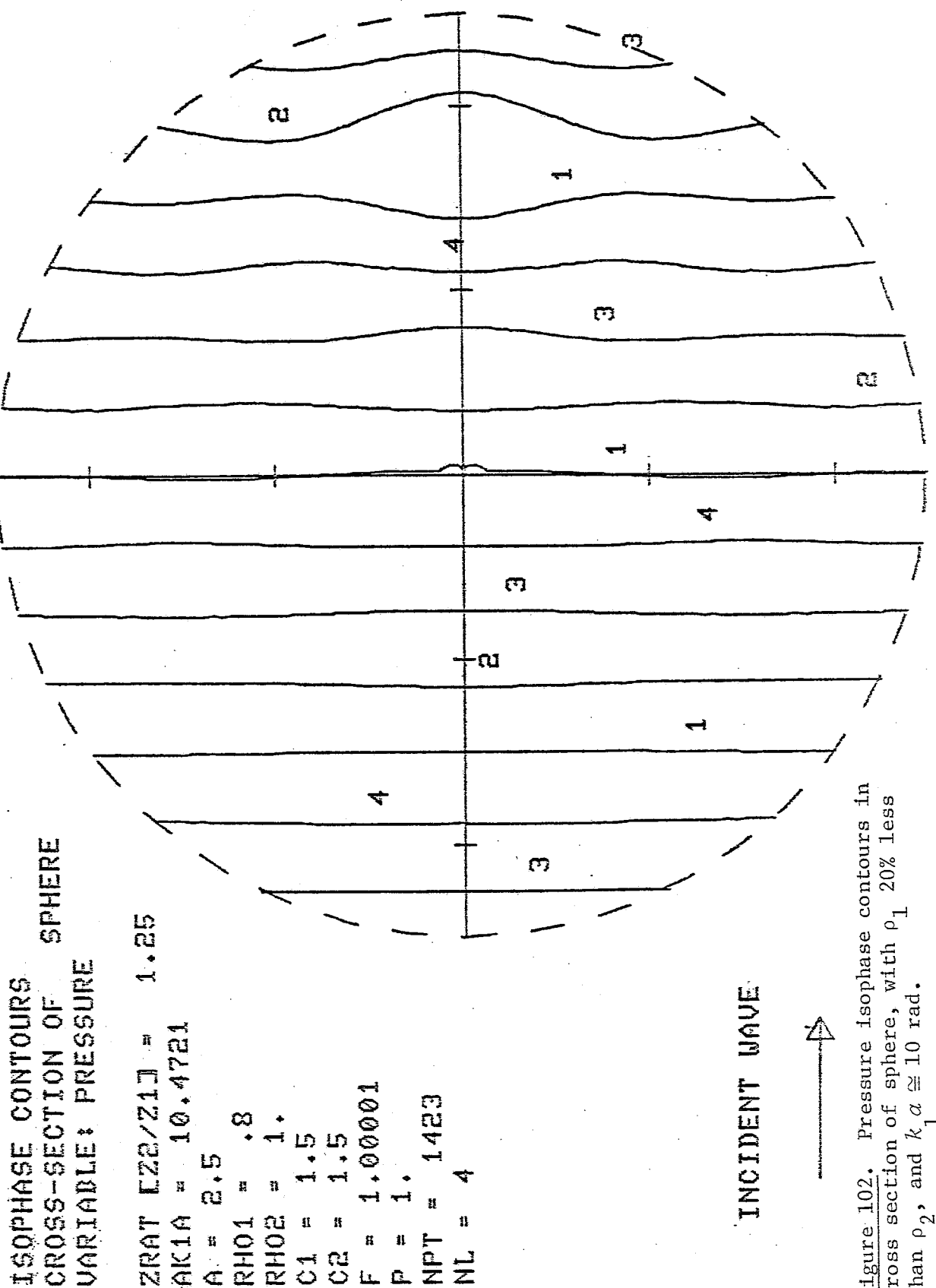


Figure 102. Pressure isophase contours in cross section of sphere, with ρ_1 20% less than ρ_2 , and $k_1 a \approx 10$ rad.